High-pressure synthesis and structural characterisation of novel rare-earth metals carbides

Doctoral Thesis

submitted to obtain the academic degree of Doctor of Natural Sciences
(Dr. rer. nat.)
of the Bayreuth Graduate School of Mathematical and Natural Sciences
(BayNAT)
of the University of Bayreuth

Fariia Iasmin Akbar

from *Moscow (Russian Federation)*

Bayreuth, 2024

This doctoral thesis was prepared at the Laboratory of Crystallography (Material Physics and Technology at Extreme Conditions Group) and the Bavarian Research Institute of Experimental Geochemistry and Geophysics (BGI) at the University of Bayreuth from 10/2021 until 04/2024 and was supervised by Prof. Dr. Leonid Dubrovinsky and Prof. Dr. Natalia Dubrovinskaia.

This is a full reprint of the thesis submitted to obtain the academic degree of Doctor of Natural Sciences (Dr. rer. nat.) and approved by the Bayreuth Graduate School of Mathematical and Natural Sciences (BayNAT) of the University of Bayreuth.

Form of the dissertation. Cumulative thesis

Date of submission: 07.05.2024

Admission by the executive board: 08.05.2024

Date of defence: 13.08.2024

Acting director: Prof. Dr. Jürgen Köhler

Doctoral committee:

Prof. Dr. Leonid Dubrovinsky (reviewer)
Prof. Dr. Sander van Smaalen (reviewer)
PD Dr. Gerd Steinle-Neumann (chair)
Prof. Dr. Natalia Dubrovinskaya

Zusammenfassung

In-situ-Untersuchungen der Chemie von Materialien unter Hochdruck-Hochtemperatur-Bedingungen (HPHT) sind für die heutige Festkörperphysik, Chemie, Materialwissenschaft sowie für die geologischen und planetarischen Wissenschaften von großer Bedeutung. Die vorliegende kumulative Dissertation stellt eine experimentelle Erforschung der Chemie von Seltenerdmetall-Kohlenstoff-Systemen unter extremen Bedingungen dar, die bisher nur unzureichend verstanden wurde. In dieser Arbeit werden die Ergebnisse verschiedener Experimente zusammengefasst, die für verschiedene Seltenerdmetall-Kohlenstoff-Systeme durchgeführt wurden und die für die Materialwissenschaft von Bedeutung sind. Diese Experimente führten zu mehreren bedeutenden Erkenntnissen, wie der Entdeckung zahlreicher bisher unbekannter Verbindungen und Strukturtypen sowie der Aufdeckung der komplexen Kristallchemie und der Regelmäßigkeiten in der strukturellen Organisation von Seltenerdmetall-Karbiden.

Zu den wichtigsten Werkzeugen, die bei diesen Studien eingesetzt wurden, gehören die laserbeheizte Diamant-Stempelzelle (DAC) zur Erzeugung hoher Drücke und hoher Temperaturen sowie die *In-situ*-Pulver- und Einkristall-Röntgenbeugung (XRD) zur Phasenidentifizierung und Strukturbestimmung und -verfeinerung. Die chemische Zusammensetzung der neuen Verbindungen wurde anhand von Einkristall-XRD-Daten bestimmt. Erste Grundsatzberechnungen im Rahmen der Dichtefunktionaltheorie (DFT) wurden durchgeführt, um zusätzliche Informationen über die strukturellen Merkmale der neuen Materialien zu erhalten.

Die systematischen Studien begannen mit Dy als repräsentativem Seltenerdelement und wurden später auf weitere Seltenerdelemente (Sc, Y, La, Nd, Sm, Gd, Dy und Yb) ausgeweitet. Ihre Reaktionen mit Kohlenstoff wurden in einem breiten Druckbereich von ~20-125 GPa bei etwa 2200-2800 K untersucht. Die Seltenerdmetallcarbide wurden durch direkte chemische Reaktionen zwischen dem Kohlenstoff aus den Diamantstempeln und den Seltenerdmetallen in DACs synthetisiert.

Erste Studien zu den chemischen Reaktionen zwischen Dysprosium und Kohlenstoff wurden bei Drücken von 19, 55 und 58 GPa und Temperaturen von ~2500 K durchgeführt. Die *In-situ*-Synchrotron-Röntgenbeugungsanalyse der Reaktionsprodukte ergab die Bildung neuartiger Dysprosiumkarbide, Dy_4C_3 und Dy_3C_2, sowie des Dysprosium-Sesquicarbids Dy_2C_3, das bisher nur unter Umgebungsbedingungen bekannt war. Es wurde festgestellt, dass

die Struktur von Dy_4C_3 eng mit der des Dysprosium-Sesquicarbids Dy_2C_3 mit der Pu_2C_3-Struktur verwandt ist.

Weitere Experimente mit Dy-Karbiden bei höheren Drücken bis zu ~95 GPa und Temperaturen bis zu ~2800 K ergaben die Bildung von drei neuen Dysprosiumkarbiden, γ-DyC_2, Dy_5C_9 und γ-Dy_4C_5, neben den bereits berichteten Dy_3C_2 und Dy_4C_3. Die Kristallstrukturen von γ-DyC_2 und Dy_5C_9 zeigen unendliche flache polyacenartige Kohlenstoffbänder bzw. *cis*-polyacetylenartige Ketten. In der Struktur von γ-Dy_4C_5 bilden die Kohlenstoffatome Dimere und nicht-lineare Trimere. Dy_3C_2 enthält ethanidartige Kohlenstoffhanteln, und Dy_4C_3 ist ein Methanid mit einzelnen Kohlenstoffatomen.

Die Experimente, die mit einer Reihe von Seltenen Erden (REE = Sc, Y, La, Nd, Sm, Gd, Dy, und Yb) durchgeführt wurden, führten zur Beobachtung neuer Strukturtypen: β-LaC, γ-SmC, γ-Y_4C_5, Nd_5C_7, La_3C_5, Dy_5C_9, γ-DyC_2, δ-NdC_2 und ε-LaC_2. Der β-LaC-Strukturtyp ist für LaC, NdC und SmC üblich; der γ-SmC-Strukturtyp – für SmC; der γ-Y_4C_5-Strukturtyp – für Sm_4C_5, Gd_4C_5, Dy_4C_5 und Yb_4C_5; der Nd_5C_7-Strukturtyp – für Nd_5C_7, Sm_5C_7, Gd_5C_7 und Yb_5C_7; der La_3C_5-Strukturtyp – für La_3C_5; der Dy_5C_9-Strukturtyp – für Y_5C_9, Nd_5C_9, Sm_5C_9, Gd_5C_9, Dy_5C_9 und Yb_5C_9; der γ-DyC_2-Strukturtyp – für YC_2, SmC_2 und DyC_2; der δ-NdC_2-Strukturtyp – für NdC_2 und SmC_2; der ε-LaC_2-Strukturtyp – für LaC_2. Es wurde festgestellt, dass Nd_5C_7 und γ-Sm_4C_5 (isostrukturell zu γ-Y_4C_5) bei Umgebungsbedingungen rückgewinnbar sind. Die bei Drücken bis zu 124 GPa und Temperaturen von ~2500 K synthetisierten Verbindungen zeigen eine reiche Vielfalt möglicher Kohlenstoffgebilde, darunter Kohlenstoffhanteln [C_2], nichtlineare Trimere [C_3], Naphthalin-Decalin-ähnliche Kohlenstofffragmente, Kohlenstoffketten und polyacenartige Bänder.

Im Zuge der Erforschung der Y-C- und Dy-C-Systeme wurden eine Reihe neuartiger Chloride, Y_2Cl und DyCl, sowie Chloridcarbide, Y_2ClC und Dy_2ClC, durch chemische Reaktionen der Proben mit den Druckmedien NaCl oder KCl bei ~40 GPa und ~2000 K synthetisiert. Obwohl diese Verbindungen nicht im Mittelpunkt dieser Studie standen, wurden ihre Strukturen gelöst und verfeinert und in die Dissertation aufgenommen, da sie als Nebenprodukte in den von uns untersuchten komplexen Systemen betrachtet wurden.

Zusammenfassend lässt sich sagen, dass die bei 20-125 GPa und ~2500 K durchgeführte Hochdruck-Hochtemperatursynthese von Seltenerdmetallcarbiden und ihre strukturelle Charakterisierung 32 neue Verbindungen ergeben hat, die zu 13 Strukturtypen gehören, von denen 9 bisher unbekannt waren. Die Tatsache, dass bestimmte Strukturtypen bei mehreren Metallen vorkommen, ist ein Beleg für die Regelmäßigkeiten in der Chemie der Seltenerdkarbide unter hohem Druck.

Summary

In situ studies of the chemistry of materials under high-pressure high-temperature (HPHT) conditions are of significant importance for contemporary solid-state physics, chemistry, materials science, as well as geological and planetary sciences. The present cumulative thesis represents an experimental exploration of the chemistry of the rare-earth metal – carbon systems under extreme conditions, which has remained poorly understood until now. This thesis compiles outcomes of various experiments performed for different rare-earth metal – carbon systems relevant to materials science, which resulted in several significant findings, such as the discovery of numerous previously unknown compounds and structural types, as well as in revealing the complex crystallochemistry and regularities in the structural organisation of rare-earth metals carbides.

The primary tools employed in these studies include the laser-heated diamond anvil cell (DAC) technique for generating high pressures and high temperatures, and *in situ* powder and single-crystal X-ray diffraction (XRD) for phase identification and structure solution and refinement. The chemical composition of the novel compounds was determined from single-crystal XRD data. First-principles calculations in the framework of the density functional theory (DFT) were conducted to provide additional information on the structural features of the novel discovered materials.

The systematic studies began with Dy as a representative rare-earth element and were subsequently expanded to include various rare-earth elements (Sc, Y, La, Nd, Sm, Gd, Dy, and Yb). Their reactions with carbon were studied in a wide pressure range of ~20-125 GPa at about 2200-2800 K. The rare-earth metal carbides were synthesized through direct chemical reactions in DACs between rare-earth metals and carbon from the diamond anvils.

Initial studies on the chemical reactions between dysprosium and carbon were studied at pressures of 19, 55, and 58 GPa and temperatures of ~2500 K. *In situ* single-crystal synchrotron X-ray diffraction analysis of the reaction products revealed the formation of novel dysprosium carbides, Dy_4C_3 and Dy_3C_2, and the dysprosium sesquicarbide Dy_2C_3 previously known only at ambient conditions. The structure of Dy_4C_3 was found to be closely related to that of dysprosium sesquicarbide Dy_2C_3 with the Pu_2C_3-type structure.

Further experiments on Dy carbides at higher pressures up to ~95 GPa and temperatures up to ~2800 K revealed the formation of three novel dysprosium carbides, γ-DyC_2, Dy_5C_9, and γ-Dy_4C_5, along with the previously reported Dy_3C_2 and Dy_4C_3. The crystal structures of γ-DyC_2 and Dy_5C_9 feature infinite flat carbon polyacene-like ribbons and *cis*-polyacetylene-type

chains, respectively. In the structure of γ-Dy_4C_5, carbon atoms form dimers and non-linear trimers. Dy_3C_2 contains ethanide-type carbon dumbbells, and Dy_4C_3 is methanide featuring single carbon atoms.

The experiments carried out on a series of rare-earth elements (REE = Sc, Y, La, Nd, Sm, Gd, Dy, and Yb) resulted in the observation of novel structure types: β-LaC, γ-SmC, γ-Y_4C_5, Nd_5C_7, La_3C_5, Dy_5C_9, γ-DyC_2, δ-NdC_2, and ε-LaC_2. The β-LaC structure type is common for LaC, NdC, and SmC; the γ-SmC structure type – for SmC; the γ-Y_4C_5 structure type – for Sm_4C_5, Gd_4C_5, Dy_4C_5, and Yb_4C_5; the Nd_5C_7 structure type – for Nd_5C_7, Sm_5C_7, Gd_5C_7, and Yb_5C_7; the La_3C_5 structure type – for La_3C_5; the Dy_5C_9 structure type – for Y_5C_9, Nd_5C_9, Sm_5C_9, Gd_5C_9, Dy_5C_9, and Yb_5C_9; the γ-DyC_2 structure type – for YC_2, SmC_2, and DyC_2; the δ-NdC_2 structure type – for NdC_2 and SmC_2; the ε-LaC_2 structure type – for LaC_2. Nd_5C_7 and γ-Sm_4C_5 (isostructural to γ-Y_4C_5) were found to be recoverable at ambient conditions. The compounds synthesized at pressures up to 124 GPa and temperatures of ~2500 K demonstrate a rich diversity of possible carbon entities encompassing carbon dumbbells [C_2], non-linear trimers [C_3], naphthalene-decalin-like carbon fragments, carbon chains, and polyacene-like ribbons.

In the course of the exploration of the Y-C and Dy-C systems, a number of novel chlorides, Y_2Cl and DyCl, and chloride carbides, Y_2ClC and Dy_2ClC, have been synthesized as a result of chemical reactions of the samples with the NaCl or KCl pressure media at ~40 GPa and ~2000 K. Although such compounds were not the focus of this study, their structures were solved and refined, and included in the thesis considering them as by-products in the complex systems we have investigated.

To summarise, high-pressure high-temperature synthesis of rare-earth metals carbides, realized at 20-125 GPa and ~2500 K, and their structural characterisation revealed 32 novel compounds, which belong to 13 structural types, among which 9 were previously unknown. The fact that certain structure types are common for several metals gives evidence of the regularities in the chemistry of rare-earth carbides under high pressure.

Acknowledgments

I would like to express my gratitude to my supervisors, Prof. Dr. Leonid Dubrovinsky and Prof. Dr. Natalia Dubrovinskaia, for their invaluable guidance, support, and patience. As a newcomer to the field of high-pressure high-temperature science, I entered with a willingness to learn and gain new experiences. I am thankful for the inspiration I received through our discussions and for the opportunity to work in such a wonderful scientific atmosphere, surrounded by the most friendly and supportive group I could have imagined.

I am also thankful to all members of the BGI, with whom I spent the majority of my working time, for a pleasant and amiable environment. Special thanks to Prof. Dr. Hans Keppler, Prof. Dr. Tomoo Katsura, Prof. Dr. Dan Frost, Dr. Catherine McCammon, and Dr. Tiziana Boffa-Ballaran. Their lectures, insightful discussions, and corrections played a significant role in introducing me to the field of geoscience and enhancing my skills. I would like to extend my gratitude to the administrative and technical staff of BGI, Petra Buchert, Janina Potzel, Anna Dinius, Olga Gaspert, Detlef Krausse, Stefan Übelhack, Sven Linhardt, Raphael Njul, and Trenz Ulrike, for their invaluable assistance with various matters. Many thanks to Dorothea Wiesner, whose patient guidance and support were instrumental in my learning of SEM and TEM techniques. I am particularly appreciative of Dr. Gerd Steinle-Neumann for his extremely helpful discussions, assistance, and advice during my learning of theoretical calculation fundamentals. I am truly grateful to Dr. Florian Heidelbach for translating the Summary of this thesis into German.

I would like to thank everyone at the Laboratory of Crystallography for such a welcoming and warm environment. I especially appreciate the support and informative lectures given by Prof. Dr. Sander van Smaalen and PD Dr. Andreas Schönleber. Additionally, I am thankful to Denis Kelk-Huth, the secretary, for always being available to assist with any administrative questions or issues.

Having conducted numerous synchrotron experiments, I express my gratitude to the local contacts who provided support and assistance. I am thankful for the indispensable help from Dr. Hanns-Peter Liermann, Dr. Konstantin Glazyrin, and Dr. Timofey Fedotenko at P02.2 (Petra III, DESY), Dr. Vitali Prakapenka and Dr. Stella Chariton at IDD-13 (APS), Dr. Michael Hanfland, Dr. Jonathan Wright, Dr. Gaston Garbarino, Dr. Alexander Chumakov, Dr. Georgios Aprilis, Dr. Anna Pakhomova, Dr. Eleanor Lawrence Bright, and Dr. Davide Comboni at ESRF. Without their assistance, this work would be considerably more challenging to accomplish.

Sincere thanks to Prof. Dr. Maxim Bykov, Prof. Dr. Elena Bykova, Dr. Dominique Laniel, and Dr. Sergey Ovsyannikov, great teachers and advisors. I highly appreciate all the things you taught me during our time together. Your expertise has been invaluable in helping me master new skills and knowledge. Thank you very much!

I am very thankful to my big “Bayreuth family”, Alena Aslandukova, Andrii Aslandukov, Arina Aslandukova, Pavel Milkin, Ilia Sadilov, Anatoly Arkhipin, Yuqing Yin, Alexander Kurnosov, Naira Martirosyan, Dmitry Bondar, Artem Chanyshev, Edith Kubik, Amrita Chakraborti, and everyone who participated in “Thursdays”, providing me with pleasant moments after work. I want to express my heartfelt gratitude to all of you for the time we have shared, your kindness, your support, and the knowledge and skills you helped me to acquire. From the long days and nights we have spent together during beamtimes, to the holidays and travels we have enjoyed, you have all been there for me through it all. All of these things mean more to me than words can express. Thank you all for everything over these past three years.

I feel fortunate to have immersed myself in the world of science. I am deeply grateful to Prof. Dr. Andrey Rafailovich Kaul, my first scientific mentor, who showed me the charm of science and inspired me.

It is impossible to fully express my gratitude to my mother, Irina Nikolaeva, and my sister, Fakhima Iasmin Akbar. They are the most important people in my life and are always on my side through life's challenges. I am especially grateful for their invaluable advice whenever I need it. Thank you both for your understanding, unwavering support, and love.

Table of Contents

1. Introduction

Carbon, next to hydrogen, helium, and oxygen, is one of the most abundant elements in the Universe and plays a crucial role in the chemical evolution of galaxies [1]. The convincing evidence that the bulk Earth has a relative rare-earth elements (REE) distribution similar to that of chondritic meteorites allows to present elements abundances of the Earth's mantle normalized to CI chondrite and the refractory element Ti, where REE normalized abundance is equal to 1 (Fig. 1.1a) [2–4]. Since the Earth's mantle undergoes pressures ranging from 24 to 135 GPa and temperatures spanning 1900 to 4000 K (Fig. 1.1b), it becomes intriguing to explore chemical processes involving REE contained in the Earth's mantle and products of the chemical reactions under extreme conditions. It is especially important in light of the lack of available data on high-pressure chemistry of rare-earth metals carbides and related materials, which almost have not been investigated under high pressure [5–12]. At the same time, the published data revealed promising perspectives and highlighted the potential for further exploration under extreme conditions.

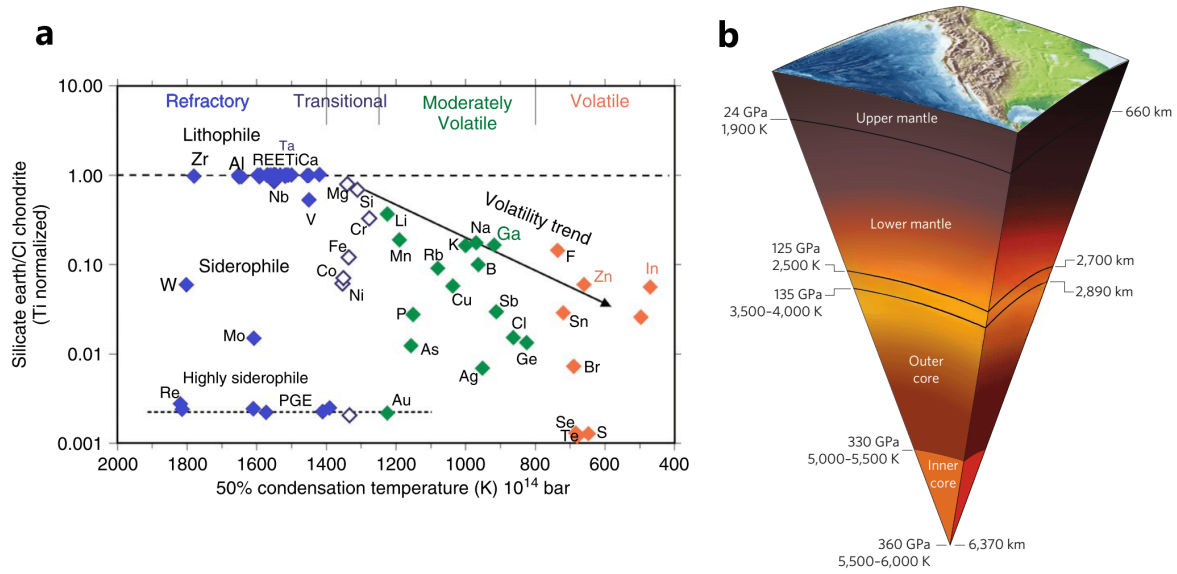

Figure 1.1. (a) Element abundances of the Earth's mantle normalized to CI chondrite and the refractory element Ti plotted against their 50% condensation temperatures (modified after [3,4]). (b) Cross-section of Earth's interior (modified after [13]).

Carbides themselves are known for their chemical inertness, high melting points, and interesting electrical properties which make the reason to explore such systems [14–16]. Structural variations as a function of composition and external parameters (pressure and temperature) often result in the formation of carbides with various types of chemical bonding, as well as with fascinating crystal chemistry [15,17–19]. Taking into account the relatively low

number of known binary compounds containing carbon in comparison with oxygen-containing ones (1329 vs 4768 according to the ICSD database Version 5.2.0 (build 20240410-1029) - Data Release 2024.1), it can be established that, in general, the chemistry of carbides is still insufficiently studied. This is especially true for rare-earth metal carbides. Despite this, the lanthanide carbides family shows an extensive variety of known phases with different stoichiometry and structure [5].

Carbide systems encompass a wide range of materials, including binary and ternary two-dimensional compounds known as ‘MXenes’ and ‘MAXenes’ [20,21]. These materials possess promising features, which make them appealing for applications in fields such as optoelectronics, storage materials, sensors, biomedicine, and others (Fig. 1.2) [20].

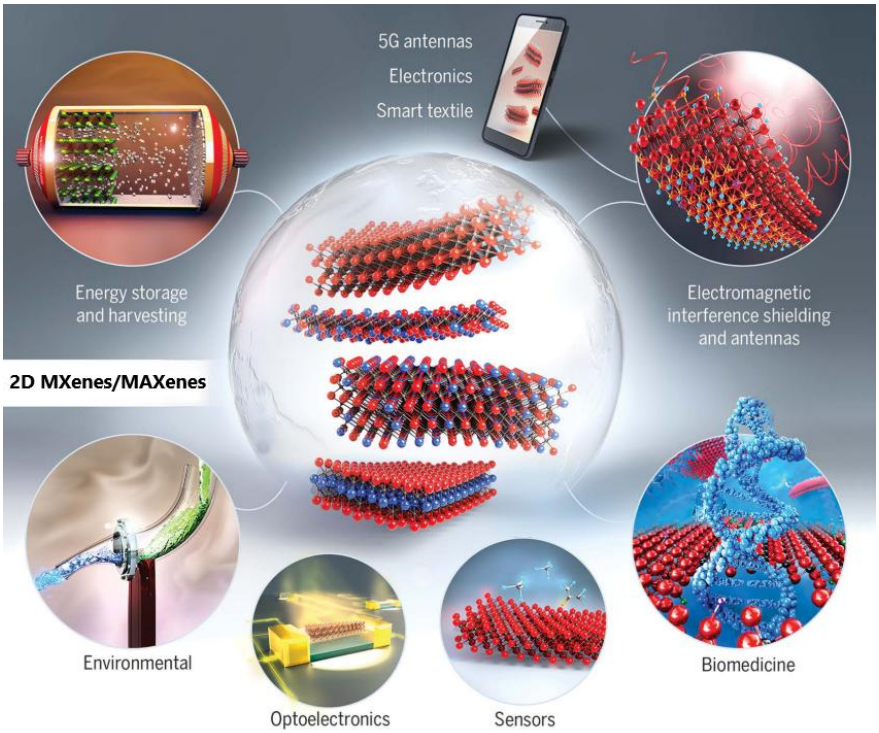

Figure 1.2. Structure and applications of 2D carbides and nitrides (MXenes/MAXenes) (modified after [20]).

The high-pressure approach serves as a valuable method for delving into the crystal chemistry of compounds that remain undiscovered under ambient conditions. This method unveils novel forms of chemical bonding and promising properties, including high hardness, chemical inertness, electrical, magnetic, optical properties, and even superconductivity, traits well-established in carbides under ambient conditions [15,16,22,23]. Through this methodology, we can broaden the range of carbide compounds, which hold significant relevance in both science and technology due to their interesting characteristics. This is particularly true for the rare-earth carbides, which have the potential to exhibit promising

properties due to the accessibility of enormous magnetic moments [24], that could hold significant implications in single-molecule magnetism and the design of new bulk magnet materials. Larger magnetic moments can decline the magnetization tunnelling in molecular materials, which is currently one of the serious disadvantages in the design of single-molecule magnets with increased temperatures of hysteresis [25]. Structural adaptations driven by composition and external factors like pressure and temperature frequently give rise to carbides with diverse forms of chemical bonding, revealing a rich landscape of captivating crystal chemistry.

Rare-earth carbides have predominantly been investigated at ambient pressure (Table 1.1) [5]. Carbides of anti-$CdCl_2$ and NaCl structural types have been predominantly synthesized through arc-melting or arc-welding compressed pellets containing the stoichiometric mixture of filings of the rare-earth element and carbon [26–32], or by heating weighed amounts of the metal and carbon at 1200-2500°C [18,33–35].

The crystal structure of anti-$CdCl_2$-type rare-earth carbides is represented by space group *R*-3*m* (#166) and $Z = 3$ formula units per cell for Sc [5,27], Y [5,28], Gd [5,29], Tb [5,30], Dy [5,30], Ho [5,31], Yb [5,32]. In the case of Sc_2C [27], the lattice parameters are $a = 3.33675(11)$ Å and $c = 16.3458(12)$ Å. The rare-earth metal atoms occupy the 6*c* Wyckoff position, and carbon atoms occupy the 3*a* site. The Sc-C bond length is 2.29308(8) Å, and the coordination number (CN) of Sc is 3. Both the metal and carbon atoms form a distorted cubic close packing (*ccp*) (Fig. 1.3a, b).

The other known scandium carbide polymorph, Sc_2C [36], crystallizes in the space group *P*-3*m*1 (#164) with $Z = 1$ and lattice parameters $a = 3.387(1)$ Å and $c = 6.703(2)$ Å. Scandium atoms occupy the 2*d* Wyckoff site, while carbon atoms are at the 1*b* site. The Sc-C interatomic distance is 2.2900(6) Å (CN = 3). Scandium atoms are arranged in a distorted hexagonal close packing (*hcp*) (Fig. 1.3c).

Carbides of defect NaCl structure type (space group *Fm*-3*m*, #225, $Z = 4$) are known for Sc [5,33,34], Y [5,18,26], Ce [35], Sm [5,18], Eu [5], Gd-Lu [5,18]. For example, the lattice parameter of $YC_{0.44}$ is $a = 5.115(2)$ Å (CN(Y) = 6). The Wyckoff sites 4*a* and 4*b* are occupied by the metal and carbon atoms, respectively. Both the metal and carbon atoms form a *ccp* (Fig. 1.3d).

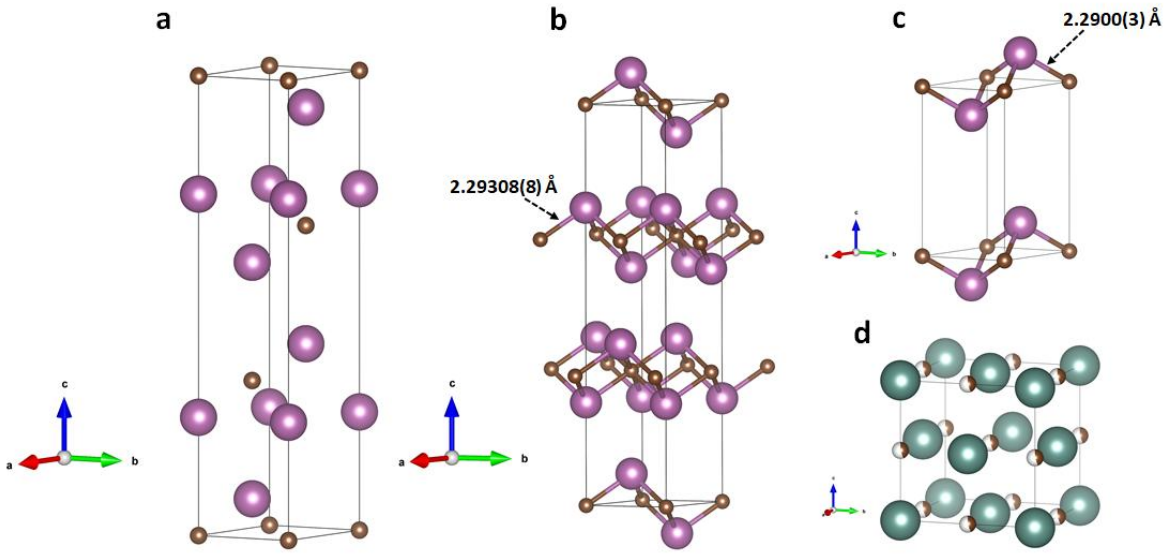

Figure 1.3. Crystal structures of (a)-(b) *hR*9 Sc_2C [27], (c) *hP*3 Sc_2C [36], (d) *cF*8 $YC_{0.44}$ [26].

Carbides of anti-Th_3P_4, α-Y_4C_5, $Sc_{15}C_{19}$, Sc_3C_4, α-Ho_4C_7, and Lu_4C_7 structural types (Table 1.1) were mainly synthesized by arc-melting small cold-pressed pellets of the elemental components taken in specific ratios in an atmosphere of argon [19,37–42]. In contrast, sesquicarbides of rare-earth elements with Pu_2C_3-type structure, as reported in the literature, have been synthesized using more diverse range of methods: 1) reaction of pure metal and graphite in high vacuum at 1200°C [33], 2) synthesis in a multi-anvil high-pressure apparatus at 3.5-5.0 GPa and 1400-1600°C [10], 3) arc-melting a compressed mixture of metal and carbon powder [18], 4) heating weighed amounts of metal and carbon in a Ta bomb at 1200-2000°C [18], and 5) synthesis from elements followed by thermobaric treatment under pressures of 30 kbar to 90 kbar and at temperatures of 1200°C to 1400°C [43].

The anti-Th_3P_4 structural type is known only for Sc [5,42,44,45]. The Sc_4C_3 scandium carbide has a cubic unit cell (space group *I*-43*d*, #220, $Z = 4$) with lattice parameter $a = 7.2081(4)$ Å. The 16*c* Wyckoff positions are occupied by scandium atoms and the 12*a* sites are occupied by carbon atoms (Fig. 1.4a, b). The coordination polyhedron of scandium atoms is an irregular octahedron formed by six nearest carbon atoms at distances of 2.255(5)-2.778(4) Å (Fig. 1.4e).

The Pu_2C_3 structural type is known for Sc [33], Y [10], La-Nd [5,18], Sm [5,18], Eu [5,46], Gd-Ho [5,18], Er-Lu [43]. The cubic Y_2C_3 yttrium sesquicarbide (space group *I*-43*d*, #220, $Z = 8$) has unit cell parameter $a = 8.2372(3)$ Å. The 16*c* Wyckoff sites are occupied by yttrium atoms and the 24*d* positions are occupied by carbon atoms forming dumbbells [C_2]

with a C-C distance of 1.298(5) Å (Fig. 1.4c, d, g, h). The coordination environment of yttrium atoms consists of nine nearest carbon atoms at distances of 2.5102(9)-2.8097(14) Å (Fig. 1.4g).

The structures of Sc_4C_3 and Y_2C_3 are closely related (Fig. 1.4) since they are both of the same space group (*I*-43*d*). Specifically, Sc_4C_3 can be seen as derived from Y_2C_3, as the positions of the centers of carbon dimers [C_2] in the sesquicarbide align with the positions of the discrete carbon atoms in the anti-Th_3P_4-type carbide. The coordinates of metal atoms are the same in both structures, and the coordination environment of a discrete carbon atom in Sc_4C_3 is similar to that of a carbon dumbbell [C_2] in Y_2C_3 (Fig. 1.4f, h).

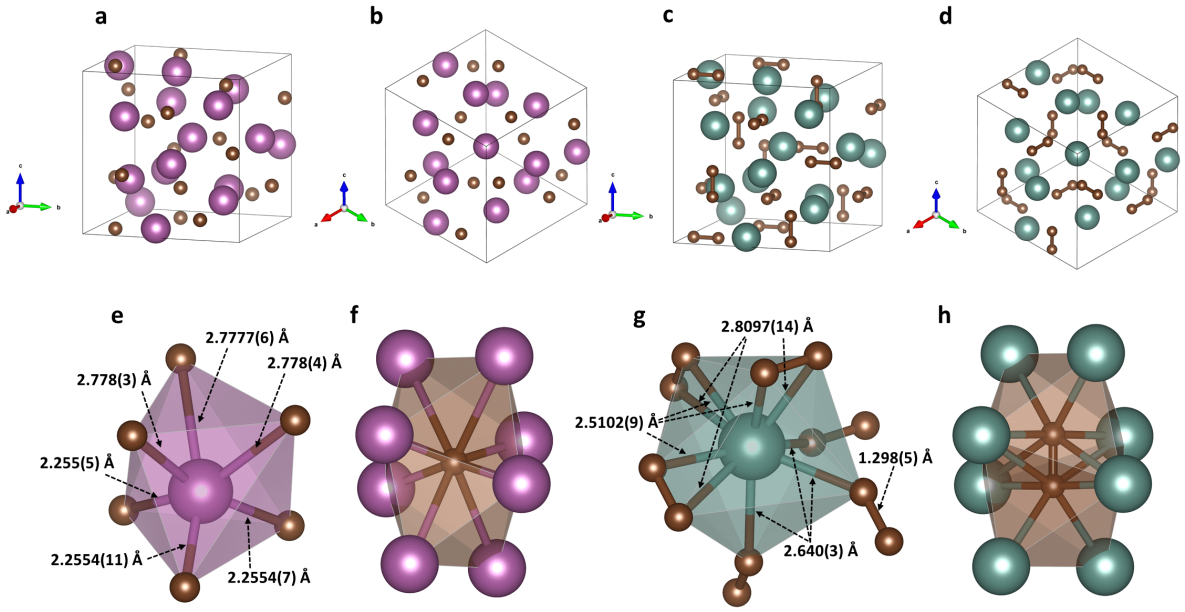

Figure 1.4. Crystal structures of (a)-(b) *cI*28 Sc_4C_3 [42,45], (c)-(d) *cI*40 Y_2C_3 [10]. Coordination environment of metal and carbon atoms in (e)-(f) Sc_4C_3, (g)-(h) Y_2C_3.

The α-Y_4C_5 structural type is known for Y and Gd-Ho [5,40]. The α-Y_4C_5 yttrium carbide crystallizes in the orthorhombic symmetry space group *Pbam* (#55) with $Z = 2$ and the lattice parameters: $a = 6.5735(9)$ Å, $b = 11.918(1)$ Å, and $c = 3.6692(5)$ Å. The Y1 and Y2 atoms occupy two crystallographically distinct positions: 4*h* and 4*g*, respectively. There are two types of carbon entities in this structure: carbon dumbbells, with d(C-C) = 1.335(16) Å, formed by C1 and C2 atoms located at the 4*g* Wyckoff position, and discrete carbon atoms, denoted as C3, at the 2*b* site (Fig. 1.5a). As seen in Fig. 1.6a, the Y1 atoms are nine-fold coordinated by C atoms forming a distorted elongated square pyramid (CN = 9) with the Y1-C distances ranging from 2.4353(13) Å to 2.873(10) Å, while the Y2 atoms are surrounded by five nearest carbon atoms forming distorted triangular bipyramid (CN = 5) with the Y2-C distances of 2.390(12) – 2.648(13) Å. The structure is presented by two alternate layers

containing Y1 atoms with discrete carbon atoms and Y2 atoms with carbon dumbbells (Fig. 1.5a).

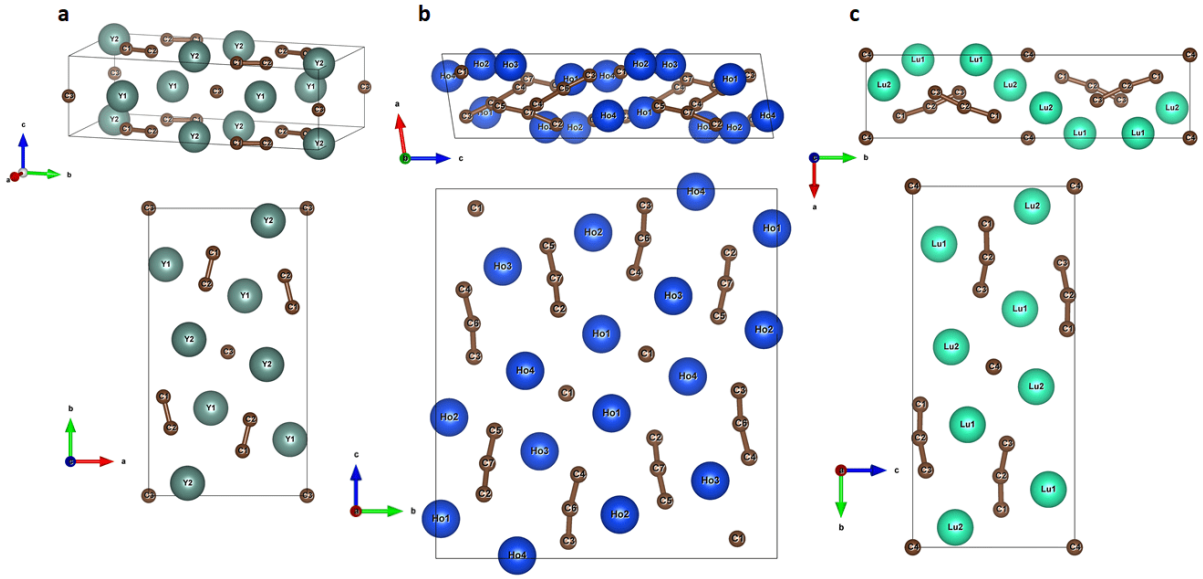

Figure 1.5. Crystal structures of (a) *oP*18 α-Y_4C_5 [40], (b) *mP*44 α-Ho_4C_7 [39], (c) *mP* Lu_4C_7 [38].

The α-Ho_4C_7-type structure, reported for Y [5,39], Dy [5], and Ho [5,39], has a monoclinic unit cell (space group $P2_1/c$, #14, $Z = 4$). The α-Ho_4C_7 lattice parameters are a = 3.6806(3) Å, b = 12.518(1) Å, c = 13.644(2) Å, β = 96.62(1)°. The structure is composed of eleven crystallographically distinct atoms, Ho1, Ho2, Ho3, Ho4, C1, C2, C3, C4, C5, C6, and C7, located at the 4*e* Wyckoff positions (Fig. 1.5b). The C2-C7 carbon atoms form almost linear trimers [C_3] with d(C2-C7) = 1.33(4) Å, d(C5-C7) = 1.31(4) Å, d(C3-C6) = 1.27(4) Å, and d(C4-C6) = 1.38(4) Å (Fig. 1.6b). The coordination numbers of the metal atoms are CN(Ho1) = 7 with d(Ho1-C) = 2.521(13)-2.89(3) Å, CN(Ho2) = 8 with d(Ho2-C) = 2.41(3)-2.67(3) Å, CN(Ho3) = 9 with d(Ho3-C) = 2.347(11)-2.92(3) Å, and CN(Ho4) = 7 with d(Ho4-C) = 2.48(3)-2.97(3) Å (Fig. 1.6b).

The Lu_4C_7 structural type is known for Y [5,37], Ho-Tm [5,38], and Lu [5,38]. The Lu_4C_7 lutetium carbide has a monoclinic unit cell (space group $P2_1/c$, #14, $Z = 2$) with the lattice parameters: a = 3.604(1) Å, b = 13.514(3) Å, c = 6.290(2) Å, β = 104.97(2)°. Crystallographically distinct metal atoms, Lu1 and Lu2, and carbon atoms, C1, C2, and C3 forming almost linear trimers [C_3] with d(C1-C2) = 1.321(10) Å and d(C2-C3) = 1.349(9) Å, occupy 4*e* Wyckoff positions. Discrete C4 atoms are at the 2*a* site (Fig. 1.5c). Lu1 atoms are nine-fold coordinated by nearest carbon atoms with d(Lu1-C) = 2.3796(14)-2.771(8) Å, while Lu2 atoms are seven-fold coordinated by nearest carbon atoms with d(Lu2-C) = 2.403(8)-2.921(8) Å (Fig. 1.6c).

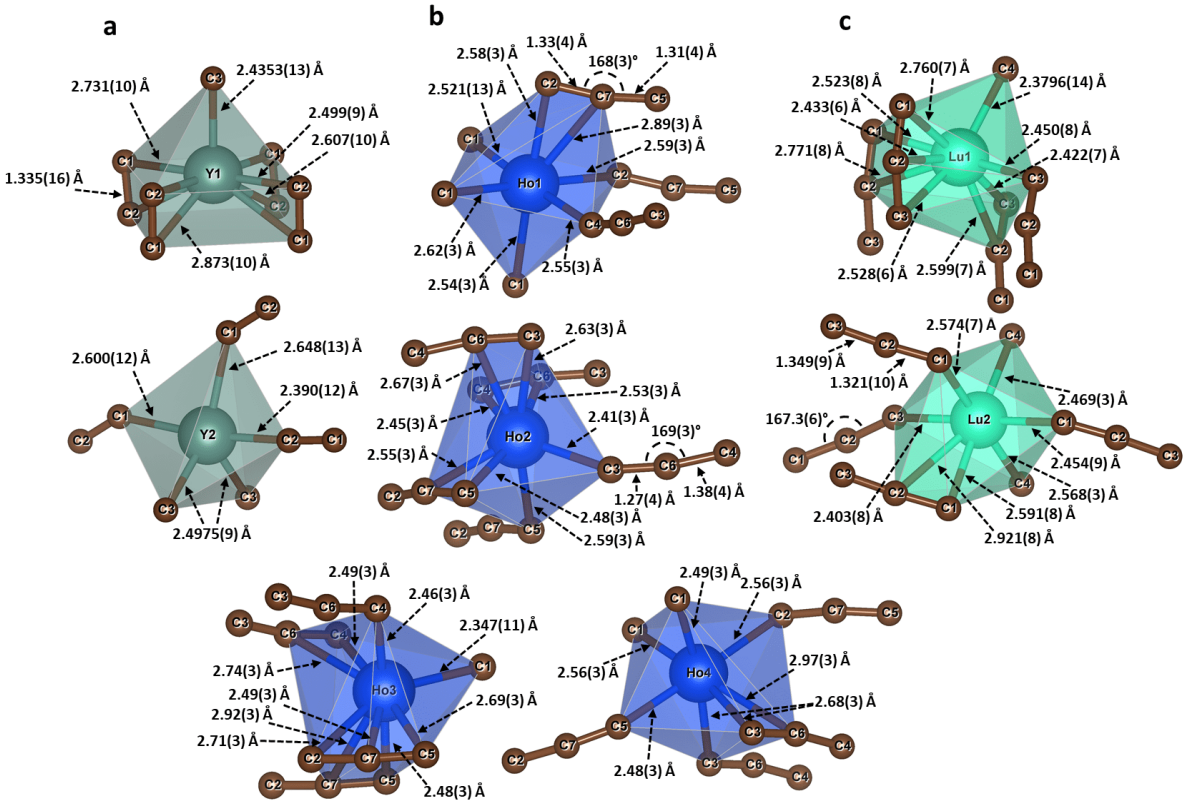

Figure 1.6. Coordination environment of metal atoms in (a) *oP*18 α-Y_4C_5 [40], (b) *mP*44 α-Ho_4C_7 [39], (c) *mP* Lu_4C_7 [38].

Considered carbides *oP*18 α-Y_4C_5 [40], *mP*44 α-Ho_4C_7 [39], and *mP*22 Lu_4C_7 [38] exhibit geometrically similar motifs. In both α-Y_4C_5 and Lu_4C_7, metal atoms are located in the unit cell projection along the *c*-axis (in α-Y_4C_5) and *a*-axis (in Lu_4C_7) in a similar manner. However, unlike α-Y_4C_5, in Lu_4C_7, the layer arranged by Lu2 atoms and [C_3] units, located between flat layers comprising Lu1 and discrete C4 atoms, is not planar (Fig. 1.5c). The α-Ho_4C_7 and Lu_4C_7 have quite close lattice parameters, with one of the parameters appearing to be "multiplied by 2" ($b_{\alpha-Ho_4C_7} \sim c_{Lu_4C_7}\times 2$). Moreover, geometrically α-Ho_4C_7 shows affinity with Lu_4C_7, especially in the projection of unit cells along the *a*-axis (Fig. 1.5b, c).

The next family of carbides includes the following analogous structural types: $Sc_{15}C_{19}$ (space group *P*-42$_1$*c*, #114) [47], $Sc_{15}C_{19}$ (space group *P*4/*mnc*, #128) [41], and Sc_3C_4 (space group *P*4/*mnc*, #128) [19] (Fig. 1.7). The rare-earth metal carbides of the stoichiometry $REE_{15}C_{19}$ (REE = Sc [47], Y [48], Ho [49], Er [50], Tm [49], Yb [51], Lu [52]) were previously reported as phases with the *P*-42$_1$*c* space group (#114). The Sc_3C_4-type structure is known for Sc [5,19], Y [5,19], Tb [5], Dy [5,37], and Ho-Lu [5,19].

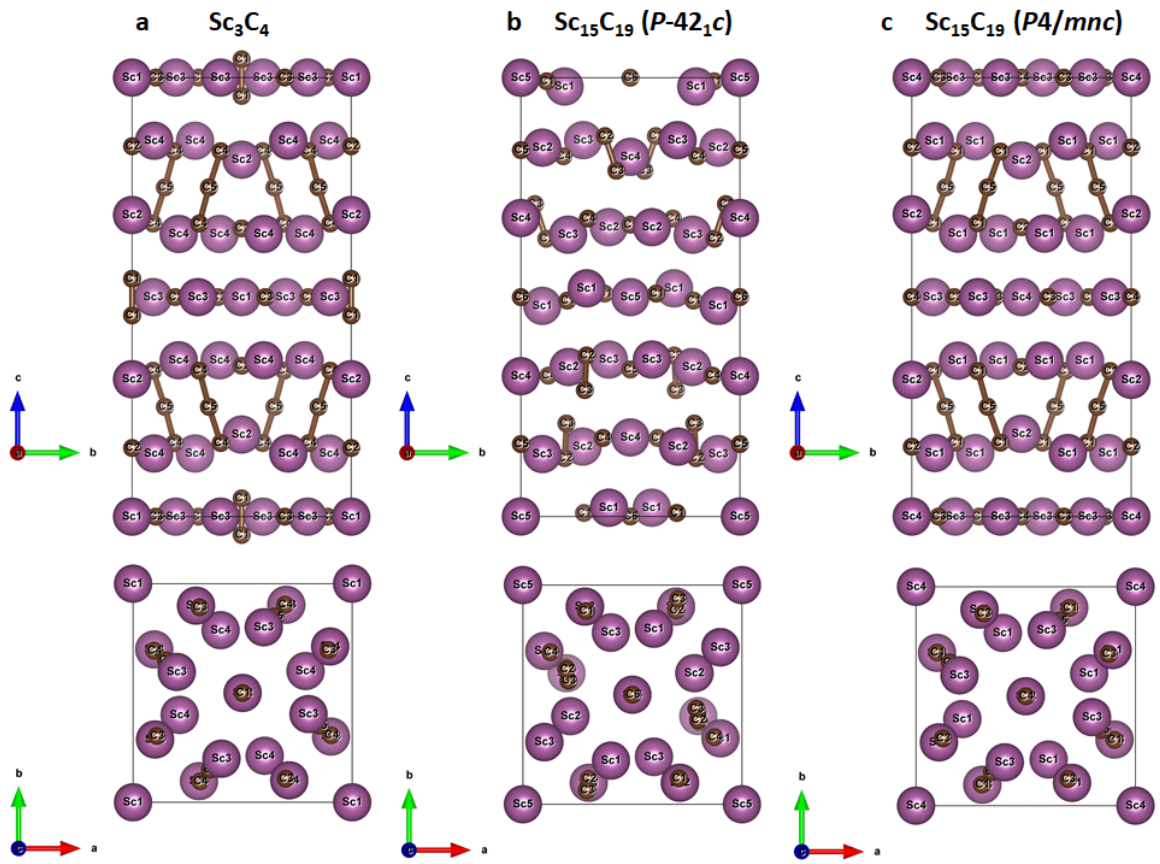

Figure 1.7. Crystal structures of (a) *tP*70 Sc_3C_4 [19], (b) *tP*68 $Sc_{15}C_{19}$ (*P*-42$_1$*c*) [47], (c) *tP*68 $Sc_{15}C_{19}$ (*P*4/mnc) [41].

The Sc_3C_4 [19] carbide crystallizes in the tetragonal space group *P*4/*mnc* (#128) with *Z* = 10 and lattice parameters *a* = 7.4873(5) Å and *c* = 15.026(2) Å. Scandium atoms occupy 2*a* (Sc1), 4*e* (Sc2), 8*h* (Sc3), and 16*i* (Sc4) Wyckoff sites, while carbon atoms are located at the 4*e* (C1 and C2), 8*h* (C3), 16*i* (C4), and 8*g* (C5) positions (Fig. 1.7a). The structure contains discrete carbon atoms (C2 and C3), carbon dimers [C_2], formed by C1 atoms with a C-C bond length of 1.253(13) Å, and trimers [C_3], formed by C4 and C5 atoms with a C-C bond length of 1.342(4) Å. The metal atoms are coordinated with various number of nearest carbon atoms: CN(Sc1) = 6 with *d*(Sc1-C) = 2.350(5) Å or 2.409(5) Å, CN(Sc2) = 6 with *d*(Sc2-C) = 2.183(7)-2.424(4) Å, CN(Sc3) = 7 with *d*(Sc3-C) = 2.301(5)-2.5188(16) Å, and CN(Sc4) = 7 with *d*(Sc4-C) = 2.1655(6)-2.668(4) Å (Fig. 1.8a).

The $Sc_{15}C_{19}$ (space group *P*-42$_1$*c*, #114, *Z* = 2) [47] is characterized by lattice parameters *a* = 7.50(1) Å and *c* = 15.00(2) Å. The metal atoms occupy the 8*e* (Sc1, Sc2, Sc3), 4*c* (Sc4), and 2*a* (Sc5) Wyckoff sites, and the carbon atoms occupy 8*e* (C1, C2, C3, C4), 4*c* (C5), and 2*b* (C6) positions (Fig. 1.7b). The carbon dumbbells [C_2] are formed by C2 and C3 atoms with a carbon-carbon bond length of 1.25(4) Å, the other carbon atoms are discrete. There are various coordination environments of scandium atoms: CN(Sc1) = 6 with *d*(Sc1-

C) = 2.27(4)-2.54(4) Å, CN(Sc2) = 7 with *d*(Sc2-C) = 2.243(6)-2.712(18) Å, CN(Sc3) = 7 with *d*(Sc3-C) = 2.252(17)-2.768(19) Å, CN(Sc4) = 8 with *d*(Sc4-C) = 2.292(17)-2.703(6) Å, CN(Sc5) = 6 with *d*(Sc5-C) = 2.34(4) Å or 2.475(16) Å (Fig. 1.8b).

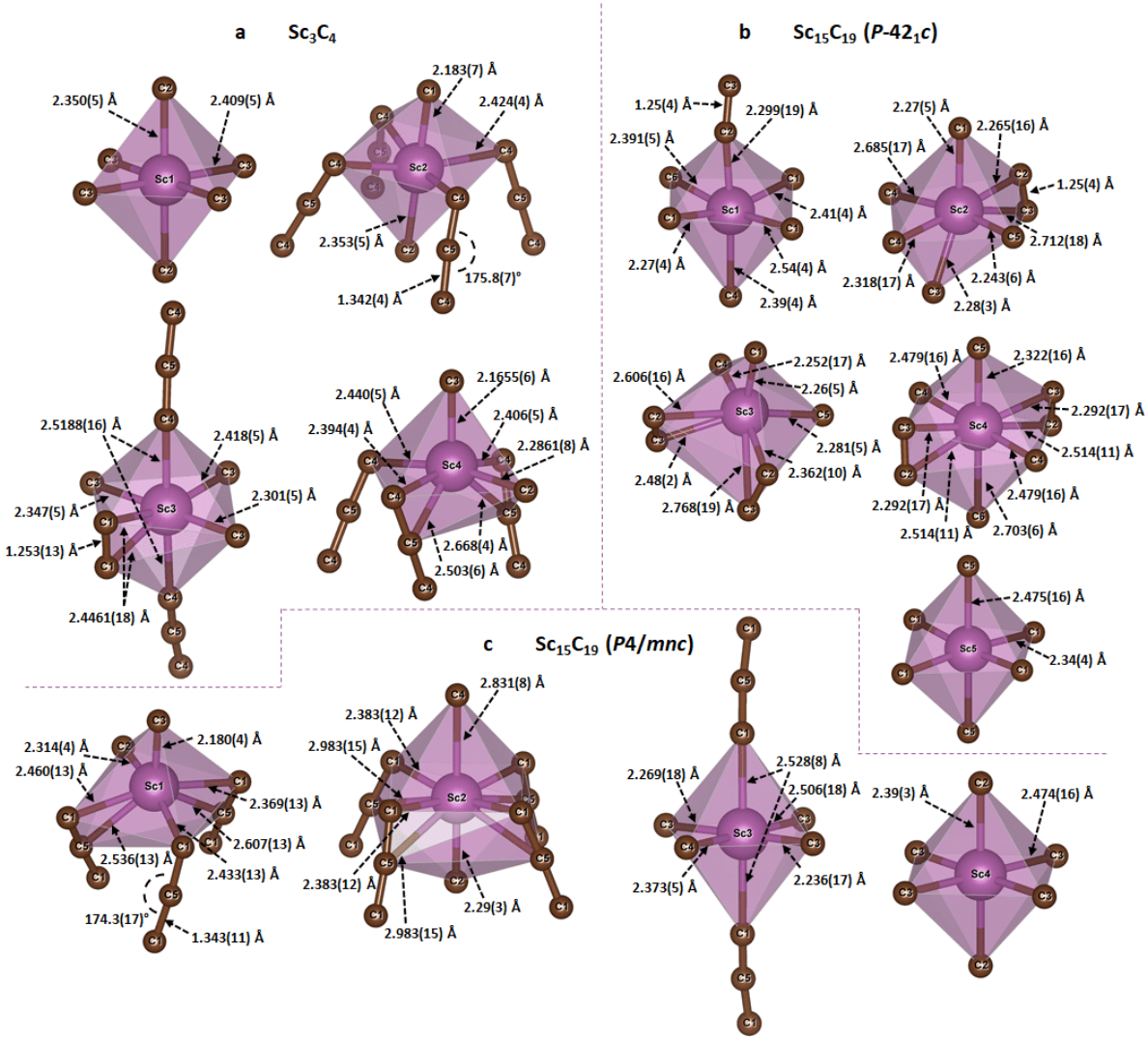

Figure 1.8. Coordination environment of metal atoms in (a) *tP*70 Sc_3C_4 [19], (b) *tP*68 $Sc_{15}C_{19}$ (*P*-42$_1$*c*) [47], (c) *tP*68 $Sc_{15}C_{19}$ (*P*4/mnc) [41].

The $Sc_{15}C_{19}$ (space group *P*4/*mnc*, #128, *Z* = 2) [41] has lattice parameters *a* = 7.4922(1) Å and *c* = 15.0095(4) Å. Its unit cell contains four crystallographically distinct metal atoms at the 16*i* (Sc1), 4*e* (Sc2), 8*h* (Sc3), and 2*b* (Sc4) Wyckoff positions, and five crystallographically distinct carbon atoms at the 16*i* (C1), 4*e* (C2), 8*h* (C3), 2*a* (C4), and 8*g* (C5) sites (Fig. 1.7c). In the crystal structure of $Sc_{15}C_{19}$, C1 and C5 atoms form almost linear carbon trimers [C_3] with a C-C bond length of 1.343(11) Å, while C2, C3, and C4 atoms are single. The coordination numbers of scandium atoms are as follows: CN(Sc1) = 7 with *d*(Sc1-C) = 2.180(4)-2.607(13) Å, CN(Sc2) = 10 with *d*(Sc2-C) = 2.29(3)-2.983(15) Å, CN(Sc3) = 6

with d(Sc3-C) = 2.236(17)-2.528(8) Å, and CN(Sc4) = 6 with d(Sc4-C) = 2.39(3) Å or 2.474(16) Å (Fig. 1.8c).

$Sc_{15}C_{19}$ (*P*-42$_1$*c*), $Sc_{15}C_{19}$ (*P*4/*mnc*), and Sc_3C_4 (*P*4/*mnc*) differ in their carbon entities. While discrete carbon atoms are found in all three structures, the carbon atoms in the $Sc_{15}C_{19}$ (*P*-42$_1$*c*) form dumbbells [C_2], contrasting with the presence of nearly linear trimers [C_3] in the $Sc_{15}C_{19}$ (*P*4/*mnc*) (Fig. 1.7c). The structure of Sc_3C_4 (*P*4/*mnc*) consists of both [C_3] and [C_2] units (Fig. 1.7a). Interestingly, the structure of $Sc_{15}C_{19}$ (*P*4/*mnc*) can be derived from that of Sc_3C_4 if carbon dimers are replaced by discrete carbon atoms (Fig. 1.7a, c).

Rare-earth dicarbides described in the literature were prepared mostly by 1) arc-melting or arc-welding stoichiometric mixtures of pure metal and graphite under a purified argon atmosphere [32,53–55] or helium atmosphere at 800 mbar [56], 2) standard direct current arc experiment applying about 20 V at 110 A under a partial hydrogen pressure of 1.3×10^4 Pa (in the case of Y_2O_3 precursor) [57], 3) carbonization of the oxide at 1600°C under a vacuum of 10^{-4} mmHg [58].

There are three known rare-earth dicarbide structural types: cubic KCN-type (La [5,53], Eu [5,56], Tb [59], Lu [5,60]), tetragonal CaC_2-type (Y [5,57], La [5,54], Ce [5,58], Pr [5,61], Nd [5,62], Sm [5,18], Eu [5,56], Gd [5,63], Tb [5,63], Dy [5,63], Ho [5,64], Er [5,55], Tm [5,18], Yb [5,32], Lu [65]), and monoclinic ThC_2-type (Eu [56]). The KCN-type carbides (space group *Fm*-3*m*, #225, Z = 4) are reported in the literature as structures, where carbon dumbbells [C_2] are completely distorted [56]. Thus, in the work [56], *cF*12 EuC_2 (the high-temperature modification) represents the structure with the lattice parameter a = 6.1378(3) Å, where centers of gravity of [C_2] dumbbells reside in the centers of the Eu_6 octahedra, which are no longer distorted so that a perfect NaCl-type structure arrangement results. Contrary, the LaC_2 [53], TbC_2 [59], and LuC_2 [60] (Fig. 1.9a) were reported as KCN-type carbides with carbon atoms partially occupying 32*f* Wyckoff sites and metal atoms at 4*a* positions.

The CaC_2-type carbides crystallize in the tetragonal space group *I*4/*mmm* (#139) with Z = 2. For example, LuC_2 lutetium carbide has lattice parameters a = 3.5630(15) Å and b = 5.964(9) Å [65]. The 2*a* Wyckoff sites are occupied by lutetium atoms, and 4*e* positions are occupied by carbon atoms forming dumbbells [C_2] with a C-C distance of 1.276(7) Å (Fig. 1.9b). The coordination environment of metal atoms consists of the ten nearest carbon atoms at distances of 2.5990(13) Å or 2.344(5) Å (Fig. 1.9e). The coordination polyhedron of carbon atoms is an octahedron formed by six nearest metal atoms (Fig. 1.9f).

EuC_2 dicarbide with ThC_2-type structure has a monoclinic unit cell (space group *C*2/*c*, #15, Z = 4) with the lattice parameters: a = 7.00746(20) Å, b = 4.40984(13) Å,

c = 7.59103(22) Å, *β* = 106.9183(16)° [56]. Europium atoms occupy *4*e Wyckoff positions, and carbon atoms are located at the 8*f* sites forming [C_2] units with a C-C bond length of 1.197(13) Å (Fig. 1.9c, d). Metal atoms are coordinated by the ten nearest carbon atoms at distances of 2.733(7)-3.199(9) Å (Fig. 1.9g). The coordination polyhedra of carbon dumbbells are similar to that in the tetragonal LuC_2 described above, however, in the monoclinic EuC_2, carbon dimers are slightly rotated inside the octahedron formed by the nearest metal atoms (Fig. 1.9f, h).

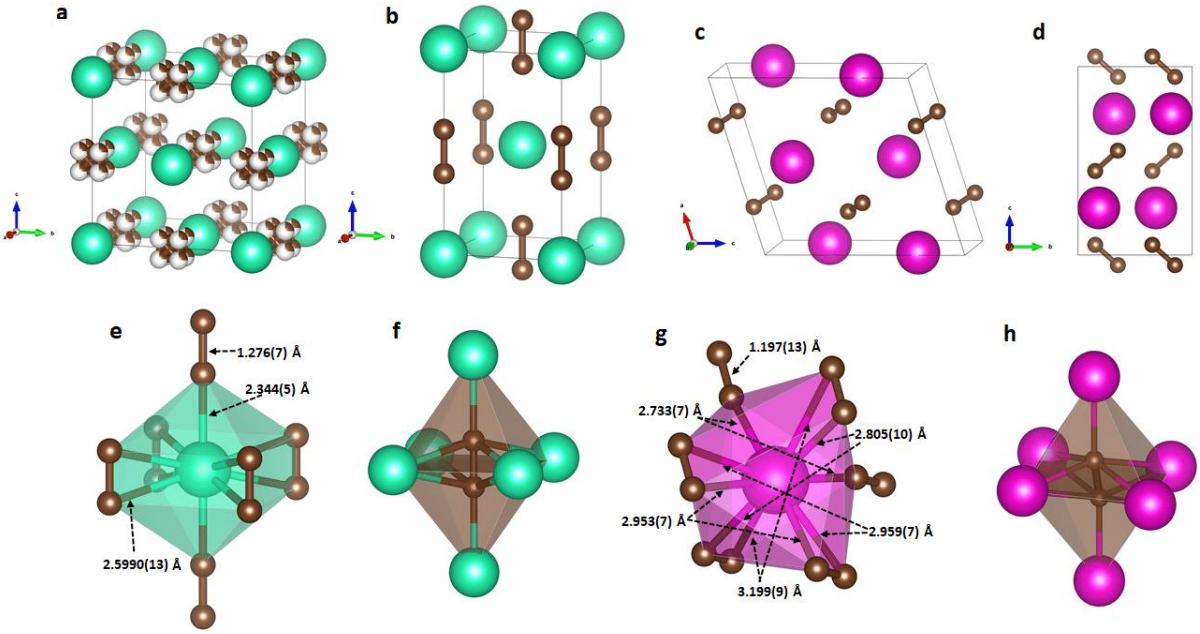

Figure 1.9. Crystal structures of (a) *cF* LuC_2 [60], (b) *tP*6 LuC_2 [65], (c)-(d) *mC*12 EuC_2 [56]. Coordination environment of metal and carbon atoms in (e)-(f) *tP*6 LuC_2 and (g)-(h) *mC*12 EuC_2.

There are three methods for synthesizing EuC_6-type compounds. The first two methods, detailed for EuC_6 and YbC_6, involve intercalating lanthanides into graphite sheets in two different ways: direct action of the metal vapor in metallic tubes sealed under vacuum (at temperatures of 450-500°C) or by heating a compressed mixture of the metal and graphite powders (at temperatures of 390-510°C) [66]. The third approach supposes the synthesis in the lithium-europium-graphite system by direct immersion of a pyrolytic graphite platelet in a molten lithium-based alloy with a carefully chosen Li/Eu ratio at 350°C [67].

The EuC_6 structural type is known for compounds containing two rare-earth metals, Eu and Yb [66]. The EuC_6 phase crystallizes in the hexagonal space group $P6_3/mmc$ (#194) with *Z* = 2 (Fig. 1.10a). It has lattice parameters *a* = 4.314(3) Å and *c* = 9.745(8) Å [66]. Carbon atoms occupy 12*i* positions, forming graphene-like sheets in the (0 0 2) planes with a C-C distance of 1.4380(10) Å. Metal atoms are located between graphene-like layers at the 2*c*

Wyckoff sites and are arranged in a *hcp*. Metal atoms are twelve-fold coordinated by nearest carbon atoms with a metal-carbon distance of 2.8290(18) Å (Fig. 1.10b).

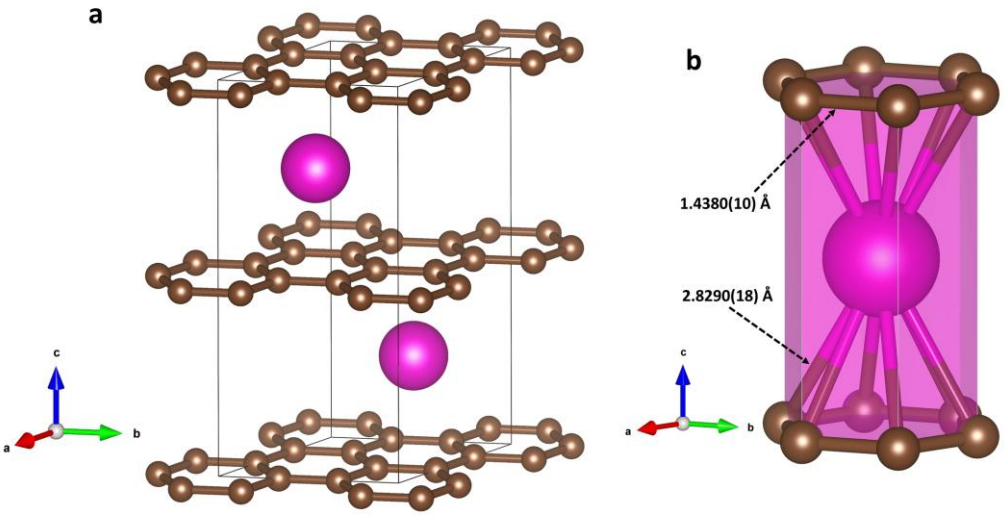

Figure 1.10. (a) Crystal structure of *hP*14 EuC_6 [66]. (b) Coordination environment of Eu atoms.

Despite the diversity of studies on rare-earth metals carbides at ambient pressure, only a handful have been recently explored under extreme conditions. In addition to the previously discussed Y_2C_3 yttrium sesquicarbide synthesized at 3.5-5.0 GPa and 1400-1600°C [10], Sm_3C_{70} and Eu_3C_{70} fullerides have been investigated at pressures ranging from ambient to 5 GPa, with reports indicating that these compounds undergo a reversible first-order structural phase transition at about 1.5 GPa [11].

A common synthesis method for rare-earth metal fullerides, as described in various publications, involves the reaction of stoichiometric amounts of rare-earth metal powder with fullerene C_{60} or C_{70} at 400-650°C under a high vacuum of about 10^{-6}-10^{-7} Torr [23,68–72]. Alongside, CeC_{82} was reported as a compound synthesized by arc-discharging a graphite composite rod at ~25 V and ~80 A under He pressure of 80 Torr [73–75]. Fullerides crystallize in cubic *Im*-3 (#204; Sm_6C_{60}, a = 10.890 Å, Z = 2 [69]; Eu_6C_{60}, a = 10.949(7) Å, Z = 2 [76]), *Fm*-3*m* (#225; Eu_9C_{70}, a = 15.0572(16) Å, Z = 4 [72]), and *Pa*-3 (#205; $Eu_{2.82}C_{60}$, a = 28.21(2) Å [68], Z = 32; CeC_{82}, a = 15.78(1) Å, Z = 4 [73]), orthorhombic *Pbca* (#61; $Sm_{2.75}C_{60}$, a = 28.1970(2) Å, b = 28.2350(2) Å, c = 28.1609(2) Å, Z = 32 [70]; $Yb_{2.75}C_{60}$, a = 27.8743(2) Å, b = 27.9804(2) Å, c = 27.8733(2) Å, Z = 32 [23,70]), and monoclinic *P*2 (#3; Sm_3C_{70}, a = 14.88(1) Å, b = 10.09(1) Å, c = 10.93(1) Å, β = 96.16(2)°, Z = 2 [71]) and *P*1 (#1, $Sm_{2.78}C_{70}$, a = 14.86(1) Å, b = 10.09(1) Å, c = 10.92(1) Å, β = 96.17(2)°, Z = 2 [11,72];

$Eu_{2.73}C_{70}$, a = 14.926(2) Å, b = 10.130(1) Å, c = 10.950(1) Å, β = 96.111(5)°, Z = 2 [72]) space groups.

Yttrium *oC*72 γ-Y_4C_5 [7] and lanthanum *oC*2 LaC [12] carbides represent the first observation of novel rare-earth metal carbide phases in a DAC during HPHT experiments. In the current research, we investigated several compounds under extreme conditions in a DAC, with many being observed for the first time: REE_3C_2 (REE = Nd, Sm, Gd, Dy; 43-68 GPa; space group *P*4/*mbm*, #127), REE_4C_3 (REE = Sc, Gd, Dy, Yb; 19-95 GPa; space group *I*-43*d*, #220), REE_xC (REE = Y, Gd, Dy, Yb; 34-46 GPa; space group *Fm*-3*m*, #225), β-REEC (REE = La, Nd, Sm; 41-68 GPa; space group *Cmcm*, #63), γ-SmC (103 GPa; space group *Cmcm*, #63), γ-REE_4C_5 (REE = Sm, Gd, Dy, Yb; 34-65 GPa; space group *Cmce*, #64), REE_5C_7 (REE = Nd, Sm, Gd, Yb; 42-60 GPa; space group *P*4/*ncc*, #130), REE_2C_3 (REE = Sm, Gd, Dy; 19-46 GPa; space group *I*-43*d*, #220), La_3C_5 (45-67 GPa; space group $P2_1/n$, #14), REE_5C_9 (REE = Y, Nd, Sm, Gd, Dy, Yb; 37-68 GPa, space group *P*4/*mnc*, #128), γ-$REEC_2$ (REE = Y, Sm, Dy; 66-124 GPa; space group *Immm*, #71), δ-$REEC_2$ (REE = Nd, Sm; 43-44 GPa; space group *Pmma*, #51), ε-LaC_2 (45-67 GPa; space group *C*2/*m*, #12).

Table 1.1. Binary compounds in the REE–carbon system with known structural data observed at ambient pressure (modified after [5]) and under extreme conditions (shown in green).

Composition	REE =	Structural type, space group	Carbon unit type	Structural types observed in the present work
REE_2C	Sc [36]	Sc_2C, *P*-3*m*1	Discrete C atoms	
	Sc [5,27], Y [5,28], Gd [5,29], Tb [5,30], Dy [5,30], Ho [5,31], Yb [5,32]	anti-$CdCl_2$, *R*-3*m*	Discrete C atoms	
REE_3C_2	Nd*, Sm*, Gd*, Dy*	U_3Si_2, *P*4/*mbm*	Dimers [C_2]	✓
REE_4C_3	Sc [5,42,44,45], Gd*, Dy*, Yb*	Anti-Th_3P_4, *I*-43*d*	Discrete C atoms	✓
$REEC_x$, x ~ 0.33–1	Sc [5,33,34], Y [5,18,26], Ce [35],	NaCl, *Fm-3m*	Discrete C atoms	✓

	Sm [5,18], Eu [5], Gd-Lu [5,18]			
REEC	La [12]	CsCl, *Pm*-3*m*	Discrete C atoms	
	La*, Nd*, Sm*	β-LaC, *Cmcm*	Dimers [C_2]	✓
	Sm*	γ-SmC, *Cmcm*	Carbon flat chains and dimers [C_2]	✓
REE_4C_5	Y [5,40], Gd-Ho [5,40]	α-Y_4C_5, *Pbam*	Dimers [C_2] and discrete C atoms	
	Y [7], Sm*, Gd*, Dy*, Yb*	γ-Y_4C_5, *Cmce*	Dimers [C_2] and trimers [C_3]	✓
$REE_{15}C_{19}$	Sc [41]	$Sc_{15}C_{19}$, *P*4/*mnc*	Trimers [C_3] and discrete C atoms	
	Sc [47], Y [48], Ho [49], Er [50], Tm [49], Yb [51], Lu [52]	$Sc_{15}C_{19}$, *P*-42$_1$*c*	Dimers [C_2] and discrete C atoms	
REE_3C_4	Sc [5,19], Y [5,19], Tb [5], Dy [5,37], Ho-Lu [5,19]	Sc_3C_4, *P*4/*mnc*	Trimers [C_3], dimers [C_2], and discrete C atoms	
REE_5C_7	Nd*, Sm*, Gd*, Yb*	Nd_5C_7, *P*4/*ncc*	Trimers [C_3] and discrete C atoms	✓
REE_2C_3	Sc [33], Y [10], La-Nd [5,18], Sm [5,18], Eu [5,46], Gd-Ho [5,18], Er-Lu [43]	Pu_2C_3, *I*-43*d*	Dimers [C_2]	✓
REE_3C_5	La*	La_3C_5, *P*2$_1$/*n*	Non-flat distorted naphthalene-decalin-like [C_{10}] entities	✓
REE_4C_7	Y [5,37], Ho-Tm [5,38], Lu [5,38]	Lu_4C_7, *P*2$_1$/*c*	Trimers [C_3] and discrete C atoms	
	Y [5,39], Dy [5], Ho [5,39]	α-Ho_4C_7, *P*2$_1$/*c*	Trimers [C_3] and discrete C atoms	

REE_5C_9	Y*, Nd*, Sm*, Gd*, Dy*, Yb*	Dy_5C_9, *P*4/*mnc*	Carbon flat chains and discrete C atoms	✓
$REEC_2$	La [5,53], Eu [5,56], Tb [59], Lu [5,60]	KCN, *Fm*-3*m*	Dimers [C_2]	
	Y [5,57], La [5,54], Ce [5,58], Pr [5,61], Nd [5,62], Sm [5,18], Eu [5,56], Gd [5,63], Tb [5,63], Dy [5,63], Ho [5,64], Er [5,55], Tm [5,18], Yb [5,32], Lu [65]	CaC_2, *I*4/*mmm*	Dimers [C_2]	
	Eu [56]	ThC_2, *C*2/*c*	Dimers [C_2]	
	Y*, Sm*, Dy*	γ-DyC_2, *Immm*	Carbon flat ribbons	✓
	Nd*, Sm*	δ-NdC_2, *Pmma*	Carbon flat chains	✓
	La*	ε-LaC_2, *C*2/*m*	Non-flat distorted naphthalene-decalin-like [C_{10}] entities	✓
$REEC_6$	Eu [5,66,77], Yb [5,66,67]	EuC_6, $P6_3/mmc$	Graphene sheets	
REE_6C_{60}	Sm [69], Eu [5,76,77]	K_6C_{60}, *Im*-3	Fullerene	
REE_9C_{70}	Eu [72]	Eu_9C_{70}, *Fm*-3*m*	Fullerene	
$REE_{2.82}C_{60}$	Eu [68]	$Eu_{2.82}C_{60}$, *Pa*-3	Fullerene	
$REE_{2.75}C_{60}$	Sm [70], Yb [23,70]	$Yb_{2.75}C_{60}$, *Pbca*	Fullerene	
REE_3C_{70}	Sm [71]	Sm_3C_{70}, *P*2	Fullerene	
REE_xC_{70}, x ~ 2.73–2.78	Sm [11,72], Eu [72]	Sm_xC_{70}, *P*1	Fullerene	
$REEC_{82}$	Ce [73]	CeC_{82}, *Pa*-3	Fullerene	

*This thesis

The structural data for all phases in the table are documented in the existing literature. In this study, Greek alphabet designations are assigned comprehensively, encompassing all previously identified phases, even those lacking structural data in the literature (such as β-Y_4C_5 [7,40]).

Extensive theoretical studies in the Li-C, Ca-C, Y-C, and Th-C systems have identified the tendency of carbon atoms polymerization behavior as pressure increases [78–80]. These calculations have uncovered a structural evolution of carbon arrangements under pressure resulting in the formation of polycarbon fragments [81–87]. It is noteworthy that the theoretical predictions for the YC_2 and ThC_2 structures show resembling manners of structural transformations as pressure increases [78,79]. Theoretically investigated systems have demonstrated the potential formation of carbon chains and ribbons, which have not been experimentally observed in the Li-C, Ca-C, Y-C, and Th-C systems. Therefore, further experimental studies are required to examine the existence, synthesis conditions, and crystal chemistry of the hypothetical phases.

Literature data overview [5,11,73,30,36,49,56,69–72] primarily revealed the formation of discrete carbon atoms, [C_2], [C_3] and fullerene units in rare-earth carbides under ambient pressure, while graphene sheets were observed exclusively in EuC_6-type carbides (Table 1.1). Remarkably, the other polyanions types, such as carbon chains and ribbons, were indicated only in high-pressure high-temperature experiments. Dy_5C_9 and γ-DyC_2 [88], Ca_3C_7 and HP-CaC_2 [89], Li_3C_4 [87], and Li_2C_2 [86] are notable examples. Among these, Dy_5C_9 contains deprotonated *cis*-polyacetylene-type carbon chains and discrete carbon atoms, while Ca_3C_7 consists of non-planar chains made of fused distorted C_6 and C_5 rings, which are isomorphous to deprotonated *para*-poly-indenoindene (*p-PInIn*) – these structures have never been theoretically predicted before.

These theoretical and experimental findings highlight the rich chemistry and diverse carbon arrangements observed in different carbide systems, paving the way for further research into their unique properties and potential applications. A comprehensive study encompassing a wide range of rare-earth elements would provide invaluable insights into the underlying principles and regularities determining the chemistry of lanthanide carbides. This motivated us to perform a thorough investigation of the Dy-C system, using dysprosium as an example of a rare-earth element, by means of single-crystal X-ray diffraction in laser-heated diamond anvil cells (LHDACs) in wide pressure and temperature ranges: from 20 to 95 GPa and up to ~2800 K. The reproduction of the novel structure of γ-Y_4C_5 containing carbon dimers and trimers [7] by γ-Dy_4C_5 [88], predicted *Immm*-YC_2 consisting of flat carbon ribbons [78] – by

γ-DyC_2 [88], and predicted *P*4/*mbm*-Ca_3C_2 comprising carbon dumbbells [82] – by Dy_3C_2 [6,88] inspired for the further systematic investigation of rare-earth carbides, which currently remain poorly understood.

Alkali halides, particularly sodium and potassium chlorides used as pressure-transmitting media and thermal insulators in the predominant part of experiments in the current thesis, are chemically very stable and are usually not considered as precursors for the synthesis of new compounds in high-pressure studies. Indeed, NaCl and KCl were thought to be chemically inert over wide pressure (up to 200 GPa) and temperature (up to 3000 K) ranges [90]. Therefore, they have often been used as pressure calibrants [91], pressure-transmitting media [92], and electrical and thermal insulators in high-pressure experiments [92–94]. Recent experimental and theoretical studies [95–97] suggest, however, that the behavior of the Na-Cl and K-Cl systems at high pressures is complex, and several compounds with an unusual stoichiometry (like $NaCl_3$,Na_3Cl, Na_2Cl, and KCl_3) have been reported. Still, NaCl and KCl are considered to be chemically stable under high pressure, as in the absence of ionization-promoting species [98,99], reactions are found in the presence of extra chlorine or sodium/potassium in a diamond anvil cell (DAC) [96,97].

Formed from highly electropositive and electronegative elements, NaCl and KCl, with stable electron configurations, are typically considered unreactive with transition or rare-earth metals. Below we report that it is not the case under pressure, as our experiments, originally designed to investigate the high-pressure behavior of metals (Y, Dy, Re, and Ag) in an "inert" pressure medium (NaCl) within a LHDAC, have revealed unexpected interaction between metals and alkali halides loaded in DACs at lower pressures than anticipated based on existing literature. This challenges the prevailing notion of their reactivity under pressure.

The primary objective of the present thesis is to explore the chemistry of rare-earth metal carbides (REE = Sc, Y, La, Nd, Sm, Gd, Dy, and Yb) under HPHT conditions, a field that remains insufficiently understood based on existing literature. We demonstrated the prevalence of regularities in the chemistry of rare-earth elements at high pressures and observed the formation of previously unknown compounds with exotic carbon entities. According to the previously assumed "chemically inert" nature, NaCl was utilized in most HPHT experiments in this research as a pressure-transmitting medium and thermal insulator. During experiments conducted in the NaCl pressure-transmitting medium, we indicated the chemical reactivity of NaCl under extreme conditions, which was further investigated in experiments with several metals (M = Y, Dy, Re, and Ag).

2. Experimental methods

2.1 Generation of the extreme conditions in DACs

High-pressure high-temperature studies are crucial in material science, unraveling the intricacies of physics and chemistry within Earth, celestial bodies, and extrasolar planets. Under extreme conditions, solid-state matter not only undergoes phase transitions but also reveals unexpected chemistry, including stoichiometry and reactions not observed at ambient conditions. Investigating the properties, structural transitions, and chemical behavior of materials under high pressures holds great significance for materials science, offering potential discoveries of novel materials with unique properties for diverse technological applications.

Pressure is clearly defined as $P = \frac{F}{A}$, where F represents the force applied perpendicular to the surface, and A denotes the area of that surface. According to this relation, there are two primary methods for applying static high pressure to a sample: either by maximizing the applied force or by reducing the area on which the force is applied. The former approach is employed in piston-cylinder [100] and multi-anvil apparatuses [101], utilizing large and/or massive devices focused on maximizing applied force for relatively large samples (ranging from ~0.1 cm to ~1 cm in linear dimensions). The alternative approach involves decreasing the sample's volume, as seen in the diamond anvil cells (DACs) technique, where typical sample sizes are about 10-100 μm. Invented in 1959 [102], the DAC has become one of the most powerful tools for generating static high pressures. Among various high-pressure devices, DACs provide the capability to reach the widest pressure range, covering conditions of the Earth's interior across the whole pressure range to the inner core ~360 GPa [103]. Recently, the diamond anvil cell has gained popularity as the sole device capable of achieving static pressures as high as 1 TPa [104], simulating conditions found in planetary bodies with masses significantly exceeding that of the Earth.

2.1.1 Diamond anvil cells

The wide electromagnetic radiation transparency of diamond makes the DAC a highly valuable tool for investigating materials under extreme conditions using various emission, scattering, and absorption methods. The fundamental concept behind pressure generation in the DAC involves compressing the material between the flat tips (culets) of two gem-quality diamond anvils precisely driven against each other. Although various DAC designs have

emerged over recent decades, the core idea remains consistent: different DAC types share the same principle features. The typical DAC (Fig. 2.1a) comprises a metal body with a pair of seats, diamond anvils precisely positioned on them, and a metallic gasket with a circular hole placed between the anvils.

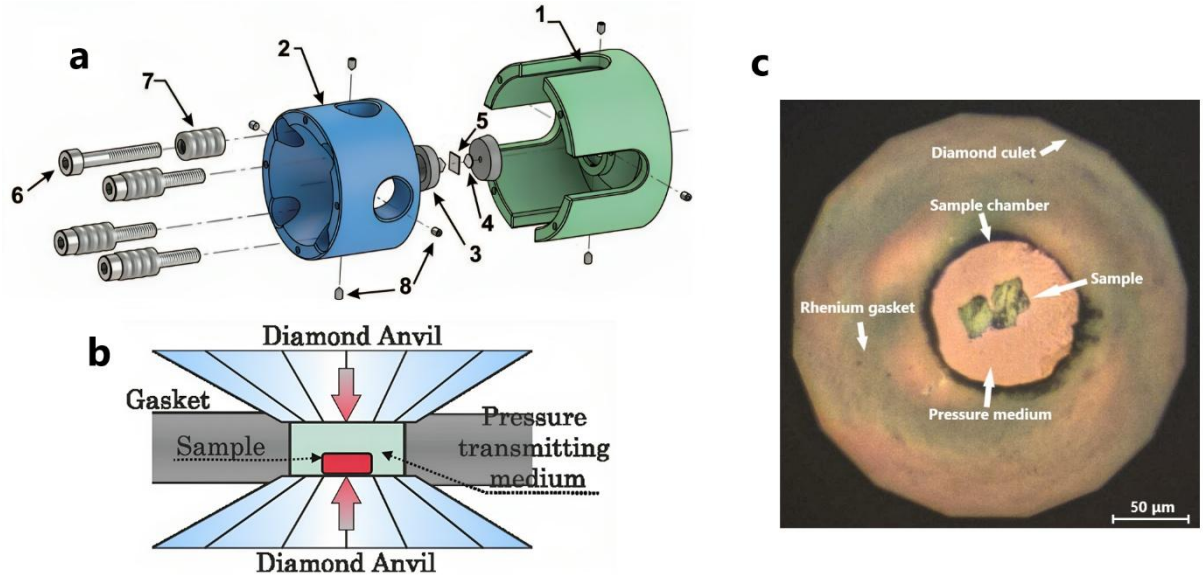

Figure 2.1. BX90-type diamond anvil cell. (a) Exploded view (modified after [105]): (1) outer cylinder part, (2) inner piston part, (3) diamond supporting plates, (4) diamond anvils, (5) metallic gasket, (6) M4 (#8-32) screws for generating loading force, (7) pack of conical spring washers (Belleville springs), (8) setscrews for diamond anvils alignment. (b) Schematic diagram of a pressure chamber. (c) A microphotograph of the DAC sample chamber was taken under an optical microscope through the diamond anvil (top view). The culet diameter is 250 μm.

Seats are typically made out of hard materials like tungsten carbide, playing a role in transferring external load onto the diamond anvils. The metallic gasket with a circular hole compressed between the diamond tips shapes the cylindrical space (Fig. 2.1b, c). This configuration enables the confining of the sample position during compression and redistributes uniaxial stress when filled with a pressure-transmitting medium. Generally, metallic gaskets are made of chemically inert at ambient conditions metals or alloys. In the studies presented below, all the gaskets were made of rhenium, a 5*d* transition metal, characterized by high bulk (above 350 GPa) and shear (above 180 GPa) moduli and melting point of 3453 K [106,107].

Polished single crystals of diamonds oriented according to the [100]-direction of the highest strength commonly serve as diamond anvils – an important part of DAC. The size of the diamond anvil culet can range from approximately a millimeter to tens of micrometers, playing a key role in setting the upper limit of attainable pressure. Smaller culets, exhibiting a

beveled shape (Fig. 2.2), enable the attainment of higher pressures but come with the restriction of the studied sample size.

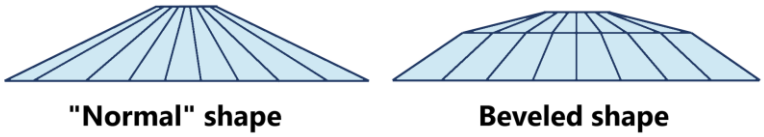

Figure 2.2. Schematic examples of the culet shapes. Diamond anvils with culets diameter below 150 μm are usually beveled.

The combination of the diamond cut's geometry, seat shape, and the aperture of the metallic body represents critical parameters. Standard brilliant cut anvils and seats are typical in spectroscopic experiments, where the DAC position remains fixed during measurements (Fig. 2.3a). However, for experiments involving sample rotation, like X-ray diffraction, larger aperture Boehler-Almax diamond anvils and seats are essential (Fig. 2.3b).

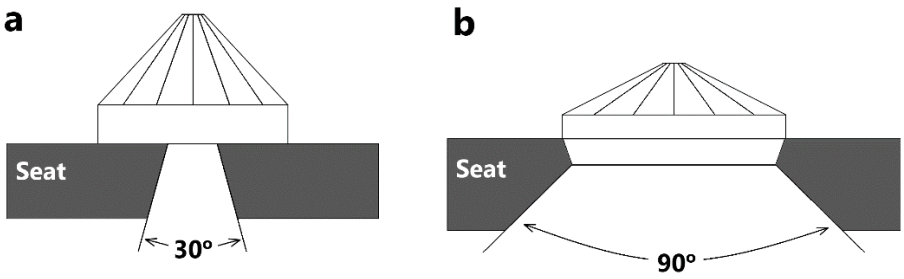

Figure 2.3. Different types of diamond anvils and seats. (a) Standard brilliant-cut diamond and seat for spectroscopic measurements; (b) Boehler-Almax designed diamond anvil and seat for X-ray diffraction experiments.

In this thesis, the BX90-type DACs were employed [105]. Diamonds featuring various culet diameters (ranging from 80 to 250 μm) were of Boehler-Almax design with a large aperture [108] for X-ray diffraction studies and a standard brilliant-cut design for optical measurements. The selection of culet size depends on the targeted pressure range. Specifically, anvils with 250 μm culet diameters are usually used for pressures up to 70 GPa, 120 μm culets – for pressures below 125 GPa, and 80 μm culets – for pressures up to 190 GPa.

2.1.2 Pressure transmitting media

By default, the DAC functions as a uniaxial compression device, leading to high shear strains and limiting access to pressure as a thermodynamic variable (pressure is a thermodynamic variable only under the assumption of hydrostatic conditions). To achieve

quasi-hydrostatic conditions and a homogeneous pressure distribution, a pressure-transmitting medium (PTM) is used. PTM fills the sample chamber, surrounding the sample to ensure quasi-hydrostatic stress transmission from the diamond anvil. Known liquids, including alcohol mixtures and paraffin oil, solidify at ambient temperature under pressures exceeding ~10-15 GPa [109]. Ideal solid PTM should possess relatively low bulk and shear moduli and, ultimately, low tensile strength.

Certain materials, such as solid noble gases (He, Ne, Ar), and to some extent, some alkali metal halides, satisfy these criteria and can be employed. Besides facilitating uniform pressure distribution, PTMs often serve as pressure gauges (e.g., Ne, Ar), participate as reactants in chemical reactions under extreme conditions (e.g., paraffin oil, O_2, N_2), or act as thermal insulation layers during laser heating experiments (e.g., NaCl, KCl, LiF). Gases can be loaded into the DAC sample chamber using a high-pressure gas loading apparatus [110] or cryogenically, while solids and liquid PTMs (at atmospheric pressure) can be loaded manually.

In the present thesis, three PTMs were used. Ar was loaded in a gas-loading system [110], where the gas was pumped into the vessel with a DAC up to ~1.2 kbar. Upon releasing the external gas pressure, the DAC was sealed by manually tightening the screws in the piston-driving mechanism. NaCl and KCl, pre-calcined at ~200°C to eliminate moisture, were loaded as thermal insulators in a separate part of the experiments.

2.1.3 Pressure determination

The precise determination of pressure within the DAC sample chamber is a crucial aspect of any DAC experiment. Common methods involve the use of various pressure calibrants. A material with a well-known response to applied pressure can be loaded into the DAC alongside the sample and probed using analytical techniques. The pressure dependence of ruby (Cr-doped Al_2O_3) fluorescence is the most widely used technique in the pressure range up to 100 GPa [111].

The DAC sample chamber contains a microsphere of ruby along with the sample and pressure medium. Typically, a micrometer-sized ruby sphere is placed inside the pressure chamber and its fluorescence induced by laser light is observed. The pressure-dependent relationship between the central position of the ruby R1 spectral peak and pressure is described by the following equation [112]:

$$P(GPa) = A\left(\frac{\Delta\lambda}{\lambda_0}\right)\left[1 + B\left(\frac{\Delta\lambda}{\lambda_0}\right)\right] \qquad Equation\ 2.1$$

In this equation, A and B represent the calibration constants (A = 1.87(1)·10^3, B = 5.5), λ_0 is the position of the R1 peak at ambient pressure (Fig. 2.4a), and $\Delta\lambda$ denotes the relative shift of the R1 peak at pressure P.

As pressure rises, the intensity of the ruby fluorescence signal significantly diminishes, becoming absent beyond 100 GPa. The presence of ruby within the DAC sample chamber may pose a risk of involvement in chemical reactions, potentially causing contamination, especially in high-temperature experiments.

To avoid this concern in the experiments described below, we opted for an alternative method for spectroscopic pressure determination, relying on the pressure dependence of the first-order Raman mode of a diamond culet [113]. At the center of the culet, normal stress is known to correlate with the high-wavenumber edge of the Raman band as follows:

$$P(GPa) = K_0\left(\frac{\Delta v}{v_0}\right)\left[1+\frac{1}{2}(K'-1)\left(\frac{\Delta v}{v_0}\right)\right] \qquad Equation\ 2.2$$

where K_0 = 547 GPa and K_0' = 3.75 are calibration constants, v_0 is the position of the high-wavenumber Raman edge at ambient pressure, and Δv is the difference between positions at ambient and measured pressures. The position of the edge is defined as a local minimum of the first derivative of the Raman spectra (Fig. 2.4b). This technique is less accurate than Ruby fluorescence measurements, primarily because of its empirical nature and the uncertainties introduced by focusing and positioning the probing laser beam on the diamond culet surface. Nevertheless, it remains preferable in experiments conducted in a pressure range exceeding 100 GPa or when the use of ruby is undesirable.

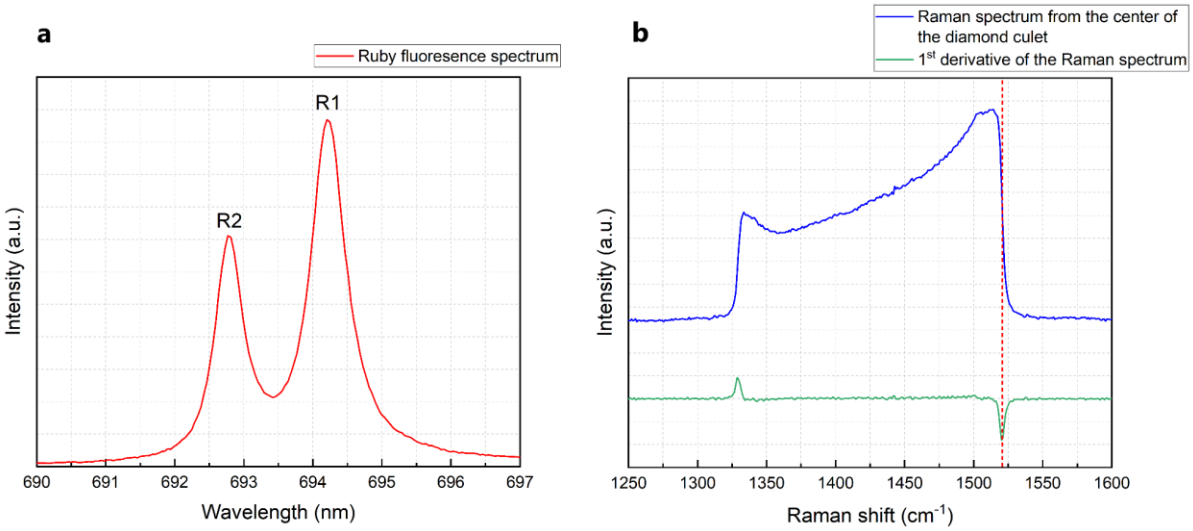

Figure 2.4. Indicators of pressure inside the diamond anvil cell. (a) Ruby fluorescence spectral peaks R1 and R2. The position of peak R1 is used as a pressure gauge; (b) Raman shift spectrum of a diamond anvil under stress. The high-wavenumber edge position (red dashed line) is used as a pressure gauge.

In situ X-ray diffraction stands out as the most precise method for pressure determination. A small quantity of a pressure calibrant with a well-known equation of state (EoS) can be loaded into the DAC along with the sample and probed by X-ray diffraction. This allows for accurate determination of the unit-cell parameters of the calibrant, resulting in high precision in pressure determination. Usually, calibrants are chemically inert compounds with high crystal symmetry, such as Au, Pt, W, and sometimes Re [90,114,115]. The absence of pressure-induced phase transitions is desirable in the pressure regions of interest. An alternative approach involves using the PTM itself as a pressure marker: solids like Ne, Ar, NaCl, KCl, LiF, KBr, and MgO [90,116–122] have well-established equations of state over a wide pressure range.

The equation of state for a system establishes the relationship among thermodynamic variables such as volume (V), pressure (P), and temperature (T) through parameters like bulk modulus and thermal expansion. In this thesis, all equations of state were determined at a constant (ambient) temperature of 293 K. Various types of analytical isothermal EoSes exist [123,124], with the 3rd-order Birch-Murnaghan EoS (Equation 2.3) being one of the most prevalent [124]. This equation expresses the pressure-volume relationship of matter at constant temperature through the bulk modulus ($K_0 = -V\left(\frac{\partial P}{\partial V}\right)$) and its pressure derivatives, particularly $K' = \frac{\partial K}{\partial P}$. Expressions for the 2nd-order Birch-Murnaghan EoS can be obtained by setting $K' = 4$ in Equation 2.3.

$$P = \frac{3K_0}{2}\left[\left(\frac{V_0}{V}\right)^{\frac{7}{3}} - \left(\frac{V_0}{V}\right)^{\frac{5}{3}}\right]\left\{1 - \frac{3}{4}(4 - K')\left[\left(\frac{V_0}{V}\right)^{\frac{2}{3}} - 1\right]\right\} \qquad Equation\ 2.3$$

2.1.4 Generation of high temperatures in DACs

The transparency of diamonds in a broad range of electromagnetic radiation is a significant advantage in DAC experiments, simplifying sample observation and probing. This allows a high-power laser beam to be focused on the sample while keeping diamond anvils unharmed [125]. Laser wavelength selection depends on sample absorption characteristics, with CO_2-based infrared (λ = 10.6 μm [126]) and Nd:YAG near-infrared lasers (NIR, λ ~ 1064 nm [127]) being common. NIR lasers are ideal for heating non-transparent materials, while transparent materials are heated by CO_2 infrared lasers.

Since the diamond has one of the best thermal conductivity among all materials found in nature [128], intensive heat dissipation through the diamond anvil during laser heating is one

of the major problems. Insulation using compounds like NaCl, KCl, KBr, and LiF helps stabilize temperature during laser heating in DACs. A portable double-sided laser-heating setup (Fig. 2.5) [129], enabling *in situ* temperature determination, was used in the experiments described in the present thesis.

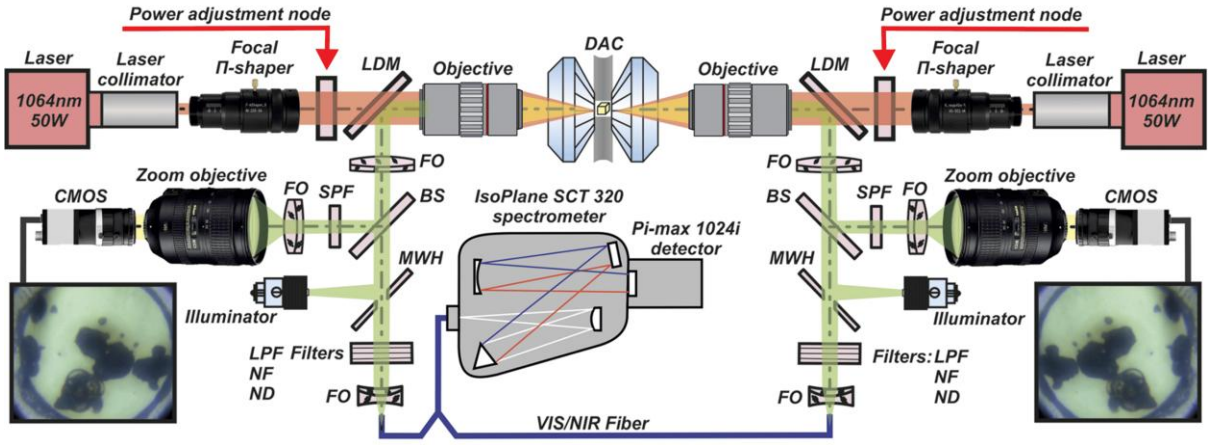

Figure 2.5. Schematic diagram of the double-sided laser heating system for diamond anvil cells. LDMs are the long-pass dichromic mirrors; FOs are the focusing optics; BSs are 50/50 beam splitters; SPFs are the short-pass filters with a cutoff at 800 nm; CMOSs are the cameras for optical observation; MWHs are the mirrors with a hole; LPFs are the long-pass filters with a cut-on wavelength of 550 nm; NFs are the notch filters at 1064 nm; and NDs are neutral density filters (modified after [129]).

2.2 Raman spectroscopy

Raman spectroscopy is a spectroscopic technique based on the inelastic scattering of monochromatic optical radiation on the irradiated sample. The method has become an important analytical and research tool in many scientific fields and provides information on molecular vibrations and crystal structure.

When light interacts with matter, the majority of photons undergo elastic scattering known as Rayleigh scattering, preserving their energy ($E = E_0$, Fig. 2.6). However, a minute fraction (~10^{-6} %) of incident light experiences inelastic scattering, resulting in either a loss (i.e., $E > E_0$, Stokes Raman scattering) or gain (i.e., $E < E_0$, anti-Stokes Raman scattering) of energy. In the case of Rayleigh scattering, incident light of energy E_0 and frequency ν_0 interacts with a molecule, exciting the cloud of electrons from the ground level to a "virtual" level. This "virtual" state is unstable, leading photons to return to the ground level. Since there is no energy loss in this process, Rayleigh scattering maintains the same energy and frequency (E_0, ν_0) as the incident light, constituting elastic scattering.

Stokes Raman scattering happens when the electron cloud absorbs a portion of the incident radiation and falls to a vibrational level (i.e. an excited level) instead of the ground level. In this case, Stokes Raman scattering possesses lower energy than the incident light. Anti-Stokes Raman scattering occurs when the incident light encounters the electron cloud already in a vibrational state. The cloud is excited to the virtual level and then falls to the ground level with more energy and higher frequency than the incident light. The intensity ratio between Stokes and anti-Stokes scattering relies on the population of vibrational levels described by Boltzmann's law. Consequently, at ambient temperature, the Stokes component predominates in the inelastic spectra and is commonly the sole consideration. The frequency of the Raman peak is associated with specific molecular or lattice vibrations, such as symmetric or asymmetric stretching or bending.

In the present work, Raman analyses of the samples were performed using LabRam systems equipped with a He-Ne (632 nm) laser source. The He-Ne laser operates in continuous mode with a constant power of 50 mW. Raman spectra were collected in the range of 200 – 4000 cm^{-1} with a resolution of 0.5 cm^{-1}.

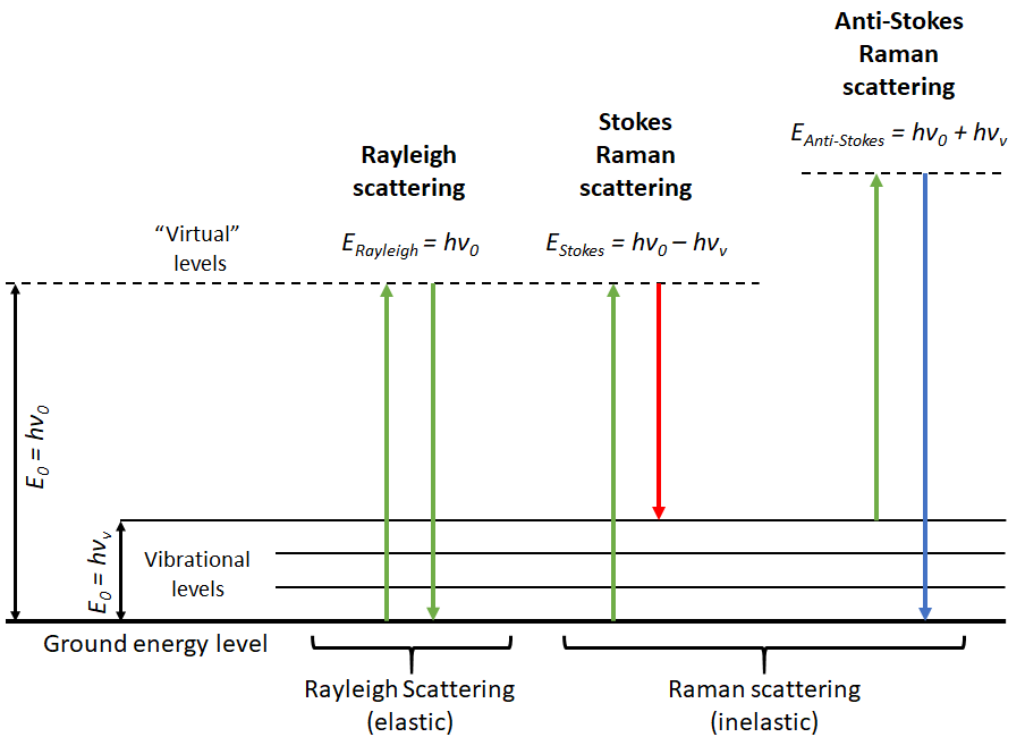

Figure 2.6. Energy level diagram for Rayleigh and Raman scattering processes (modified after [130]). A molecule is excited from the ground level to the virtual state absorbing a photon and returns to the ground state emitting a lower energy photon. The excitation energy, $E_0 = hv_0$, is the energy of the incident photon, h is Planck's constant, and v_v is the frequency corresponding to molecular vibrations.

2.3 X-ray diffraction in DACs

2.3.1 Basic principles

X-ray crystallography stands as a cornerstone in high-pressure science, serving as the primary method for determining the atomic structure of crystalline solids [131,132]. It is based on Bragg's law, which is a special case of X-ray diffraction.

X-ray diffraction is the phenomenon where X-ray photons undergo elastic scattering by the electrons of atoms. The wavelengths of X-ray photons fall within the angstrom range (0.1 – 100 Å), a scale relevant to the interatomic distances in a solid's crystal lattice. Consequently, incident monochromatic X-rays that are in phase can be constructively or destructively interfered with when scattered from a periodic crystal lattice. The condition for constructive interference is described by Bragg's law:

$$2d \cdot \sin(\theta) = n\lambda \qquad Equation\ 2.4$$

where d is the spacing between the diffracting family of *hkl* crystallographic planes, θ is the angle of the incident X-ray, n is an integer number, and λ is the wavelength of the beam (Fig. 2.7). According to this model, the scattering entities are electrons associated with atoms, organized within a 3D periodic framework where interatomic distances are on a scale comparable to the X-ray wavelength. Presuming atoms are organized in layers (planes) with a constant spacing between them, the X-rays reflected from these atomic planes undergo constructive interference when the difference in path lengths of the two waves equals to an integer multiple (n) of wavelengths. The total path difference for two interfering waves is given by $2d \cdot sin(\theta)$.

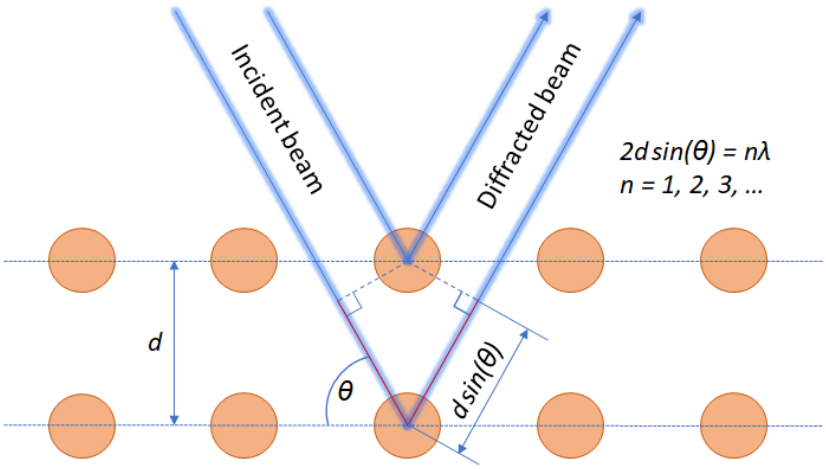

Figure 2.7. Schematic interpretation of Bragg's law (modified after [133]). Incident X-rays approach parallel planes of atoms in crystals and diffracted X-ray beam scattered on the lower plane traverses an extra length of $2d \cdot sin(\theta)$. Constructive interference occurs when the difference in the path lengths is equal to an integer number of the wavelength.

The crystalline matter causes incident X-rays to diffract in specific directions defined by its structure. Through the measurement of angles and intensities of the diffracted radiation, it becomes possible to solve the inverse problem: determining the three-dimensional distribution of electronic density within the crystal. Subsequently, this allows for the identification of atomic positions and the extraction of information regarding interatomic distances, crystallographic disorder, and other significant properties of solids.

2.3.2 Powder and single-crystal X-ray diffraction in DACs

Traditionally, X-ray diffraction (XRD) is categorized into two approaches: powder and single-crystal. Powder XRD involves working with crystalline material in powdered form, consisting of random orientations of fine grains. This results in Debye-Scherrer rings in the diffraction pattern (Fig. 2.8a). By defining the *d*-spacings of these diffraction peaks, one could identify the phase and determine its lattice parameters. However, this approach encounters challenges if there are new phases in the sample. In the case of powder XRD, a direct structure solution becomes nearly impossible due to the loss of data related to reciprocal vectors.

In contrast, single-crystal XRD is a more advanced technique. Typical single-crystal XRD patterns feature diffraction spots at specific intervals (Fig. 2.8b). As Bragg conditions for a given *d*-spacing and wavelength are met only at defined θ-angles, the crystal should be irradiated in various orientations with respect to the incident beam to ensure proper measurement of all reflections. The primary advantage of single-crystal XRD over powder XRD lies in its ability to directly provide information on the atomic arrangement within the unit cell, as reflected in the intensities of Bragg reflections.

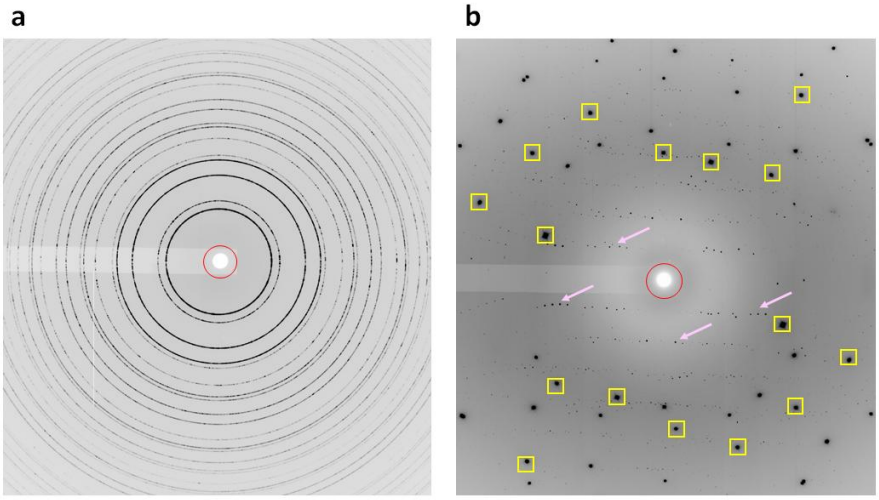

Figure 2.8. XRD patterns produced by a powder (a) and a single crystal sample (b). The red circles mark the positions of the direct beam, where a beamstop is placed to protect the

detector from excessive radiation. Yellow rectangles show examples of the intense reflections from the diamond anvil. Pink arrows point to examples of the reflections from the sample in the DAC, in this case, an enstatite crystal.

In contrast to diffraction studies under normal conditions, applying XRD in DACs experiments presents challenges. Firstly, the sample environment contributes additional XRD signals, including parasitic scattering originating from diamond anvils, the metallic gasket, and the solidified PTM. Secondly, the metallic body of a DAC shadows over 60% of diffraction reflections, leading to poorer diffraction statistics in the collected data. Thirdly, in routine DAC experiments (up to 100 GPa), the sample size is typically about 10-20 μm, and at multimegabar pressures, sample dimensions do not exceed 3-5 μm. Materials synthesized in a DAC after laser heating often appear as multi-phased mixtures of single-crystalline grains, frequently of submicron size. Consequently, successfully performing XRD experiments in laser-heated DACs at megabar pressure range requires a precise motorization system combined with a micron or submicron-sized X-ray beam.

2.3.3 DAC alignment on goniometer

Accurate alignment of the sample within the DAC is crucial for obtaining high-quality XRD data. The standard alignment procedure relies on X-ray absorption. As the DAC undergoes movement along the *y*- and *z*-motors, which are perpendicular to the direction of the beam (Fig. 2.9a), the diode records the intensity of the X-ray beam (Fig. 2.9b). The resulting absorption curve has a characteristic profile when the beam passes through the indented part of the gasket and the sample chamber. The center of the gasket is defined from the absorption curves obtained during *y*- and *z*-scans.

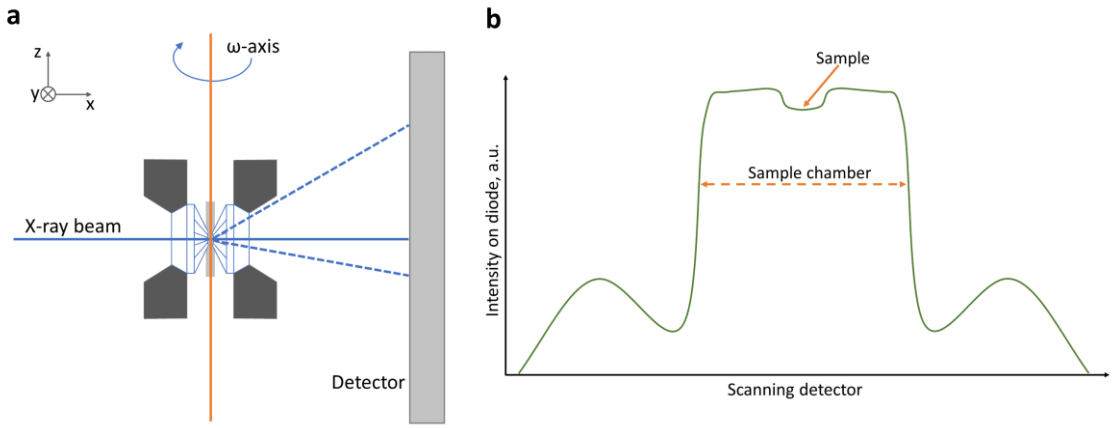

Figure 2.9. Scheme of the XRD experiment in a diamond anvil cell at synchrotron facilities. (a) The experiment geometry (modified after [134]); (b) an illustration of the absorption profile acquired during the alignment procedure.

The positioning of the DAC on the rotation axis is established through triangulation. If the ω axis is initially aligned with the primary beam (Fig. 2.10a, b), alignment along the *x*-direction is achieved by scanning the sample in a horizontal direction at two different ω positions (-ω and ω).

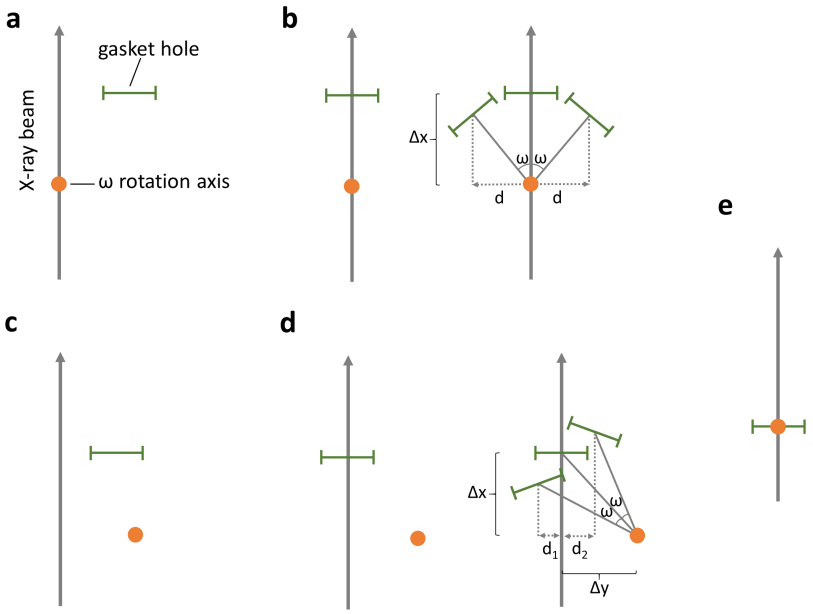

Figure 2.10. Typical process of sample centering shown in the projection along the *z*-axis (modified after [134]). (a) Initial state: the gasket hole is away from the ω rotation axis aligned with the primary beam. (b) After several scans in the plane perpendicular to the primary beam direction, the gasket hole is aligned with the beam. (c) Second possible initial state: both gasket hole and ω axis are away from the primary beam. (d) After several scans in the plane perpendicular to the primary beam direction, the gasket hole is aligned with the beam; the ω axis is away from the beam; DAC is rotated around the ω axis; three horizontal scans are performed in order to determine the distance between the centers of the gasket hole at different ω positions; correction of *x*- and *y*-motors should be applied. (e) The gasket hole is aligned with the primary beam and with the ω axis.

The correction must be applied using the *x*-translation motor above the ω-axis with the formula: $\Delta x_{high} = \frac{d}{sin(\omega)}$. In cases where the ω axis is initially not aligned with the primary beam (Fig. 2.10c, d), additional *y*-corrections are necessary. Therefore, a third scan at the position $\omega = 0$ is required. In this scenario, the correction for the *x*-position is defined as: $\Delta x_{high} = \frac{d_1+d_2}{2 \cdot sin(\omega)}$, and *y*-corrections should be applied as follows: $\Delta y_{low} = \frac{d_2-d_1}{4 \cdot sin^2(\frac{\omega}{2})}$, $\Delta y_{high} = -\Delta y_{low}$ – for both below and above the rotation axis. The alignment procedure should be repeated until the absolute value of any correction is less than the size of the X-ray beam. The entire alignment procedure should be performed after each possible displacement of the DAC,

such as after a manual pressure increase/decrease or laser heating when the DAC could be moved during annealing or cooling cycles.

2.3.4 Two-dimensional X-ray mapping of a sample in the DAC

In LHDAC experiments, the sample often comprises a multigrain assemblage of crystallites, sometimes belonging to different phases. To identify the optimal spot for single-crystal XRD data collection or to obtain information about the distribution of different phases, a 2D map of diffraction images can be generated.

The user sets up a script that moves the sample in small steps along the *y*- and *z*-directions. At each step, an XRD image is collected with or without *ω*-oscillations. Later, this set of images can be analyzed manually using the Dioptas program [135]. Alternatively, it can be imported into the XDI software [136], which constructs contrast maps based on the intensity of a selected region of interest defined by a specific *d*-spacing (Fig. 2.11). For this, the user needs to identify the unique non-overlapping diffraction peaks of the phase of interest.

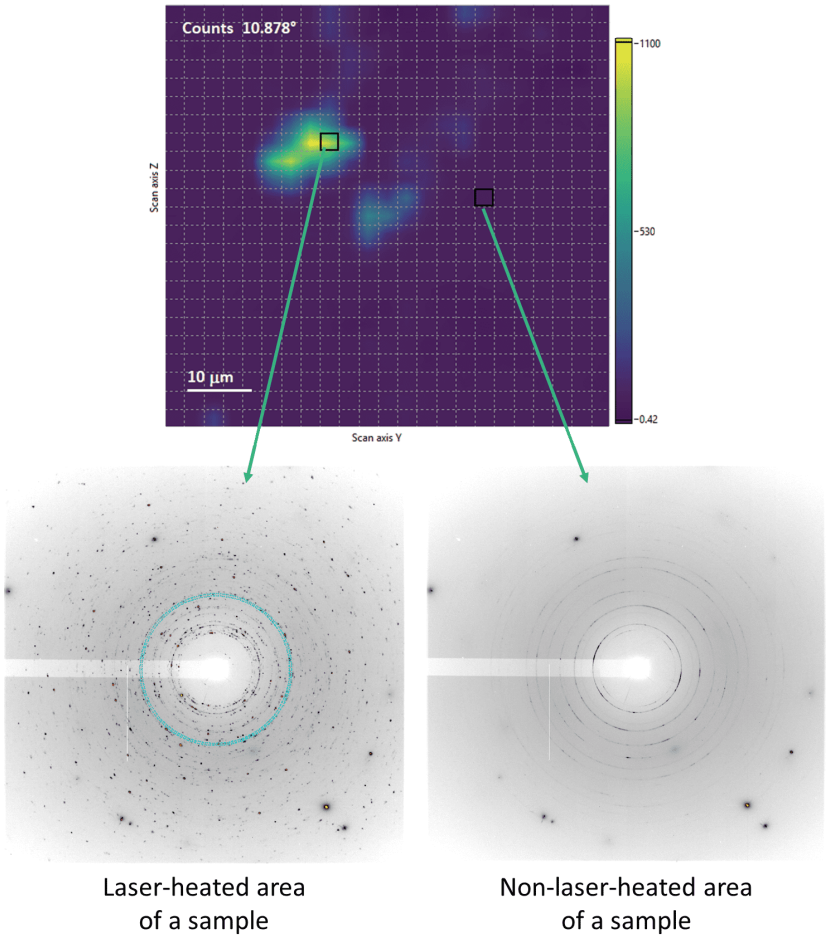

Figure 2.11. Built 2D X-ray map illustrating the spatial distribution of synthesized phases and a non-laser-heated area within the pressure chamber. The reconstructed X-ray image of the

sample chamber highlights positions featuring the most intense reflections of the phase of interest (exemplified at 10.878°).

2.3.5 Data processing

Since most of the present thesis was based on single-crystal XRD, and powder XRD was used as an auxiliary method, the focus of this section will be devoted to the data processing routine of single-crystal XRD datasets. In the present thesis, the single-crystal XRD data analysis, involving diffraction peaks indexing, data integration, frame scaling, and absorption correction, was performed using the CrysAlis^{PRO} software package [137]. A crystal of orthoenstatite $(Mg_{1.93}Fe_{0.06})(Si_{1.93},Al_{0.06})O_6$ (space group *Pbca*, a = 8.8117(2) Å, b = 5.18320(10) Å, and c = 18.2391(3) Å) served as a calibration standard for refinement of the instrumental parameters of the diffractometer, encompassing adjustments to the sample-to-detector distance, the detector's origin, offsets of the goniometer angles and rotations of the X-ray beam and the detector around the instrument axis. Structure solution and refinement were carried out in OLEX2 software [138] with the ShelXT structure solution program [139] using intrinsic phasing and refined with the ShelXL [140] refinement package using least-squares minimization, and some aspects of the process were completed in JANA2006 [141]. Generally, the processing of single-crystal XRD data includes several sequential steps:

1) Peak hunting

The peak hunting procedure starts with the 'ph s' command, extracting peak intensities and coordinates from the experimental diffraction frames. Upon specifying an appropriate ω-angular range, the extraction algorithm must be selected – options include automatic, traditional (where the user defines intensity thresholds and the area size of diffraction peaks), smart, or 3D. Afterward, the software reconstructs the positions of peaks in reciprocal space. The resulting list of peaks can be reviewed using the 'pt e' command, displaying a table with Miller indices (*hkl*), *xyz* coordinates, and experimental intensities for each Bragg's reflection. By default, the software uses the orientation matrix of the calibrant to derive Miller indices, which can be modified in subsequent steps. Information about all diffraction peaks can be saved using the 'wd t' command in *.tabbin format. This peak table can later be imported into an open CrysAlis project using the 'rd t' command.

2) Unit cell finding

The next step involves identifying the unit cell of the phase of interest. This can be undertaken by manually inspecting all reflections in the reciprocal space viewer, activated

using the ‘pt ewald’ command. The standard peak hunting algorithms do not differentiate between genuine diffraction signals and parasitic signals arising from diamonds, the gasket, dead pixels of the detector, and powder diffraction arcs originating from the PTM. This contamination significantly complicates the data processing procedure (Fig. 2.12a). The parasitic reflections can be removed by using the ‘Advanced filtering’ option in CrysAlis^{Pro} with the tolerance typically set to 3 (Fig. 2.12b, c). Once the initial cleaning is completed, the user can manually select reflections that constitute a 3-dimensional lattice in reciprocal space and initiate an automatic indexing procedure with the ‘um ttt’ command (Fig. 2.12d). At this stage, the software determines the orientation matrix of the single-crystalline grain, which can later be obtained using the ‘ty u’ command. The resulting unit cell should be refined against the entire set of reflections using the ‘um i’ command.

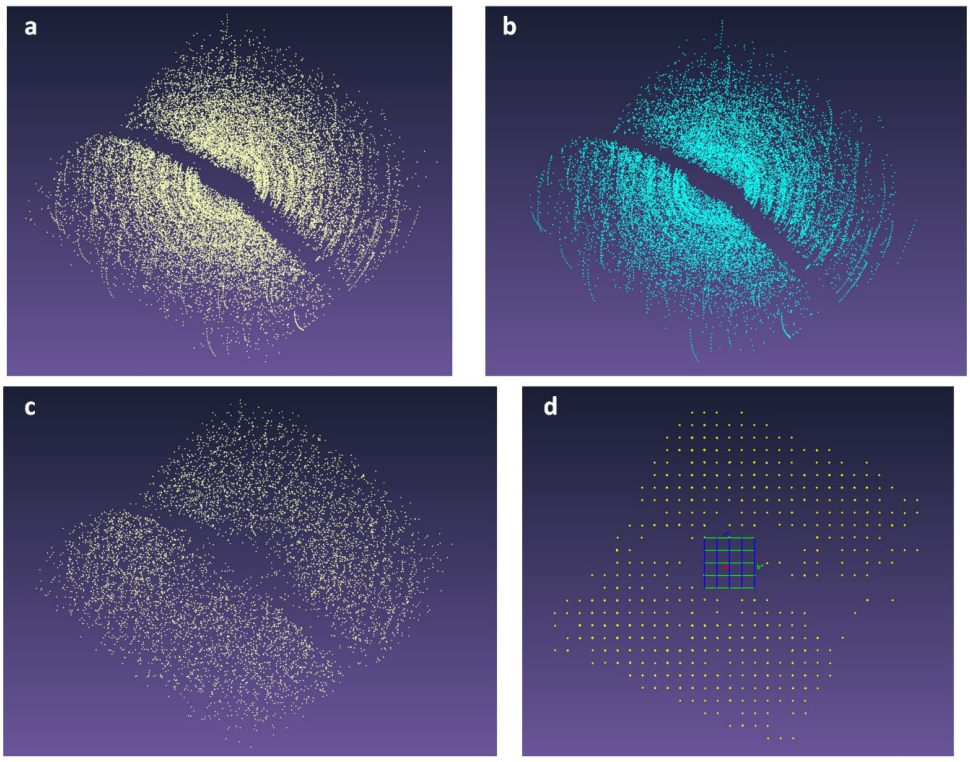

Figure 2.12. Reciprocal space representing single-crystal XRD data from a sample in a DAC laser-heated at ~20 GPa and ~2500 K. (a) An example of the initial dataset in a reciprocal space. (b) Trash signal from the sample environment defined by ‘Advanced filtering’ with a tolerance of 3. (c) Signal from the sample. (d) Reflections of group 1 represented along *a** axis.

Typically, identifying the starting peaks for unit cell determination is challenging, especially for laser-heated samples containing numerous crystallites. The latest innovation in high-pressure crystallography, DAFi software [142], effectively solves the problem of searching for regular lines of reflections in reciprocal space forming the unit cell in multi-grain samples.

3) Data reduction

For the given orientation matrix (UB-matrix), the precise extraction of Bragg's peaks intensities could be initiated with the 'dc proffit' command. CrysAlis^{Pro} predicts the positions of the reflections based on the UB-matrix and integrates their intensities, admitting the reflections' shape and the background level. Analyzing the systematic absences, the software indicates a space group, and the user checks the data quality by reviewing the frame scaling curve and confidence values provided by the program: R_σ and $F_{obs}^2/\sigma_{int}(F_{obs}^2)$ and the quality of merging intensities of the symmetry-equivalent reflections R_{int}. These values could be represented through the following equations:

$$R_\sigma = \frac{\sum[\sigma_{int}(F_{obs}^2)]}{\sum[F_{obs}^2]} \qquad Equation\ 2.5$$

$$\sigma_{int}(F_{obs}^2) = \sqrt{\frac{\sum[F_{obs}^2 - \langle F_{obs}^2\rangle]^2}{n}} \qquad Equation\ 2.6$$

$$R_{int} = \frac{\sum|F_{obs}^2 - \langle F_{obs}^2\rangle|}{\sum|F_{obs}^2|} \qquad Equation\ 2.7$$

where summation includes all input reflections for which more than one symmetry equivalent is averaged; F_{obs}^2 is intensity corrected for Lorentz-polarization, and $\langle F_{obs}^2\rangle$ is its average value over all measured equivalents; n is the number of redundant reflections. If the integration is of dissatisfied quality, it is possible to rerun the process by adjusting variables that influence the treatment of detector images, involving background correction, masking of reflections, integration range, etc. After data reduction, the software produces a file that lists all *hkl* reflections with their intensities which is then used by a separate software to solve the structure.

4) Data finalization

The final step in CrysAlis^{Pro} includes data finalization, performed once the user has achieved satisfactory integration quality. The user re-checks error factors and systematic absences and determines the space group. Following that procedure, CrysAlis^{Pro} generates files documenting the data processing performed. Among these files, the most crucial ones are standard reflection and instruction files identified by their file extensions: .hkl, .cif-od, .cif, and .ins, designed for compatibility with the various structure-solution software packages.

5) Structure solution and refinement

The files produced in the previous step (reflection files and instruction files) are subsequently imported into structure solution software. In the current thesis, the JANA2006 [141] and OLEX2 [138] are used.

The process of structure solution comprises utilizing the intensities of collected reflections for the computation of atomic positions and thermal parameters. The diffracted X-rays not only carry information on the reciprocal vectors but also provide details regarding the electronic density distribution within the unit cell of a sample. The Bragg reflections are characterized by intensities (I_{hkl}) proportional to the square of the structure factor (F_{hkl}) according to the following formula:

$$F_{hkl}^2 = \frac{I_{hkl}}{k \cdot L_p \cdot A} \qquad Equation\ 2.8$$

where k is a scale factor, L_p is the Lorentz-polarization correction, A is the transmission factor.

The structure factor holds the information about the types of atoms and their positions within the unit cell:

$$\boldsymbol{F}_{hkl} = F_{hkl} \cdot exp(i\alpha_{hkl}) =$$
$$= \sum_j f_j \cdot exp\left[-B_j \cdot \left(\frac{\sin(\theta)}{\lambda}\right)^2\right] \cdot exp\left[2\pi i \cdot \left(hx_j + ky_j + lz_j\right)\right] \qquad Equation\ 2.9$$

where the summing is carried out for the atoms within the unit cell; α_{hkl} is the phase of the diffracted beam; x_j, y_j, z_j and f_j are the coordinates and the scattering factor of the j^{th} atom, respectively; B_j is a B-factor directly related to the mean square isotropic displacement of the j^{th} atom; θ is the scattering angle and λ is the X-ray wavelength.

Therefore, the electron density in an xyz position inside the unit cell (ρ_{xyz}) can be obtained by applying inverse Fourier transformation, leading to the following equation:

$$\rho_{xyz} = \frac{1}{V}\sum_{hkl} \boldsymbol{F}_{hkl} \cdot \exp[-2\pi i \cdot (hx + ky + lz)] \qquad Equation\ 2.10$$

where V is the unit cell volume; the sum is over all the crystal lattice planes characterized by Miller indices.

In diffraction experiments, the intensities of waves scattered from the lattice planes in the crystal are measured, enabling the determination of the electronic density and, consequently, positions of all the atoms. Based on a set of experimental structural amplitudes, F_{hkl}^2, the process of structure solution can be characterized as a calculation of atomic coordinates and atomic thermal displacement parameters. Regrettably, the experimental values of F_{hkl}^2 are real numbers, whereas F_{hkl}, essential for the calculation of electronic density, is a complex function. Hence, the direct determination of the α_{hkl} phase becomes unfeasible, representing what is well-known as the "phase problem" [143]. Overcoming the phase problem is an automated procedure nowadays and many phasing methods are implemented in software, such as the Patterson synthesis, direct methods, heavy-atom methods, charge-flipping

algorithms, dual-space methods, and others [139,141]. Using any of these methods, it becomes possible to establish the distribution of electronic density and complete the initial structural model. At the subsequent stage, the structural model undergoes refinement against the experimental dataset through a least-squares minimization, adjusting parameters such as atomic coordinates, occupancies, and anisotropic thermal displacement parameters.

The quality of the refined structural model is defined by agreement between the model and experimental data represented by R-factors:

$$R_1 = \frac{\sum\left||F_{obs}| - |F_{calc}|\right|}{\sum|F_{obs}|} \qquad Equation\ 2.11$$

$$wR_2 = \left[\frac{\sum w|F_{obs}^2 - F_{calc}^2|}{\sum wF_{obs}^2}\right]^{\frac{1}{2}} \qquad Equation\ 2.12$$

where F_{obs} is the observed structure factor amplitude, F_{calc} is the calculated structure factor amplitude based on the model, and w is the weighting factor individually derived for each measured reflection based on its standard uncertainty. The structural model is of high quality if:

1) The R-factors are small (i.e. R_1 = 1-2% is excellent, R_1 = 10% is acceptable, and R_1 > 15% indicates serious problems with the data quality or the model solution).
2) The data to refined parameters ratio is high (i.e. ratio > 10 is excellent, 10 > ratio > 8 is good, 8 > ratio > 6 is acceptable if good reasoning is provided, ratio < 6 is unacceptable).
3) No major positive or negative electron residual densities exist.
4) The model makes sense from the crystallographic and chemical point of view.

2.4 Computational approaches

Density functional theory (DFT) [144,145] is the method of choice for the calculation of structure-property relations of crystalline materials. First-principles calculations based on DFT have emerged as a powerful tool for exploring material properties in recent decades [146,147]. The DFT approach is especially valuable for investigating materials under extreme conditions, as experiments under high pressure have limitations in directly measuring the properties of samples in DACs. For known structures, computing properties like the bulk modulus is typically straightforward using established packages such as VASP [148], ABINIT [149], QUANTUM ESPRESSO [150], CASTEP [151], or similar codes.

From Bloch's theorem for periodic systems [152], the solution of Schrödinger's equation can be separated into two parts,

$$\psi(r) = e^{ikr}u(r) \qquad Equation\ 2.13$$

where ψ is the wavefunction, k is the wave vector, e^{ikr} is a plane wave, and $u(r)$ is a periodic function. This naturally leads to a planewave representation of the electronic wavefunctions. Periodic boundary conditions are usually used in combination with plane waves in *ab initio* calculations, which make use of periodicity to create an infinite system from the unit cell in a crystal or supercells in aperiodic systems [153].

In this study, the properties of synthesized compounds are determined through the first-principles calculations using the framework of DFT as implemented in the Vienna *ab initio* simulation package (VASP) code [148]. To expand the electronic wave function in plane waves, we used the Projector-Augmented-Wave (PAW) method [154]. The Generalized Gradient Approximation (GGA) functional was used for calculating the exchange-correlation energies, as proposed by Perdew–Burke–Ernzerhof (PBE) [155]. The PAW potentials with the following valence configurations of 5*s*5*p*6*s*5*d* for lanthanides, 4*s*4*p*5*s*4*d* for Y, 3*p*4*s*3*d* for Fe, 3*s*3*p* for Cl, and 2*s*2*p* for C were used to describe the interaction between the core and the valence electrons in frozen *f*-electrons approximation for lanthanides [156]. Convergence tests with a threshold of 2 meV per atom in energy led to an energy cutoff for the plane wave expansion of 600-750 eV for synthesized phases. Harmonic lattice dynamics calculations were performed with the PHONOPY software [157] using the finite displacement method for constructed supercells with respectively adjusted *k*-points. The tetrahedron method was used for Brillouin zone integrations, employing a mesh of adjusted *k*-points for investigated structures [158,159]. The tetrahedron method replaces the continuous integral over the Brillouin zone with a weighted sum over a finite number of *k*-points. The weight factors are determined under the assumption that the function to be integrated is linear inside each tetrahedron. The integrated values of the crystal orbital bond index (ICOBI) [160] and Mulliken charges were calculated using LOBSTER v4.1.0 software [161], where ICOBI correlates with the bond order, and on the other hand, represents a measure of the bond ionicity. For instance, strongly covalent molecules such as HI, HBr, and HCl show a bond index very close to the expected value of 1. While the difference in electronegativity grows, the bond index continuously approaches smaller values until it eventually reaches 0.04 (CsF) for the largest electronegativity difference in the example [160]. The Mulliken charges approach is a concept in molecular physics and chemistry that refers to the distribution of electronic charge within a

molecule. The Mulliken charges are calculated based on the electronic population analysis using LCAO-MO (Linear Combination of Atomic Orbital-Molecular Orbital) wave functions [162–165]. The charge distribution in the ionic approximation based on a generalization of Pauling's concept of bond strength [166] was made using CHARDI2015 [167]. In our calculations, temperature, configurational entropy, and the entropy contribution due to lattice vibrations were neglected.

The performed calculations are based on frozen *f*-electrons potentials of lanthanides instead of those that take into account the contribution of *f*-electrons due to the cluster resources limitations and appearance of related difficulties in the theoretical calculations. In the theoretical part of the current study, we are focused on checking of convergence of experimental results and theoretical calculations in the available approximation, as well as computing some of the properties such as bulk modulus, type of chemical bonds, and phonon and electron density of states.

3. Thesis synopsis

This part provides a short overview of the results presented in Chapter 4 as manuscripts, which have been either published or prepared for submission to peer-review journals. For the list of the manuscripts please see section 3.3. Section 3.1 is dedicated to the study of hitherto unknown dysprosium carbides formed under extreme conditions and presents the study of Dy-C compounds formation at ~20-60 GPa and temperatures of ~2500 K (manuscript "High-pressure synthesis of dysprosium carbides", Section 4.1), as well as the synthesis of Dy-C compounds demonstrating the more pronounced structural diversity at pressures ~70 GPa and temperatures up to ~2800 K (manuscript "High-Pressure Dysprosium Carbides Containing Carbon Dimers, Trimers, Chains, and Ribbons", Section 4.2) and the systematic exploration of rare-earth elements carbides chemistry under extreme conditions in a wide pressure range – ~20-125 GPa and temperatures of ~2200-2800 K (manuscript "High-Pressure Synthesis of Rare-Earth Metals Carbides Featuring Carbon Polyanions", Section 4.3). In the course of the exploration of the Y-C and Dy-C systems, a number of novel chlorides, Y_2Cl and DyCl, and chloride carbides, Y_2ClC and Dy_2ClC, have been synthesized as a result of chemical reactions of samples with NaCl or KCl pressure media at ~40 GPa and ~2000 K. We solved and refined their structures, which are briefly presented in Section 3.2 (manuscript "Synthesis of rare-earth metal compounds through enhanced reactivity of alkali halides at high pressures", Section 4.4).

3.1 Structural diversity and systematics of rare-earth metals carbides synthesized in LHDACs under HPHT conditions

The lanthanide carbides family shows a large variety of possible phases with different stoichiometry at ambient pressure: REE_4C_3 (REE = Sc), $REEC_x$ (x ~ 0.33-1, REE = Sc, Y, Ce, Sm-Lu), REE_4C_5 (REE = Y, Gd-Ho), REE_3C_4 (REE = Sc, Y, Tb-Lu), REE_2C_3 (REE = La-Nd, Sm-Ho), REE_4C_7 (REE = Y, Dy-Tm, Lu), $REEC_2$ (REE = Y, La-Lu), $REEC_6$ (REE = Eu) [5]. Still, the number of known binary carbon compounds is significantly smaller than the number of known binary oxygen compounds (1329 vs 4768) according to the ICSD database (Version 5.2.0 (build 20240410-1029) - Data Release 2024.1). Considering that a vast amount of the data corresponds to ambient conditions, the chemistry of carbides under high pressure has been poorly studied in principle. The limited knowledge of the lanthanides carbides chemistry under high-pressure conditions, particularly those containing heavy lanthanides, emphasizes the importance of enhancing our comprehension of their behavior.

The chemistry of binary compounds drastically changes at high pressures. Recent striking examples include the synthesis of novel polyhalides [97,168], polynitrides [169–176], polyborides [177,178], and polyhydrides [179–181]. In contrast to conventional solid-state materials, many of these new compounds comprise various homonuclear chemical species, such as dimers, trimers, pentagonal and hexagonal rings, polymeric chains, atomic layers, and 3D networks. Homonuclear chemical bonding between carbon atoms is at the heart of organic chemistry and the number of arrangements for carbon connections (or catenation) known at ambient pressure is enormous. Theoretical calculations for metal carbides at high pressure predict carbon polyanions with unusual geometry and chemical bonding [79,82,182]. Moreover, recent experimental observations suggest the possible existence of carbon polyanions at high pressures, which were previously unknown under ambient conditions and were not theoretically predicted [7,86,87,183]. These predictions and discoveries call for systematic experimental studies of high-pressure carbides.

In sections 4.1 and 4.2, the lanthanides carbides chemistry under extreme conditions was explored using the example of Dy-C compounds. Dysprosium flakes were loaded between one of the diamond anvils and the layer of dry NaCl served as a thermal insulator and a pressure-transmitting medium; diamond anvils were used as a carbon source. Samples were compressed to the desired pressures and laser-heated up to 2800 K. Laser heating of the samples was carried out using our *in house* double-sided YAG laser (1064 nm wavelength) heating setup [129]. The chemical reactions of dysprosium and carbon in diamond anvil cells at pressures of ~19-95 GPa and temperatures of ~2500-2800 K resulted in the formation of five novel dysprosium carbides, namely γ-DyC_2 (*Immm*), Dy_5C_9 (*P4/mnc*), γ-Dy_4C_5 (*Cmce*), Dy_3C_2 (*P*4/*mbm*), and Dy_4C_3 (*I*-43*d*), and one compound previously known at ambient condition, Dy_2C_3 (*I*-43*d*) (Fig. 3.1). The most notable features of new carbides are polyacene-like ribbons in γ-DyC_2 and *cis*-polyacetylene-type chains in Dy_5C_9. These findings demonstrate the tendency of the formation of carbides with complex polyanions at high pressures.

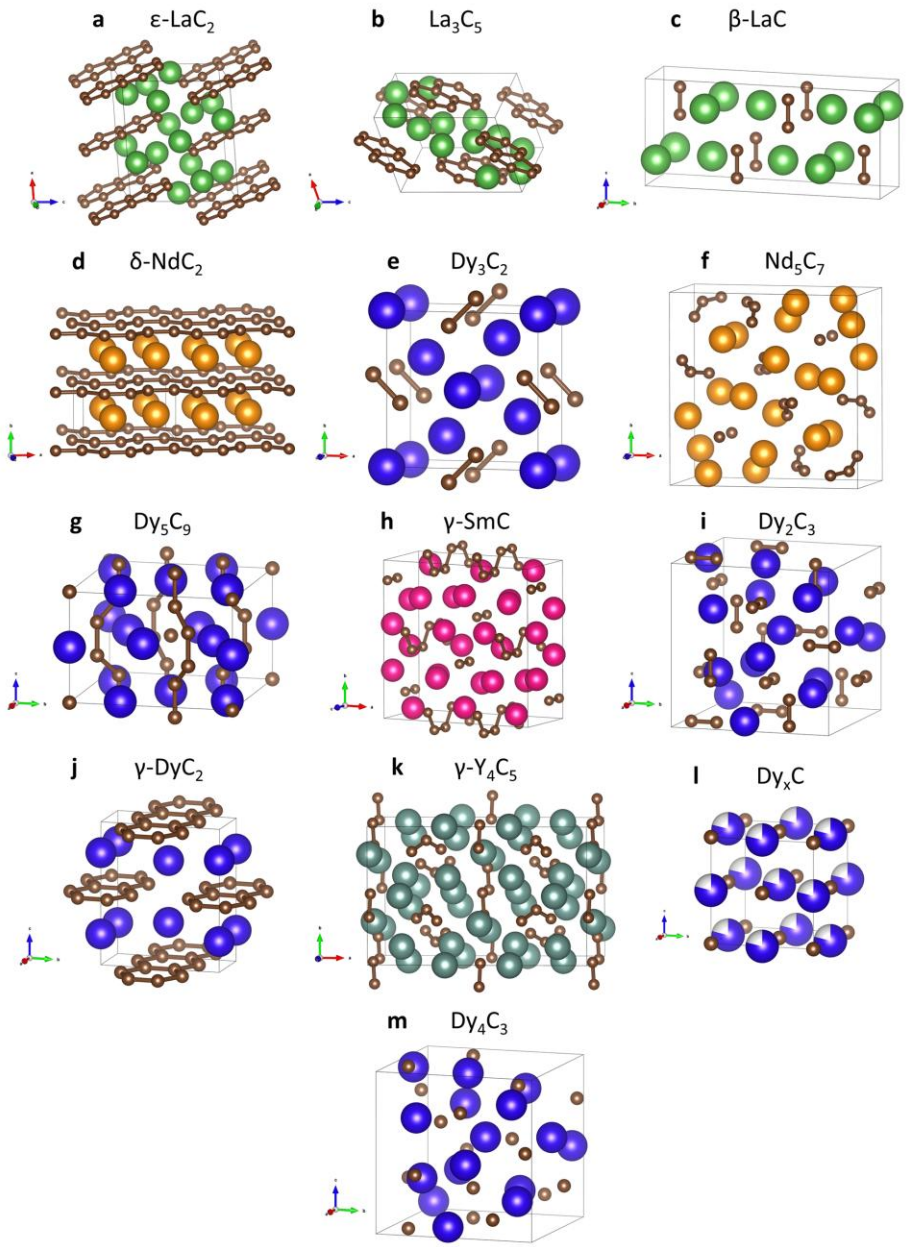

Figure 3.1. Crystal structures of rare-earth metals carbides synthesized under extreme conditions: (a) ε-LaC_2, (b) La_3C_5, (c) β-LaC (β-NdC, β-SmC), (d) δ-NdC_2 (δ-SmC_2), (e) Dy_3C_2 (Nd_3C_2, Sm_3C_2, Gd_3C_2), (f) Nd_5C_7 (Sm_5C_7, Gd_5C_7, Yb_5C_7), (g) Dy_5C_9 (Y_5C_9, Nd_5C_9, Sm_5C_9, Gd_5C_9, Yb_5C_9), (h) γ-SmC, (i) Dy_2C_3 (Y_2C_3, Sm_2C_3, Gd_2C_3), (j) γ-DyC_2 (γ-YC_2, γ-SmC_2), (k) γ-Y_4C_5 (γ-Sm_4C_5, γ-Gd_4C_5, γ-Dy_4C_5), (l) Dy_xC (Y_xC, Gd_xC, Yb_xC), (m) Dy_4C_3 (Sc_4C_3, Gd_4C_3, Yb_4C_3). Yttrium carbides Y_2C_3 and γ-Y_4C_5 were synthesized and characterized earlier in [7].

In section 4.3, we show that the increasing pressure contributes to the formation of more complex carbon arrangements, progressing from carbon dumbbells and trimers to carbon chains and ribbons for a number of rare-earth metals – carbon systems. Moreover, the tendency of regularities in the chemistry of rare-earth metals carbides was observed and explored during the direct chemical reaction between carbon from diamond anvils and loaded into DACs rare-

earth metals (REE = Sc, Y, La, Nd, Sm, Gd, Dy, and Yb) in the HPHT experiments at pressures of ~34-124 GPa and temperatures of ~2200-2500 K. The dysprosium carbides have been studied in the previous sections; this section provides Dy-C compounds, accompanied by relevant references, for systematic exploration of REE-C compounds discussed in the current work. In most experiments, dry NaCl served as a thermal insulator and a pressure-transmitting medium preserving the experiment geometry of "diamond anvil – rare-earth metal flake – a layer of dry NaCl". A couple of experiments were carried out in the Ar pressure-transmitting medium.

The crystal structures of synthesized REE_xC_y (REE = Sc, Y, La, Nd, Sm, Gd, Dy, and Yb) carbides were determined and refined on the basis of single-crystal synchrotron XRD. The synthesized γ-Sm_4C_5 isostructural to the recently discovered γ-Y_4C_5 [7] and novel Nd_5C_7 were found to be quenchable to ambient conditions. High-pressure high-temperature synthesis of the rare-earth metals carbides and their structural characterization yielded 32 novel compounds, which belong to 13 structural types, among which 9 were previously unknown (Fig. 3.1). Clear chemical regularities were revealed by comparing all the rare-earth carbides synthesized in this thesis (Fig. 3.2).

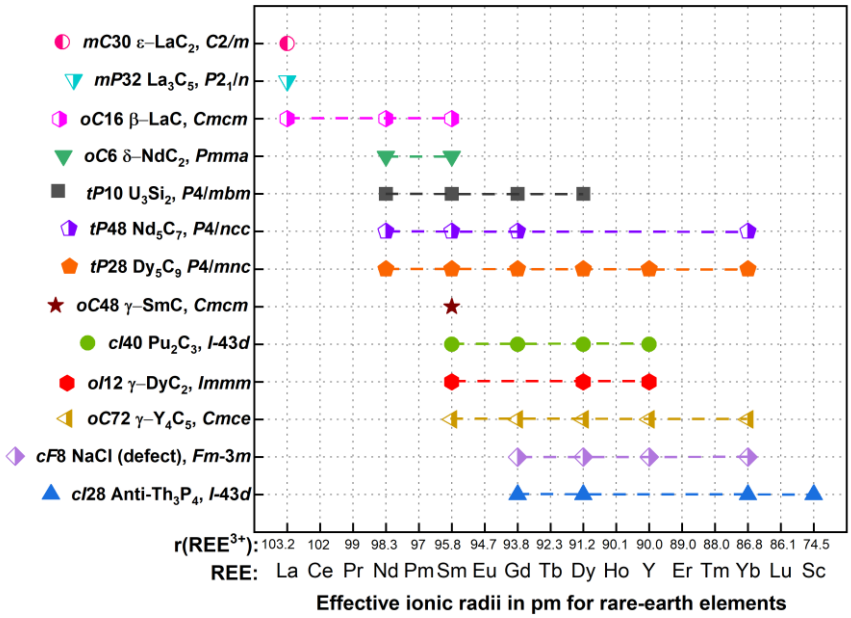

Figure 3.2. Summary of the high-pressure high-temperature experiments (ionic radii of rare-earth elements $r(REE^{3+})$ are from [184]). Yttrium carbides Y_2C_3 and γ-Y_4C_5 were synthesized and characterized earlier in [7].

The carbides with the highest metal-to-carbon ratio synthesized in the present thesis are compounds of the U_3Si_2 structural type, first observed in the Dy-C system at 55 GPa and described in section 4.1. The carbides REE_3C_2 (REE = Nd, Sm, Gd, and Dy) have a tetragonal

unit cell (space group *P*4/*mbm*, #127, *Z* = 2) with the following unit cell parameters for Dy_3C_2 at 55 GPa: *a* = 5.9896(13) Å and *c* = 3.3880(12) Å. Rare-earth metal carbides of such stoichiometry have not been previously observed [5], but the U_3Si_2-type structure is common for silicides [185], borides [186], and intermetallides [187]. Such structure was also theoretically predicted for a high-pressure calcium carbide Ca_3C_2 [82]. The *a*/*c* ratio for the synthesized lanthanides carbides lies in the range of 1.71 – 1.77 Å, according to the obtained data at pressures of 20-68 GPa. Based on the known at ambient pressure data, the *a*/*c* ratio for isostructural compounds varies from ~1.8 – 1.87 (for borides Ta_3B_2 [188] and silicides La_3Si_2 [189], Ce_3Si_2 [190], and U_3Si_2 [191]) to ~1.96 – 2.08 (for intermetallic compounds Ga_2Ta_3 [192], Gd_3Pd_2 [193], and La_3Au_2 [194]). In the structure of Dy_3C_2 (Fig. 3.1e and 3.3) carbon atoms occupy a single 4*g* Wyckoff position and form [C_2] dumbbells. Two crystallographically distinct dysprosium atoms occupy the Wyckoff positions 2*a* (Dy1) and 4*h* (Dy2). Dy1 atoms lie in the same *ab* plane as the [C_2] dumbbells, forming together the Cairo pentagonal tiling comprised of $(Dy1)_2C_3$ pentagons (Fig. 3.3b). Dy2 atoms are located in a parallel plane, separated from the described one by ½ *c* (Fig. 3.3c). The Dy2-C distances are of 2.413(9) Å or 2.574(10) Å (Fig. 3.3d). As seen in Fig. 3.3b, the Dy1 atoms are four-fold coordinated by C atoms with the Dy1-C distance equal to 2.519(12) Å at 55 GPa. The length of the [C_2] dumbbell is equal to 1.51(3) Å (Fig. 3.3e).

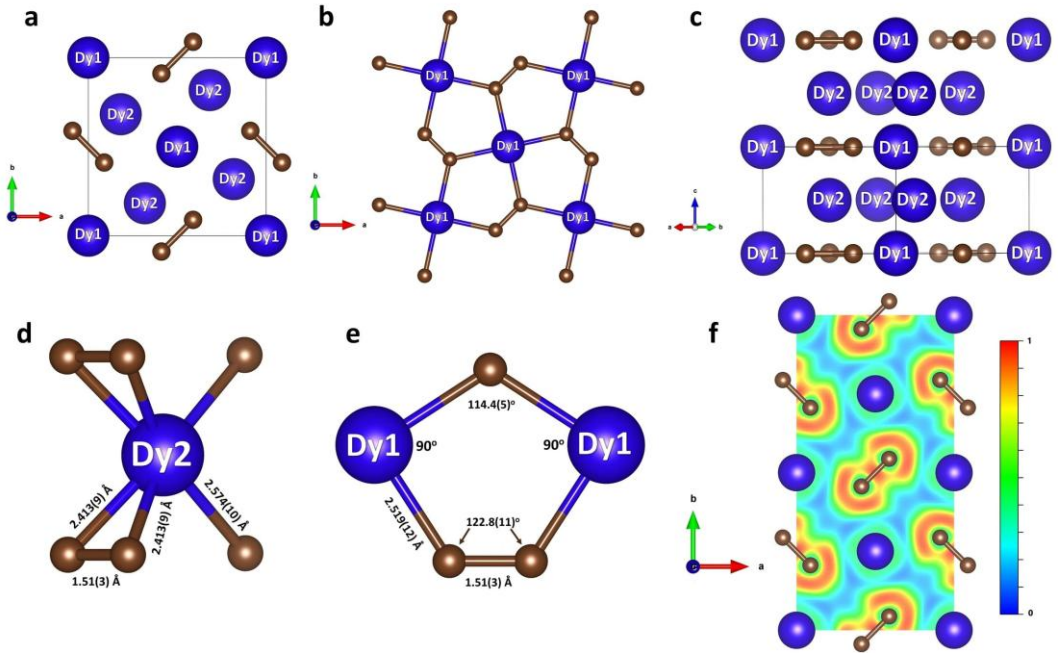

Figure 3.3. Crystal structure of Dy_3C_2 at 55 GPa and a cross section of the calculated ELF. The blue and brown spheres represent dysprosium and carbon, respectively. (a) The structure viewed along the *c*-axis; (b) the Dy1-C plane with the highlighted Cairo pentagonal tiling formed by Dy1 and C atoms; (c) the projection of the structure along the [1 1 0] direction highlighting the Dy1-C and Dy2 layers stacking in the *c* direction; (d) coordination

of Dy2 atoms by carbon atoms; (e) interatomic distances in the Dy1-C plane; (f) the 2D electron localization function (ELF) shown in *ab* plane containing carbon dumbbells and Dy1 atoms.

Rare-earth metal carbides of REE_4C_3 stoichiometry (REE = Sc, Gd, Dy, and Yb) were observed at 19-64 GPa after laser heating the samples. The compounds have the anti-Th_3P_4-type structure (space group *I*-43*d*, #220, *Z* = 4) shown in Fig. 3.4, which has been described for scandium carbide, Sc_4C_3, but not observed for other rare-earth metal carbides [5,44]. At 19 GPa its unit cell parameter is equal to *a* = 7.4774(8) Å for Dy_4C_3. In the structure of Dy_4C_3 (Fig. 3.1m and 3.4), dysprosium and carbon atoms occupy the 16*c* and 12*a* Wyckoff sites, respectively. The coordination polyhedron of Dy cations is an irregular octahedron formed by the six nearest carbon atoms at distances of either 2.3819(5) Å or 2.8240(5) Å at 19 GPa (Fig. 3.4b). Carbon atoms are surrounded by eight Dy atoms forming strongly distorted cubes (octaverticons) (Fig. 3.4c).

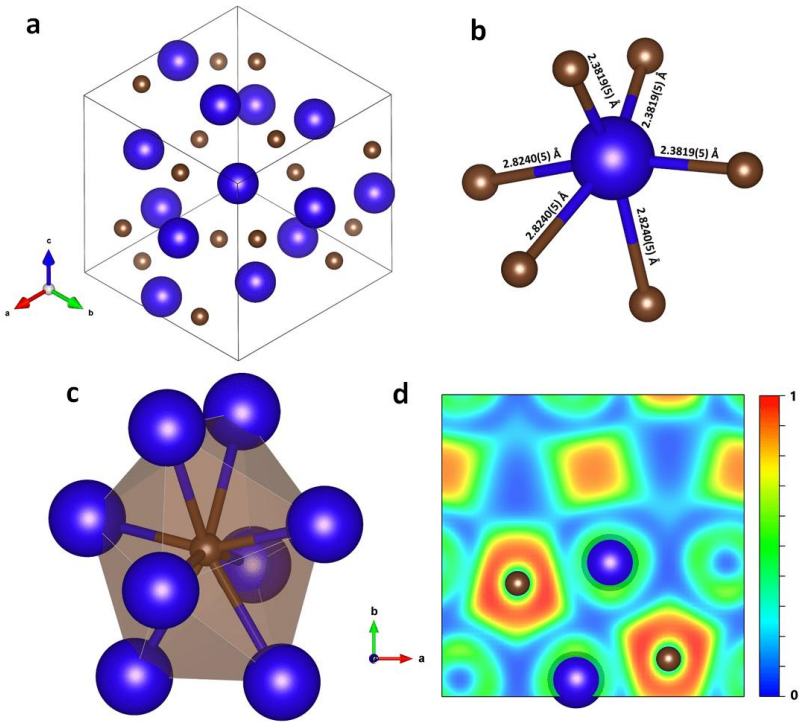

Figure 3.4. Crystal structure of Dy_4C_3 at 19 GPa and a cross section of the calculated ELF. The blue and brown spheres represent dysprosium and carbon, respectively. (a) Unit cell in projection along the [1 1 1] direction. (b) Coordination polyhedron of Dy. (c) Coordination environment of a carbon atom. (d) The 2D ELF shown in the (0 0 1) plane.

Compounds β-REEC (REE = La, Nd, Sm) obtained at 41-68 GPa represent a new structural type *oC*16 β-LaC (space group *Cmcm*, #63, *Z* = 8) that have not been observed previously. For instance, the unit cell of β-LaC at 41 GPa is described by the following lattice parameters: *a* = 3.2858(8) Å, *b* = 12.0825(19) Å, and *c* = 5.3937(12) Å (Fig. 3.1c and 3.5). The

crystal structure reveals two crystallographically distinct positions of the metal atoms 4*c* (La1 and La2) and one of the carbon atoms 8*f* (C1). The La1 atoms have a coordination number (CN) of 6 with respect to the nearest carbon atoms, four of which belong to the two [C_2] dimers in a side-on orientation with the La1-C distance *d*(La1-C1) = 2.507(5) Å, and two more atoms come from the two end-on oriented [C_2] units with *d*(La1-C1) = 2.600(7) Å (Fig. 3.5c). The La2 atoms possess the highest coordination number, CN = 8, with the contribution of two carbon dumbbells [C_2] in a side-on orientation with *d*(La2-C1) = 2.589(5) Å, and four atoms from the four end-on oriented [C_2] units with *d*(La2-C1) = 2.696(6) Å (Fig. 3.5d). Dimers [C_2] are oriented along the *c*-axis (Fig. 3.5b). The bond length in [C_2] units is ~1.4 Å.

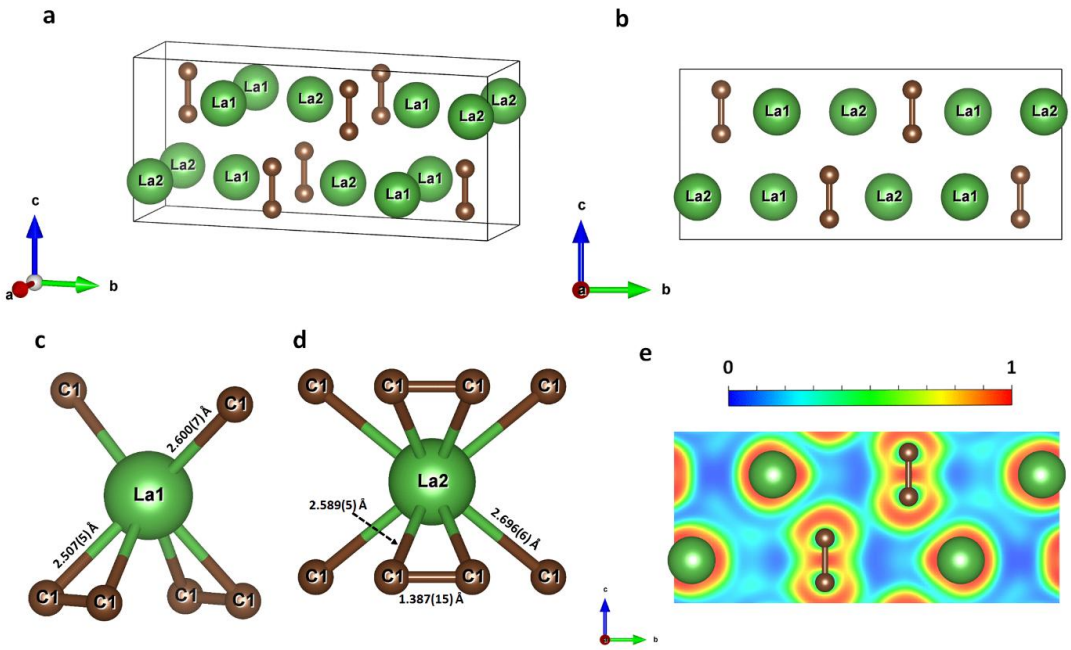

Figure 3.5. Crystal structure of β-LaC at 41 GPa and a cross section of the calculated ELF. The green and brown spheres represent lanthanum and carbon atoms, respectively. (a) A view of the crystal structure. (b) The structure viewed along the *a*-axis. (c) The coordination environment of La1 atoms. (d) The coordination environment of La2 atoms. (e) The 2D ELF shown in *bc* plane containing carbon dumbbells.

Newly found samarium carbide *oC*48 γ-SmC possesses the orthorhombic space group *Cmcm*, #63 (*Z* = 24). The unit cell parameters are *a* = 10.0193(14) Å, *b* = 9.897(9) Å, and *c* = 4.7921(5) Å at 103 GPa (Fig. 3.1h and 3.6). Four Wyckoff positions 4*c*, 8*g*, 4*c*, and 8*g* are occupied by samarium atoms, whereas the 8*f* and 16*h* sites host carbon atoms. There are two types of carbon entities: carbon dimers formed by C1 atoms and 1D *cis*-polyacetylene type deprotonated carbon chains with sp^2-hybridized C2 carbon atoms and conjugated π-electron system. These entities are oriented along the *c*-axis (Fig. 3.6a, b). The Sm1 atoms have the highest coordination number, CN = 10, in relation to the nearest carbon atoms, two of which

belong to the [C_2] unit in a side-on orientation with *d*(Sm1-C1) = 2.88(3) Å, while the remaining eight carbon atoms originate from the two carbon chains with *d*(Sm1-C2) = 2.361(14) Å and 2.389(8) Å (Fig. 3.6c). The Sm2 atoms have an eight-fold coordination environment (CN = 8) comprised of one [C_2] dimer in a side-on orientation with *d*(Sm2-C1) = 2.48(3) Å, two C atoms from two [C_2] dimers in an end-on orientation with *d*(Sm2-C1) = 2.340(12) Å, and four C atoms deriving from the nearby carbon chain with *d*(Sm2-C2) = 2.350(12) Å and 2.490(7) Å (Fig. 3.6d). The Sm3 atoms are six-fold coordinated (CN = 6) by two carbon atoms from two end-on oriented [C_2] dimers with *d*(Sm3-C1) = 2.31(3) Å and four carbon atoms from two neighboring chains with *d*(Sm3-C2) = 2.390(14) Å (Fig. 3.6e). The Sm4 atoms also have a CN of 6 with the coordination environment consisting of one side-on oriented [C_2] dumbbell with *d*(Sm4-C1) = 2.315(14) Å and four C atoms stemming from the two nearest carbon chains with *d*(Sm4-C2) = 2.364(16) Å and 2.558(16) Å (Fig. 3.6f). At 103 GPa, the C-C bond length within carbon [C_2] dumbbells is equal to 1.360(18) Å, while the distance between carbon atoms in the *cis*-polyacetylene-type chains alternates between 1.50(4) Å and 1.511(14) Å.

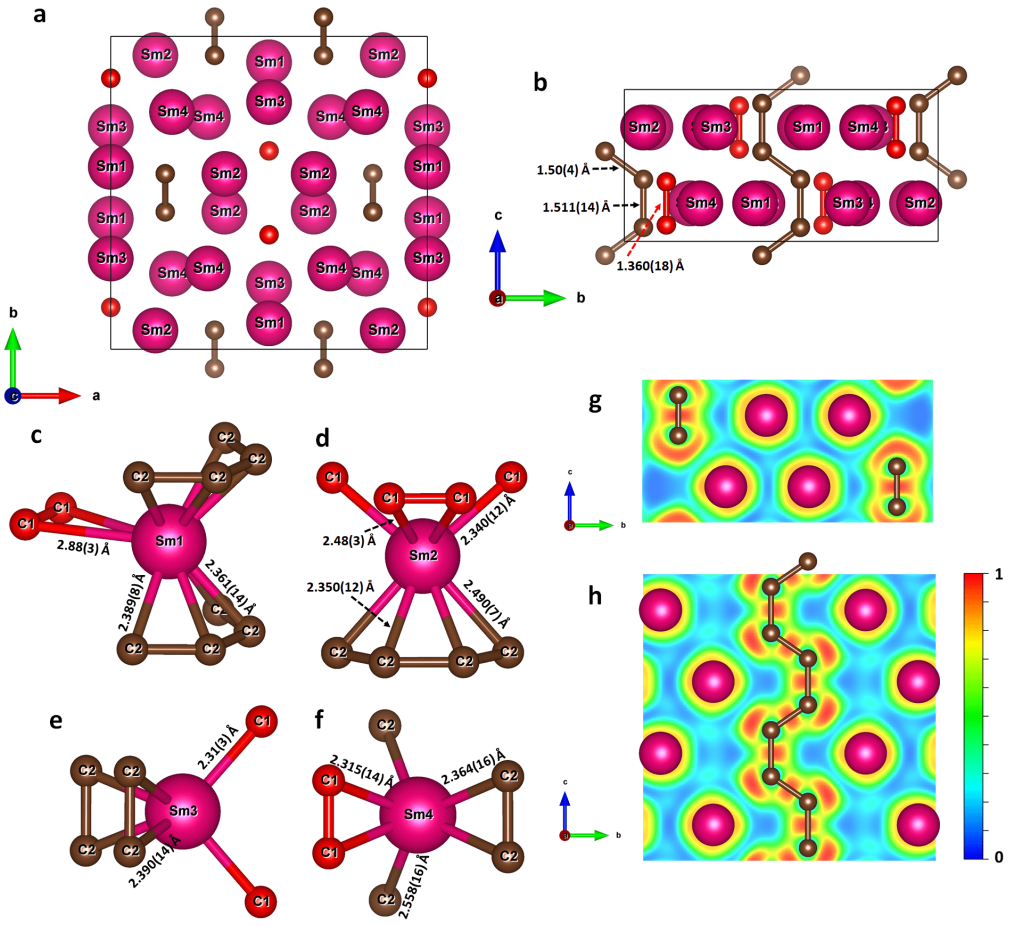

Figure 3.6. Crystal structure of γ-SmC at 103 GPa and a cross section of the calculated ELF. The pink, red, and brown spheres represent samarium, carbon atoms formed dumbbells, and

carbon atoms formed chains, respectively. (a) Unit cell in projection along the *c*-axis. (b) The view of the crystal structure along the *a*-axis. (c) The coordination environment of Sm1 atoms. (d) The coordination environment of Sm2 atoms. (e) The coordination environment of Sm3 atoms. (f) The coordination environment of Sm4 atoms. (g) The 2D ELF calculated in the *bc* plane containing carbon dumbbells [C_2]. (h) The 2D ELF calculated in the *bc* plane containing carbon chains.

Carbides of defect NaCl structure type (space group *Fm*-3*m*, #225, *Z* = 4) (Fig. 3.1l) are known at ambient conditions for Sc, Y, and Sm-Lu [5]. In this study carbides with alterable stoichiometry REE_xC (REE = Y, Gd, Dy, Yb; x ~ 0.6-1) were formed at ~34-46 GPa. Metal and carbon atoms occupy 4*b* and 4*a* Wyckoff positions, respectively. The full experimental crystallographic data of REE_xC carbides are provided in section 4.3.

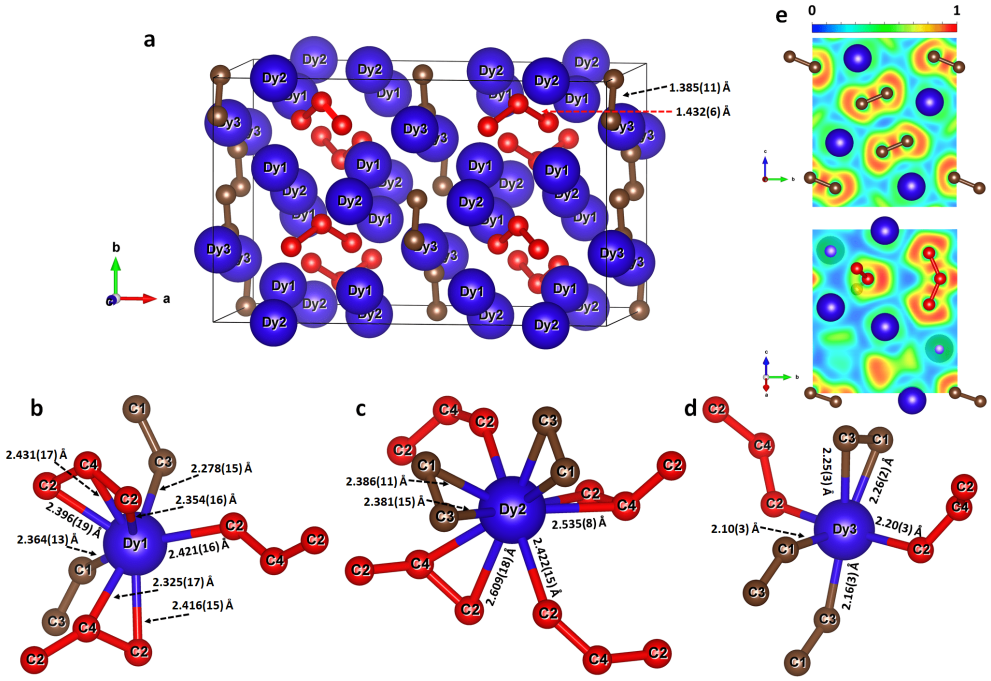

Figure 3.7. Crystal structure of γ-Dy_4C_5 at 65 GPa and a cross section of the calculated ELF. The blue, brown, and red spheres represent dysprosium, carbon atoms formed dumbbells, and carbon atoms formed trimers, respectively. (a) A view of the crystal structure. (b)-(d) The coordination environment of the Dy1, Dy2, and Dy3 atoms. (e) The 2D ELF calculated in the *bc* plane containing carbon dumbbells [C_2] (upper figure) or in the plane containing carbon trimers [C_3] (bottom figure).

Recently uncovered *oC*72 γ-Y_4C_5 structure type (space group *Cmce*, #64, *Z* = 8) [7] was observed through HPHT experiments at ~34-65 GPa for several lanthanides: Sm, Gd, Dy, and Yb. For instance, the unit cell parameters for γ-Dy_4C_5 are *a* = 11.800(6) Å, *b* = 7.2291(15) Å, and *c* = 8.416(2) Å at 65 GPa (Fig. 3.1k and 3.7). In the crystal structure, Dy1, Dy2, and Dy3 atoms occupy the 16*g*, 8*d* and 8*f* Wyckoff positions, and C1, C2, C3, and C4 are at the 8*f*, 16*g*, 8*f*, and 8*e* Wyckoff sites, respectively. C1 and C3 atoms form [C_2] dimers lying in the *bc* plane, while C2 and C4 form [C_3] trimers. Metal atoms are coordinated by carbon atoms from dimers

and trimers with varying orientations and have coordination numbers: CN(Dy1) = 8 (*d*(Dy1-C) = 2.278(15)-2.431(17) Å), CN(Dy2) = 10 (*d*(Dy2-C) = 2.609(18)-2.381(15) Å), CN(Dy3) = 6 (*d*(Dy3-C) = 2.10(3)-2.26(2) Å) (Fig. 3.7b-d). In γ-Dy_4C_5, bond lengths of [C_2] and [C_3] units are 1.385(11) and 1.432(6) Å, respectively. These values are consistent with C-C bond lengths in reported γ-Y_4C_5 [7], which suggests the nature of synthesized compounds is similar to the earlier considered yttrium carbide.

Novel structural type *tP*48 Nd_5C_7 (space group *P*4/*ncc*, #130, *Z* = 4) has been discovered for Nd, Sm, Gd, and Yb carbides at ~42-60 GPa (Fig. 3.1f and 3.8). The tetragonal unit cell of Nd_5C_7 is described by the following parameters: *a* = 10.2129(17) Å and *c* = 5.3143(14) Å at 57 GPa. There are two crystallographically non-equivalent metal atoms occupying Wyckoff positions 4*a* (Nd1) and 16*g* (Nd2). Three Wyckoff positions are occupied by carbon atoms: 16*g* (C1), 8*f* (C2), and 4*c* (C3), with C1 and C2 atoms forming [C_3] trimers. The Nd1 atoms are surrounded by the ten nearest carbon atoms (CN = 10), where six atoms are contributed by two [C_3] trimers in a side-on orientation with *d*(Nd1-C1) = 2.474(10) Å and 2.619(10) Å, and four more atoms are from the four end-on oriented [C_3] units with *d*(Nd1-C2) = 2.480(9) Å (Fig. 3.8c). The Nd2 atoms are eight-fold coordinated (CN = 9) by four differently oriented [C_3] trimers (*d*(Nd2-C1) = 2.361(9)-2.520(10) Å, *d*(Nd2-C2) = 2.493(8)-3.077(9) Å) and two discrete carbon atoms (*d*(Nd2-C3) = 2.607(11) Å and 2.660(12) Å) (Fig. 3.8d). The C-C distance in trimers, equal to ~1.4 Å, supposes a non-integer bond order in the range of 1.0-1.5, analogously to γ-Y_4C_5 [7].

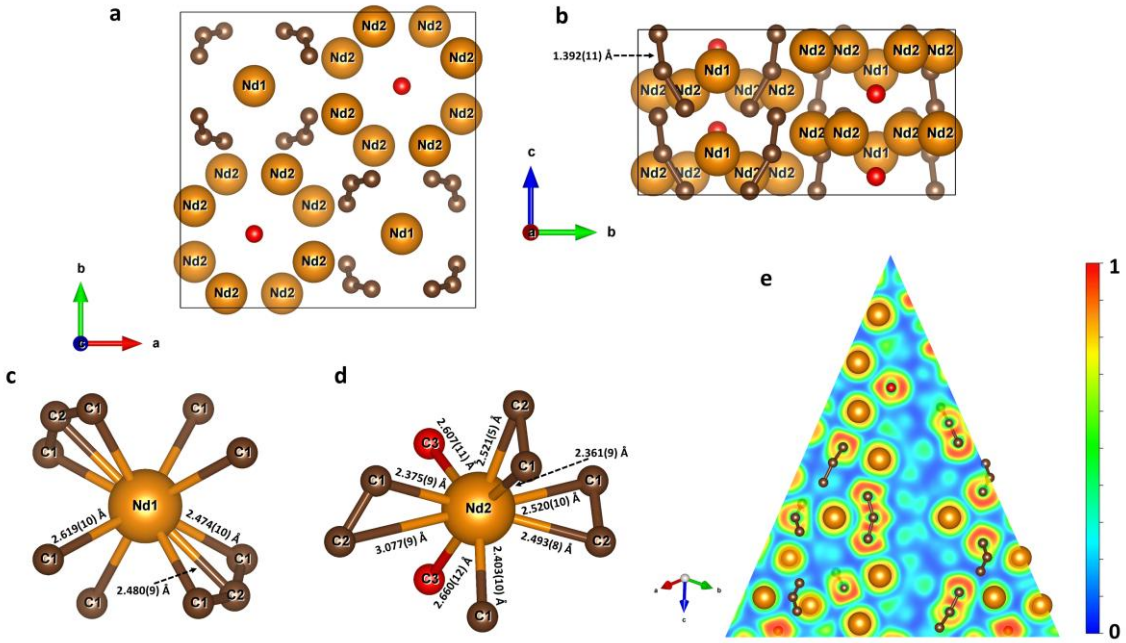

Figure 3.8. Crystal structure of Nd_5C_7 at 57 GPa and a cross section of the calculated ELF. The orange, red, and brown spheres represent neodymium, discrete carbon atoms, and carbon

atoms forming trimers. (a) Unit cell in projection along the *c*-axis. (b) The view of the crystal structure along the *a*-axis. (c) The coordination environment of Nd1 atoms. (d) The coordination environment of Nd2 atoms. (e) The 2D ELF calculated in the plane containing carbon trimers [C_3].

Sesquicarbides REE_2C_3 (REE = Y, Sm, Gd, Dy), which are known at ambient conditions [5,10,33], were found as products of HPHT synthesis in a DAC at pressures of ~19-57 GPa. These compounds belong to a known structural type Pu_2C_3 characterized by cubic space group *I-43d*, #220 and *Z* = 8 (Fig. 3.1i and 3.9). The lattice parameter is *a* = 7.9208(5) Å for Dy_2C_3 at 19 GPa. The dysprosium sesquicarbide Dy_2C_3 was earlier reported at ambient conditions with the lattice parameter *a* = 8.198(2) Å at 1 bar [18]. The dysprosium and carbon atoms occupy the 16*c* and 24*d* Wyckoff sites, respectively. The synthesized rare-earth carbides of such structure contain [C_2] carbon dumbbells with a C-C bond length of ~1.3 Å.

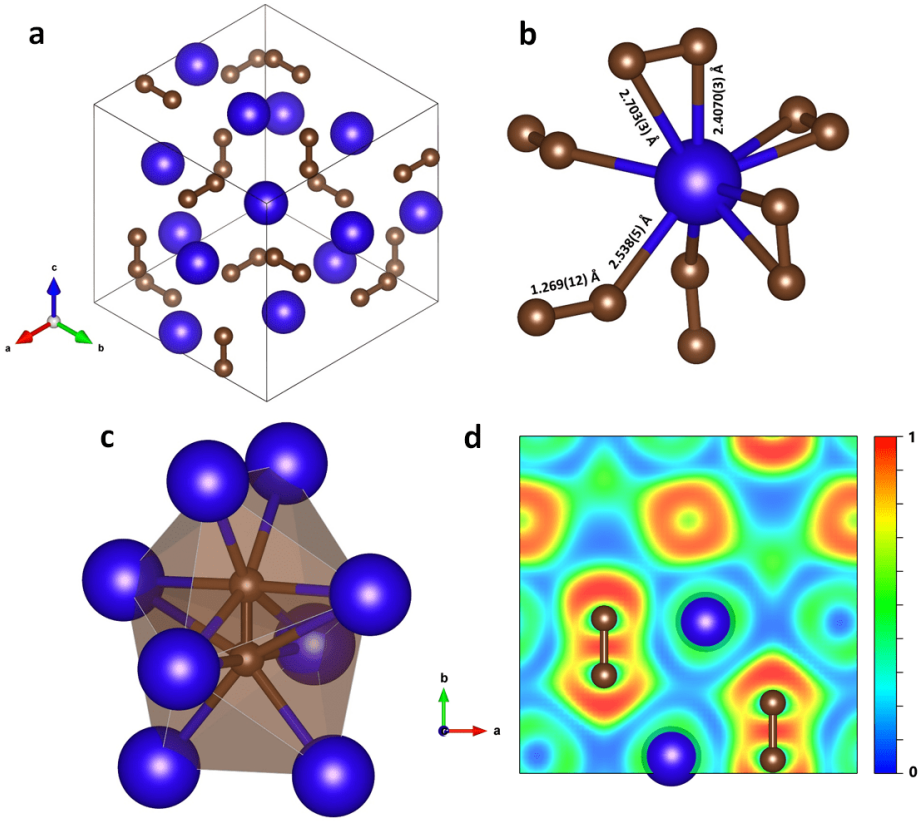

Figure 3.9. Crystal structure of Dy_2C_3 at 19 GPa and a cross section of the calculated ELF. The blue and brown spheres represent dysprosium and carbon, respectively. (a) Unit cell in projection along the [1 1 1] direction. (b) Coordination polyhedron of Dy. (c) Carbon dumbbell in a cage of eight Dy atoms. (d) The 2D ELF shown in the (0 0 1) plane.

The structures of Dy_2C_3 and Dy_4C_3 (described above) are closely related (Fig. 3.4 and 3.9): they have the same space group (*I*-43*d*), and the former can be easily derived from the latter, as the positions of the centers of [C_2] dumbbells in Dy_2C_3 coincide with the positions of single carbon atoms in Dy_4C_3, whereas the coordinates of Dy atoms are the same in both

structures. Thus, the coordination number of Dy atoms in Dy_2C_3 increases to nine (Fig. 3.9b), whereas the coordination environment of [C_2] dumbbells (Fig. 3.9c) is similar to that of a single carbon atom in Dy_4C_3 (Fig. 3.4c).

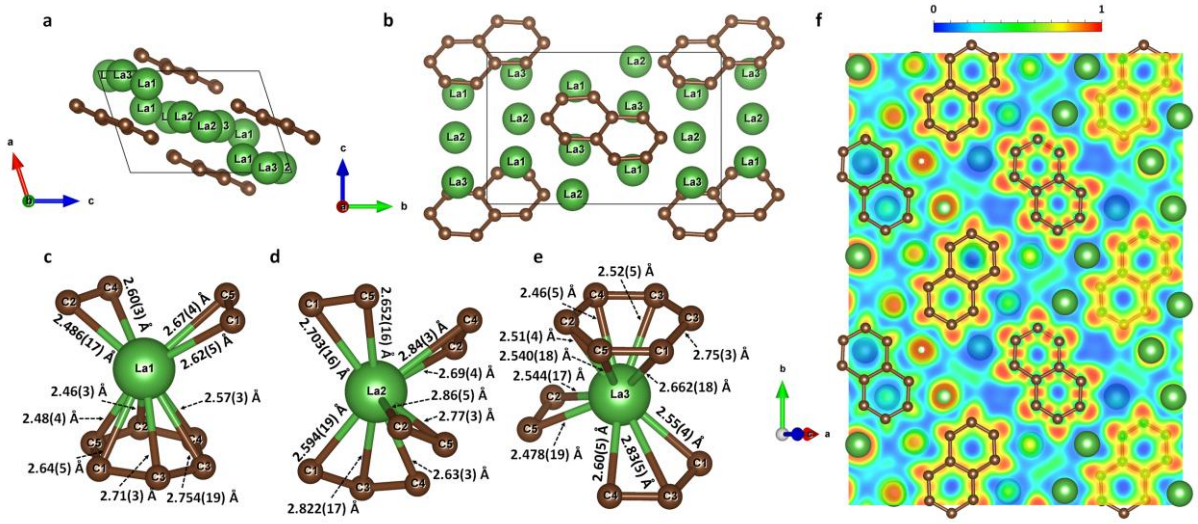

Figure 3.10. Crystal structure of La_3C_5 at 45 GPa and a cross section of the calculated ELF. The green and brown spheres represent lanthanum and carbon atoms, respectively. (a) The projection of the structure along the *b*-axis. (b) The structure viewed along the *a*-axis. (c) The coordination environment of La1 atoms. (d) The coordination environment of La2 atoms. (e) The coordination environment of La3 atoms. (f) The 2D ELF calculated in the plane containing carbon naphthalene-decalin-like rings.

The structure of *mP*32 La_3C_5 has a monoclinic unit cell (space group $P2_1/n$, #14, $Z = 4$) with lattice parameters $a = 4.869(12)$ Å, $b = 10.846(5)$ Å, $c = 7.366(4)$ Å, and $\beta = 107.79(13)°$ at 45 GPa (Fig. 3.1b and 3.10). It is comprised of 8 crystallographically distinct atoms, three La and five C, all of them are at Wyckoff sites 4*e*. The lanthanum atoms have different coordination numbers: CN(La1) = 10, CN(La2) = 9, CN(La3) = 11. The La-C distances within the polyhedra vary in the ranges: *d*(La1-C) = 2.46(3)-2.754(19) Å, *d*(La2-C) = 2.594(19)-2.86(5) Å, *d*(La3-C) = 2.46(5)-2.83(5) Å (Fig. 3.10c-e). In the synthesized La_3C_5, naphthalene-decalin-like entities are slightly bent. The distortion of the naphthalene-decalin-like rings in this structure is slightly more pronounced in comparison with ε-LaC_2 described below due to the larger angle deviations and unequal C-C bond lengths: *d*(C1-C3) = 1.54(5) Å, *d*(C1-C5) = 1.47(3) Å, *d*(C2-C5) = 1.44(5) Å, *d*(C2-C4) = 1.44(5) Å, *d*(C3-C4) = 1.44(3) Å, *d*(C3-C3) = 1.45(6) Å (Fig. 3.11a, b). These values lie between the bond distances in naphthalene $C_{10}H_8$ [195] and decalin $C_{10}H_{18}$ [196], supposing the intermediate state of the carbon fragments.

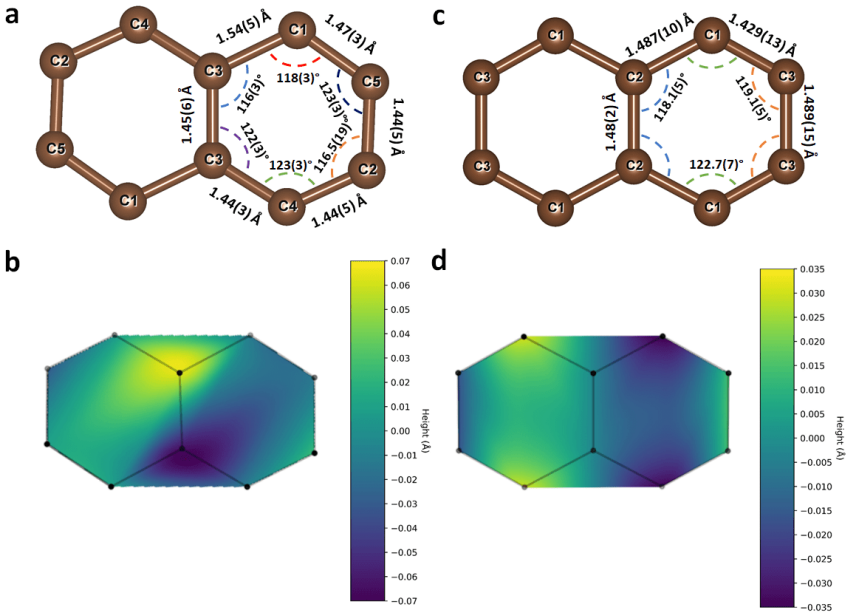

Figure 3.11. The naphthalene-decalin-like entities in synthesized (a), (b) *mP*32 La_3C_5 and (c), (d) *mC*30 ε-LaC_2 at 45 GPa. The maximum deviation from the averaging plane is (b) ~0.068 Å for La_3C_5 and (d) ~0.032 Å for ε-LaC_2.

The structure of Dy_5C_9 carbide (Fig. 3.1g and 3.12) is unprecedented in the sense that we were not able to find any structural analogues, and it was not predicted. This structural type has also been identified as a product of HPHT synthesis in the Y-C, Nd-C, Sm-C, Gd-C, and Yb-C systems, leading to appearance of new compounds Y_5C_9, Nd_5C_9, Sm_5C_9, Gd_5C_9, and Yb_5C_9 at ~42-68 GPa. The phase Dy_5C_9 crystallises in tetragonal symmetry (space group *P4/mnc*, #128, $Z = 2$) with lattice parameters $a = 7.2218(7)$ Å and $c = 4.8618(4)$ Å at 68 GPa. The unit cell contains two types of dysprosium atoms (Dy1 and Dy2 occupying 8*h* and 2*b* Wyckoff positions, respectively), and two types of carbon atoms (C1 and C2 occupying 16*i* and 2*a* Wyckoff positions, respectively). Dysprosium atoms form slightly distorted square layers in the (0 0 2) plane with a distance between layers of 1/2*c*; each consequent layer rotated relative to the previous one by ~40° (Fig. 3.12b). Different dysprosium atoms have different environments – Dy2 atoms are located in bicapped square prisms with *d*(Dy2-C1) = 2.358(10) Å and *d*(Dy2-C2) = 2.4309(3) Å, and Dy1 atoms are in irregular polyhedra with 11 vertices with *d*(Dy1-C1) = 2.228(10)-2.591(10) Å and *d*(Dy1-C2) = 2.1965(8) Å (Fig. 3.12c, d). The carbon atoms C2 have isolated positions in the structure like the carbon in methanides (Fig. 3.12). The C1 carbon atoms form zig-zag chains with four atoms per repeating element (Fig. 3.12). Chains are propagating along the [0 0 1] direction. According to experimental single crystal X-ray data for Dy_5C_9 at 68 GPa, the C-C distance in the carbon chains is of

~1.46 Å and the ∠C-C-C angle is of ~132°. All atoms of the chain lie in the same plane, as the torsion angle is zero (Fig. 3.12e).

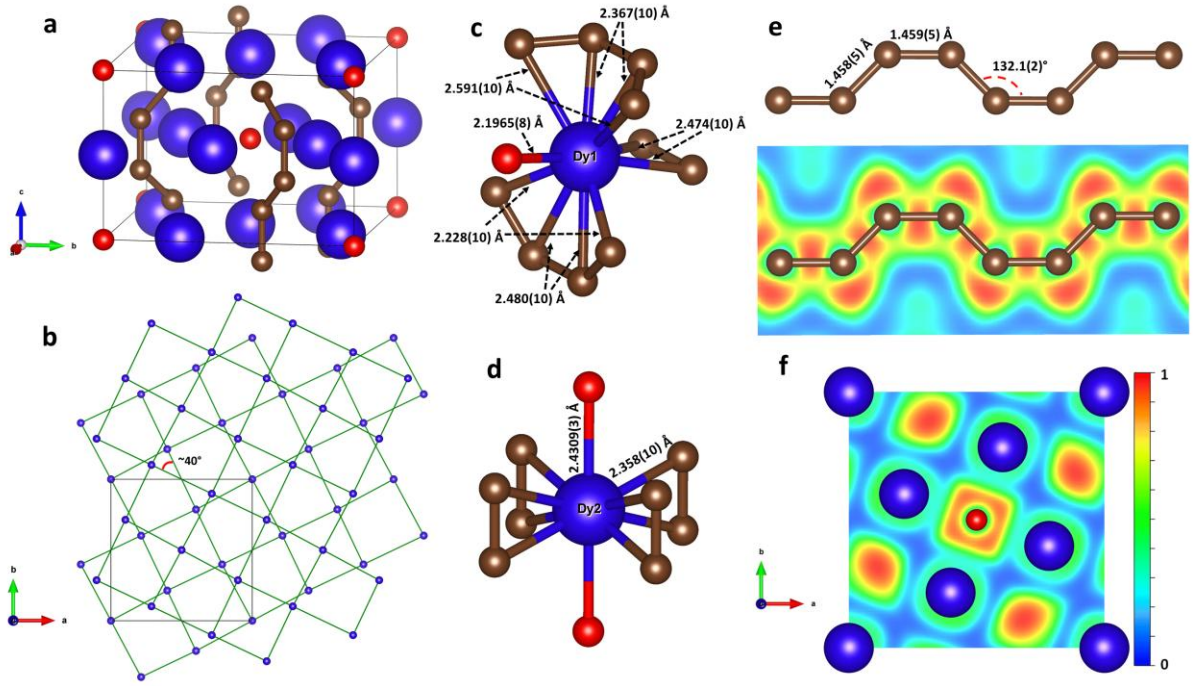

Figure 3.12. Crystal structure of Dy_5C_9 at 68 GPa and a cross section of the calculated ELF. All Dy atoms are blue, C atoms formed chains are brown, and discrete C atoms are red. (a) A view of the crystal structure. (b) Arrangement of parallel planes comprised of Dy atoms rotated relative to each other by ~40°. (c) and (d) The coordination environment of the Dy1 and Dy2 atoms. (e) The carbon chain geometry (upper figure) and the electron localization function calculated in the plane containing a carbon chain (bottom figure). (f) The 2D ELF calculated in the (0 0 2) plane containing discrete carbon atoms.

The structure of lanthanum dicarbide *mC*30 ε-LaC_2 has a monoclinic unit cell (space group *C*2/*m*, #12, *Z* = 10) with lattice parameters *a* = 7.883(3) Å, *b* = 5.8534(6) Å, *c* = 6.9388(5) Å, and *β* = 94.010(18)° at 45 GPa (Fig. 3.1a and 3.13). It is composed of six crystallographically distinct atoms, La1, La2, La3, C1, C2, and C3, on the 2*d*, 4*i*, 4*i*, 8*j*, 4*g*, and 8*j* Wyckoff sites, respectively. Each of the three lanthanum atoms is twelve-fold coordinated by carbon atoms, CN(La) = 12 (Fig. 3.13c-e). The La-C distances within the La1 atom polyhedron range from 2.686(10) Å to 3.083(15) Å, while for the La2 atom polyhedron, the *d*(La-C) values are from 2.419(8) Å to 2.785(3) Å, and for the La3 atom polyhedron, the metal-carbon distances vary between 2.490(13) Å and 2.698(9) Å (Fig. 3.13c-e). Analogously to the La_3C_5 discussed above, the naphthalene-decalin-like rings of ε-LaC_2 are slightly bent and are not flat. Additionally, there are minor deviations from the ideal angle of 180° within the six-membered rings, where the C-C bond lengths vary as follows: *d*(C1-C2) = 1.487(10) Å, *d*(C1-C3) = 1.429(13) Å, *d*(C2-C2) = 1.48(2) Å, and *d*(C3-C3) = 1.489(15) Å (Fig. 3.11c, d). These

values also lie between the bond distances in naphthalene $C_{10}H_8$ [195] and decalin $C_{10}H_{18}$ [196], like in La_3C_5.

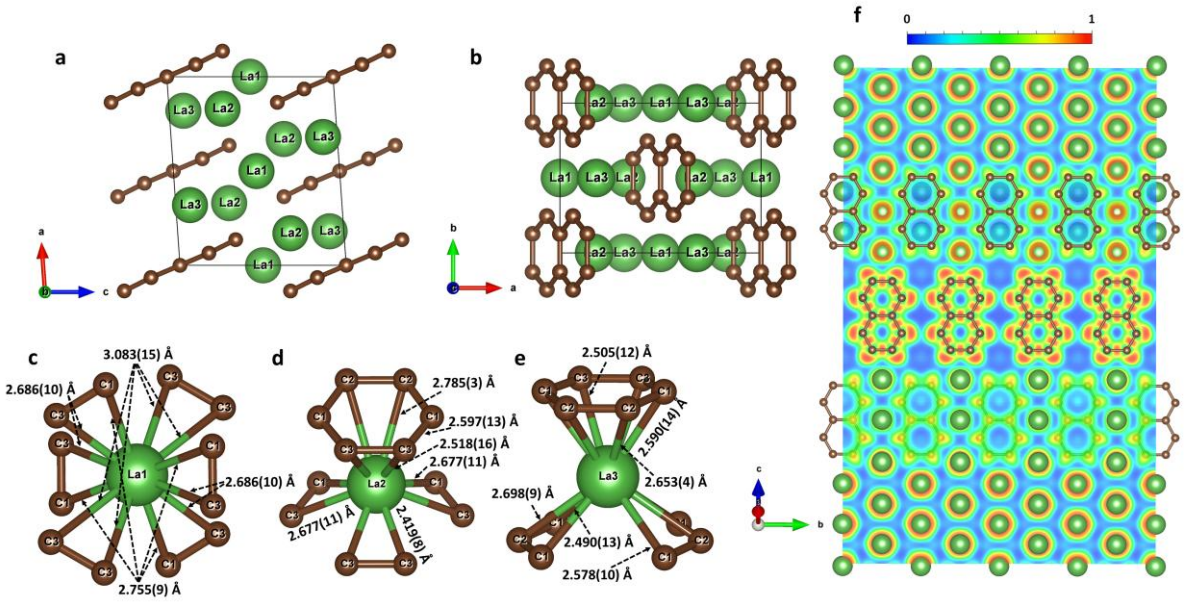

Figure 3.13. Crystal structure of ε-LaC_2 at 45 GPa and a cross section of the calculated ELF. The green and brown spheres represent lanthanum and carbon atoms, respectively. (a) The projection of the structure along the *b*-axis. (b) The structure viewed along the *c*-axis. (c) The coordination environment of La1 atoms. (d) The coordination environment of La2 atoms. (e) The coordination environment of La3 atoms. (f) The 2D ELF calculated in the plane containing carbon naphthalene-decalin-like rings.

The novel dicarbides *oC*6 δ-NdC_2 and δ-SmC_2 crystallized in the orthorhombic space group *Pmma*, #51 (*Z* = 2) as a result of HPHT experiments at 43-55 GPa. The unit cell parameters for δ-NdC_2 at 43 GPa are *a* = 4.9714(12) Å, *b* = 3.1475(5) Å, and *c* = 3.8083(3) Å (Fig. 3.1d and 3.14). In the δ-NdC, 2*f* and 4*i* Wyckoff sites are occupied by Nd1 and C1 atoms, respectively. There are two distinct layers of metal atoms and carbon *cis*-polyacetylene-type chains, which are situated within the *ac* plane. These layers alternate along the *b*-axis (Fig. 3.14a, b). Nd1 atoms are twelve-fold coordinated (CN = 12) by C atoms from nearest carbon chains with *d*(Nd1-C1) = 2.508(8)-2.607(6) Å (Fig. 3.14c). The carbon atoms form flat chains along the *a*-axis, featuring alternating interatomic distances between carbon atoms of 1.41(2) Å and 1.501(17) Å, and the ∠C-C-C angle of 135.7(7)° in δ-NdC_2 at 43 GPa.

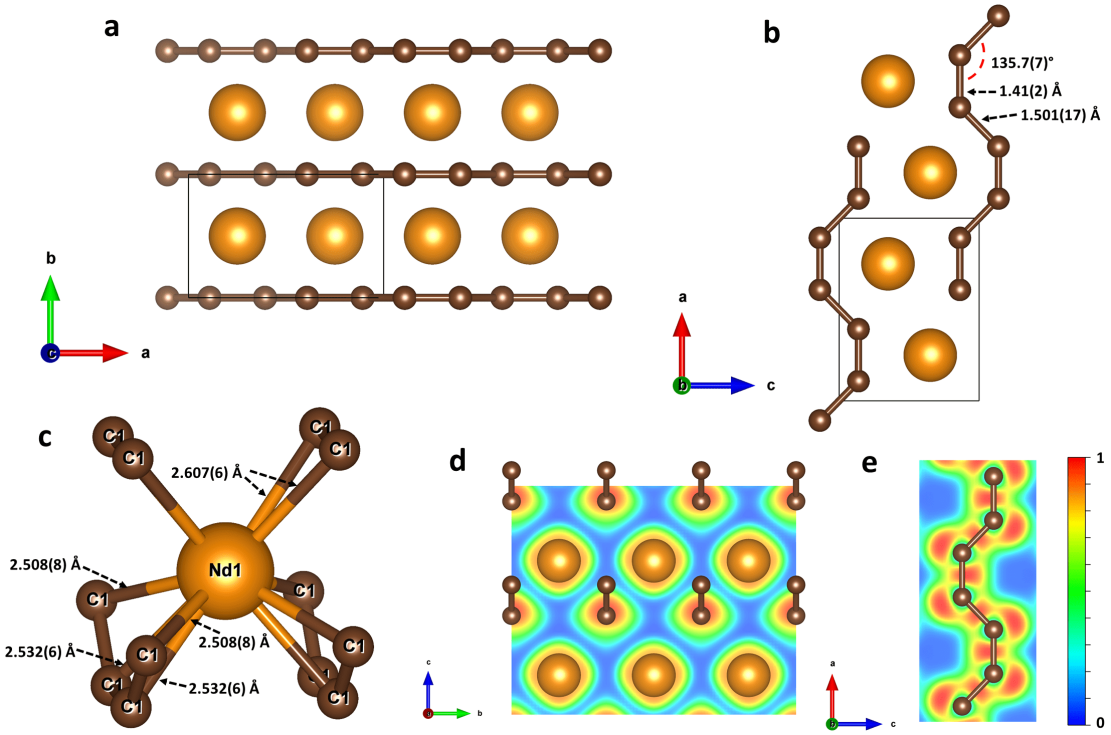

Figure 3.14. Crystal structure of δ-NdC_2 at 43 GPa and a cross section of the calculated ELF. Neodymium atoms are given in orange, carbon atoms are shown in brown. (a) Projection of the unit cell along the *c*-axis emphasizing the arrangement of layers in the [0 1 0] direction. (b) The view of the crystal structure along the *b*-axis. (c) The coordination environment of neodymium atoms. (d) The 2D ELF calculated in the *bc* plane containing Nd atoms. (e) The 2D ELF calculated in the *ac* plane containing a carbon chain.

The novel structural type *oI*12 γ-DyC_2 (space group *Immm*, #71, Z = 4), initially uncovered for the rare-earth metal Dy with lattice parameters a = 2.6355(12) Å, b = 5.707(3) Å, and c = 6.737(3) Å at 66 GPa, has been successfully reproduced in HPHT experiments with two more rare-earth elements, Y and Sm at 62-124 GPa, where carbide γ-YC_2 is the theoretically predicted compound [78]. The unit cell consists of four dysprosium atoms occupying Wyckoff site 4*i* and eight carbon atoms occupying two distinct crystallographic positions: 4*h*(C1) and 4*g*(C2) (Fig. 3.15). In the structure of γ-DyC_2, dysprosium atoms form distorted, slightly buckled closed packed layers in the *ab* plane (Fig. 3.15b). Dysprosium atoms have 12 carbon neighbors arranged in hexagonal prism with unequal bases with d(Dy1-C1) = 2.403(11) Å and 2.411(10) Å, d(Dy1-C2) = 2.436(4) Å and 2.570(10) Å (Fig. 3.15c). Carbon atoms lie in the (0 0 2) plane in the middle between planes of Dy atoms (Fig. 3.15). They are arranged in polymerized hexagonal rings – flat one-dimensional ribbons propagating along the [1 0 0] direction (Fig. 3.15). Thus, the carbon atoms form exotic $^{1}_{\infty}[C_4]$ one-dimensionally infinite polyanions. The C-C distances in the hexagons, refined at 66 GPa, are equal to 1.451(9) Å and 1.508(5) Å for the C2-C2 and C1-C2 bonds, respectively. Two angles in the hexagon are 122.5(7)°, while the other four angles are 118.8(3)° (Fig. 3.15d).

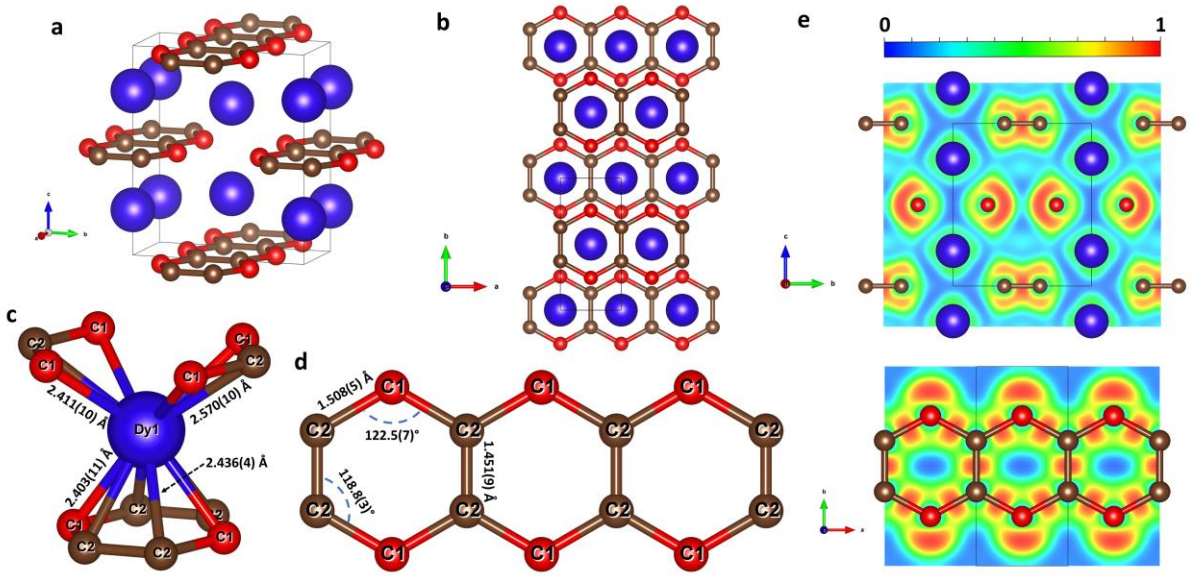

Figure 3.15. Crystal structure of γ-DyC_2 at 66 GPa and a cross section of the calculated ELF. Dy1 atoms are blue, C1 atoms are red, C2 atoms are brown. (a) A view of the crystal structure. (b) The crystal structure along the *c*-axis. (c) The coordination environment of the dysprosium atom. (d) A view of the carbon ribbon. (e) The 2D ELF calculated in (1 0 0) (upper figure) or (0 0 1) plane containing carbon ribbons (bottom figure).

Performed DFT calculations reproduced well crystal structures synthesized and investigated in the present thesis. The bulk moduli were obtained from constructed EoSes after structure relaxation at several pressure points for each compound. Analysis of ELF maps (Fig. 3.3-3.15) suggests the ionic nature of bonding between metal atoms and carbon species in the synthesized compounds, that allows to consider them as salt carbides [197]. Strong covalent bonding between carbon atoms in carbon entities is also evident from the ELF maps (Fig. 3.3-3.15).

The dynamical stability of the relaxed structures was revealed from the computed phonon density of states (pDOS). For instance, according to our theoretical calculations, lanthanides carbides isostructural to previously discovered γ-Y_4C_5 [7] have shown dynamical stability at ambient pressure in contrast to the reported γ-Y_4C_5 [7] (Fig. 3.16a-d). Indeed, in our experiments, carbide γ-Sm_4C_5 was quenched in air at ambient pressure. Conversely, calculations performed for Dy_3C_2-type carbides have demonstrated minor instability in *Z*-points at synthesis pressure, indicating theoretical limitations for lanthanides compounds in the utilized approximation (Fig. 3.16e, f).

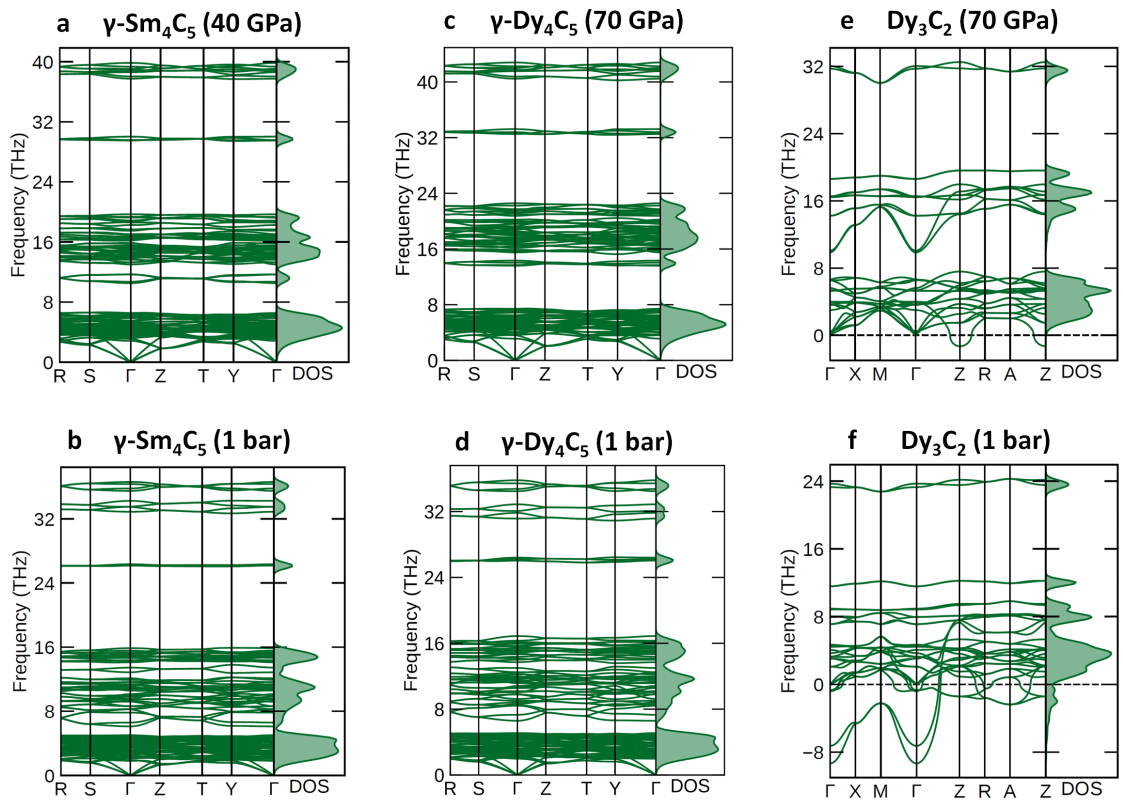

Figure 3.16. Calculated properties of γ-Sm_4C_5, γ-Dy_4C_5, and Dy_3C_2. Phonon dispersion curves along high-symmetry directions in the Brillouin zone and phonon density of states: γ-Sm_4C_5 at (a) 40 GPa and (b) ambient pressure, γ-Dy_4C_5 at (c) 70 GPa and (d) ambient pressure, and Dy_3C_2 at (e) 70 GPa and (f) ambient pressure.

The electron density of states (eDOS) calculations suggested that the synthesized carbides are metals (Fig. 3.17). Mulliken charge analysis results are in good agreement with corresponding literature data on compounds containing rare-earth elements with similar charge distribution and oxidation state of metal atoms, which confirms the proposed formal charges of synthesized compounds. The computations were performed in frozen *f*-electrons approximation for lanthanides.

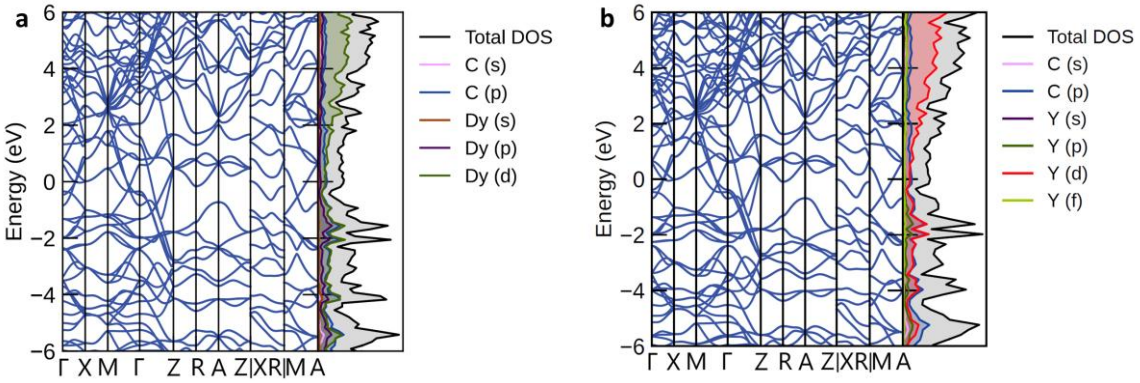

Figure 3.17. An example of DFT-based calculations of electron density of states (eDOS) and band structure along high-symmetry directions in the Brillouin zone for (a) Dy_5C_9 (in frozen-core approximation) and (b) Y_5C_9 at 70 GPa.

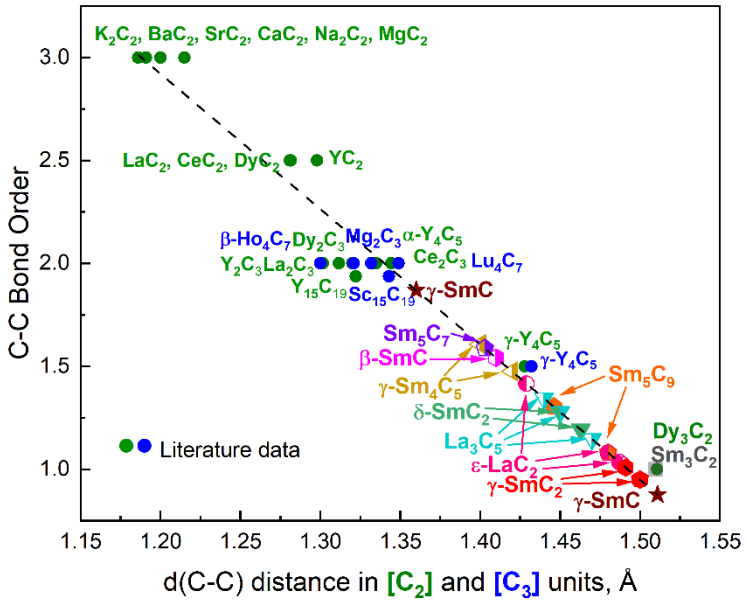

Figure 3.18. Correlation between the C-C distances in [C_2] and [C_3] units, *d*(C-C), and their bond order in a number of binary metal-carbon compounds. Literature data are from experiments [18,38,40,41,48,54,57,61,63,198–207], with the exception of γ-Y_4C_5 [7] and Dy_2C_3 and Dy_3C_2 [6] (DFT-computed structures were fully relaxed at 1 bar). Straight line is a result of the fit of literature data ("green" and "blue" data-points) and described by equation: $EBO = 10.81 - 6.57 \times d(C\text{-}C)$.

In the structures of the carbon compounds synthesized in this study, there are complex carbon arrangements, including infinite chains and ribbons of fused carbon rings, that imposed a necessity to introduce the effective bond order (EBO) into consideration to comprehend the relationship between the C-C bond lengths and formal charges of individual carbon atoms or their groups. With the linear equation obtained by fitting calculated EBO for a number of binary metal-carbon compounds from literature, we determined the bond order for C-C bonds for carbides studied here, using the values of *d*(C-C) obtained experimentally from single-crystal XRD (Fig. 3.18). There is a correlation (Fig. 3.19a) between compressibility and ratio $R=\langle d\rangle^3/(Z_{REE}*Z_C)$ ($\langle d\rangle$ is average REE-C distance in the first coordination sphere, Z_{REE} and Z_C are the 'charges' on the rare-earth metal and carbon). An increase of bulk moduli with decreasing *R* is well-known for ionic and ionic-covalent compounds [169,208], and this trend is observed for carbides with anti-Th_3P_4-type, La_3C_5-type, and ε-LaC_2-type structures, establishing the ionic nature of the compressibility dependence on the *R* for these compounds. However, the trend for the carbides of γ-SmC, γ-Y_4C_5, Nd_5C_7, Pu_2C_3, Dy_5C_9, δ-NdC_2, and γ-DyC_2 structural types is opposite (Fig. 3.19a). This indicates an unusual compression mechanism for the studied rare-earth carbides that is in line with the observation of the almost

linear correlation between compressibility and the average bond order in carbon entities (Fig. 3.19b).

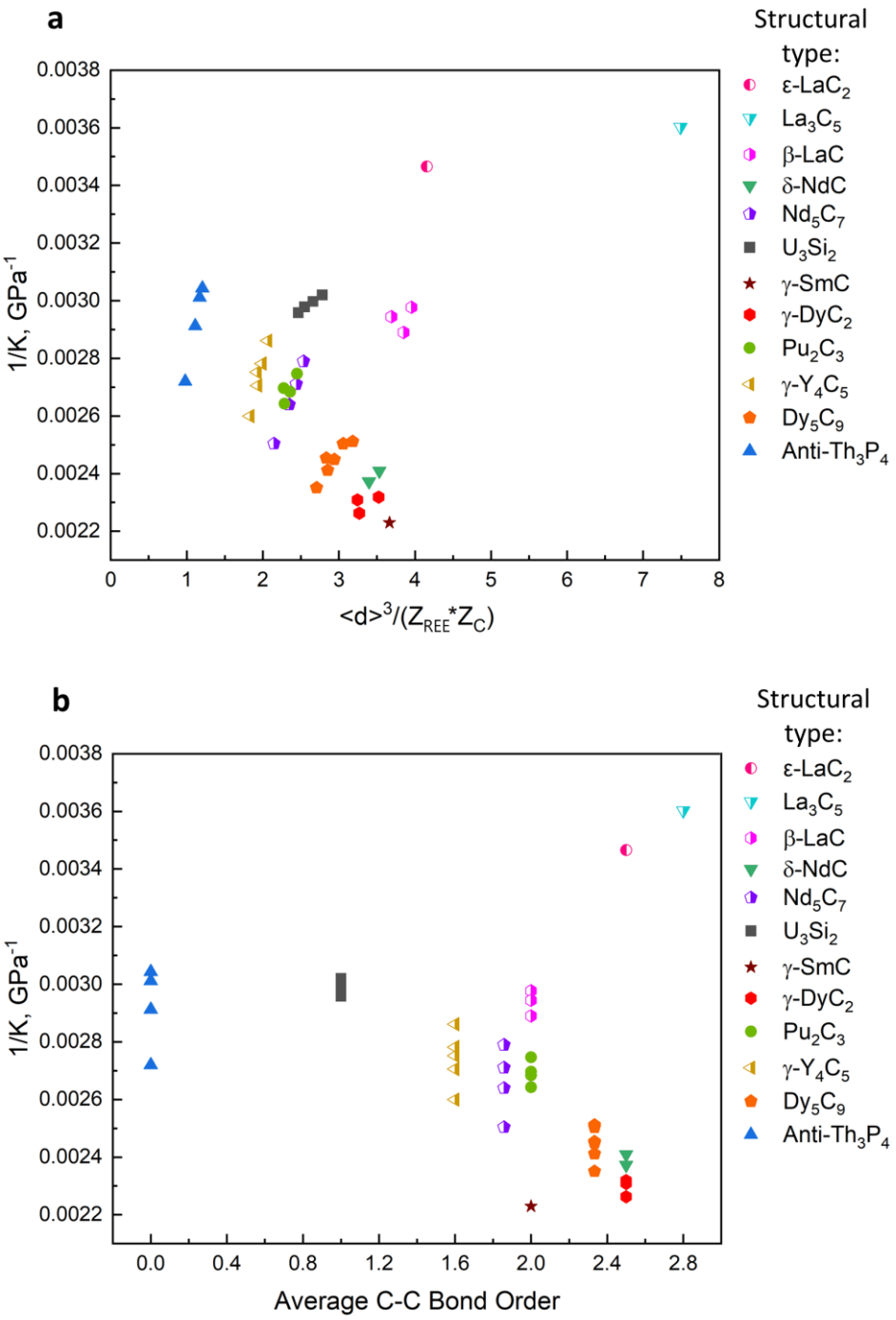

Figure 3.19. Compressibility of synthesized compounds plotted with respect to (a) ratio $R=\langle d\rangle^3/(Z_{REE}*Z_C)$ ($\langle d\rangle$ is average REE-C distance in the first coordination sphere, Z_{REE} and Z_C are the 'charges' on the rare-earth metal and carbon) and (b) 'average bond order' of carbon atoms in synthesized compounds.

Our findings demonstrate the tendency of the formation of carbides with complex polyanions at high pressures. The systematic study of rare-earth carbides under high pressures

revealed the presence of regularities in their chemistry under extreme conditions, as a significant contribution to materials science, solid-state physics, and high-pressure chemistry.

3.2 Synthesis of rare-earth metal compounds through enhanced reactivity of alkali halides at high pressures

Chemical stability of the alkali halides NaCl and KCl has allowed for their use as inert media in high-pressure high-temperature experiments. Being formed by highly electropositive and electronegative elements, NaCl and KCl, having a stable electron configuration, are not expected to react with transition or rare-earth metals. In section 4.4, we have shown that it is not the case under pressure, as our experiments, originally designed to study the HP behavior of metals (Y, Dy, Re, and Ag) in an "inert" pressure medium (NaCl) in a LHDAC, resulted in the synthesis of previously unknown chlorides, Y_2Cl (*I*4/*mcm*) and DyCl (*P*6$_3$/*mmc*), and chloride carbides, Y_2ClC and Dy_2ClC (*R*-3*m*), at about 40 GPa and 2000 K. An iron chloride, $FeCl_2$ (*Pa*-3), with the HP-PdF_2-type structure, was found to be a product of a chemical reaction between FeO and KCl in a LHDAC at about 160 GPa and 2100 K.

Here we report the crystal structures of the chloride phases, Y_2Cl and DyCl, and chloride carbides Y_2ClC and Dy_2ClC, as well as the structure of iron chloride, $FeCl_2$ (Fig. 3.20). The structures were solved and refined using *in situ* high-pressure synchrotron single-crystal X-ray diffraction in a DAC. Our *ab initio* calculations are in good agreement with the experimental results.

The yttrium-chlorine compound, Y_2Cl, synthesized at 41 GPa and 2000 K crystallizes in a structure with the tetragonal space group *I*4/*mcm*, #140 (*Z* = 4). The lattice parameters are *a* = 6.1279(3) Å and *c* = 5.4050(7) Å. Y atoms occupy the 8*h* Wyckoff site while the Cl atoms occupy the 4*a* site with Y-Cl distance of 2.6734(4) Å (Fig. 3.20a-c). Yttrium atoms form 3^2.4.3.4 nets in the *ab* plane (Fig. 3.20b). The nets are stacked along the *c* direction with a ½ period and rotated by 90° from one another (Fig. 3.20b). The chlorine atoms are located in the centers of square antiprisms formed between the layers of Y atoms (Fig. 3.20c).

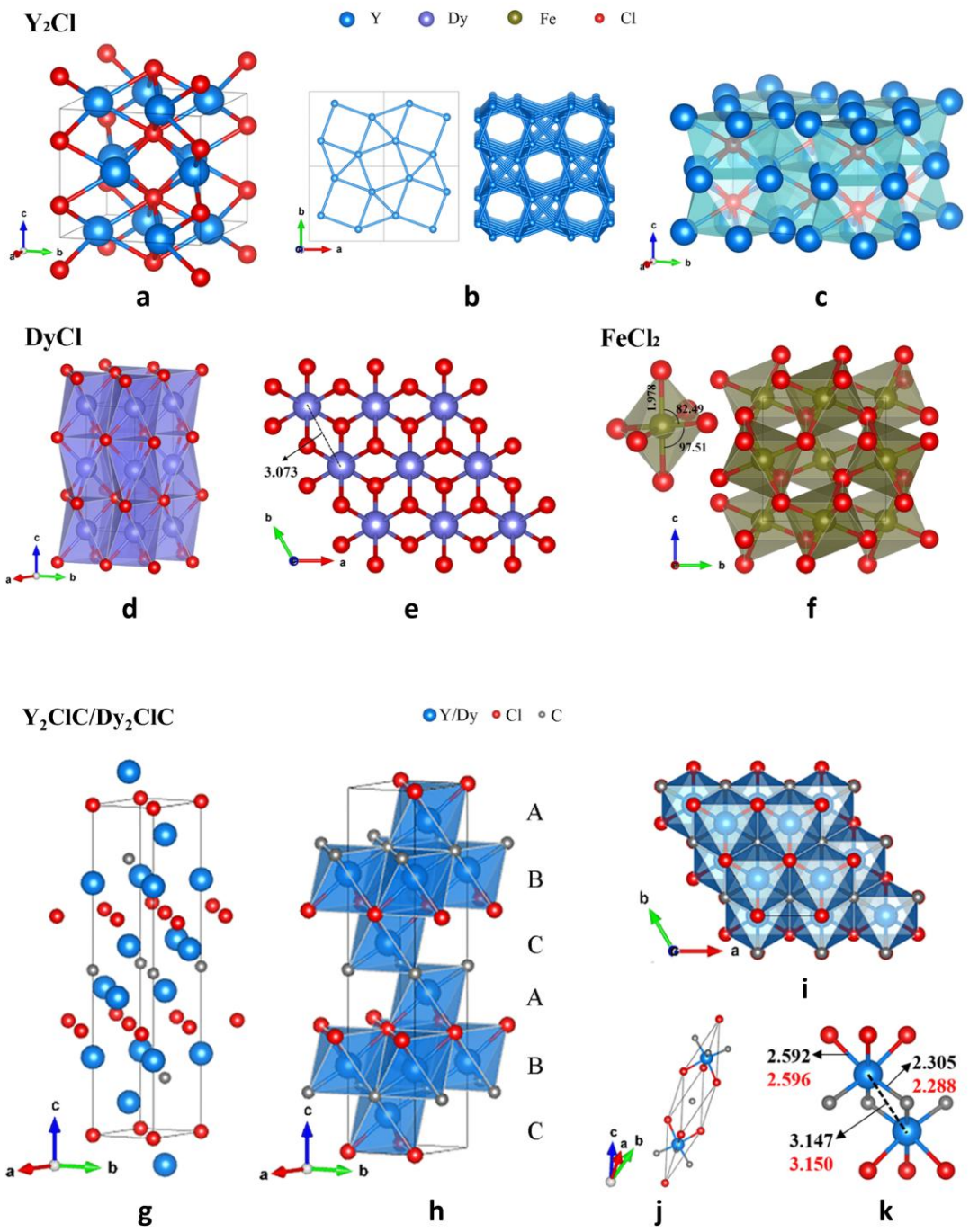

Figure 3.20. Crystal structures of novel chlorides of Y, Dy, and Fe, and chloride carbides of Y and Dy. (a) Stick-and-ball model of Y_2Cl structure at 41(1) GPa; (b) view of the Y metal framework in Y_2Cl along the *c*-direction; (c) square antiprisms geometry around the Cl center in Y_2Cl. (d) Polyhedral model of the crystal structure of DyCl at 40(1) GPa built of $DyCl_6$ octahedra; (e) view of the structure along the *c*-direction: Cl atoms form hexagonal close packing (*hcp*) and Dy atoms occupy the space in between. (f) Polyhedral model of $FeCl_2$ at 160(1) GPa. (g) Ball model in a hexagonal setting of Y_2ClC/Dy_2ClC structure. (h) Polyhedral model built of (YC_3Cl_3) octahedra; A, B, C letters highlight the *ccp* formed by Y/Dy atoms. (i) View of the structure along the *c*-direction; C and Cl atoms together form the *ccp*. (j) Crystal structure in the rhombohedral setting. (k) Interatomic distances (in Å) in Y_2ClC (black numbers) and Dy_2ClC (red numbers). Y, Dy, Fe, Cl, and C atoms are shown in blue, purple, tan, red, and grey colors, respectively.

The structure of dysprosium chloride, DyCl, has a hexagonal unit cell with the lattice parameters a = 3.0787(19) Å and c = 7.621(5) Å (Z = 2) at 40 GPa (Fig. 3.20d, e), and the space group symmetry $P6_3/mmc$ (#194) with the Dy atoms occupying the 2*a* Wyckoff site, and Cl atoms occupying the 2*c* site. The Dy-Cl distance is 2.6057(12) Å. In this NiAs (B8) type structure, the Cl atoms form a hexagonal close packing (*hcp*), in which Dy atoms occupy the centers of the edge-sharing octahedra. Although there are other rare-earth chlorides known at atmospheric pressure (REE = Sc, Y, Gd, and La) [209–211], they possess ZrCl-type structure, which is different from that of the HP Dy and Y chlorides.

The HP phase of $FeCl_2$ crystalized at 160 GPa in the HP-PdF_2 type structure with the *Pa*-3 (#205) space group and the lattice parameter a = 4.8289(11) Å (Z = 4) (Fig. 3.20f). Fe atoms occupy the 4*b* Wyckoff site, while Cl atoms occupy the 8*c* site, and form vertex-sharing Cl_6 octahedra with Fe atoms in the centers. The Fe-Fe, Fe-Cl, and Cl-Cl distances at 160 GPa are d(Fe-Fe) = 3.4145(8) Å, d(Fe-Cl) = 1.9775(9) Å, and d(Cl-Cl) = 2.4762(16) Å, 2.6076(9) Å, and 2.9738(11) Å.

Ternary compounds Y_2ClC and Dy_2ClC are isostructural (space group *R*-3*m*, #166, Z = 3) and have similar lattice parameters: a = 3.3690(7) Å and c = 17.703(6) Å for Y_2ClC, a = 3.3193(7) Å and b = 18.004(10) Å for Dy_2ClC. Y and Dy atoms occupy the Wyckoff site 6*c*, Cl atoms occupy the 3*a* site, and C atoms occupy the 3*b* site. As shown in Fig. 3.20k, the metal-C contacts (d(Y-C) = 2.3051(10) Å and d(Dy-C) = 2.2879(9) Å) are significantly shorter than the metal-Cl ones (d(Y-Cl) = 2.5923(12) Å and d(Dy-Cl) = 2.5958(12) Å), as expected due to the smaller ionic radius for C atoms. But the Y-Y and Dy-Dy contacts between layers AB, CA, and BC (Fig. 3.20h) are relatively short (~3.15 Å), and this distance is close to that of Dy-Dy in DyCl.

Performed *ab initio* calculations well reproduced the experimental crystal structures and confirmed their dynamical stability at synthesis pressures. The calculated bulk modulus of K_0 = 96.9(14) GPa (K_0' = 4.45(2); V_0 = 185.5(4) Å^3) for $FeCl_2$ was determined by fitting the 3rd-order Birch-Murnaghan equation of state to the calculated P-V data. The calculated band structure along specific high-symmetry directions suggests that the cubic $FeCl_2$ phase is a typical example of normal semimetals [212], in which electron and hole pockets coexist on the Fermi surface (Fig. 3.21).

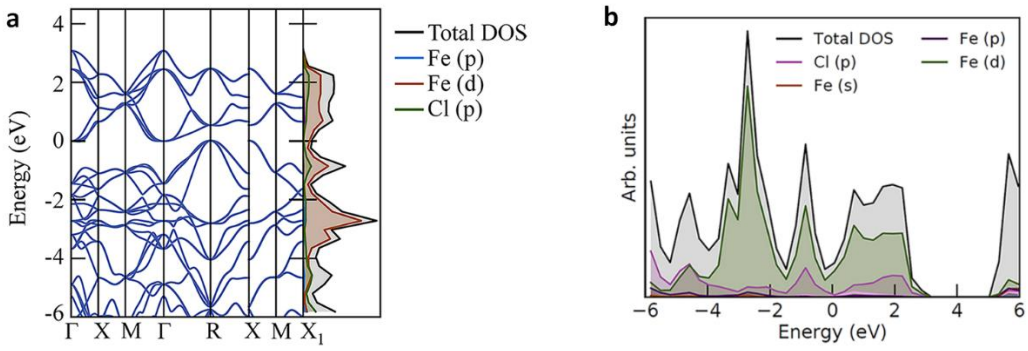

Figure 3.21. (a) Calculated band structure and electron density of states of $FeCl_2$ at 150 GPa; (b) total and projected electron densities of states (TDOS and PDOS) curves of $FeCl_2$ at 150 GPa. The Fermi energy level was set to 0 eV.

Considering that Y_2ClC and Dy_2ClC are isostructural, the computed total and projected electron densities of states (TDOS and PDOS) are illustrated in Fig. 3.22a taking Y_2ClC as an example. At 40 GPa, Y_2ClC is a metal, as it shows a non-zero density of states at the Fermi level, and the main contribution at the Fermi level comes from the yttrium *d*-states. Interestingly, the calculated electron localization function (ELF) of Y_2ClC at 40 GPa not only gives evidence of ionic bonding between the Y-Cl and Y-C atoms but features weak ELF values in the centers of the Y_4 tetrahedra (Fig. 3.22b–d), forming bridges connecting the C atoms (see the highlighted red dashed lines in Fig. 3.22b, d). One can speculate from the ELF values that these ELF bridges are caused by the hybridization of the Y-*d* orbitals (for ELF < 0.5, the metal bonding is undoubtedly more pronounced [213]).

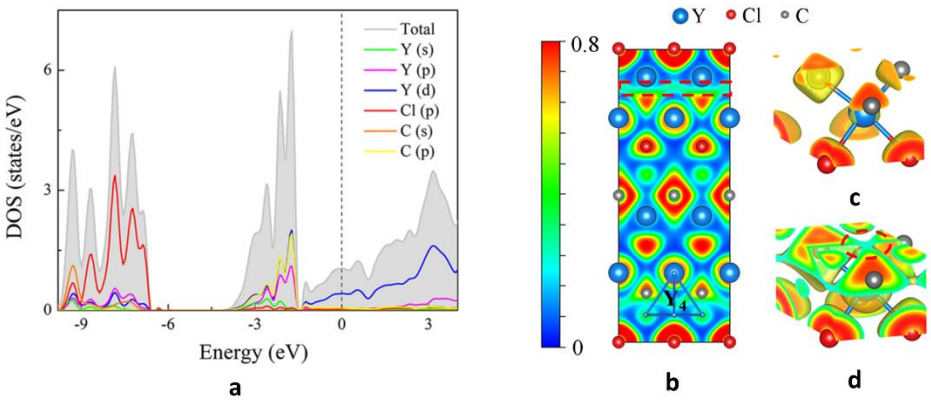

Figure 3.22. Results of theoretical calculations. (a) The total and projected densities of states (TDOS and PDOS) curves of Y_2ClC at 40 GPa; the Fermi energy level was set to 0 eV. (b) The 2D electron localization function (ELF) map of Y_2ClC in the (1 0 0) plane; (c), (d) ELF with the isosurfaces value set as (c) 0.7 and (d) 0.25. Y, Cl, and C atoms are shown in blue, red, and grey colors. One Y_4 tetrahedron is highlighted in (b), and the weak ELF value in its center is highlighted with the red dashed circle in (d). These weak ELF values in the centers of the Y_4 tetrahedra form bridges connecting the C atoms (highlighted with the red dashed square in (b)).

In addition to their significance in materials science, solid-state physics, and high-pressure chemistry, our findings should be considered when planning experiments in laser-heated DACs at high pressures. These results highlight limitations on the application of alkali halides as thermal insulators and pressure media in LHDACs. As reactants, they provide a surprisingly simple route for the preparation of halogen-containing compounds.

3.3 List of manuscripts and statement of authors' contribution

[1] F. I. Akbar (FA), A. Aslandukova (AlA), A. Aslandukov (AnA), Y. Yin (YY), F. Trybel (FT), S. Khandarkhaeva (SK), T. Fedotenko (TF), D. Laniel (DL), M. Bykov (MB), E. Bykova (EB), N. Dubrovinskaia (ND), L. Dubrovinsky (LD), High-Pressure Synthesis of Dysprosium Carbides, *Front. Chem.* **11**, 1–9 (2023), DOI: 10.3389/fchem.2023.1210081.

FA, LD, and ND conceptualised the research. FA prepared the samples and DACs. FA, AnA, YY, SK, TF, DL, MB, and EB performed synchrotron experiments. FA and LD processed the data. FA, AlA, and FT performed theoretical calculations. FA, LD, and ND analysed the results and wrote the paper with contributions from all co-authors.

[2] F. I. Akbar (FA), A. Aslandukova (AlA), Y. Yin (YY), A. Aslandukov (AnA), D. Laniel (DL), E. Bykova (EB), M. Bykov (MB), E. L. Bright (ELB), J. Wright (JW), D. Comboni (DC), M. Hanfland (MH), N. Dubrovinskaia (ND), L. Dubrovinsky (LD), High-Pressure Dysprosium Carbides Containing Carbon Dimers, Trimers, Chains, and Ribbons. Submitted to *Carbon*.

FA, LD, and ND conceptualised the research. FA prepared the samples and DACs. FA, YY, AnA, DL, EB, MB, ELB, JW, DC, and MH performed synchrotron experiments. FA processed the data. FA and AlA performed theoretical calculations. FA, LD, and ND analysed the results and wrote the paper with contributions from all co-authors.

[3] F. I. Akbar (FA), A. Aslandukova (AlA), A. Aslandukov (AnA), Y. Yin (YY), E. Bykova (EB), M. Bykov (MB), D. Laniel (DL), P. Milkin (PM), W. Zhou (WZ), T. Fedotenko (TF), K. Glazyrin (KG), H.-P. Liermann (HL), E. L. Bright (ELB), J. Wright (JW), A. Pakhomova (AP), G. Garbarino (GG), M. Mezouar (MM), S. Chariton (SC), V. Prakapenka (VP), D. Comboni (DC), M. Hanfland (MH), N. Dubrovinskaia (ND), L. Dubrovinsky (LD), High-Pressure Synthesis of Rare-Earth Metals Carbides Featuring Carbon Polyanions. To be submitted to *JACS*.

FA, LD, and ND conceptualised the research. FA prepared the samples and DACs. FA, AlA, AnA, YY, EB, MB, DL, PM, TF, KG, HL, ELB, JW, AP, GG, MM, SC, VP, DC, and MH performed synchrotron experiments. FA processed the data. FA and AlA performed theoretical calculations. WZ helped to visualise the carbon entities' distortion in lanthanum carbides. FA, LD, and ND analysed the results and wrote the paper with contributions from all co-authors.

[4] Y. Yin (YY), F. I. Akbar (FA), E. Bykova (EB), A. Aslandukova (AlA), D. Laniel (DL), A. Aslandukov (Ana), M. Bykov (MB), M. Hanfland (MH), G. Garbarino (GG), Z. Jia (ZJ), L. Dubrovinsky (LD), N. Dubrovinskaia (ND), Synthesis of Rare-Earth Metal

Compounds through Enhanced Reactivity of Alkali Halides at High Pressures, *Commun. Chem.* **5**, 8–13 (2022), DOI: 10.1038/s42004-022-00736-x.

LD, ND, and YY designed the study. LD and ND supervised the research. YY, FA, EB, DL, AnA, MB, LD, MH, GG conducted the experiments. FA conducted experiments with dysprosium and processed the data. YY, FA, EB, and LD analyzed all X-ray diffraction data. Theoretical calculations were performed by YY and AlA. YY, LD, and ND wrote the paper with contributions from FA and all co-authors. LD, ND, ZJ, AlA, DL, AnA, and MB involved in the revision of the manuscript.

References

[1] T. Bensby, S. Feltzing, The Origin and Chemical Evolution of Carbon in the Galactic Thin and Thick Discs, *Mon. Not. R. Astron. Soc.* **367**, 1181–1193 (2006).

[2] P. Henderson, *Rare Earth Element Geochemistry*, *Developments in Geochemistry*, Vol. 2 (1984).

[3] D. C. Rubie, F. Nimmo, H. J. Melosh, Formation of Earth's Core, *Treatise Geophys.* **9**, 51–90 (2007).

[4] B. J. Wood, M. J. Walter, J. Wade, Accretion of the Earth and Segregation of Its Core, *Nature* **441**, 825–833 (2006).

[5] V. Babizhetskyy, B. Kotur, V. Levytskyy, H. Michor, Alloy Systems and Compounds Containing Rare Earth Metals and Carbon, *Handb. Phys. Chem. Rare Earths* **52**, 1–263 (2017).

[6] F. I. Akbar, A. Aslandukova, A. Aslandukov, Y. Yin, F. Trybel, S. Khandarkhaeva, T. Fedotenko, D. Laniel, M. Bykov, E. Bykova, N. Dubrovinskaia, L. Dubrovinsky, High-Pressure Synthesis of Dysprosium Carbides, *Front. Chem.* **11**, 1–9 (2023).

[7] A. Aslandukova, A. Aslandukov, L. Yuan, D. Laniel, S. Khandarkhaeva, T. Fedotenko, G. Steinle-Neumann, K. Glazyrin, N. Dubrovinskaia, L. Dubrovinsky, Novel High-Pressure Yttrium Carbide γ-Y4C5 Containing [C2] and Nonlinear [C3] Units with Unusually Large Formal Charges, *Phys. Rev. Lett.* **127**, 135501 (2021).

[8] V. Babizhetskyy, J. Bauer, R. Gautier, K. Hiebl, A. Simon, J. F. Halet, Structural, Electronic, and Physical Properties of Solid-State Rare-Earth Boride Carbides, *Handb. Phys. Chem. Rare Earths* **53**, 145–269 (2018).

[9] Y. Yin, F. I. Akbar, E. Bykova, A. Aslandukova, D. Laniel, A. Aslandukov, M. Bykov, M. Hanfland, G. Garbarino, Z. Jia, L. Dubrovinsky, N. Dubrovinskaia, Synthesis of Rare-Earth Metal Compounds through Enhanced Reactivity of Alkali Halides at High Pressures, *Commun. Chem.* **5**, 8–13 (2022).

[10] T. Mochiku, T. Nakane, H. Kito, H. Takeya, S. Harjo, T. Ishigaki, T. Kamiyama, T. Wada, K. Hirata, Crystal Structure of Yttrium Sesquicarbide, *Phys. C Supercond. Its Appl.* **426**–**431**, 421–425 (2005).

[11] D. H. Chi, Y. Iwasa, K. Uehara, T. Takenobu, T. Ito, T. Mitani, E. Nishibori, M. Takata, M. Sakata, Y. Ohishi, K. Kato, Y. Kubozono, Pressure-Induced Structural Phase Transition in Fullerides Doped with Rare-Earth Metals, *Phys. Rev. B* **67**, 094101 (2003).

[12] D. Laniel, F. Trybel, B. Winkler, F. Knoop, T. Fedotenko, S. Khandarkhaeva, A.

Aslandukova, T. Meier, S. Chariton, K. Glazyrin, V. Milman, V. Prakapenka, I. A. Abrikosov, L. Dubrovinsky, N. Dubrovinskaia, High-Pressure Synthesis of Seven Lanthanum Hydrides with a Significant Variability of Hydrogen Content, *Nat. Commun.* **13**, 1–9 (2022).

[13] T. S. Duffy, Mineralogy at the Extremes, *Nature* **451**, 269–270 (2008).

[14] V. L. Yupko, G. N. Makarenko, Y. B. Paderno, Physical Properties of Carbides of Rare-Earth Metals, *Refract. Carbides* 251–259 (1974).

[15] T. Sakai, G. Adachi, T. Yoshida, J. Shiokawa, Magnetic and Electrical Properties of LaC2, CeC2, PrC2, NdC2, and SmC2, *J. Chem. Phys.* **75**, 3027–3032 (1981).

[16] W. Lengauer, *Carbides: Transition-Metal Solid-State Chemistry* (2012).

[17] H. O. Pierson, Interstitial Carbides, Structure and Composition, *Handb. Refract. Carbides Nitrides* 17–54 (1996).

[18] F. H. Spedding, K. Gschneidner Jr., A. H. Daane, The Crystal Structures of Some of the Rare Earth Carbides, *J. Am. Chem. Soc.* **80**, 4499–4503 (1958).

[19] R. Pöttgen, W. Jeitschko, Sc3C4, a Carbide with C3 Units Derived from Propadiene, *Inorg. Chem.* **30**, 427–431 (1991).

[20] A. VahidMohammadi, J. Rosen, Y. Gogotsi, The World of Two-Dimensional Carbides and Nitrides (MXenes), *Science* **372**, 1–14 (2021).

[21] M. Sokol, V. Natu, S. Kota, M. W. Barsoum, On the Chemical Diversity of the MAX Phases, *Trends Chem.* **1**, 210–223 (2019).

[22] K. Kobayashi, K. Horigane, R. Horie, J. Akimitsu, Superconductivity of Carbides, *Phys. Chem. Carbon-Based Mater. Springer* 149–209 (2019).

[23] E. Özdaş, A. R. Kortan, N. Kopylov, A. P. Ramirez, T. Siegrist, K. M. Rabe, H. E. Bair, S. Schuppler, P. H. Citrin, Superconductivity and Cation-Vacancy Ordering in the Rare-Earth Fulleride Yb2.75C60, *Nature* **375**, 126–129 (1995).

[24] T. Sakai, G. Y. Adachi, T. Yoshida, J. Shiokawa, Magnetic and Electrical Properties of Rare Earth Dicarbides and Their Solid Solutions, *J. Less-Common Met.* **81**, 91–102 (1981).

[25] K. R. Meihaus, M. E. Fieser, J. F. Corbey, W. J. Evans, J. R. Long, Record High Single-Ion Magnetic Moments Through 4fn5d1 Electron Configurations in the Divalent Lanthanide Complexes [(C5H4SiMe3)3Ln]-, *J. Am. Chem. Soc.* **137**, 9855–9860 (2015).

[26] M. Atoji, M. Kikuchi, Crystal Structures of Cubic and Trigonal Yttrium Hypocarbides; A Dimorphically Interphased Single-Crystal Study, *J. Chem. Phys.* **51**, 3863–3872

(1969).

[27] L. M. McRae, R. C. Radomsky, J. T. Pawlik, D. L. Druffel, J. D. Sundberg, M. G. Lanetti, C. L. Donley, K. L. White, S. C. Warren, Sc2C, a 2D Semiconducting Electride, *J. Am. Chem. Soc.* **144**, 10862–10869 (2022).

[28] J. Park, J. Y. Hwang, K. H. Lee, S. G. Kim, K. Lee, S. W. Kim, Tuning the Spin-Alignment of Interstitial Electrons in Two-Dimensional Y2C Electride via Chemical Pressure, *J. Am. Chem. Soc.* **139**, 17277–17280 (2017).

[29] K. A. Gschneidner, A. Pecharsky, K. W. Dennis, Some Observations on the Gd-Rich Side of the Gd-C System, *J. Alloys Compd.* **260**, 107–110 (1997).

[30] M. Atoji, Neutron-Diffraction Studies of Tb2C and Dy2C in the Temperature Range 4-296 K, *J. Chem. Phys.* **75**, 1434–1441 (1981).

[31] M. Atoji, Neutron-diffraction Study of Ho2C at 4–296 K, *J. Chem. Phys.* **74**, 1893–1897 (1981).

[32] J. M. Haschke, H. A. Eick, Phase Investigation of the Ytterbium-Carbon System, *J. Am. Chem. Soc.* **92**, 1526–1530 (1970).

[33] H. Rassaerts, H. Nowotny, G. Vinek, F. Benesovsky, Zum System Scandium-Kohlenstoff, 1. Mitt.:, *Monatshefte Für Chemie* **98**, 460–468 (1967).

[34] H. Nowotny, H. Auer-Welsbach, Über Das Scandiumcarbid, *Monatshefte Für Chemie* **92**, 789–793 (1961).

[35] L. Brewer, O. Krikorian, Reactions of Refractory Silicides with Carbon and Nitrogen, *J. Electrochem. Soc.* **103**, 38–51 (1956).

[36] M. Onoda, Y. Shi, A. Leithe-Jasper, T. Tanaka, Structure Refinement of the Layered Composite Crystal Sc2B1.1C3.2 in a Five-Dimensional Formalism, *Acta Cryst.* **B57**, 449–457 (2001).

[37] T. Hüfken, W. Jeitschko, The High-Temperature (β) Modification of Y4C7 with Lu4C7 Type and Dy3C4 with Sc3C4 Type Structure, *J. Alloys Compd.* **278**, 161–164 (1998).

[38] R. Czekalla, W. Jeitschko, R.-D. Hoffmann, H. Rabeneck, Preparation, Crystal Structure, and Properties of the Lanthanoid Carbides Ln4C7 with Ln = Ho, Er, Tm, and Lu, *Zeitschrift Für Naturforsch. B* **51**, 646–654 (1996).

[39] H. Mattausch, T. Gulden, R. K. Kremer, J. Horakh, A. Simon, Ho4C7, Y4C7: Carbide Mit C34- - Und C4- -Ionen / Ho4C7, Y4C7: Carbides with C34- and C4- Ions, *Zeitschrift Für Naturforsch. B* **49**, 1439–1443 (1994).

[40] R. Czekalla, T. Hüfken, W. Jeitschko, R. D. Hoffmann, R. Pöttgen, The Rare Earth Carbides R4C5 with R=Y, Gd, Tb, Dy, and Ho, *J. Solid State Chem.* **132**, 294–299

(1997).

[41] H. Ninomiya, T. Koshinuma, T. Nishio, H. Fujihisa, K. Kawashima, I. Hase, S. Ishida, H. Ogino, A. Iyo, Y. Yoshida, Y. Gotoh, H. Eisaki, Experimental and Computational Determination of Optimal Boron Content in Layered Superconductor Sc20C8-XBxC20, *Inorg. Chem.* **59**, 14290–14295 (2020).

[42] N. H. Krikorian, A. L. Bowman, M. C. Krupka, G. P. Arnold, The Preparation and Crystal Structure of Sc4C3, *High Temp. Sci.* **1**, 360–366 (1969).

[43] V. I. Novokshonov, Synthesis of Sesquicarbides of Heavy Rare Earths and Yttrium at High Pressures and Temperatures, *Zhurnal Neorg. Khimii* **25**, 684–689 (1980).

[44] G.-Y. Adachi, N. Imanaka, Z. Fuzhong, *Rare Earth Carbides*, in *Handbook on the Physics and Chemistry of Rare Earths*, Vol. 15 (1991), pp. 61–189.

[45] N. H. Krikorian, A. L. Giorgi, E. G. Szklarz, M. C. Krupka, B. T. Matthias, Preparation and Superconductivity of Germanium-Stabilized Sc13C10, *J. Less Common Met.* **19**, 253–257 (1969).

[46] I. Colquhoun, N. N. Greenwood, I. J. McColm, G. E. Turner, Preparation, Characterisation, and Europium-151 Mössbauer Spectra of Some Carbides, Nitrides, Nitride-Carbides, Cyanides, and Thiocyanates of Europium, *J. Chem. Soc. Dalt. Trans.* 1337–1341 (1972).

[47] H. Jedlicka, H. Nowotny, F. Benesovsky, *Zum System Scandium-Kohlenstoff, 2. Mitt.: Kristallstruktur Des C-Reichen Carbids*, Vol. 102 (1971).

[48] T. W. Button, I. J. McColm, Reaction of Carbon with Lanthanide Silicides IV: The Y5Si3-C System, *J. Less-Common Met.* **97**, 237–244 (1984).

[49] J. Bauer, D. Ansel, Synthesis of the so Called “Low Symmetry Form of Holmium and Thulium Sesquicarbides” — Ho15C19 and Tm15C19, *J. Less-Common Met.* **109**, L9–L13 (1985).

[50] J. Bauer, Contribution à l’étude de La Structure Cristalline de La Phase Er15C19, *J. Less-Common Met.* **37**, 161–165 (1974).

[51] J. Bauer, H. Bienvenu, *Yb15C19*, https://www.ccdc.cam.ac.uk/structures/search?pid=ccdc:200833&DatabaseToSearch=ICSD.

[52] J. Bauer, H. Bienvenu, *Lu15C19*, https://www.ccdc.cam.ac.uk/structures/search?pid=ccdc:601559&DatabaseToSearch=ICSD.

[53] A. L. Bowman, N. H. Krikorian, G. P. Arnold, T. C. Wallace, N. G. Nereson, The Crystal

Structure of LaC2, *Acta Crystallogr*. **B24**, 459–460 (1968).

[54] V. Babizhetskyy, O. Jepsen, R. K. Kremer, A. Simon, B. Ouladdiaf, A. Stolovits, Structure and Bonding of Superconducting LaC2, *J. Phys. Condens. Matter* **26**, 025701 (2014).

[55] D. W. Jones, I. J. McColm, J. Yerkess, Tetragonal and Cubic Crystal Structures of Some Binary and Ternary Metal Dicarbides in the Series Ce-Er, Ce-Lu, U-La, and U-Ce, *J. Solid State Chem.* **92**, 301–311 (1991).

[56] D. Wandner, P. Link, O. Heyer, J. Mydosh, M. A. Ahmida, M. M. Abd-Elmeguid, M. Speldrich, H. Lueken, U. Ruschewitz, Structural Phase Transitions in EuC2, *Inorg. Chem.* **49**, 312–318 (2010).

[57] Y. Yosida, Surface Superconductivity and Structural Analysis of YC2 Single Crystals Encapsulated in Carbon Nanocages, *J. Appl. Phys.* **92**, 5494–5497 (2002).

[58] G.-Y. Adachi, T. Nishihata, J. Shiokawa, Rare-Earth Mixed Dicarbides, *Journul Less-Common Met.* **32**, 301–306 (1973).

[59] N. H. Krikorian, T. C. Wallace, M. G. Bowman, *TbC2*, https://www.ccdc.cam.ac.uk/structures/search?pid=ccdc:618870&DatabaseToSearch=ICSD.

[60] K. A. Gschneidner, F. W. Calderwood, The C-Lu (Carbon-Lutetium) System, *Bull. Alloy Phase Diagrams* **7**, 555–556 (1986).

[61] M. Atoji, Magnetic and Crystal Structures of CeC2, PrC2, NdC2, TbC2, and HoC2 at Low Temperatures, *J. Chem. Phys.* **46**, 1891–1901 (1967).

[62] G.-Y. Adachi, K. Ueno, J. Shiokawa, Heats of Transformation in Lanthanide Dicarbides and Mixed Lanthanide Dicarbide Solid Solutions, *J. Less Common Met.* **37**, 313–314 (1974).

[63] G. Y. Adachi, Y. Shibata, K. Ueno, J. Shiokawa, Heats of the Tetragonal-Cubic Transformation in Rare Earth Dicarbides and Mixed Rare Earth Dicarbide Solid Solutions, *J. Inorg. Nucl. Chem.* **38**, 1023–1026 (1976).

[64] I. J. McColm, Transformation Temperatures and Hydrolysis Rates of Three Series of Dicarbide Solid Solutions: YC2-HoC2, YC2-LuC2 and GdC2-ErC2, *J. Alloys Compd.* **189**, 31–35 (1992).

[65] M. Atoji, Neutron Diffraction Studies of CaC2, YC2, LaC2, CeC2, TbC2, YbC2, LuC2, and UC2, *J. Chem. Phys.* **35**, 1950–1960 (1961).

[66] M. El Makrini, D. Guérard, P. Lagrange, A. Hérold, Insertion de Lanthanoides Dans Le Graphite, *Carbon N. Y.* **18**, 203–209 (1980).

[67] H. Rida, S. Cahen, C. Hérold, P. Lagrange, Bulk Synthesis and Crystal Structure of the First Stage Europium–Graphite Intercalation Compound, *Carbon N. Y.* **48**, 3190–3195 (2010).

[68] D. Claves, Y. Ksari-Habiles, G. Chouteau, P. Touzain, Crystal Chemistry of Europium Fullerides, *Solid State Commun.* **106**, 431–435 (1998).

[69] X. H. Chen, Z. S. Liu, S. Y. Li, D. H. Chi, Y. Iwasa, Structure and Properties of a Fulleride Sm6C60, *Phys. Rev. B* **60**, 6183–6186 (1999).

[70] Z. Sun, X. H. Chen, T. Takenobu, Y. Iwasa, Structure and Raman Behaviour of Sm2.75C60, *J. Phys. Condens. Matter* **12**, 8919–8926 (2000).

[71] X. H. Chen, D. H. Chi, Z. Sun, T. Takenobu, Z. S. Liu, Y. Iwasa, Synthesis, Structure, and Transport Properties of Novel Fullerides A3C70 (A = Ba and Sm), *J. Am. Chem. Soc.* **122**, 5729–5732 (2000).

[72] T. Takenobu, D. H. Chi, S. Margadonna, K. Prassides, Y. Kubozono, A. N. Fitch, K. ichi Kato, Y. Iwasa, Synthesis, Structure, and Magnetic Properties of the Fullerene-Based Ferromagnets Eu3C70 and Eu9C70, *J. Am. Chem. Soc.* **125**, 1897–1904 (2003).

[73] Y. Rikiishi, Y. Kubozono, T. Hosokawa, K. Shibata, Y. Haruyama, Y. Takabayashi, A. Fujiwara, S. Kobayashi, S. Mori, Y. Iwasa, Structural and Electronic Characterizations of Two Isomers of Ce@C82, *J. Phys. Chem. B* **108**, 7580–7585 (2004).

[74] T. Kanbara, K. Shibata, S. Fujiki, Y. Kubozono, S. Kashino, T. Urisu, M. Sakai, A. Fujiwara, R. Kumashiro, K. Tanigaki, N-Channel Field Effect Transistors with Fullerene Thin Films and Their Application to a Logic Gate Circuit, *Chem. Phys. Lett.* **379**, 223–229 (2003).

[75] S. Iida, Y. Kubozono, Y. Slovokhotov, Y. Takabayashi, T. Kanbara, T. Fukunaga, S. Fujiki, S. Emura, S. Kashino, Structure and Electronic Properties of Dy@C82 Studied by UV–VIS Absorption, X-Ray Powder Diffraction and XAFS, *Chem. Phys. Lett.* **338**, 21–28 (2001).

[76] H. Ootoshi, K. Ishii, A. Fujiwara, T. Watanuki, Y. Matsuoka, H. Suematsu, Crystal Structure of Europium C 60 Compounds, *Mol. Cryst. Liq. Cryst. Sci. Technol. Sect. A. Mol. Cryst. Liq. Cryst.* **340**, 565–570 (2000).

[77] I. Margiolaki, S. Margadonna, K. Prassides, T. Hansen, K. Ishii, H. Suematsu, Magnetic Structure of the Europium Fulleride Ferromagnet Eu6C60, *J. Am. Chem. Soc.* **124**, 11288–11289 (2002).

[78] X. Feng, S. Lu, C. J. Pickard, H. Liu, S. A. T. Redfern, Y. Ma, Carbon Network Evolution from Dimers to Sheets in Superconducting Ytrrium Dicarbide under Pressure,

Commun. Chem. **1**, 1–7 (2018).

[79] Y. Guo, C. Yu, J. Lin, C. Wang, C. Ren, B. Sun, P. Huai, R. Xie, X. Ke, Z. Zhu, H. Xu, Pressure-Induced Structural Transformations and Polymerization in ThC2, *Sci. Rep.* **7**, 11 (2017).

[80] D. Benson, Y. Li, W. Luo, R. Ahuja, G. Svensson, U. Häussermann, Lithium and Calcium Carbides with Polymeric Carbon Structures, *Inorg. Chem.* **52**, 6402–6406 (2013).

[81] J. Nylén, S. Konar, P. Lazor, D. Benson, U. Häussermann, Structural Behavior of the Acetylide Carbides Li2C2 and CaC2 at High Pressure, *J. Chem. Phys.* **137**, 224507 (2012).

[82] Y. L. Li, S. N. Wang, A. R. Oganov, H. Gou, J. S. Smith, T. A. Strobel, Investigation of Exotic Stable Calcium Carbides Using Theory and Experiment, *Nat. Commun.* **6**, 1–9 (2015).

[83] M. Debessai, J. J. Hamlin, J. S. Schilling, D. Rosenmann, D. G. Hinks, H. Claus, Superconductivity for CaC6 to 32 GPa Hydrostatic Pressure, *Phys. Rev. B - Condens. Matter Mater. Phys.* **82**, 3–5 (2010).

[84] A. Gauzzi, S. Takashima, N. Takeshita, C. Terakura, H. Takagi, N. Emery, C. Hérold, P. Lagrange, G. Loupias, Enhancement of Superconductivity and Evidence of Structural Instability in Intercalated Graphite CaC6 under High Pressure, *Phys. Rev. Lett.* **98**, 15–18 (2007).

[85] L. Zhang, Y. Xie, T. Cui, Y. Li, Z. He, Y. Ma, G. Zou, Pressure-Induced Enhancement of Electron-Phonon Coupling in Superconducting Ca C6 from First Principles, *Phys. Rev. B - Condens. Matter Mater. Phys.* **74**, 1–5 (2006).

[86] L. Wang, X. Dong, Y. Wang, H. Zheng, K. Li, X. Peng, H. K. Mao, C. Jin, Y. Meng, M. Huang, Z. Zhao, Pressure-Induced Polymerization and Disproportionation of Li2C2 Accompanied with Irreversible Conductivity Enhancement, *J. Phys. Chem. Lett.* **8**, 4241–4245 (2017).

[87] X. Dong, L. Wang, K. Li, H. Zheng, Y. Wang, Y. Meng, H. Shu, H. K. Mao, S. Feng, C. Jin, Tailored Synthesis of the Narrowest Zigzag Graphene Nanoribbon Structure by Compressing the Lithium Acetylide under High Temperature, *J. Phys. Chem. C* **122**, 20506–20512 (2018).

[88] F. I. Akbar, A. Aslandukova, Y. Yin, A. Aslandukov, D. Comboni, M. Hanfland, N. Dubrovinskaia, High-Pressure Dysprosium Carbides Containing Carbon Dimers, Trimers, Chains, and Ribbons, *Submitt. to Carbon* (2024).

[89] S. Khandarkhaeva, T. Fedotenko, A. Aslandukova, F. I. Akbar, M. Bykov, D. Laniel, A. Aslandukov, U. Ruschewitz, C. Tobeck, B. Winkler, S. Chariton, V. Prakapenka, K. Glazyrin, C. Giacobbe, E. L. Bright, M. Belov, N. Dubrovinskaia, L. Dubrovinsky, Extending Carbon Chemistry at High-Pressure by Synthesis of CaC2 and Ca3C7 with Deprotonated Polyacene- and Para-Poly(Indenoindene)-like Nanoribbons, *Nat. Commun.* **15**, 2855 (2024).

[90] P. I. Dorogokupets, A. Dewaele, Equations of State of MgO, Au, Pt, NaCl-B1, and NaCl-B2: Internally Consistent High-Temperature Pressure Scales, *High Press. Res.* **27**, 431–446 (2007).

[91] D. L. Decker, Equation of State of NaCl and Its Use as a Pressure Gauge in High-Pressure Research, *J. Appl. Phys.* **36**, 157–161 (1965).

[92] J. Hu, J. Xu, M. Somayazulu, Q. Guo, R. Hemley, H. K. Mao, X-Ray Diffraction and Laser Heating: Application of a Moissanite Anvil Cell, *J. Phys. Condens. Matter* **14**, 10479–10481 (2002).

[93] M. Armentrout, A. Kavner, High Pressure, High Temperature Equation of State for Fe2SiO4 Ringwoodite and Implications for the Earth's Transition Zone, *Geophys. Res. Lett.* **38**, 1–4 (2011).

[94] B. Langerome, M. Verseils, F. Capitani, J. B. Brubach, E. Amzallag, E. Calandrini, J. Creuze, P. Roy, Probing NaCl at High Pressure through Optical Studies and Ab Initio Calculations, *J. Phys. Chem. C* **123**, 15724–15728 (2019).

[95] F. A. Redeker, H. Beckers, S. Riedel, Matrix-Isolation and Comparative Far-IR Investigation of Free Linear [Cl3]- and a Series of Alkali Trichlorides, *Chem. Commun.* **53**, 12958–12961 (2017).

[96] W. Zhang, A. R. Oganov, Q. Zhu, S. S. Lobanov, E. Stavrou, A. F. Goncharov, Stability of Numerous Novel Potassium Chlorides at High Pressure, *Sci. Rep.* **6**, 1–6 (2016).

[97] W. Zhang, A. R. Oganov, A. F. Goncharov, Q. Zhu, S. E. Boulfelfel, A. O. Lyakhov, E. Stavrou, M. Somayazulu, V. B. Prakapenka, Z. Konôpková, Unexpected Stable Stoichiometries of Sodium Chlorides, *Science* **342**, 1502–1505 (2013).

[98] H. Yuan, L. Man, D. Y. Kim, D. Popov, Y. Meng, HP-PdF2-Type FeCl2 as a Potential Cl-Carrier in the Deep Earth, *Am. Miner.* **107**, 313–317 (2022).

[99] E. Koemets, L. Yuan, E. Bykova, K. Glazyrin, E. Ohtani, L. Dubrovinsky, Interaction between FeOOH and NaCl at Extreme Conditions: Synthesis of Novel Na2FeCl4OHx Compound, *Minerals* **10**, 1–7 (2020).

[100] F. R. Boyd, J. L. England, Apparatus for Phase-Equilibrium Measurements at Pressures

up to 50 Kilobars and Temperatures up to 1750°C, *J. Geophys. Res.* **65**, 741–748 (1960).

[101] N. Kawai, S. Endo, The Generation of Ultrahigh Hydrostatic Pressures by a Split Sphere Apparatus, *Rev. Sci. Instrum.* **41**, 1178–1181 (1970).

[102] J. C. Jamieson, A. W. Lawson, N. D. Nachtrieb, New Device for Obtaining X-Ray Diffraction Patterns from Substances Exposed to High Pressure, *Rev. Sci. Instrum.* **30**, 1016–1019 (1959).

[103] B. Li, C. Ji, W. Yang, J. Wang, K. Yang, R. Xu, W. Liu, Z. Cai, J. Chen, H. kwang Mao, Diamond Anvil Cell Behavior up to 4 Mbar, *Proc. Natl. Acad. Sci. U. S. A.* **115**, 1713–1717 (2018).

[104] N. Dubrovinskaia, L. Dubrovinsky, N. A. Solopova, A. Abakumov, S. Turner, M. Hanfland, E. Bykova, M. Bykov, C. Prescher, V. B. Prakapenka, S. Petitgirard, I. Chuvashova, B. Gasharova, Y. L. Mathis, P. Ershov, I. Snigireva, A. Snigirev, Terapascal Static Pressure Generation with Ultrahigh Yield Strength Nanodiamond, *Sci. Adv.* **2**, e1600341 (2016).

[105] I. Kantor, V. Prakapenka, A. Kantor, P. Dera, A. Kurnosov, S. Sinogeikin, N. Dubrovinskaia, L. Dubrovinsky, BX90: A New Diamond Anvil Cell Design for X-Ray Diffraction and Optical Measurements, *Rev. Sci. Instrum.* **83**, 125102 (2012).

[106] S. Anzellini, A. Dewaele, F. Occelli, P. Loubeyre, M. Mezouar, Equation of State of Rhenium and Application for Ultra High Pressure Calibration, *J. Appl. Phys.* **115**, 043511 (2014).

[107] M. H. Manghnani, K. Katahara, E. S. Fisher, Ultrasonic Equation of State of Rhenium, *Phys. Rev. B* **9**, 1421–1431 (1974).

[108] R. Boehler, K. De Hantsetters, New Anvil Designs in Diamond-Cells, *High Press. Res.* **24**, 391–396 (2004).

[109] A. Jayaraman, Diamond Anvil Cell and High-Pressure Physical Investigations, *Rev. Mod. Phys.* **55**, 65–108 (1983).

[110] A. Kurnosov, I. Kantor, T. Boffa-Ballaran, S. Lindhardt, L. Dubrovinsky, A. Kuznetsov, B. H. Zehnder, A Novel Gas-Loading System for Mechanically Closing of Various Types of Diamond Anvil Cells, *Rev. Sci. Instrum.* **79**, 045110 (2008).

[111] K. Syassen, Ruby under Pressure, *High Press. Res.* **28**, 75–126 (2008).

[112] G. Shen, Y. Wang, A. Dewaele, C. Wu, D. E. Fratanduono, J. Eggert, S. Klotz, K. F. Dziubek, P. Loubeyre, O. V. Fat'yanov, P. D. Asimow, T. Mashimo, R. M. M. Wentzcovitch, Toward an International Practical Pressure Scale: A Proposal for an IPPS Ruby Gauge (IPPS-Ruby2020), *High Press. Res.* **40**, 299–314 (2020).

[113] Y. Akahama, H. Kawamura, Pressure Calibration of Diamond Anvil Raman Gauge to 310 GPa, *J. Appl. Phys.* **100**, 043516 (2006).

[114] A. Dewaele, M. Torrent, P. Loubeyre, M. Mezouar, Compression Curves of Transition Metals in the Mbar Range: Experiments and Projector Augmented-Wave Calculations, *Phys. Rev. B* **78**, 104102 (2008).

[115] Y. Fei, A. Ricolleau, M. Frank, K. Mibe, G. Shen, V. Prakapenka, Toward an Internally Consistent Pressure Scale, *Proc. Natl. Acad. Sci.* **104**, 9182–9186 (2007).

[116] A. Dewaele, F. Datchi, P. Loubeyre, M. Mezouar, High Pressure–High Temperature Equations of State of Neon and Diamond, *Phys. Rev. B* **77**, 094106 (2008).

[117] M. Ross, H. K. Mao, P. M. Bell, J. A. Xu, The Equation of State of Dense Argon: A Comparison of Shock and Static Studies, *J. Chem. Phys.* **85**, 1028–1033 (1986).

[118] T. Sakai, E. Ohtani, N. Hirao, Y. Ohishi, Equation of State of the NaCl-B2 Phase up to 304 GPa, *J. Appl. Phys.* **109**, 084912 (2011).

[119] A. Dewaele, A. B. Belonoshko, G. Garbarino, F. Occelli, P. Bouvier, M. Hanfland, M. Mezouar, High-Pressure–High-Temperature Equation of State of KCl and KBr, *Phys. Rev. B* **85**, 214105 (2012).

[120] S. Tateno, T. Komabayashi, K. Hirose, N. Hirao, Y. Ohishi, Static Compression of B2 KCl to 230 GPa and Its P-V-T Equation of State, *Am. Mineral.* **104**, 718–723 (2019).

[121] Y. Ye, S.-H. Shim, V. Prakapenka, Y. Meng, Equation of State of Solid Ne Inter-Calibrated with the MgO, Au, Pt, NaCl-B2, and Ruby Pressure Scales up to 130 GPa, *High Press. Res.* **38**, 377–395 (2018).

[122] A. Dewaele, Equations of State of Simple Solids (Including Pb, NaCl and LiF) Compressed in Helium or Neon in the Mbar Range, *Minerals* **9**, 684 (2019).

[123] P. Vinet, J. Ferrante, J. H. Rose, J. R. Smith, Compressibility of Solids, *J. Geophys. Res.* **92**, 9319–9325 (1987).

[124] F. Birch, Finite Elastic Strain of Cubic Crystals, *Phys. Rev.* **71**, 809–824 (1947).

[125] W. A. Bassett, Diamond Anvil Cell, 50th Birthday, *High Press. Res.* **29**, 163–186 (2009).

[126] J. Xie, A. Kar, J. A. Rothenflue, W. P. Latham, Temperature-Dependent Absorptivity and Cutting Capability of CO2, Nd:YAG and Chemical Oxygen–Iodine Lasers, *J. Laser Appl.* **9**, 77–85 (1997).

[127] R. M. Sobhi, N. A. H. Adawy, I. S. Zaky, "Comparative Study between the Efficacy of Fractional CO2 Laser, Q-Switched Nd:YAG Laser (1064 Nm), and Both Types in Treatment of Keratosis Pilaris," *Lasers Med. Sci.* **35**, 1367–1376 (2020).

[128] J. E. Graebner, *Thermal Conductivity of Diamond*, in *Diamond: Electronic Properties and Applications* (Springer US, Boston, MA, 1995), pp. 285–318.

[129] T. Fedotenko, L. Dubrovinsky, G. Aprilis, E. Koemets, A. Snigirev, I. Snigireva, A. Barannikov, P. Ershov, F. Cova, M. Hanfland, N. Dubrovinskaia, Laser Heating Setup for Diamond Anvil Cells for in Situ Synchrotron and in House High and Ultra-High Pressure Studies, *Rev. Sci. Instrum.* **90**, 104501 (2019).

[130] T. Y. Subramaniam, P. Premanand, Infrared Laser Excitation to Study Transitions in Fullerene (C60) Molecule, *J. Lasers, Opt. Photonics* **5**, 5 (2018).

[131] Y. Waseda, E. Matsubara, K. Shinoda, *X-Ray Diffraction Crystallography* (Springer Berlin Heidelberg, Berlin, Heidelberg, 2011).

[132] B. D. Cullity, S. R. Stock, *Elements of X-Ray Diffraction, Pearson New International Edition, 3rd Edition* (2013).

[133] R. E. Newnham, *Properties of Materials: Anisotropy, Symmetry, Structure* (2005).

[134] M. Bykov, *Structural Aspects of Pressure- and Temperature-Induced Phase Transitions in Low-Dimensional Systems*.

[135] C. Prescher, V. B. Prakapenka, DIOPTAS: A Program for Reduction of Two-Dimensional X-Ray Diffraction Data and Data Exploration, *High Press. Res.* **35**, 223–230 (2015).

[136] R. Hrubiak, J. S. Smith, G. Shen, Multimode Scanning X-Ray Diffraction Microscopy for Diamond Anvil Cell Experiments, *Rev. Sci. Instrum.* **90**, (2019).

[137] *Rigaku Oxford Diffraction. CrysAlisPro Software System.*, (2015).

[138] O. V. Dolomanov, L. J. Bourhis, R. J. Gildea, J. A. K. Howard, H. Puschmann, OLEX2: A Complete Structure Solution, Refinement and Analysis Program, *J. Appl. Crystallogr.* **42**, 339–341 (2009).

[139] G. M. Sheldrick, SHELXT – Integrated Space-Group and Crystal-Structure Determination, *Acta Crystallogr. Sect. A Found. Adv.* **71**, 3–8 (2015).

[140] G. M. Sheldrick, Crystal Structure Refinement with SHELXL, *Acta Crystallogr. Sect. C Struct. Chem.* **71**, 3–8 (2015).

[141] V. Petříček, M. Dušek, L. Palatinus, Crystallographic Computing System JANA2006: General Features, *Zeitschrift Für Krist. - Cryst. Mater.* **229**, 345–352 (2014).

[142] A. Aslandukov, M. Aslandukov, N. Dubrovinskaia, L. Dubrovinsky, Domain Auto Finder (DAFi) Program: The Analysis of Single-Crystal X-Ray Diffraction Data from Polycrystalline Samples, *J. Appl. Crystallogr.* **55**, 1383–1391 (2022).

[143] G. Taylor, The Phase Problem, *Acta Crystallogr. Sect. D Biol. Crystallogr.* **59**, 1881–

1890 (2003).

[144] P. Hohenberg, W. Kohn, Inhomogeneous Electron Gas, *Phys. Rev.* **136**, B864–B871 (1964).

[145] W. Kohn, L. J. Sham, Self-Consistent Equations Including Exchange and Correlation Effects, *Phys. Rev.* **140**, A1133–A1138 (1965).

[146] J. P. Perdew, A. Ruzsinszky, J. Tao, V. N. Staroverov, G. E. Scuseria, G. I. Csonka, Prescription for the Design and Selection of Density Functional Approximations: More Constraint Satisfaction with Fewer Fits, *J. Chem. Phys.* **123**, 062201 (2005).

[147] A. E. Mattsson, In Pursuit of the "Divine" Functional, *Science* **298**, 759–760 (2002).

[148] G. Kresse, J. Furthmüller, Efficient Iterative Schemes for Ab Initio Total-Energy Calculations Using a Plane-Wave Basis Set, *Phys. Rev. B* **54**, 11169 (1996).

[149] X. Gonze, B. Amadon, P.-M. Anglade, J.-M. Beuken, F. Bottin, P. Boulanger, F. Bruneval, D. Caliste, R. Caracas, M. Côté, T. Deutsch, L. Genovese, P. Ghosez, M. Giantomassi, S. Goedecker, D. R. Hamann, P. Hermet, F. Jollet, G. Jomard, S. Leroux, M. Mancini, S. Mazevet, M. J. T. Oliveira, G. Onida, Y. Pouillon, T. Rangel, G.-M. Rignanese, D. Sangalli, R. Shaltaf, M. Torrent, M. J. Verstraete, G. Zerah, J. W. Zwanziger, ABINIT: First-Principles Approach to Material and Nanosystem Properties, *Comput. Phys. Commun.* **180**, 2582–2615 (2009).

[150] P. Giannozzi, S. Baroni, N. Bonini, M. Calandra, R. Car, C. Cavazzoni, D. Ceresoli, G. L. Chiarotti, M. Cococcioni, I. Dabo, A. Dal Corso, S. de Gironcoli, S. Fabris, G. Fratesi, R. Gebauer, U. Gerstmann, C. Gougoussis, A. Kokalj, M. Lazzeri, L. Martin-Samos, N. Marzari, F. Mauri, R. Mazzarello, S. Paolini, A. Pasquarello, L. Paulatto, C. Sbraccia, S. Scandolo, G. Sclauzero, A. P. Seitsonen, A. Smogunov, P. Umari, R. M. Wentzcovitch, QUANTUM ESPRESSO: A Modular and Open-Source Software Project for Quantum Simulations of Materials, *J. Phys. Condens. Matter* **21**, 395502 (2009).

[151] S. J. Clark, M. D. Segall, C. J. Pickard, P. J. Hasnip, M. I. J. Probert, K. Refson, M. C. Payne, First Principles Methods Using CASTEP, *Zeitschrift Für Krist. - Cryst. Mater.* **220**, 567–570 (2005).

[152] C. Kittel, *Introduction to Solid State Physics*, Vol. 6 (2004).

[153] G. Makov, M. C. Payne, Periodic Boundary Conditions in Ab Initio Calculations, *Phys. Rev. B* **51**, 4014–4022 (1995).

[154] P. E. Blöchl, Projector Augmented-Wave Method, *Phys. Rev. B* **50**, 17953–17979 (1994).

[155] J. P. Perdew, K. Burke, M. Ernzerhof, Generalized Gradient Approximation Made

Simple, *Phys. Rev. Lett.* **77**, 3865–3868 (1996).

[156] G. Kresse, J. Furthmüller, Efficiency of Ab-Initio Total Energy Calculations for Metals and Semiconductors Using a Plane-Wave Basis Set, *Comput. Mater. Sci.* **6**, 15–50 (1996).

[157] A. Togo, I. Tanaka, First Principles Phonon Calculations in Materials Science, *Scr. Mater.* **108**, 1–6 (2015).

[158] J. Rath, A. J. Freeman, Generalized Magnetic Susceptibilities in Metals: Application of the Analytic Tetrahedron Linear Energy Method to Sc, **11**, 2109–2117 (1975).

[159] C. Friedrich, Tetrahedron Integration Method for Strongly Varying Functions: Application to the GT Self-Energy, *Phys. Rev. B* **100**, 075142(15) (2019).

[160] P. C. Müller, C. Ertural, J. Hempelmann, R. Dronskowski, Crystal Orbital Bond Index: Covalent Bond Orders in Solids, *J. Phys. Chem. C* **125**, 7959–7970 (2021).

[161] S. Maintz, V. L. Deringer, A. L. Tchougréeff, R. Dronskowski, LOBSTER: A Tool to Extract Chemical Bonding from Plane-Wave Based DFT, *J. Comput. Chem.* **37**, 1030–1035 (2016).

[162] R. S. Mulliken, Electronic Population Analysis on LCAO-MO Molecular Wave Functions. I, *J. Chem. Phys.* **23**, 1833–1840 (1955).

[163] R. S. Mulliken, Electronic Population Analysis on LCAO-MO Molecular Wave Functions. II. Overlap Populations, Bond Orders, and Covalent Bond Energies, *J. Chem. Phys.* **23**, 1841–1846 (1955).

[164] R. S. Mulliken, Electronic Population Analysis on LCAO-MO Molecular Wave Functions. III. Effects of Hybridization on Overlap and Gross AO Populations, *J. Chem. Phys.* **23**, 2338–2342 (1955).

[165] R. S. Mulliken, Electronic Population Analysis on LCAO-MO Molecular Wave Functions. IV. Bonding and Antibonding in LCAO and Valence-Bond Theories, *J. Chem. Phys.* **23**, 2343–2346 (1955).

[166] L. Pauling, The Principles Determining the Structure of Complex Ionic Crystals, *J. Am. Chem. Soc.* **51**, 1010–1026 (1929).

[167] M. Nespolo, B. Guillot, CHARDI2015: Charge Distribution Analysis of Non-Molecular Structures, *J. Appl. Crystallogr.* **49**, 317–321 (2016).

[168] Y. Yin, A. Aslandukova, N. Jena, F. Trybel, I. A. Abrikosov, B. Winkler, S. Khandarkhaeva, T. Fedotenko, E. Bykova, D. Laniel, M. Bykov, A. Aslandukov, F. I. Akbar, K. Glazyrin, G. Garbarino, C. Giacobbe, E. L. Bright, Z. Jia, L. Dubrovinsky, N. Dubrovinskaia, Unraveling the Bonding Complexity of Polyhalogen Anions: High-

Pressure Synthesis of Unpredicted Sodium Chlorides Na2Cl3 and Na4Cl5 and Bromide Na4Br5, *JACS Au* **3**, 1634−1641 (2023).

[169] D. Laniel, B. Winkler, T. Fedotenko, A. Aslandukova, A. Aslandukov, S. Vogel, T. Meier, M. Bykov, S. Chariton, K. Glazyrin, V. Milman, V. Prakapenka, W. Schnick, L. Dubrovinsky, N. Dubrovinskaia, High-Pressure Na3(N2)4, Ca3(N2)4, Sr3(N2)4, and Ba(N2)3 Featuring Nitrogen Dimers with Noninteger Charges and Anion-Driven Metallicity, *Phys. Rev. Mater.* **6**, 023402 (2022).

[170] A. Aslandukov, F. Trybel, A. Aslandukova, D. Laniel, T. Fedotenko, S. Khandarkhaeva, G. Aprilis, C. Giacobbe, E. Lawrence Bright, I. A. Abrikosov, L. Dubrovinsky, N. Dubrovinskaia, Anionic N18 Macrocycles and a Polynitrogen Double Helix in Novel Yttrium Polynitrides YN6 and Y2N11 at 100 GPa, *Angew. Chemie - Int. Ed.* **61**, (2022).

[171] M. Bykov, E. Bykova, G. Aprilis, K. Glazyrin, E. Koemets, I. Chuvashova, I. Kupenko, C. McCammon, M. Mezouar, V. Prakapenka, H. P. Liermann, F. Tasnádi, A. V. Ponomareva, I. A. Abrikosov, N. Dubrovinskaia, L. Dubrovinsky, Fe-N System at High Pressure Reveals a Compound Featuring Polymeric Nitrogen Chains, *Nat. Commun.* **9**, 1–8 (2018).

[172] A. Aslandukov, A. Aslandukova, D. Laniel, S. Khandarkhaeva, Y. Yin, F. I. Akbar, S. Chariton, V. Prakapenka, E. L. Bright, C. Giacobbe, J. Wright, D. Comboni, M. Hanfland, N. Dubrovinskaia, L. Dubrovinsky, M. Han, N. Dubrovinskaia, L. Dubrovinsky, Stabilization of N6 and N8 Anionic Units and 2D Polynitrogen Layers in High-Pressure Scandium Polynitrides, *Nat. Commun.* **15**, 2244 (2024).

[173] B. A. Steele, E. Stavrou, J. C. Crowhurst, J. M. Zaug, V. B. Prakapenka, I. I. Oleynik, High-Pressure Synthesis of a Pentazolate Salt, *Chem. Mater.* **29**, 735–741 (2017).

[174] D. Laniel, F. Trybel, Y. Yin, T. Fedotenko, S. Khandarkhaeva, A. Aslandukov, G. Aprilis, A. I. Abrikosov, T. Bin Masood, C. Giacobbe, E. L. Bright, K. Glazyrin, M. Hanfland, J. Wright, I. Hotz, I. A. Abrikosov, L. Dubrovinsky, N. Dubrovinskaia, Aromatic Hexazine [N6]4− Anion Featured in the Complex Structure of the High-Pressure Potassium Nitrogen Compound K9N56, *Nat. Chem.* **15**, 641–646 (2023).

[175] Y. Wang, M. Bykov, I. Chepkasov, A. Samtsevich, E. Bykova, X. Zhang, S. Jiang, E. Greenberg, S. Chariton, V. B. Prakapenka, A. R. Oganov, A. F. Goncharov, Stabilization of Hexazine Rings in Potassium Polynitride at High Pressure, *Nat. Chem.* **14**, 794–800 (2022).

[176] N. P. Salke, K. Xia, S. Fu, Y. Zhang, E. Greenberg, V. B. Prakapenka, J. Liu, J. Sun, J.-F. Lin, Tungsten Hexanitride with Single-Bonded Armchairlike Hexazine Structure at

High Pressure, *Phys. Rev. Lett.* **126**, 065702 (2021).

[177] Y. Zhang, L. Wu, B. Wan, Y. Zhao, R. Gao, Z. Li, J. Zhang, H. Gou, H. K. Mao, Structural Variety beyond Appearance: High-Pressure Phases of CrB4 in Comparison with FeB4, *Phys. Chem. Chem. Phys.* **18**, 2361–2368 (2016).

[178] E. Bykova, E. Johansson, M. Bykov, S. Chariton, H. Fei, S. V. Ovsyannikov, A. Aslandukova, S. Gabel, H. Holz, B. Merle, B. Alling, I. A. Abrikosov, J. S. Smith, V. B. Prakapenka, T. Katsura, N. Dubrovinskaia, A. F. Goncharov, L. Dubrovinsky, Novel Class of Rhenium Borides Based on Hexagonal Boron Networks Interconnected by Short B2Dumbbells, *Chem. Mater.* **34**, 8138–8152 (2022).

[179] A. P. Drozdov, P. P. Kong, V. S. Minkov, S. P. Besedin, M. A. Kuzovnikov, S. Mozaffari, L. Balicas, F. F. Balakirev, D. E. Graf, V. B. Prakapenka, E. Greenberg, D. A. Knyazev, M. Tkacz, M. I. Eremets, Superconductivity at 250 K in Lanthanum Hydride under High Pressures, *Nature* **569**, 528–531 (2019).

[180] D. Laniel, B. Winkler, E. Bykova, T. Fedotenko, S. Chariton, V. Milman, M. Bykov, V. Prakapenka, L. Dubrovinsky, N. Dubrovinskaia, Novel Sulfur Hydrides Synthesized at Extreme Conditions, *Phys. Rev. B* **102**, 134109 (2020).

[181] V. V. Struzhkin, D. Y. Kim, E. Stavrou, T. Muramatsu, H. K. Mao, C. J. Pickard, R. J. Needs, V. B. Prakapenka, A. F. Goncharov, Synthesis of Sodium Polyhydrides at High Pressures, *Nat. Commun.* **7**, 1–8 (2016).

[182] C. Su, J. Zhang, G. Liu, X. Wang, H. Wang, Y. Ma, Catenation of Carbon in LaC2 Predicted under High Pressure, *Phys. Chem. Chem. Phys.* **18**, 14286–14291 (2016).

[183] T. A. Strobel, O. O. Kurakevych, D. Y. Kim, Y. Le Godec, W. Crichton, J. Guignard, N. Guignot, G. D. Cody, A. R. Oganov, Synthesis of β-Mg2C3: A Monoclinic High-Pressure Polymorph of Magnesium Sesquicarbide, *Inorg. Chem.* **53**, 7020–7027 (2014).

[184] N. N. Greenwood, A. Earnshaw, *Chemistry of the Elements (2nd Edition)* (Butterworth-Heinemann, 1997).

[185] W. H. Zachariasen, Crystal Chemical Studies of the 5f-Series of Elements. I. New Structure Types, *Acta Crystallogr.* **1**, 265–268 (1948).

[186] A. B. Riabov, V. A. Yartys, B. C. Hauback, P. W. Guegan, G. Wiesinger, I. R. Harris, Hydrogenation Behaviour, Neutron Diffraction Studies and Microstructural Characterization of Boron Oxide-Doped Zr-V Alloys, *J. Alloys Compd.* **293**, 93–100 (1999).

[187] P. Chai, J. D. Corbett, Two New Compounds, β-ScTe and Y3Au2, and a Reassessment of Y2Au, *Acta Crystallogr. Sect. C Cryst. Struct. Commun.* **67**, 53–55 (2011).

[188] K. I. Portnoi, V. M. Romashov, S. E. Salibekov, Constitution Diagram of the System Tantalum-Boron, *Sov. Powder Metall. Met. Ceram.* **10**, 925–927 (1971).

[189] R. Archana, V. V. Ramakrishna, V. Suresh, S. Kavita, P. Bhatt, R. Deepika, M. Ramya, S. M. Yusuf, R. Gopalan, Magnetocaloric Effect, Magnetic Interactions and Phase Transition in La1.3Fe11.6-XSi1.4Gax Alloys, *J. Supercond. Nov. Magn.* **35**, 2505–2518 (2022).

[190] H. Haschke, H. Nowotny, F. Benesovsky, Untersuchungen Im System Cer-Silicium-Germanium, *Monatshefte Für Chemie* **97**, 1452–1458 (1966).

[191] K. Remschnig, T. Le Bihan, H. Noël, P. Rogl, Structural Chemistry and Magnetic Behavior of Binary Uranium Silicides, *J. Solid State Chem.* **97**, 391–399 (1992).

[192] A. Koffi, M. Ade, H. Hillebrecht, Single Crystal Studies of Binary Compounds Ta/Ga – A System with Experimental and Crystallographic Peculiarities, *J. Solid State Chem.* **238**, 88–102 (2016).

[193] K. H. J. Buschow, D. B. de Mooij, The Effect of H2 Absorption on the Magnetic Properties of Gd-Pd Intermetallic Compounds, *Phys. Status Solidi* **84**, 207–213 (1984).

[194] A. Ovchinnikov, A.-V. Mudring, Overlooked Binary Compounds Uncovered in the Reinspection of the La–Au System: Synthesis, Crystal Structures, and Electronic Properties of La7Au3, La3Au2, and La3Au4, *Inorg. Chem.* **60**, 12158–12171 (2021).

[195] D. W. J. Cruickshank, R. A. Sparks, Experimental and Theoretical Determinations of Bond Lengths in Naphthalene, Anthracene and Other Hydrocarbons, *Proc. R. Soc. London. Ser. A. Math. Phys. Sci.* **258**, 270–285 (1960).

[196] S. Eibl, A. Fitch, M. Brunelli, A. D. Evans, P. Pattison, M. Plazanet, M. R. Johnson, C. Alba-Simionesco, H. Schober, Tarns-Decahydronaphthalene (Decalin) from Powder Diffraction Data, *Acta Crystallogr. Sect. C Cryst. Struct. Commun.* **C65**, 278–280 (2009).

[197] U. Ruschewitz, Binary and Ternary Carbides of Alkali and Alkaline-Earth Metals, *Coord. Chem. Rev.* **244**, 115–136 (2003).

[198] K. Klöss, D. Hinz-Hübner, U. Ruschewitz, Über Eine Neue Modifikation Des Na2C2, *Zeitschrift Für Anorg. Und Allg. Chemie* **628**, 2701–2704 (2002).

[199] S. Hemmersbach, B. Zibrowius, U. Ruschewitz, Na2C2 Und K2C2: Synthese, Kristallstruktur Und Spektroskopische Eigenschaften, *Z. Anorg. Allg. Chem.* **625**, 1440–1446 (1999).

[200] H. Fjellvág, P. Karen, Crystal Structure of Magnesium Sesquicarbide, *Inorg. Chem.* **31**, 3260–3263 (1992).

[201] P. Karen, A. Kjekshus, Q. Huang, V. L. Karen, The Crystal Structure of Magnesium Dicarbide, *J. Alloys Compd.* **282**, 72–75 (1999).

[202] V. Vohn, W. Kockelmann, U. Ruschewitz, On the Synthesis and Crystal Structure of BaC2, *J. Alloys Compd.* **284**, 132–137 (1999).

[203] V. Vohn, M. Knapp, U. Ruschewitz, Synthesis and Crystal Structure of SrC2, *J. Solid State Chem.* **151**, 111–116 (2000).

[204] M. Atoji, Neutron Diffraction Study of Ce2C3 at Low Temperatures, *J. Chem. Phys.* **46**, 4148–4149 (1967).

[205] M. C. Krupka, A. L. Giorgi, N. H. Krikorian, E. G. Szklaizz, High-Pressure Synthesis of Yttrium-Thorium Sesquicarbide: A New High-Temeperature Superconductor, *J. Less-Common Met.* **19**, 113–119 (1969).

[206] M. Atoji, K. Gschneidner, A. H. Daane, R. E. Rundle, F. H. Spedding, The Structures of Lanthanum Dicarbide and Sesquicarbide by X-Ray and Neutron Diffraction, *J. Am. Chem. Soc.* **80**, 1804–1808 (1958).

[207] O. Reckeweg, A. Baumann, H. A. Mayer, J. Glaser, H. J. Meyer, On the Coexistence of Tetragonal and Monoclinic CaC2: Structural and Spectroscopic Studies on Alkaline Earth Metal Acetylides, MC2 (M = Ca, Sr, Ba), *Zeitschrift Fur Anorg. Und Allg. Chemie* **625**, 1686–1692 (1999).

[208] R. M. Hazen, L. W. Finger, Bulk Modulus-Volume Relationship for Cation-Anion Polyhedra, *J. Geophys. Res.* **84**, 6723–6728 (1979).

[209] B. Wan, Y. Lu, Z. Xiao, Y. Muraba, J. Kim, D. Huang, L. Wu, H. Gou, J. Zhang, F. Gao, H. Mao, H. Hosono, Identifying Quasi-2D and 1D Electrides in Yttrium and Scandium Chlorides via Geometrical Identification, *Npj Comput. Mater.* **4**, 77 (2018).

[210] A. Simon, H. Mattausch, N. Holzer, Monochloride von Lanthanoiden: GdCl Und TbCl, *Angew. Chemie* **88**, 685–686 (1976).

[211] R. E. Araujo, J. D. Corbett, Lanthanum Monochloride and Lanthanum Sesquichloride, *Inorg. Chem.* **20**, 3082–3086 (1981).

[212] C. Shekhar, A. K. Nayak, Y. Sun, M. Schmidt, M. Nicklas, I. Leermakers, U. Zeitler, Y. Skourski, J. Wosnitza, Z. Liu, Y. Chen, W. Schnelle, H. Borrmann, Y. Grin, C. Felser, B. Yan, Extremely Large Magnetoresistance and Ultrahigh Mobility in the Topological Weyl Semimetal Candidate NbP, *Nat. Phys.* **11**, 645–649 (2015).

[213] A. Savin, R. Nesper, S. Wengert, T. Fässler, ELF: The Electron Localization Function, *Angew. Chem., Int. Ed. Engl.* **36**, 1808–1832 (1997).

4. Manuscripts of the thesis

4.1 High-pressure synthesis of dysprosium carbides

Fariia Iasmin Akbar[1,2*], Alena Aslandukova[1], Andrey Aslandukov[1,2], Yuqing Yin[1,3], Florian Trybel[4], Saiana Khandarkhaeva[1], Timofey Fedotenko[5], Dominique Laniel[6], Maxim Bykov[7], Elena Bykova[2], Natalia Dubrovinskaia[1,4], Leonid Dubrovinsky[2]

[1]Material Physics and Technology at Extreme Conditions, Laboratory of Crystallography, University of Bayreuth, 95440 Bayreuth, Germany
[2]Bayerisches Geoinstitut, University of Bayreuth, 95440 Bayreuth, Germany
[3]State Key Laboratory of Crystal Materials, Shandong University, Jinan 250100, China
[4]Department of Physics, Chemistry and Biology (IFM), Linköping University 58183 Linköping (Sweden)
[5]Deutsches Elektronen-Synchrotron DESY, Notkestrasse 85, 22607 Hamburg, Germany
[6]Centre for Science at Extreme Conditions and School of Physics and Astronomy, University of Edinburgh, EH9 3FD Edinburgh, United Kingdom
[7]Institute of Inorganic Chemistry, University of Cologne, Greinstrasse 6, 50939 Cologne, Germany

*** Corresponding author:** Fariia Iasmin Akbar Fariia.Akbar@uni-bayreuth.de

Keywords: high-pressure[1], diamond anvil cell[2], rare-earth carbides[3], carbides[4], rare-earth elements[5], lanthanides carbides[6], dysprosium carbide[7].

Front. Chem. **11**, 1–9 (2023), DOI: 10.3389/fchem.2023.1210081

4.1.1 Abstract

Chemical reactions between dysprosium and carbon were studied in laser-heated diamond anvil cells at pressures of 19, 55, and 58 GPa and temperatures of ~2500 K. *In situ* single-crystal synchrotron X-ray diffraction analysis of the reaction products revealed the formation of novel dysprosium carbides, Dy_4C_3 and Dy_3C_2, and dysprosium sesquicarbide Dy_2C_3 previously known only at ambient conditions. The structure of Dy_4C_3 was found to be closely related to that of dysprosium sesquicarbide Dy_2C_3 with the Pu_2C_3-type structure. *Ab initio* calculations reproduce well crystal structures of all synthesized phases and predict their

compressional behavior in agreement with our experimental data. Our work gives evidence that high-pressure synthesis conditions enrich the chemistry of rare earth metal carbides.

4.1.2 Introduction

Carbides are important compounds in science and technology due to their useful chemical, mechanical, electrical, magnetic, and optical properties (Sakai et al., 1981a; Davaasuren et al., 2010; Lengauer, 2012). The structure, bonding, and phase transitions of lanthanide carbides are of interest due to their potential applications in mechanical and electrical devices. Structural variations at high-pressure conditions can lead to a sharp change in the properties and unusual crystal chemistry of carbides.

Metal carbides containing $[C_2]^{2-}$ ion are known for many elements at ambient conditions (for instance, Ca, Sr, Ba, Y, La-Nd, Sm, Gd-Dy, Er-Lu) (Yupko et al., 1974; Sakai et al., 1981b). Carbon dimers are particularly interesting due to the relationship between their lengths and the superconducting transition temperatures T_c (Kobayashi et al., 2019) of the compounds which feature these dimers. Since the C-C bond is quite short, the phonon frequency for the C-C stretching phonon modes is expected to be very high. Thus, for example, relatively high T_c values in La_2C_3 and Y_2C_3 (up to 13.4 K (Kim et al., 2007) and 18 K (Amano et al., 2004; Nakane et al., 2004), respectively) are ascribed to electron-phonon coupling between high-frequency phonons and C-C antibonding states at the Fermi level.

The lanthanide carbides family shows a large variety of possible phases with different stoichiometry at ambient pressure: RC_6 (R = Eu), RC_2 (R = Y, La-Lu), R_4C_7 (R = Y, Dy-Tm, Lu), R_2C_3 (La-Nd, Sm-Ho), R_3C_4 (Sc, Y, Tb-Lu), R_4C_5 (Y, Gd-Ho), R_4C_3 (R = Sc), RC_x (x ~ 0.33-0.54, R = Sc, Y, Sm-Lu) (Babizhetskyy et al., 2017). Still, the number of known binary carbon compounds is significantly smaller than the number of known binary oxygen compounds (1290 *vs* 4331) according to the ICSD database (Version 4.9.0 (build 20221006-1701) - Data Release 2022.2). Considering that vast amount of the data corresponds to ambient conditions, the chemistry of carbides under high pressure has been poorly studied in principle. A recent discovery (Aslandukova et al., 2021) of the new γ-Y_4C_5 phase with non-linear $[C_3]$ groups synthesized above 40 GPa illustrates the importance of investigations of carbides at high pressures and motivates further studies of lanthanides carbides at non-ambient conditions. In this work, we report the high-pressure synthesis in laser-heated diamond anvil cells (DACs) of two novel carbides Dy_4C_3 and Dy_3C_2, and the formation of dysprosium sesquicarbide Dy_2C_3, already known at ambient conditions.

4.1.3 Experimental

The summary of all experiments is presented in **Supplementary Table S1** (see Supplementary Information). In our experiments we used BX90-type diamond anvil cells with a large X-ray aperture (Kantor et al., 2012). As anvils we employed Boehler-Almax-type diamonds with culets diameter of 250 μm. Rhenium gaskets with an initial thickness of 200 μm were indented to ~28 μm and a hole of ~100 μm in diameter was drilled in the center of the indentation. Dysprosium flakes (99.9% purity, Merc Inc.) were loaded between one of the diamond anvils and a layer of dry sodium chloride (99.999% purity, ChemPUR) which played the role of a thermal insulator and a pressure transmitting medium; diamond anvils were used as a carbon source. Samples were compressed to the desired pressures and laser heated up to 2500 K. Laser heating of the samples was carried out using our *in house* double-sided YAG laser (1064 nm wavelength) heating setup (Fedotenko et al., 2019). Thermal emission spectra from the heated area were collected using an IsoPlane SCT 320 spectrometer with a 1024×2560 PI-MAX 4 camera. Pressure was determined using the equation of states (EoS) of NaCl (Dorogokupets and Dewaele, 2007; Sakai et al., 2011).

The reaction products were analyzed by single-crystal X-ray diffraction (SCXRD) at several synchrotron beamlines: P02.2 of DESY, Hamburg, Germany (λ = 0.2894 Å, beam size ~ 2 × 2 μm^2) (Liermann et al., 2015); ID11 (λ = 0.2844 Å, beam size ~ 0.75 × 0.75 μm^2) and ID15B (λ = 0.4100 Å, beam size ~ 1.5 × 2 μm^2) of ESRF, Grenoble, France. During single-crystal data collection, the cell was rotated from –38° to +38° around the vertical ω axis with narrow 0.5° steps. XRD maps were created using the XDI software (Hrubiak et al., 2019) and helped to visualize the special distribution of various phases within the pressure chamber as well as to locate the areas where the step-scans should be performed. Powder XRD (PXRD) images were collected upon continuous rotation of the sample in a range of ±20° around the vertical ω axis at DESY, and ±1° around the vertical ω axis at ESRF. The CrysAlis^{Pro} software package (CrysAlisPRO) was used for the analysis of the single-crystal XRD data (peak hunting, indexing, data integration, frame scaling, and absorption correction). The DAFi program (Aslandukov et al., 2022) was used for the search of reflections' groups belonging to individual single-crystal domains. Using the OLEX2 software package (Dolomanov et al., 2009), the structures were solved with the ShelXT structure solution program (Sheldrick, 2015b) using intrinsic phasing and refined with the ShelXL (Sheldrick, 2015a) refinement package using least-squares minimization. Crystal structure visualization was made with the VESTA software (Momma and Izumi, 2011).

The properties of the Dy_4C_3, Dy_2C_3 and Dy_3C_2 were determined through the first-principles calculations using the framework of density functional theory (DFT) as implemented in the VASP (Vienna *ab initio* simulation package) code (Kresse and Furthmüller, 1996). To expand the electronic wave function in plane waves we used the Projector-Augmented-Wave (PAW) method (Blöchl, 1994). The Generalized Gradient Approximation (GGA) functional was used for calculating the exchange-correlation energies, as proposed by Perdew–Burke–Ernzerhof (PBE) (Perdew et al., 1996). The PAW potentials with the following valence configurations of 5*s*5*p*6*s*5*d* for Dy and 2*s*2*p* for C were used to describe the interaction between the core and the valence electrons in frozen *f*-electrons approximation for Dy (Kresse and Furthmüller, 1996). Convergence tests with a threshold of 2 meV per atom in energy led to an energy cutoff for the plane wave expansion of 600 eV for all phases and a Monkhorst-Pack (Monkhorst and Pack, 1976) *k*-point grid of $4 \times 4 \times 4$ for Dy_4C_3 and Dy_2C_3, and *k*-point grid of $5 \times 5 \times 9$ for Dy_3C_2. Computations were performed for eight volumes that cover the pressure range of 0-100 GPa. Harmonic lattice dynamics calculations were performed with the PHONOPY software (Togo and Tanaka, 2015a) using the finite displacement method for $2 \times 2 \times 2$ (Dy_4C_3 and Dy_2C_3) and $2 \times 2 \times 3$ (Dy_3C_2) supercells with respectively adjusted k-points. The tetrahedron method was used for Brillouin zone integrations, employing a mesh of $8 \times 8 \times 8$ k-points for Dy_4C_3 and Dy_2C_3, and $10 \times 10 \times 18$ k-points for Dy_3C_2 (Rath and Freeman, 1975; Friedrich, 2019). The integrated values of the crystal orbital bond index (ICOBI) (Müller et al., 2021) and Mulliken charges were calculated using LOBSTER v4.1.0 software (Maintz et al., 2016). The charge distribution in the ionic approximation based on a generalization of Pauling's concept of bond strength (Pauling, 1929) was made using CHARDI2015 (Nespolo and Guillot, 2016). In our calculations, temperature, configurational entropy, and the entropy contribution due to lattice vibrations were neglected.

4.1.4 Results

4.1.4.1 Structure of a novel dysprosium carbide Dy_4C_3

The dysprosium carbide Dy_4C_3 was synthesized at 19, 55, and 58 GPa (**Supplementary Table S1**). This compound was hitherto unknown. It has the anti-Th_3P_4-type structure (space group *I*-43*d*) shown in **Figures 1A-C**, which has been described for scandium carbide, Sc_4C_3, but not observed in lanthanide carbides or Y carbides (Adachi et al., 1991; Babizhetskyy et al., 2017). At 19 GPa its unit cell parameter is equal to a = 7.4774(8) Å.

In the structure of Dy_4C_3 (**Figures 1A-C**, **Table 1**), dysprosium and carbon atoms occupy the 16*c* and 12*a* Wyckoff sites, respectively (**Supplementary Tables S2-S4**). The

coordination polyhedron of Dy cations is an irregular octahedron formed by the six nearest carbon atoms at distances of either 2.3819(5) Å or 2.8240(5) Å at 19 GPa (**Figure 1B**). Carbon atoms are surrounded by eight Dy atoms forming strongly distorted cubes (octaverticons) (**Figure 1C**).

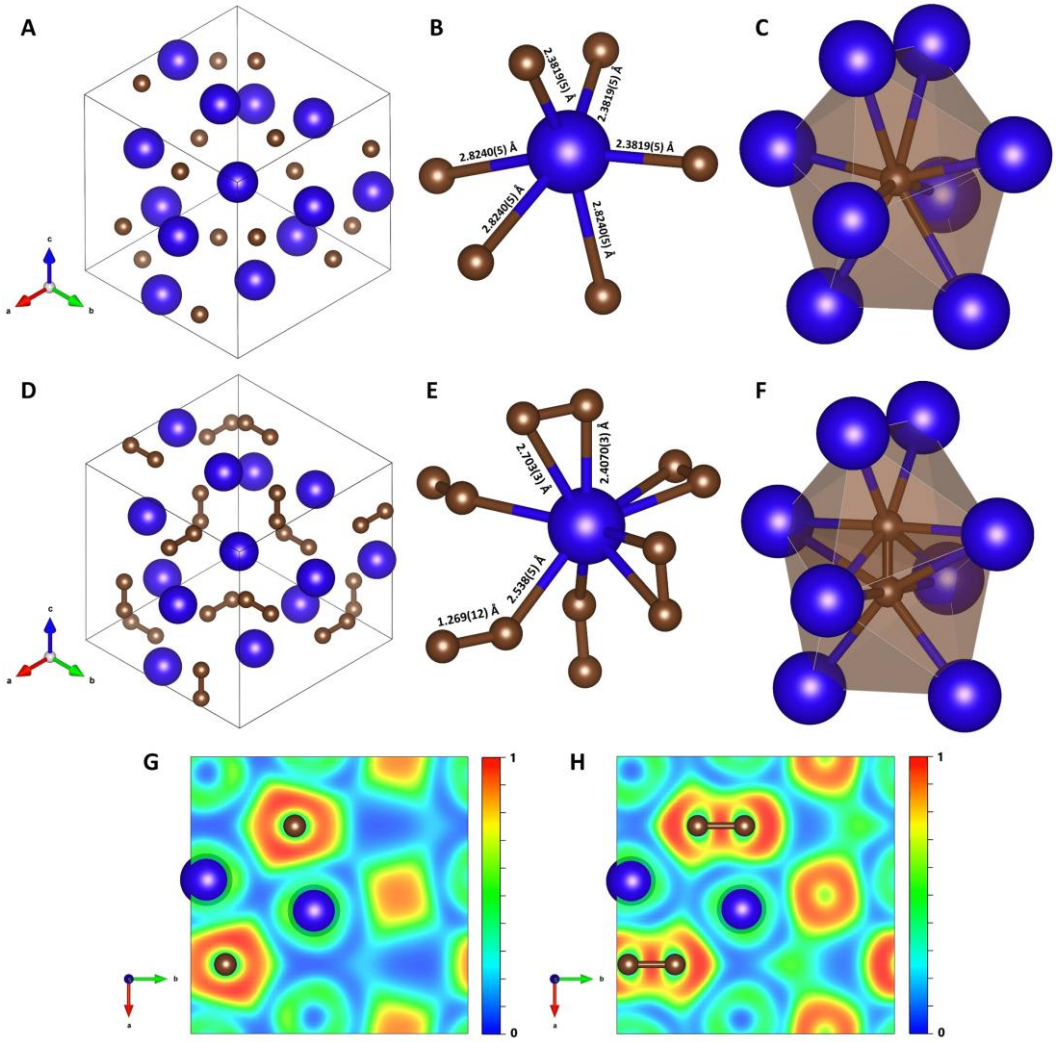

Figure 1. Crystal structures and corresponding 2D electron localization function (ELF) maps of Dy_4C_3 and Dy_2C_3 at 19 GPa. The blue and brown spheres represent dysprosium and carbon, respectively. Dy_4C_3: **(A)** Unit cell in projection along the [111] direction; **(B)** coordination polyhedron of Dy; **(C)** coordination environment of a carbon atom. Dy_2C_3: **(D)** Unit cell in projection along the [111] direction; **(E)** coordination polyhedron of Dy; **(F)** carbon dumbbell in a cage of eight Dy atoms. **(G)** and **(H)** are cross sections of the computed ELF shown in the (001) plane in Dy_4C_3 and Dy_2C_3, respectively.

4.1.4.2 Structure of dysprosium sesquicarbide Dy_2C_3

The cubic Dy_2C_3 sesquicarbide was synthesized in this work at 19 GPa (**Supplementary Table S1**). It has the Pu_2C_3-type structure (space group *I*-43*d*) with the unit cell parameter a = 7.9208(5) Å at 19 GPa (**Figures 1D-F**, **Table 1**). The Dy_2C_3 sesquicarbide was earlier reported at ambient conditions with the lattice parameter equal to a = 8.198(2) Å at

1 bar (Spedding et al., 1958). The dysprosium and carbon atoms occupy the 16*c* and 24*d* Wyckoff sites, respectively (**Supplementary Table S5**). The structure of Dy_2C_3 contains [C_2] dumbbells with a length of ~1.27 Å at 19 GPa.

The structures of Dy_2C_3 and Dy_4C_3 (described above) are closely related (see **Figure 1**): they have the same space group (*I*-43*d*), and the former can be easily derived from the latter, as the positions of the centers of [C_2] dumbbells in Dy_2C_3 coincide with the positions of single carbon atoms in Dy_4C_3, whereas the coordinates of Dy atoms are the same in both structures. Thus, the coordination number of Dy atoms in Dy_2C_3 increases to nine (**Figure 1E**), whereas the coordination environment of [C_2] dumbbells (**Figure 1F**) is similar to that of a single carbon atom in Dy_4C_3 (**Figure 1C**).

Table 1. Selected experimental details of crystal structures of the carbides reported in this work.

Chemical formula	Dy_4C_3	Dy_2C_3	Dy_3C_2
Pressure (GPa)	19(1)	19(1)	55(1)
Space group	*I-43d*	*I-43d*	*P4/mbm*
Space group number	#220	#220	#127
Structure type	anti-Th_3P_4	Pu_2C_3	U_3Si_2
a (Å)	7.4774(8)	7.9208(5)	5.9896(13)
c (Å)			3.3880(12)
V (Å^3)	418.07(13)	496.94(9)	121.55(7)
Z	4	8	2
R_{int}	5.42%	2.85%	2.42%
R_1	3.76%	1.50%	5.92%
No. of reflections	274	281	197
No. of parameters	7	11	11

4.1.4.3 Structure of a novel dysprosium carbide Dy_3C_2

One more dysprosium carbide, Dy_3C_2, with a tetragonal unit cell (space group *P4/mbm*), was discovered at 55 GPa (**Supplementary Table S1**). At this pressure it has the

following unit cell parameters: a = 5.9896(13) Å, c = 3.3880(12) Å (**Figure 2**, **Table 1**). Rare-earth metal carbides of such a stoichiometry have not been previously observed (Babizhetskyy et al., 2017), but the structure of the new Dy_3C_2 was found to be of the U_3Si_2-type, which is common for silicides (Zachariasen, 1948), borides (Riabov et al., 1999), and intermetallides (Chai and Corbett, 2011). Such structure was also theoretically predicted for a high-pressure calcium carbide Ca_3C_2 (Li et al., 2015).

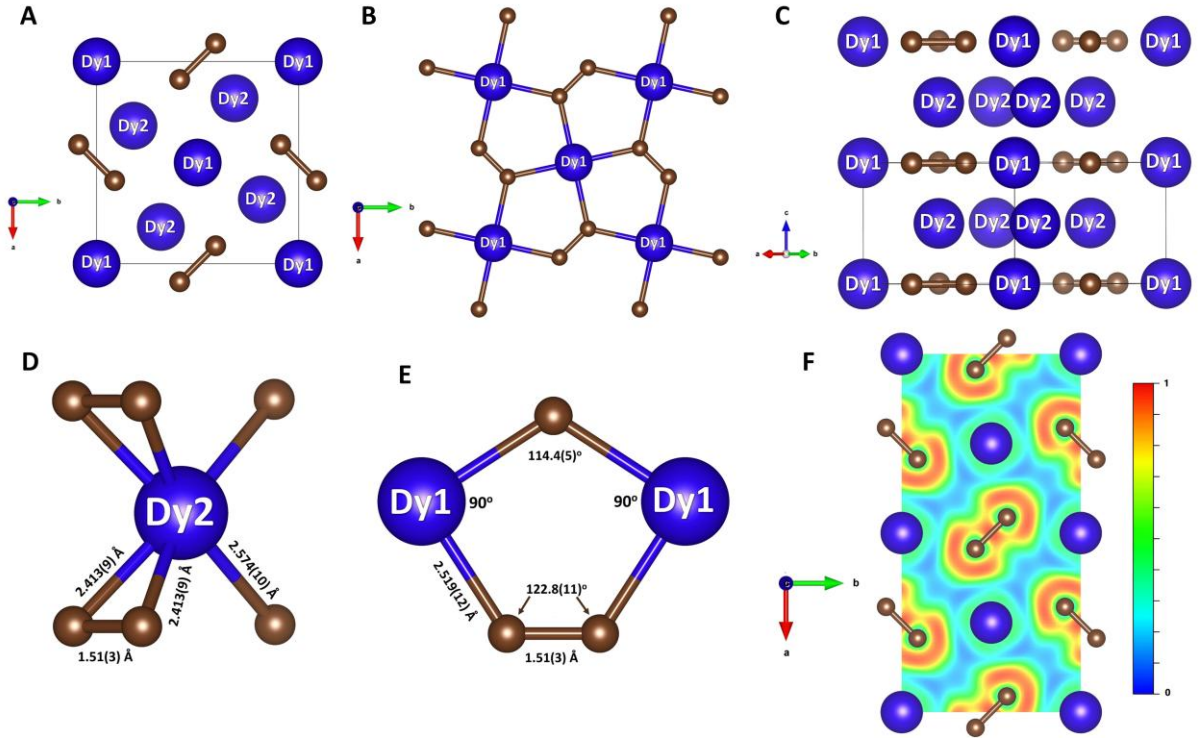

Figure 2. Crystal structure of Dy_3C_2 at 55 GPa and a cross section of the computed ELF. Blue and brown spheres represent dysprosium and carbon, respectively. **(A)** The structure viewed along the c direction; **(B)** the Dy1-C plane with the highlighted Cairo pentagonal tiling formed by Dy1 and C atoms; **(C)** the projection of the structure along the (110) direction highlighting the Dy1-C and Dy2 layers stacking in the c direction; **(D)** coordination of Dy2 atoms by carbon atoms; **(E)** interatomic distances in the Dy1-C plane; **(F)** the 2D ELF shown in the Dy1-C plane.

In the structure of Dy_3C_2 (**Figure 2**, **Table 1**) carbon atoms occupying a single 4*g* Wyckoff position and form $[C_2]$ dumbbells. Two dysprosium atoms are crystallographically distinct, occupying the Wyckoff positions 2*a* (Dy1) and 4*h* (Dy2). **Figure 2A** shows the structure of Dy_3C_2, as viewed along the *c* direction. Dy1 atoms lie in the same *ab* plane as the $[C_2]$ dumbbells, forming together the Cairo pentagonal tiling comprised of $(Dy1)_2C_3$ pentagons (**Figure 2B**). Such a structural motif is known in nickel diazenide NiN_2, whose structure possesses atomic-thick layers comprised of Ni_2N_3 pentagons (Bykov et al., 2021), and in other compounds (Shao et al., 2018; Deng et al., 2020; Duan et al., 2022). Dy2 atoms are located in a parallel plane, separated from the described one by ½ *c* (**Figure 2C**). The Dy2-C inter-layer

distances are of 2.413(9) Å or 2.574(10) Å (**Figure 2D**). As seen in **Figure 2B**, the Dy1 atoms are four-fold coordinated by C atoms with the Dy1-C distance equal to 2.519(12) Å at 55 GPa. The length of the [C_2] dumbbell is equal to 1.51(3) Å (**Figure 2E**).

4.1.5 Discussion

4.1.5.1 Compressional behavior of Dy carbides

Dysprosium carbide Dy_4C_3 was synthesized at three different pressures (19, 55, and 58 GPa) that enabled us to analyse its structural response to compression. As expected, the shorter Dy-C contacts are less flexible than the longer ones: those being 2.3819(5) Å and 2.8240(5) Å at 19 GPa (**Figure 1B**) contract by ~3.6% and ~9.7%, respectively, upon compression to 58 GPa. The results of our DFT calculations agree well with the experimental data, suggesting ~3.3% and ~8.5%, correspondingly (**Supplementary Tables S2-S4**). Due to the anisotropy of compression, DyC_6 polyhedra become less distorted with the distortion indices (D) equal to 0.085 and 0.053 at 19 and 58 GPa, respectively. A distortion index characterizes the average deviation of interatomic distances and angles from their mean values (Baur, 1974). *Ab initio* calculations reproduced well the experimental data with D = 0.084 at 19 GPa *vs* D = 0.057 at 58 GPa.

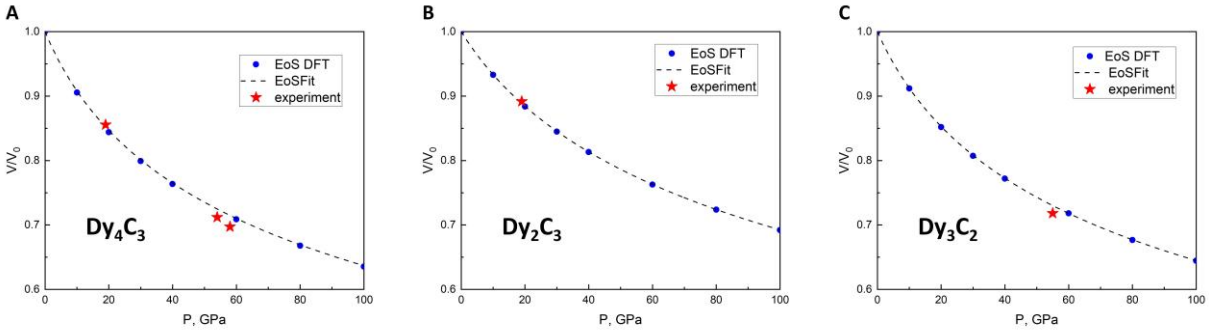

Figure 3. Pressure dependence of the relative volume for three Dy carbides. **(A)** Dy_4C_3, **(B)** Dy_2C_3 and **(C)** Dy_3C_2. The density functional theory (DFT)-calculated volumes for given pressures are shown by blue dots and dashed lines. Red stars indicate experimental data points.

In order to obtain the pressure dependence of the volume for the three dysprosium carbides and to determine the parameters of their equations of states (EOSes), we would need to measure volumes on decompression. However, as we performed our experiments in a solid pressure transmitting medium (NaCl), such data could not be reliable because of stresses. Due to that, we instead performed *ab initio* density functional theory (DFT) calculations in the pressure range up to 100 GPa. Their results are shown in **Figure 3**, and the parameters of the

3rd order Birch-Murnaghan (BM3) EOS, based on DFT calculations for Dy_2C_3, Dy_3C_2, and Dy_4C_3, are summarised in **Table 2**.

Table 2. Parameters of Birch-Murnaghan equation of state of studied dysprosium carbides obtained from ab initio calculations.

Compound	V_0 (Å^3)	K_0 (GPa)	K´
Dy_4C_3	488.7(7)	84.1(11)	4.25(3)
Dy_2C_3	557.28(19)	125.8(5)	4.169(14)
Dy_3C_2	169.25(18)	89.9(9)	4.20(3)

4.1.5.2 Charge analysis, bonding, and electronic properties

Dysprosium sesquicarbide Dy_2C_3 contains $[C_2]$ dumbbells with a length of ~1.27 Å at 19 GPa, which is slightly shorter than the length of the double bond in ethylene and sesquicarbides Y_2C_3 and La_2C_3 at ambient pressure (Gready, 1984; Craig et al., 2006; Kim et al., 2007; Kobayashi et al., 2019). This suggests a formal charge of 4- for the $[C_2]$ dumbbell, so that the formula of Dy_2C_3 can be written as $Dy^{3+}{}_4[C_2]^{4-}{}_3$, and the compound can be called dysprosium (III) ethenide. The $[C_2]$ units in Dy_3C_2 have a length of ~1.51 Å at 55 GPa, which is just a bit shorter than the C-C bond length in ethane (Gready, 1984). The compound may be described as $Dy^{2+}{}_3[C_2]^{6-}$ and called dysprosium (II) ethanide. The Dy_4C_3 consists of single carbon atoms. With the formula $Dy^{3+}{}_4C^{4-}{}_3$ it is dysprosium (III) methanide.

In order to get a deeper insight into the crystal chemistry of the novel compounds, we performed a detailed charge and bond order analysis. Mulliken charge analysis (Müller et al., 2021) for the dysprosium atoms in carbides synthesized in this work yields the values of 1.62 in Dy_4C_3, 1.72 in Dy_2C_3, and 1.01 for Dy1 and 1.12 for Dy2 in Dy_3C_2 (**Supplementary Table S7**). The values for Dy_4C_3 and Dy_2C_3 are in agreement with Mulliken charges known for other dysprosium-containing compounds (Gupta et al., 2016; Ahuja et al., 2017). Our calculations of Mulliken charges for trivalent Dy carbides known at ambient conditions (DyC_2 and Dy_4C_5; (Spedding et al., 1958; Adachi et al., 1976; Czekalla et al., 1997) are in a good agreement with those obtained for Dy_4C_3 and Dy_2C_3 (**Supplementary Table S8**). For Dy_3C_2, Mulliken charges of dysprosium are obviously lower, thus supporting our assessment of the cation in this compound as Dy^{2+} (see above). Notable is that at the same pressure of 55 GPa, the Dy-C

distance in Dy_3C_2 is larger than in Dy_4C_3 (**Supplementary Tables S3, S6**), which also speaks in favor of a lower charge of dysprosium in the novel ethanide.

Assuming all Dy atoms to have integer charges, one can analyse carbon charges and the C-C chemical bonds in carbon dimers in different dysprosium carbides. The integrated crystal orbital bond indexes (ICOBI) obtained for DyC_2 (Adachi et al., 1976), Dy_4C_5 (Czekalla et al., 1997), and Dy_2C_3 are close to 2 (**Supplementary Table S8**). The small deviations can be explained by shared-electron interactions due to the metallicity of the studied solids. This suggests a C=C double bond in these compounds, which is in a good agreement with its C-C distance (**Supplementary Table S9**). For Dy_3C_2 the ICOBI index for the C-C bond in the $[C_2]$ dimer differs significantly from those in other carbides (1.116) and suggests the bond order of 1, which is also consistent with the C-C bond length. Additionally, the assigned bond orders are well reflected in individual charges of C atoms and their anions, as obtained in both Mulliken and CHARDI approximations (**Supplementary Table S8**) (Nespolo and Guillot, 2016; Müller et al., 2021).

The character of the chemical bonding can be judged from calculated electron localization functions (ELF) (Savin et al., 1991). Relevant cross sections of ELFs at 19 GPa for Dy_4C_3 and Dy_3C_2 are shown in **Figures 1G, H**. They reveal ionic bonding between Dy and C in both compounds and strong covalent bonding in the $[C_2]$ dimers of Dy_2C_3. The 2D ELF for Dy_3C_2 at 55 GPa is shown in **Figure 2F**. It gives evidence of strong covalent bonding between carbon atoms in dimers and ionic bonds between Dy and C atoms.

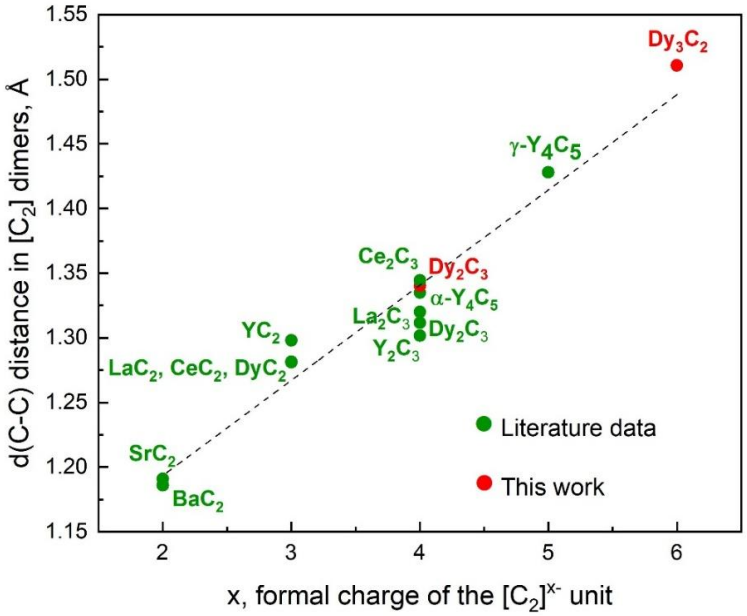

Figure 4. A correlation between the lengths of $[C_2]$ dimers, d(C-C), and their formal charges x in a number of binary metal-carbon compounds containing $[C_2]^{x-}$ species. All data corresponds to ambient pressure. Literature data are from experiments

[11,36,60,61,50,51,54–59], except for γ-Y_4C_5 [11] and for Dy_2C_3 and Dy_3C_2 (this work, DFT-computed structures fully relaxed at 1 bar).

For 19 simple binary metal-nitrogen compounds containing $[N_2]^{x-}$ species, a linear correlation was found between the length of the N–N dimers and their formal charges (Laniel et al., 2022). We used the literature data on 12 metal carbides studied at ambient conditions (Atoji et al., 1958; Spedding et al., 1958; Atoji, 1967b, 1967a; Krupka et al., 1969; Adachi et al., 1976; Czekalla et al., 1997; Vohn et al., 2000, 1999; Yosida, 2002; Babizhetskyy et al., 2014; Aslandukova et al., 2021) and our own results to analyse the relationship between the length of carbon dimers and their formal charges. For the novel Dy_3C_2, the C-C length at ambient pressure was obtained by DFT calculations, as well as for γ-Y_4C_5 in (Aslandukova et al., 2021); for Dy_2C_3 we included both the experimental value (Spedding et al., 1958) and the one DFT-calculated in this work, as they are a bit different. It appeared that the linear correlation holds also for carbides featuring $[C_2]^{x-}$ dimers at ambient conditions (**Figure 4**).

4.1.5.3 Vibrational properties and stability

According to *ab initio* simulations of the phonon densities of state (pDOS) (Togo and Tanaka, 2015b) in the harmonic approximation at 0 K, Dy_4C_3 and Dy_2C_3 compounds are dynamically stable at their synthesis pressure of 19 GPa (**Figures 5A, B**), whereas Dy_3C_2 is unstable both at its synthesis pressure of 55 GPa and at 1 bar (**Figures 5C, F**).

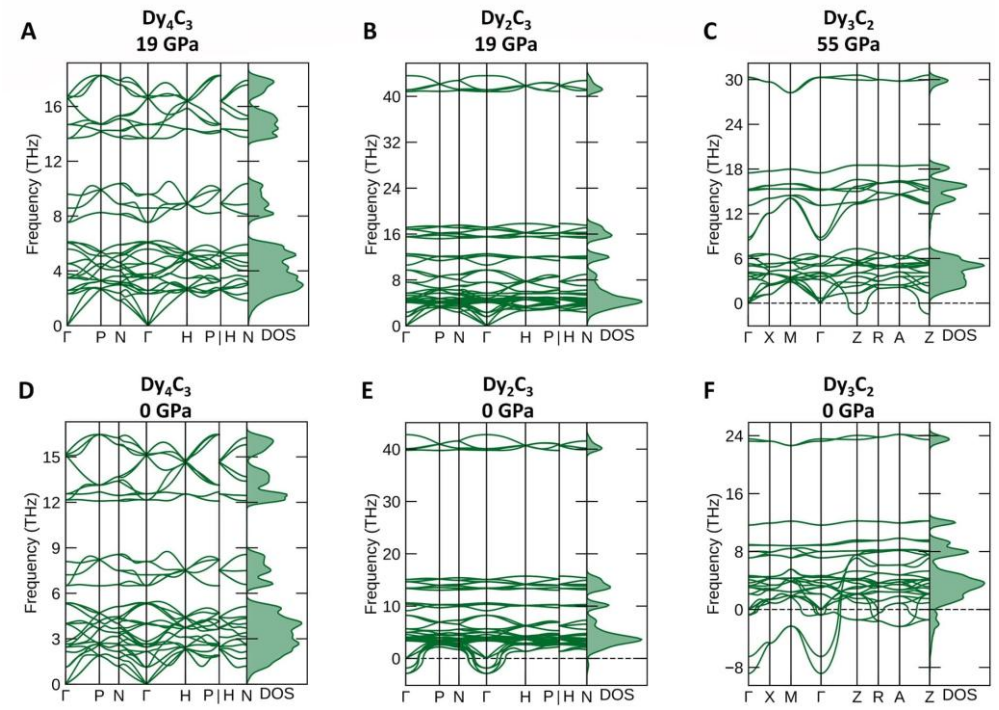

Figure 5. Phonon dispersion curves along high-symmetry directions in the Brillouin zone and phonon density of states. **(A)** Dy_4C_3, **(B)** Dy_2C_3 calculated at 19 GPa and **(C)** Dy_3C_2 at 55 GPa, **(D)** Dy_4C_3, **(E)** Dy_2C_3 and **(F)** Dy_3C_2 calculated at ambient pressure.

According to our calculations at 1 bar, Dy_2C_3 is not dynamically stable (**Figure 5E**), although it is known to exist at ambient conditions (Spedding et al., 1958). These inconsistency indicates some limitations of the theoretical analysis method we apply. Therefore, the predicted dynamical stability of Dy_4C_3 (**Figure 5D**) at ambient pressure should be considered with caution.

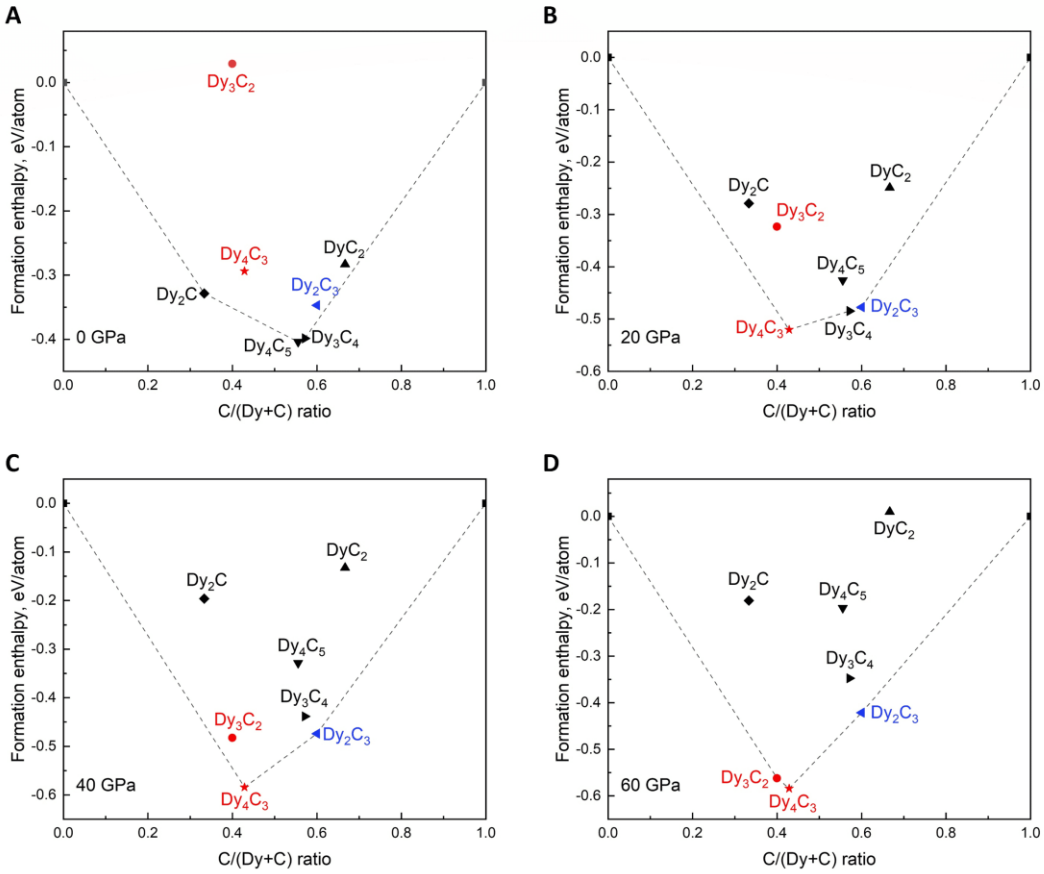

Figure 6. Calculated convex hull diagrams constructed for the Dy-C binary system for known dysprosium carbides. **(A)** 0 GPa, **(B)** 20 GPa, **(C)** 40 GPa and **(D)** 60 GPa. Dashed lines indicate the convex hulls; carbides previously reported are marked by black symbols; carbides synthesized in this work are given in red and blue, indicating previously unknown and known, respectively.

To explore the thermodynamic stability of Dy_4C_3, Dy_2C_3 and Dy_3C_2 in comparison to other Dy carbides, convex hull diagrams were constructed considering known carbides (Dy_2C (Atoji, 1981), Dy_4C_5 (Czekalla et al., 1997; Babizhetskyy et al., 2019; The Materials Project, 2020b), Dy_3C_4 (Hüfken and Jeitschko, 1998; The Materials Project, 2020a), DyC_2 (Adachi et al., 1976)) at various pressures. Structure models for Dy_4C_5 (α-Y_4C_5 type) (The Materials Project, 2020b) and Dy_3C_4 (Sc_3C_4 type) (The Materials Project, 2020a) were acquired from Materials Project database, while those for Dy_2C (Atoji, 1981) and DyC_2 (Adachi et al., 1976) – from CIFs deposited in the ICSD database. The formation enthalpies were computed relative

to the DFT total energies of the end-member elements Dy and C according to the equation: $\Delta H_f = (H_{DyCx} - H_{Dy} - x \cdot H_C)/(1+x)$. The results are shown in **Figure 6**. As seen, pressure has a very significant effect on the chemistry of the Dy-C system. Some phases (e.g., Dy_2C and Dy_4C_5), which are stable at ambient pressure, become unstable already at 20 GPa. According to the convex hull diagram computed at 60 GPa, only those phases, which we observed in this work (Dy_4C_3, Dy_2C_3 and Dy_3C_2), are expected to be thermodynamically stable at such a high pressure.

4.1.6 Conclusions

The chemical reactions of dysprosium and carbon in diamond anvil cells at pressures of 19, 55, and 58 GPa and temperatures of ~2500 K led to the synthesis of two novel dysprosium carbides, Dy_4C_3 at 19 GPa and Dy_3C_2 at 55 GPa, and one compound previously known at ambient condition, Dy_2C_3 at 19 GPa. The carbon atoms in the Dy_3C_2 and Dy_2C_3 form $[C_2]$ dumbbells, while there are single carbon atoms in Dy_4C_3. The crystal structure of Dy_4C_3 is of an anti-Th_3P_4 type. The structure of Dy_2C_3 can be derived from that of Dy_4C_3 if individual carbon atoms are replaced by dumbbells $[C_2]$. Based on our new data, as well as literature data, we found a linear correlation between the formal charges of $[C_2]^{x-}$ groups and C–C interatomic distances. Theoretical calculations support our observations and also suggest that pressure drastically changes the chemistry of the Dy-C system.

4.1.7 Data availability statement

The datasets presented in this study can be found in online repositories. The names of the repository/repositories and accession number(s) can be found below: https://www.ccdc.cam.ac.uk/structures/-, 2248722, 2248721, 2248720, 2248679, and 2248647.

4.1.8 Acknowledgments

The authors acknowledge the Deutsches Elektronen- Synchrotron (DESY, PETRA III) for provision of beam- time at the P02.2, the European Synchrotron Radiation Facility (ESRF) for the provision of beamtimes at the ID15b and ID11 beamlines. For the purpose of open access, the authors have applied a Creative Commons Attribution (CC BY) licence to any Author Accepted Manuscript version arising from this submission. FT acknowledges support from the Knut and Alice Wallenberg Foundation (Wallenberg Scholar grant no. KAW-2018.0194). Computations were enabled by resources provided by the University of Bayreuth and the Swedish National Infrastructure for Computing (SNIC) using LUMI at the IT Center

for Science (CSC), Finland (SNIC 2022/21-10). MB acknowledges the support of Deutsche Forschungsgemeinschaft (DFG Emmy-Noether project BY112/2-1).

4.1.9 References

Adachi, G.-Y., Imanaka, N., and Fuzhong, Z. (1991). “Rare earth carbides,” in *Handbook on the Physics and Chemistry of Rare Earths*, 61–189. doi: 10.1016/S0168-1273(05)80005-4.

Adachi, G. Y., Shibata, Y., Ueno, K., and Shiokawa, J. (1976). Heats of the tetragonal-cubic transformation in rare earth dicarbides and mixed rare earth dicarbide solid solutions. *J. Inorg. Nucl. Chem.* 38, 1023–1026. doi: 10.1016/0022-1902(76)80021-8.

Ahuja, G., Science, F., and Raj, U. (2017). Study of Electronic Properties of Dy2O3 using First Principles Calculations. *Int. J. Pure Appl. Phys.* 13, 123–126.

Amano, G., Akutagawa, S., Muranaka, T., Zenitani, Y., and Akimitsu, J. (2004). Superconductivity at 18 K in yttrium sesquicarbide system, Y2C3. *J. Phys. Soc. Japan* 73, 530–532. doi: 10.1143/JPSJ.73.530.

Aslandukov, A., Aslandukov, M., Dubrovinskaia, N., and Dubrovinsky, L. (2022). Domain Auto Finder (DAFi) program: the analysis of single-crystal X-ray diffraction data from polycrystalline samples. *J. Appl. Crystallogr.* 55, 1383–1391. doi: 10.1107/s1600576722008081.

Aslandukova, A., Aslandukov, A., Yuan, L., Laniel, D., Khandarkhaeva, S., Fedotenko, T., et al. (2021). Novel High-Pressure Yttrium Carbide Containing [C2] and Nonlinear [C3] Units with Unusually Large Formal Charges. *Phys. Rev. Lett.* 127, 135501. doi: 10.1103/PhysRevLett.127.135501.

Atoji, M. (1967a). Magnetic and crystal structures of CeC2, PrC2, NdC2, TbC2, and HoC2 at low temperatures. *J. Chem. Phys.* 46, 1891–1901. doi: 10.1063/1.1840950.

Atoji, M. (1967b). Neutron diffraction study of Ce2C3 at low temperatures. *J. Chem. Phys.* 46, 4148–4149. doi: 10.1063/1.1840499.

Atoji, M. (1981). Neutron-diffraction studies of Tb2C and Dy2C in the temperature range 4-296 K. *J. Chem. Phys.* 75, 1434–1441. doi: 10.1063/1.442150.

Atoji, M., Gschneidner, K., Daane, A. H., Rundle, R. E., and Spedding, F. H. (1958). The Structures of Lanthanum Dicarbide and Sesquicarbide by X-Ray and Neutron Diffraction. *J. Am. Chem. Soc.* 80, 1804–1808. doi: 10.1021/ja01541a008.

Babizhetskyy, V., Jepsen, O., Kremer, R. K., Simon, A., Ouladdiaf, B., and Stolovits, A. (2014). Structure and bonding of superconducting LaC2. *J. Phys. Condens. Matter* 26, 025701. doi: 10.1088/0953-8984/26/2/025701.

Babizhetskyy, V., Kotur, B., and Levytskyy, V. (2019). Phase Equilibria and Crystal Structure of the Ternary Compounds in Dy–B–C System at 1270 K. *Proc. Shevchenko Sci. Soc. Chem. Sci.* LVI, 45–55. doi: 10.37827/ntsh.chem.2019.56.045.

Babizhetskyy, V., Kotur, B., Levytskyy, V., and Michor, H. (2017). Alloy Systems and Compounds Containing Rare Earth Metals and Carbon. *Handb. Phys. Chem. Rare Earths* 52, 1–263. doi: 10.1016/bs.hpcre.2017.09.001.

Baur, W. H. (1974). The Geometry of Polyhedral Distortions. Predictive Relationships for the Phosphate Group. *Acta Crystallogr. Sect. B Struct. Crystallogr. Cryst. Chem.* 30, 1195–1215. doi: 10.1107/s0567740874004560.

Blöchl, P. E. (1994). Projector augmented-wave method. *Phys. Rev. B* 50, 17953–17979. doi: 10.1103/PhysRevB.50.17953.

Bykov, M., Bykova, E., Ponomareva, A. V., Tasnádi, F., Chariton, S., Prakapenka, V. B., et al. (2021). Realization of an Ideal Cairo Tessellation in Nickel Diazenide NiN2: High-Pressure Route to Pentagonal 2D Materials. *ACS Nano* 15, 13539–13546. doi: 10.1021/acsnano.1c04325.

Chai, P., and Corbett, J. D. (2011). Two new compounds, β-ScTe and Y3Au2, and a reassessment of Y2Au. *Acta Crystallogr. Sect. C Cryst. Struct. Commun.* 67, 53–55. doi: 10.1107/S010827011103589X.

Craig, N. C., Groner, P., and McKean, D. C. (2006). Equilibrium structures for butadiene and ethylene: Compelling evidence for II-electron delocalization in butadiene. *J. Phys. Chem. A* 110, 7461–7469. doi: 10.1021/jp060695b.

CrysAlisPRO. Oxford Diffraction. Yarnton, England: Agilent Technologies UK Ltd.

Czekalla, R., Hüfken, T., Jeitschko, W., Hoffmann, R. D., and Pöttgen, R. (1997). The Rare Earth Carbides R4C5 with R=Y, Gd, Tb, Dy, and Ho. *J. Solid State Chem.* 132, 294–299. doi: 10.1006/jssc.1997.7461.

Davaasuren, B., Kniep, R., and Ruck, M. (2010). Intermediate phases in the ternary systems RE-T-C (RE = Y, La, Gd-Er; T = Cr, Fe, Ru). 211.

Deng, Y., Huang, L., Dong, X., Wang, L., Ok, K. M., Zeng, H., et al. (2020). K2Sb(P2O7)F: Cairo Pentagonal Layer with Bifunctional Genes Reveal Optical Performance. *Angew. Chemie - Int. Ed.* 59, 21151–21156. doi: 10.1002/anie.202009441.

Dolomanov, O. V., Bourhis, L. J., Gildea, R. J., Howard, J. A. K., and Puschmann, H. (2009). OLEX2: a complete structure solution, refinement and analysis program. *J. Appl. Crystallogr.* 42, 339–341. doi: 10.1107/S0021889808042726.

Dorogokupets, P. I., and Dewaele, A. (2007). Equations of state of MgO, Au, Pt, NaCl-B1, and NaCl-B2: Internally consistent high-temperature pressure scales. *High Press. Res.* 27, 431–446. doi: 10.1080/08957950701659700.

Duan, R., He, Y., Zhu, C., Wang, X., Zhu, C., Zhao, X., et al. (2022). 2D Cairo Pentagonal PdPS: Air-Stable Anisotropic Ternary Semiconductor with High Optoelectronic Performance. *Adv. Funct. Mater.*, 2113255. doi: 10.1002/adfm.202113255.

Fedotenko, T., Dubrovinsky, L., Aprilis, G., Koemets, E., Snigirev, A., Snigireva, I., et al. (2019). Laser heating setup for diamond anvil cells for in situ synchrotron and in house high and ultra-high pressure studies. *Rev. Sci. Instrum.* 90, 104501. doi: 10.1063/1.5117786.

Friedrich, C. (2019). Tetrahedron integration method for strongly varying functions: Application to the GT self-energy. *Phys. Rev. B* 100, 075142(15). doi: 10.1103/PhysRevB.100.075142.

Gready, J. E. (1984). The value of the π-bond order–bond length relationship in geometry prediction and chemical bonding interpretation. *J. Comput. Chem.* 5, 411–426. doi: 10.1002/jcc.540050502.

Gupta, T., Velmurugan, G., Rajeshkumar, T., and Rajaraman, G. (2016). Role of Lanthanide-Ligand bonding in the magnetization relaxation of mononuclear single-ion magnets: A case study on Pyrazole and Carbene ligated LnIII(Ln=Tb, Dy, Ho, Er) complexes. *J. Chem. Sci.* 128, 1615–1630. doi: 10.1007/s12039-016-1147-4.

Hrubiak, R., Smith, J. S., and Shen, G. (2019). Multimode scanning X-ray diffraction microscopy for diamond anvil cell experiments. *Rev. Sci. Instrum.* 90. doi: 10.1063/1.5057518.

Hüfken, T., and Jeitschko, W. (1998). The high-temperature (β) modification of Y4C7 with Lu4C7 type and Dy3C4 with Sc3C4 type structure. *J. Alloys Compd.* 278, 161–164. doi: 10.1016/S0925-8388(98)00541-6.

Kantor, I., Prakapenka, V., Kantor, A., Dera, P., Kurnosov, A., Sinogeikin, S., et al. (2012).

BX90: A new diamond anvil cell design for X-ray diffraction and optical measurements. *Rev. Sci. Instrum.* 83, 125102. doi: 10.1063/1.4768541.

Kim, J. S., Xie, W., Kremer, R. K., Babizhetskyy, V., Jepsen, O., Simon, A., et al. (2007). Strong electron-phonon coupling in the rare-earth carbide superconductor La2C3. *Phys. Rev. B - Condens. Matter Mater. Phys.* 76, 1–12. doi: 10.1103/PhysRevB.76.014516.

Kobayashi, K., Horigane, K., Horie, R., and Akimitsu, J. (2019). Superconductivity of carbides. *Supercond. carbides. Phys. Chem. Carbon-Based Mater. Basics Appl.*, 149–209. doi: 10.1007/978-981-13-3417-7_6.

Kresse, G., and Furthmüller, J. (1996). Efficient iterative schemes for ab initio total-energy calculations using a plane-wave basis set. *Phys. Rev. B - Condens. Matter Mater. Phys.* 54, 11169–11186. doi: 10.1103/PhysRevB.54.11169.

Krupka, M. C., Giorgi, A. L., Krikorian, N. H., and Szklaizz, E. G. (1969). High-pressure synthesis of yttrium-thorium sesquicarbide: A new high-temeperature superconductor. *J. Less-Common Met.* 19, 113–119. doi: 10.1016/0022-5088(69)90026-5.

Laniel, D., Winkler, B., Fedotenko, T., Aslandukova, A., Aslandukov, A., Vogel, S., et al. (2022). High-pressure Na3(N2)4, Ca3(N2)4, Sr3(N2)4, and Ba(N2)3 featuring nitrogen dimers with noninteger charges and anion-driven metallicity. *Phys. Rev. Mater.* 6, 1–8. doi: 10.1103/PhysRevMaterials.6.023402.

Lengauer, W. (2012). Carbides: Transition-Metal Solid-State Chemistry. *Encycl. Inorg. Bioinorg. Chem.* doi: 10.1002/9781119951438.eibc0032.pub2.

Li, Y. L., Wang, S. N., Oganov, A. R., Gou, H., Smith, J. S., and Strobel, T. A. (2015). Investigation of exotic stable calcium carbides using theory and experiment. *Nat. Commun.* 6, 1–9. doi: 10.1038/ncomms7974.

Liermann, H. P., Konôpková, Z., Morgenroth, W., Glazyrin, K., Bednarčik, J., McBride, E. E., et al. (2015). The Extreme Conditions Beamline P02.2 and the Extreme Conditions Science Infrastructure at PETRA III. *J. Synchrotron Radiat.* 22, 908–924. doi: 10.1107/S1600577515005937.

Maintz, S., Deringer, V. L., Tchougréeff, A. L., and Dronskowski, R. (2016). LOBSTER: A tool to extract chemical bonding from plane-wave based DFT. *J. Comput. Chem.* 37, 1030–1035. doi: 10.1002/jcc.24300.

Momma, K., and Izumi, F. (2011). VESTA 3 for three-dimensional visualization of crystal,

volumetric and morphology data. *J. Appl. Crystallogr.* 44, 1272–1276. doi: 10.1107/S0021889811038970.

Monkhorst, H. J., and Pack, J. D. (1976). Special points for Brillonin-zone integrations. *Phys. Rev. B* 13, 5188–5192. doi: 10.1103/PhysRevB.13.5188.

Müller, P. C., Ertural, C., Hempelmann, J., and Dronskowski, R. (2021). Crystal Orbital Bond Index: Covalent Bond Orders in Solids. *J. Phys. Chem. C* 125, 7959–7970. doi: 10.1021/acs.jpcc.1c00718.

Nakane, T., Mochiku, T., Kito, H., Itoh, J., Nagao, M., Kumakura, H., et al. (2004). Superconducting properties of the 18 K phase in yttrium sesquicarbide system. *Appl. Phys. Lett.* 84, 2859–2861. doi: 10.1063/1.1702132.

Nespolo, M., and Guillot, B. (2016). CHARDI2015: Charge distribution analysis of non-molecular structures. *J. Appl. Crystallogr.* 49, 317–321. doi: 10.1107/S1600576715024814.

Pauling, L. (1929). The principles determining the structure of complex ionic crystals. *J. Am. Chem. Soc.* 51, 1010–1026. doi: 10.1021/ja01379a006.

Perdew, J. P., Burke, K., and Ernzerhof, M. (1996). Generalized gradient approximation made simple. *Phys. Rev. Lett.* 77, 3865–3868. doi: 10.1103/PhysRevLett.77.3865.

Rath, J., and Freeman, A. J. (1975). Generalized magnetic susceptibilities in metals: Application of the analytic tetrahedron linear energy method to Sc. 11, 2109–2117. doi: 10.1103/PhysRevB.11.2109.

Riabov, A. B., Yartys, V. A., Hauback, B. C., Guegan, P. W., Wiesinger, G., and Harris, I. R. (1999). Hydrogenation behaviour, neutron diffraction studies and microstructural characterization of boron oxide-doped Zr-V alloys. *J. Alloys Compd.* 293, 93–100. doi: 10.1016/S0925-8388(99)00306-0.

Sakai, T., Adachi, G. Y., Yoshida, T., and Shiokawa, J. (1981a). Magnetic and electrical properties of rare earth dicarbides and their solid solutions. *J. Less-Common Met.* 81, 91–102. doi: 10.1016/0022-5088(81)90272-1.

Sakai, T., Adachi, G., Yoshida, T., and Al., E. (1981b). Magnetic and electrical properties of LaC2, CeC2, PrC2, NdC2, and SmC2. *J. Chem. Phys.* 75, 3027–3032. doi: 10.1016/0038-1098(89)90038-0.

Sakai, T., Ohtani, E., Hirao, N., and Ohishi, Y. (2011). Equation of state of the NaCl-B2 phase

up to 304 GPa. *J. Appl. Phys.* 109, 084912. doi: 10.1063/1.3573393.

Savin, A., Becke, A. D., Flad, J., Nesper, R., Preuss, H., and von Schnering, H. G. (1991). A New Look at Electron Localization. *Angew. Chemie Int. Ed. English* 30, 409–412. doi: 10.1002/anie.199104091.

Shao, X., Liu, X., Zhao, X., Wang, J., Zhang, X., and Zhao, M. (2018). Electronic properties of a π-conjugated Cairo pentagonal lattice: Direct band gap, ultrahigh carrier mobility, and slanted Dirac cones. *Phys. Rev. B* 98, 1–10. doi: 10.1103/PhysRevB.98.085437.

Sheldrick, G. M. (2015a). Crystal structure refinement with SHELXL. *Acta Crystallogr. Sect. C Struct. Chem.* 71, 3–8. doi: 10.1107/S2053229614024218.

Sheldrick, G. M. (2015b). SHELXT - Integrated space-group and crystal-structure determination. *Acta Crystallogr. Sect. A Found. Crystallogr.* 71, 3–8. doi: 10.1107/S2053273314026370.

Spedding, F. H., Gschneidner Jr., K., and Daane, A. H. (1958). The Crystal Structures of Some of the Rare Earth Carbides. *J. Am. Chem. Soc.* 80, 4499–4503. doi: 10.1021/ja01550a017.

The Materials Project (2020a). Materials Data on Dy3C4 by Materials Project. *United States*. doi: https://doi.org/10.17188/1665344.

The Materials Project (2020b). Materials Data on Dy4C5 by Materials Project. *United States*. doi: https://doi.org/10.17188/1664795.

Togo, A., and Tanaka, I. (2015a). First principles phonon calculations in materials science. *Scr. Mater.* 108, 1–5. doi: 10.1016/j.scriptamat.2015.07.021.

Togo, A., and Tanaka, I. (2015b). First principles phonon calculations in materials science. *Scr. Mater.* 108, 1–6. doi: 10.1016/j.scriptamat.2015.07.021.

Vohn, V., Knapp, M., and Ruschewitz, U. (2000). Synthesis and crystal structure of SrC2. *J. Solid State Chem.* 151, 111–116. doi: 10.1006/jssc.2000.8630.

Vohn, V., Kockelmann, W., and Ruschewitz, U. (1999). On the synthesis and crystal structure of BaC2. *J. Alloys Compd.* 284, 132–137. doi: 10.1016/S0925-8388(98)00957-8.

Yosida, Y. (2002). Surface superconductivity and structural analysis of YC2 single crystals encapsulated in carbon nanocages. *J. Appl. Phys.* 92, 5494–5497. doi: 10.1063/1.1510946.

Yupko, V. L., Makarenko, G. N., and Paderno, Y. B. (1974). Physical Properties of Carbides of Rare-Earth Metals. *Refract. Carbides*, 251–259. doi: 10.1007/978-1-4684-8598-1_28.

Zachariasen, W. H. (1948). Crystal chemical studies of the 5f-series of elements. I. New structure types. *Acta Crystallogr.* 1, 265–268. doi: 10.1107/s0365110x48000703.

4.1.10 Supplementary Material

Supplementary Tables

Supplementary Table S1. Summary of the high-pressure high-temperature experiments in diamond anvil cells.

DAC number	Starting materials	Culet size (μm)	Pressure (GPa, ±1)	Temperature (K, ±200)	Reaction products
1	Dy and NaCl	250	19	2500	Dy_2C_3, Dy_4C_3
2	Dy and NaCl	250	55	2500	Dy_3C_2, Dy_4C_3
3	Dy and NaCl	250	58	2500	Dy_4C_3

Supplementary Table S2. Experimentally determined crystallographic data for the Dy_4C_3 phase at 19 GPa in comparison to the corresponding DFT-relaxed structure. The pressure was fixed during the relaxation process, while the volume, cell shape, and atomic coordinates were allowed to vary freely. The full crystallographic dataset was deposited to the CCDC under the deposition number 2248720.

Chemical formula		Dy_4C_3 (experiment)	Dy_4C_3 (theory)
Pressure (GPa)		19(1)	19
Space group		*I*-43*d*	*I*-43*d*
Space group number		#220	#220
a (Å)		7.4774(8)	7.4638
V ($Å^3$)		418.07(13)	415.80
Z		4	4
CN of Dy		6	6
Dy-C distances in first coordination sphere (Å)		2.3819(5)-2.8240(5)	2.3827-2.8231
Atom / Wyck. site/ Fractional atomic coordinates (x; y; z)	Dy/16*c*	0.05589(5) 0.05589(5) 0.05589(5)	0.05636 0.05636 0.05636
	C/12*a*	0.375 0 0.25	0.375 0 0.25
R_{int}		5.42%	-
R_1		3.76%	-
No. of reflections		274	-
No. of parameters		7	-

Supplementary Table S3. Experimentally determined crystallographic data for the Dy_4C_3 phase at 55 GPa in comparison to the corresponding DFT-relaxed structure. The pressure was fixed during the relaxation process, while the volume, cell shape, and atomic coordinates were allowed to vary freely. The full crystallographic dataset was deposited to the CCDC under the deposition number 2248721.

Chemical formula		Dy_4C_3 (experiment)	Dy_4C_3 (theory)
Pressure (GPa)		55(1)	55
Space group		*I*-43*d*	*I*-43*d*
Space group number		#220	#220
a (Å)		7.0335(13)	7.1099
V ($Å^3$)		347.95(19)	359.41
Z		4	4
CN of Dy		6	6
Dy-C distances in first coordination sphere (Å)		2.3046(9)-2.5760(9)	2.3179-2.6181
Atom / Wyck. site/ Fractional atomic coordinates (x; y; z)	Dy/16*c*	0.06548(10) 0.06548(10) 0.06548(10)	0.06379 0.06379 0.06379
	C/12*a*	0.375 0 0.25	0.375 0 0.25
R_{int}		2.74%	-
R_1		3.84%	-
No. of reflections		133	-
No. of parameters		6	-

Supplementary Table S4. Experimentally determined crystallographic data for the Dy_4C_3 phase at 58 GPa in comparison to the corresponding DFT-relaxed structure. The pressure was fixed during the relaxation process, while the volume, cell shape, and atomic coordinates were allowed to vary freely. The full crystallographic dataset was deposited to the CCDC under the deposition number 2248722.

Chemical formula	Dy_4C_3 (experiment)	Dy_4C_3 (theory)
Pressure (GPa)	58(1)	58
Space group	*I*-43*d*	*I*-43*d*
Space group number	#220	#220
a (Å)	6.9846(6)	7.0434
V ($Å^3$)	340.74(9)	349.42
Z	4	4
CN of Dy	6	6

Dy-C distances in first coordination sphere (Å)		2.2954(8)-2.5499(8)	2.3047-2.5834
Atom / Wyck. site/ Fractional atomic coordinates (x; y; z)	Dy/16*c*	0.06648(10) 0.06648(10) 0.06648(10)	0.06503 0.06503 0.06503
	C/12*a*	0.375 0 0.25	0.375 0 0.25
R_{int}		3.17%	-
R_1		3.70%	-
No. of reflections		123	-
No. of parameters		6	-

Supplementary Table S5. Experimentally determined crystallographic data for the Dy_2C_3 phase at 19 GPa in comparison to the corresponding DFT-relaxed structure. The pressure was fixed during the relaxation process, while the volume, cell shape, and atomic coordinates were allowed to vary freely. The full crystallographic dataset was deposited to the CCDC under the deposition number 2248647.

Chemical formula		Dy_2C_3 (experiment)	Dy_2C_3 (theory)
Pressure (GPa)		19(1)	19
Space group		*I*-43*d*	*I*-43*d*
Space group number		#220	#220
a (Å)		7.9208(5)	7.9111
V ($Å^3$)		496.94(9)	495.12
Z		8	8
CN of Dy		9	9
Dy-C distances in first coordination sphere (Å)		2.4070(3)-2.703(3)	2.4137-2.7190
C–C distance in [C_2] dimers, Å		1.269(12)	1.333
Atom / Wyck. site/ Fractional atomic coordinates (x; y; z)	Dy/16*c*	0.04974(2) 0.04974(2) 0.04974(2)	0.05070 0.05070 0.05070
	C/24*d*	0.2949 0 0.25	0.29075 0 0.25
R_{int}		2.85%	
R_1		1.50%	
No. of reflections		281	
No. of parameters		11	

Supplementary Table S6. Experimentally determined crystallographic data for the Dy_3C_2 phase at 55 GPa in comparison to the corresponding DFT-relaxed structure. The pressure was fixed during the relaxation process, while the volume, cell shape, and atomic coordinates were allowed to vary freely. The full crystallographic dataset was deposited to the CCDC under the deposition number 2248679.

Chemical formula		Dy_3C_2 (experiment)	Dy_3C_2 (theory)
Pressure (GPa)		55(1)	55
Space group		*P4/mbm*	*P4/mbm*
Space group number		#127	#127
a (Å)		5.9896(13)	5.9841
c (Å)		3.3880(12)	3.4524
V ($Å^3$)		121.55(7)	123.63
Z		2	2
CN of Dy1		4	4
CN of Dy2		6	6
Dy1-C distances in first coordination sphere (Å)		2.519(12)	2.5229
Dy2-C distances in first coordination sphere (Å)		2.413(9)-2.574(10)	2.4215-2.6134
C–C distance in [C_2] dimers, Å		1.51(3)	1.4828
∠(Dy1-C-C), °		122.8(11)	123.01
∠(Dy1-C-Dy1), °		114.4(5)	113.99
∠(C-Dy1-C), °		90	90
Atom / Wyck. site/ Fractional atomic coordinates (x; y; z)	Dy1/2*a*	0 0 0	0 0 0
	Dy2/4*h*	0.68222(14) 0.18222(14) 0.5	0.68053 0.18053 0.5
	C/4*g*	0.089(2) 0.589(2) 0	0.08761 0.58761 0
R_{int}		2.42%	-
R_1		5.92%	-
No. of reflections		197	-
No. of parameters		11	-

Supplementary Table S7. Results of charge distribution analysis using Mulliken charge calculations based on the computed charge density and charge analysis in the ionic approximation for Dy_4C_3, Dy_2C_3 and Dy_3C_2 at synthesis conditions.

	Atom / Wyckoff site	Mulliken	CHARDI

Dy_4C_3 (55 GPa)	Dy/16*c*	1.62	2.94
	C/12*a*	-2.16	-3.92
Dy_2C_3 (19 GPa)	Dy/16*c*	1.72	2.97
	C/24*d*	-1.15	-1.98
Dy_3C_2 (55 GPa)	Dy1/2*a*	1.01	1.42
	Dy2/4*h*	1.12	2.46
	C/4*g*	-1.62	-3.17

Supplementary Table S8. Results of charge analysis for carbides containing [C_2] dumbbells which were either synthesised in this work (Dy_2C_3 and Dy_3C_2) or previously known (DyC_2 (Adachi et al., 1976) and Dy_4C_5 (Czekalla et al., 1997)) (Mulliken, CHARDI). The crystal orbital bond indexes (ICOBI) are given only for C-C bonds in [C_2] units. Structure model for Dy_4C_5 (α-Y_4C_5 type) (The Materials Project, 2020) was acquired from Materials Project database, while that for DyC_2 (Adachi et al., 1976) – from CIF deposited in the ICSD database.

	Atom / Wyckoff site	Fractional atomic coordinates (x; y; z)	Mulliken	Charge of [C_2]	ICOBI for C-C bond in [C_2]	CHARDI	Charge of [C_2]
Dy_2C_3	Dy/16*c*	0.04974(2) 0.04974(2) 0.04974(2)	1.72	-2.28	1.737	2.97	-3.96
	C/24*d*	0.2949 0 0.2500(7)	-1.15			-1.98	
Dy_3C_2	Dy1/2*a*	0 0 0	1.01	-3.24	1.116	1.42	-6.36
	Dy2/4*h*	0.68222(14) 0.18222(14) 0.5	1.12			2.47	
	C/4*g*	0.089(2) 0.589(2) 0	-1.62			-3.18	
DyC_2	Dy/2*a*	0 0 0	1.97	-1.96	2.115	2.96	-2.96
	C/4*e*	0 0 0.396	-0.98			-1.48	
Dy_4C_5	Dy1/4*h*	0.39239 0.30409 0.5	1.71	-2.22	1.893	3.36	-3.99
	Dy2/4*g*	0.24481 0.04280 0	1.54			2.67	
	C1/4*g*	0.09392 0.34397 0	-1.01			-2.08	
	C2/4*g*	0.13901 0.23568 0	-1.21			-1.91	

	C3/2*b*	0 0 0.5	-2.06			-4.08	

Supplementary Table S9. The C–C distances in [C_2] units in dysprosium carbides: Dy_2C_3 and Dy_3C_2 - synthesized in this work, DyC_2 (Adachi et al., 1976), and Dy_4C_5 (Czekalla et al., 1997). For calculations, the structure model for Dy_4C_5 (α-Y_4C_5 type) (Czekalla et al., 1997; The Materials Project, 2020) was acquired from Materials Project database, while that for DyC_2 (Adachi et al., 1976) – from CIF deposited in the ICSD database.

	Pressure (GPa)	C-C distance in [C_2] units, Å (experiment)	C-C distance in [C_2] units, Å (theory)
Dy_2C_3	19	1.269(12)	1.333
Dy_3C_2	55	1.51(3)	1.4828
DyC_2	0.0001	1.282	1.3029
Dy_4C_5	0.0001	1.3304	1.3330

Supplementary References

Adachi, G. Y., Shibata, Y., Ueno, K., and Shiokawa, J. (1976). Heats of the tetragonal-cubic transformation in rare earth dicarbides and mixed rare earth dicarbide solid solutions. *J. Inorg. Nucl. Chem.* 38, 1023–1026. doi: 10.1016/0022-1902(76)80021-8.

Czekalla, R., Hüfken, T., Jeitschko, W., Hoffmann, R. D., and Pöttgen, R. (1997). The Rare Earth Carbides R4C5 with R=Y, Gd, Tb, Dy, and Ho. *J. Solid State Chem.* 132, 294–299. doi: 10.1006/jssc.1997.7461.

The Materials Project (2020). Materials Data on Dy4C5 by Materials Project. *United States*. doi: 10.17188/1664795.

4.2 High-Pressure Dysprosium Carbides Containing Carbon Dimers, Trimers, Chains, and Ribbons

Fariia Iasmin Akbar[1,2*], Alena Aslandukova[1], Yuqing Yin[2,3], Andrey Aslandukov[1,2], Dominique Laniel[4], Elena Bykova[5], Maxim Bykov[6], Eleanor Lawrence Bright[7], Jonathan Wright[7], Davide Comboni[7], Michael Hanfland[7], Natalia Dubrovinskaia[2,3], and Leonid Dubrovinsky[1*]

[1] Bavarian Research Institute of Experimental Geochemistry and Geophysics (BGI), University of Bayreuth, Univesitaetsstrasse 30, 95440 Bayreuth, Germany

[2] Material Physics and Technology at Extreme Conditions, Laboratory of Crystallography, University of Bayreuth, Univesitaetsstrasse 30, 95440 Bayreuth, Germany

[3] Department of Physics, Chemistry and Biology (IFM), Linköping University, SE-581 83, Linköping, Sweden

[4] Centre for Science at Extreme Conditions and School of Physics and Astronomy, University of Edinburgh, EH9 3FD Edinburgh, United Kingdom

[5] Institute of Geosciences, Goethe University Frankfurt, Altenhöferallee 1, 60438 Frankfurt am Main, Germany

[6] Institute of Inorganic and Analytical Chemistry, Goethe University Frankfurt, Max-von-Laue-Straße 7, 60438 Frankfurt am Main, Germany

[7] European Synchrotron Radiation Facility, CS 40220, 38043 Grenoble Cedex 9, France

***Corresponding authors:** Fariia Iasmin Akbar Fariia.Akbar@uni-bayreuth.de; Leonid Dubrovinsky Leonid.Dubrovinsky@Uni-Bayreuth.de

Keywords: high-pressure, diamond anvil cell, rare-earth carbides, carbides, rare-earth elements, lanthanides carbides, dysprosium carbide.

Submitted to *Carbon*

4.2.1 Abstract

Exploring the chemistry of materials at high pressure leads to discoveries of previously unknown compounds and phenomena. Here chemical reactions between elemental dysprosium and carbon were studied in laser-heated diamond anvil cells at pressures up to 95 GPa and temperatures of ~2800 K. *In situ* single-crystal synchrotron X-ray diffraction (SCXRD) analysis of the reaction products revealed the formation of novel dysprosium carbides, γ-DyC_2,

Dy_5C_9, and γ-Dy_4C_5, along with previously reported Dy_3C_2 and Dy_4C_3. The crystal structures of γ-DyC_2 and Dy_5C_9 feature infinite flat carbon polyacene-like ribbons and *cis*-polyacetylene-type chains, respectively. In the structure of γ-Dy_4C_5, carbon atoms form dimers and non-linear trimers. Dy_3C_2 contains ethanide-type carbon dumbbells, and Dy_4C_3 is methanide featuring single carbon atoms. Density functional theory calculations reproduce well the crystal structures of high-pressure dysprosium carbides and reveal conjugated π-electron systems in novel infinite carbon polyanions. This work demonstrates that complex carbon homoatomic species previously unknown in organic chemistry can be synthesised at high pressures by direct reactions of carbon with metals.

4.2.2 Introduction

The chemistry of binary compounds drastically changes and expands at high pressures. Recent striking examples include the synthesis of novel polyhalides [1,2], polynitrides [3–10], polyborides [11,12], polyhydrides [13–15], whose structures possess various homonuclear chemical species, such as dimers, trimers, pentagonal and hexagonal rings, polymeric chains, atomic layers and 3D networks previously unobserved in binary compounds at ambient pressures. The observed tendency of forming homonuclear chemical bonds is well understood by theory [16]: in very general terms, with increasing pressure the distances between atoms decrease and the value of resonance integrals increases, resulting in a larger gap between bonding and antibonding states and stronger bonds. Modern *a priori* structure prediction techniques, however, are not precise enough to provide an exhaustive list of possible chemical compositions and phases at given thermodynamic conditions. Even moderate-pressure experiments report phases and crystal structures never predicted or previously considered [1,4,5,8,13].

Homonuclear chemical bonding between carbon atoms is at the heart of organic chemistry and the number of arrangements for carbons connections (or catenation) known at ambient pressure is enormous. Strikingly, recent experimental observations indicate that carbon polyanions in metal carbides at high pressures may be unknown and even not foreseen at ambient pressure. For example, novel yttrium carbide γ-Y_4C_5 at 44-51 GPa possesses significantly bent carbon trimers [C_3] isoelectronic with ozone O_3 [17]. Polycarbides of different compositions have been claimed in the Li-C system: due to the polymerization of Li_2C_2 acetelenide upon compression [18] or formation of LiC_2 graphenide and Li_3C_4 polyacenide [19] after laser heating. Beyond these, theoretical calculations for metal carbides at high pressure predict carbon polyanions with unusual geometry and chemical bonding [20–

22], for example, in numerous polycarbides in the Ca-C, Y-C and Th-C systems [20,22–27]. Some of these novel carbon compounds are expected to have quite exotic structures, in which carbon atoms are polymerized to form infinite quasi-1D ribbons built of fused six-membered rings, and the synthesis of high-pressure CaC_2 phase (HP-CaC_2) with polyacene-like ribbons was recently reported [28]. All these predictions and discoveries call for systematic experimental studies of high-pressure carbides.

Recently, we reported the synthesis of Dy_3C_2 and Dy_4C_3 at high temperatures and pressures below ~58 GPa [29]. Here we have extended the pressure range up to 95 GPa and report the results of our systematic high-pressure high-temperature (HPHT) investigations of the Dy-C system using laser-heated diamond anvil cells (DACs).

4.2.3 Materials and methods

4.2.3.1 Nomenclature

For the sake of clarity for readers, in this paper we use simplified nomenclature of anionic units in the crystal structures of Dy-C compounds. In particular, if not specified otherwise we will mean completely deprotonated species. So, by using the term ethanide, we will mean ethanehexaide C_2^{6-}. Polyacetylide stands for fully deprotonated polyacetylene poly-[ethene-1,2-diyl]. Polyacenide is derived by full deprotonation of polyacene or poly(buta-1,3,-diene-1,4:3,2-tetrayl).

4.2.3.2 Sample preparation

In our experiments, we used BX90-type diamond anvil cells with a large X-ray aperture [30]. As anvils, we employed Boehler−Almax-type diamonds with culets diameter of 80/120 μm. Rhenium gaskets with an initial thickness of 200 μm were indented to ~16/22 μm and a hole of ~35/55 μm laser-drilled in the center of the indentation. The dysprosium (99.9% purity, Merc Inc.) flakes were loaded between one of the diamonds and a layer of dry sodium chloride (99.999% purity, ChemPUR) that played a role of a thermal insulator and pressure transmitting medium; diamond anvils were used as a carbon source. Samples were compressed to the desired pressure and laser-heated up to ~2800 K. Laser heating of the samples was carried out using an *in house* double-sided YAG laser (1064 nm wavelength) heating setup [31]. Thermal emission spectra from the heated area were collected via IsoPlane SCT 320 spectrometer with a 1024×2560 PI-MAX 4 camera [31]. The pressure was determined using the NaCl equation of states (EoS) [32,33].

4.2.3.3 X-ray diffraction

The reaction products were analyzed by single-crystal X-ray diffraction measurements at the two synchrotron beamlines: ID11 of ESRF, Grenoble, France (λ = 0.2846 Å, beam size ~ 0.75 × 0.75 μm^2); ID15B of ESRF, Grenoble, France (λ = 0.4100 Å, beam size ~1.5 × 2 μm^2). Powder XRD images were collected upon continuous rotation of the sample in a range ±1° around the vertical ω axis at ESRF. During single-crystal collection, the cell was rotated from –38° to +38° with narrow 0.5° steps. Creating maps with XDI software [34] helps to visualize the phase distribution within the pressure chamber and to locate areas where the step-scans should be performed. The CrysAlis^{Pro} software package [35] was used for the analysis of the single-crystal XRD data (peak hunting, indexing, data integration, frame scaling, and absorption correction). To calibrate an instrument model in the CrysAlis^{Pro} software, i.e. the sample-to-detector distance, detector's origin, offsets of the goniometer angles, and rotation of both the X-ray beam and detector around the instrument axis, we used a single crystal of orthoenstatite [$(Mg_{1.93}Fe_{0.06})(Si_{1.93},Al_{0.06})O_6$, *Pbca* space group, a = 8.8117(2) Å, b = 5.18320(10) Å, and c = 18.2391(3) Å]. The DAFi program was used for the search of reflection's groups belonging to the individual single crystal domains [36]. Using the OLEX2 software package [37], the structures were solved with the ShelXT structure solution program [38] using intrinsic phasing and refined with the ShelXL [39] refinement package using least-squares minimization. Crystal structure visualization was made with the VESTA software [40]. The equations of state were obtained by fitting the pressure-volume dependence data using the EoSFit7-GUI [41].

Accurate determination of the positions of light carbon atoms in the presence of heavy dysprosium atoms is challenging. In order to improve both precision and accuracy in determining C-C distances, 12 to 27 domains with $R_{int} < 5\%$ and $R_1 < 8\%$ for each of the studied carbides were identified, their structures were refined, and C-C distances for each corresponding domain were averaged. That allows reduce the standard error of C-C distances to smaller than 0.009 Å, and the corresponding data presented in the main text of the paper.

4.2.3.4 Theoretical calculations

The properties of the synthesized compounds were determined through the first-principles calculations using the framework of density functional theory (DFT) as implemented in the VASP (Vienna ab initio simulation package) code [42]. To expand the electronic wave function in plane waves we used the Projector-Augmented-Wave (PAW) method [43]. The Generalized Gradient Approximation (GGA) functional was used for calculating the exchange-

correlation energies, as proposed by Perdew–Burke–Ernzerhof (PBE) [44]. The PAW potentials with the following valence configurations of 5s5p6s5d for Dy ("Dy_3") and 2s2p for C ("C") were used to describe the interaction between the core and the valence electrons in frozen f-electrons approximation for Dy [42]. Convergence tests with a threshold of 1 meV per atom in energy led to an energy cutoff for the plane wave expansion of 750 eV for all phases and a Monkhorst-Pack [45] k-point grid of 15 × 7 × 6 for γ-DyC_2, 4 × 4 × 6 for Dy_5C_9, 3 × 5 × 4 for γ-Dy_4C_5, 6 × 6 × 11 for Dy_3C_2, and 4 × 4 × 4 for Dy_4C_3. Computations were performed for eight volumes that cover the pressure range of 0-100 GPa. Harmonic lattice dynamics calculations were performed with the PHONOPY software [46] using the finite displacement method for 3 × 3 × 3 (γ-DyC_2), 2 × 2 × 3 (Dy_5C_9), 2 × 2 × 2 (γ-Dy_4C_5), 2 × 2 × 3 (Dy_3C_2) and 2 × 2 × 2 (Dy_4C_3) supercells with respectively adjusted k-points. The tetrahedron method was used for Brillouin zone integrations, employing a mesh of 16 × 16 × 16 k-points for γ-DyC_2, 8 × 8 × 12 k-points for Dy_5C_9, 10 × 10 × 8 k-points for γ-Dy_4C_5, 12 × 12 × 22 k-points for Dy_3C_2 and 8 × 8 × 8 k-points for Dy_4C_3 [47,48]. The integrated values of the crystal orbital bond index (ICOBI) [49] and Mulliken charges were calculated using LOBSTER v4.1.0 software [50]. The charge distribution in the ionic approximation based on a generalization of Pauling's concept of bond strength [51] was made using CHARDI2015 [52]. In our calculations, temperature, configurational entropy, and the entropy contribution due to lattice vibrations were neglected.

4.2.4 Results and Discussion

A summary of our experiments is presented in Table S1. High-pressure reactions between dysprosium and carbon in DACs at pressures of ~70 and ~95 GPa and temperatures of ~2800 K resulted in the formation of five dysprosium carbides, namely γ-DyC_2, Dy_5C_9, γ-Dy_4C_5, Dy_3C_2, and Dy_4C_3 (Table S2). The first three are novel polycarbides.

The DyC_2 phase synthesized at ~70 GPa has a crystal structure different from that of the two previously known DyC_2 polymorphs, α-DyC_2 (CaC_2-type structure, tetragonal space group *I*4/*mmm*) [53] and β-DyC_2 (KCN-type structure, cubic space group *Fm*-3*m*) [54,55]. Naturally, we named it γ-DyC_2. The γ-DyC_2 phase (space group *Immm*, #71, *Z* = 4, Tables S2 and S3) is isostructural to the previously observed HP-CaC_2 (*Immm*) [28] and the predicted YC_2 (*Immm*) [23]. Its orthorhombic unit cell contains four dysprosium atoms occupying the Wyckoff site 4*i* and eight carbon atoms occupying two distinct crystallographic positions: C1 – 4*h* and C2 – 4*g* (Fig. 1, Table S3).

In the structure of γ-DyC_2, (Fig. 1, Tables S2 and S3) dysprosium atoms form distorted, slightly buckled closed packed layers in the (0 0 1) plane (Fig. 1b). Dysprosium atoms have 12 carbon neighbors arranged in a hexagonal prism with unequal bases (Fig. 1c). Carbon atoms lie in the (0 0 2) plane in the middle between planes of Dy atoms (Fig. 1). They are arranged in polymerized hexagonal rings – flat one-dimensional ribbons propagating along the [1 0 0] direction (Fig. 1). Thus, the carbon atoms form exotic $^{1}_{\infty}[C_4]$ one-dimensionally infinite polyanions.

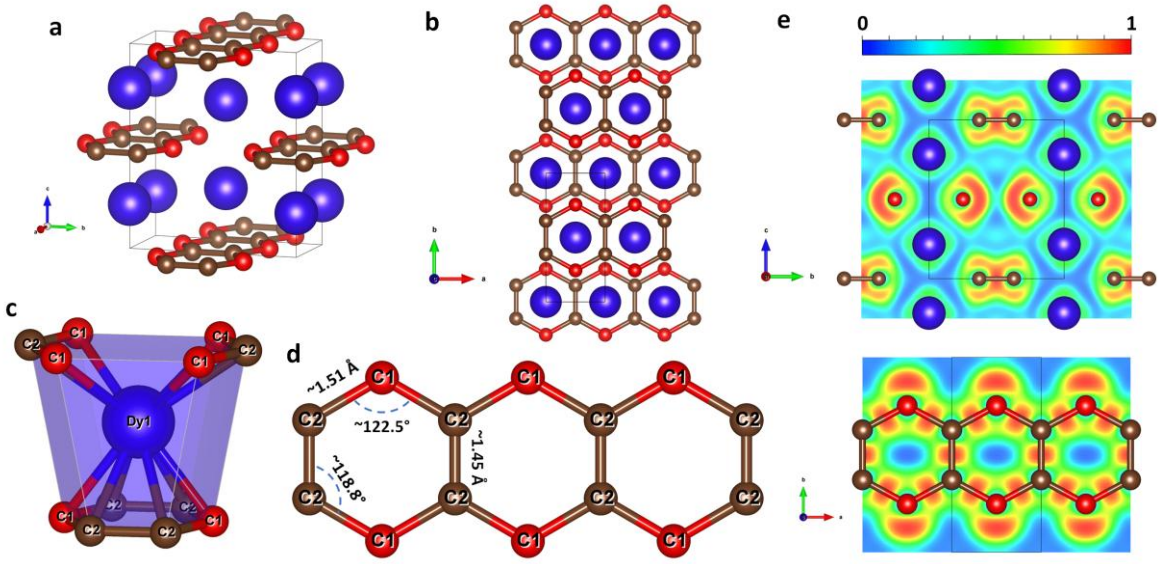

Fig. 1. Crystal structure of DyC_2 at 66(3) GPa. Dy1 atoms are blue, C1 atoms are red, C2 atoms are brown; grey thin lines outline the unit cell. (a) A general view of the crystal structure. (b) The crystal structure viewed along the *c*-axis. (c) The coordination environment of the dysprosium atom. (d) A view of the carbon ribbon. (e) The electron localization function calculated in the (1 0 0) (top) and (0 0 1) plane containing carbon ribbons (bottom).

The structure of the Dy_5C_9 carbide (space group *P4/mnc*, #128, *Z* = 2) (Tables S2 and S4) is unprecedented, for we found neither any structural analogue, nor a relevant prediction from theoretical methods. Its unit cell contains two crystallographically distinct dysprosium atoms (Dy1 and Dy2 occupying 8*h* and 2*b* Wyckoff positions, respectively) and two types of carbon atoms (C1 and C2 occupying 16*i* and 2*a* Wyckoff positions, respectively). Dysprosium atoms form slightly distorted square layers in the (0 0 1) plane at a distance of 1/2*c*; each layer is rotated relatively to an adjacent one by ~40° (Fig. 2b and S1). The distinct dysprosium atoms have different environments – Dy1 atoms are in irregular polyhedra with 11 vertices, while Dy2 atoms are located in bicapped square prisms (Fig. 2c, d). The carbon atoms C2 have isolated positions in the structure like the carbon in methanides (Fig. 2). The C1 carbon atoms form zig-zag chains with four atoms per repeating element (Fig. 2). Chains are propagating along the [0 0 1] direction.

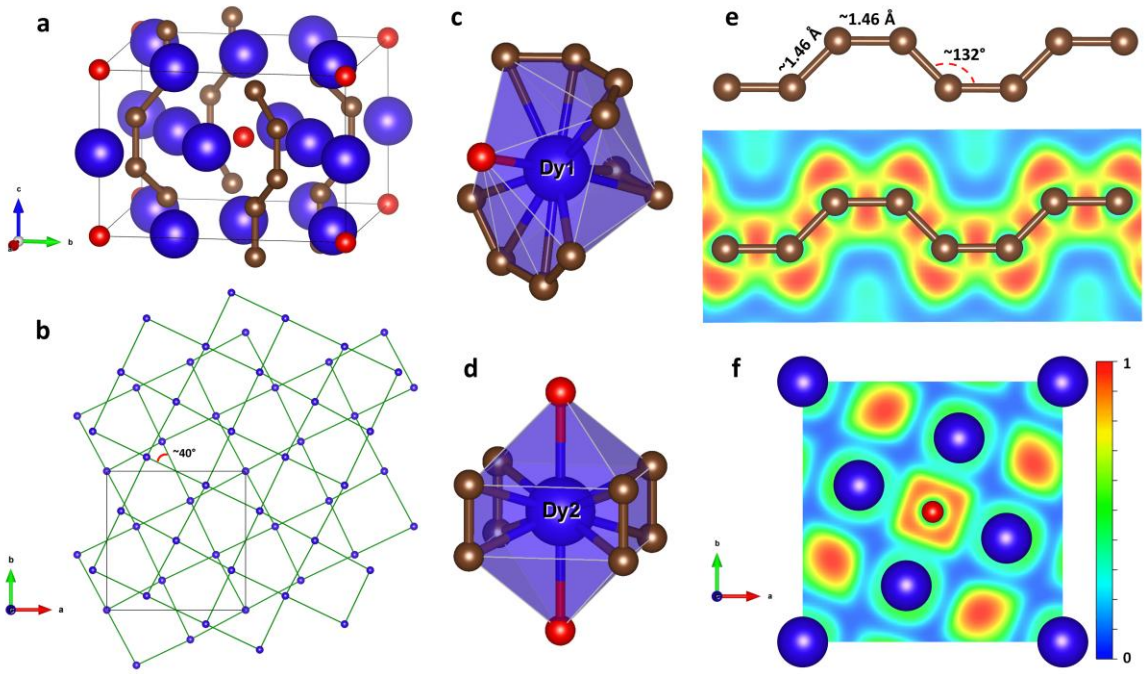

Fig. 2. Crystal structure of Dy_5C_9 at 68(3) GPa. All Dy atoms are blue, C atoms forming chains are brown, discrete C atoms are red; grey thin lines outline the unit cell. (a) A general view of the crystal structure. (b) Arrangement of parallel planes comprised of Dy atoms rotated relative to each other by ~40°. (c) and (d) The coordination environment of the Dy1 and Dy2 atoms. (e) A carbon chain geometry (top) and the electron localization function calculated in the plane containing the carbon chain (bottom). (f) The electron localization function calculated in the (0 0 2) plane.

The dysprosium carbide isostructural with the recently discovered γ-Y_4C_5 phase [17] is referred to as γ-Dy_4C_5 (orthorhombic space group *Cmce*, #64, Z = 8) (Tables S2 and S5, Fig. S2). Its structure described previously [17] contains carbon dimers [C_2] (dumbbells) and non-linear trimers [C_3] (the angle ∠(C2-C4-C2) is of ~132°, Fig. S2). Two other carbides observed in this work (Table S2), dysprosium (III) methanide Dy_4C_3, and dysprosium (II) ethanide Dy_3C_2, have been synthesised at ~55 GPa in our previous study [29]. For completeness, their structures at ~70 GPa (Dy_3C_2) and ~95 GPa (Dy_4C_3) are shown in Fig. S3 and S4 and structural data are given in Tables S6 and S7.

The analysis of the chemical nature of the novel dysprosium carbides containing polyanions requires a complex approach, especially because *ab initio* methods (see *Methods* section for details) do not always accurately reproduce experimental observations for the *f*-element Dy [29,56,57]. Therefore, we first conduct the crystal-chemical analysis and then complement the analysis with theoretical calculations for isostructural (experimentally observed or hypothetical) compounds of analogous elements devoid of *f*-electrons (like Ca or Y).

In γ-DyC_2, the carbon ribbons are flat. The C-C distances in the hexagons, refined at 70 GPa, are equal to 1.451(9) Å and 1.508(5) Å for the C2-C2 and C1-C2 bonds, respectively. Two angles in the hexagon are found to be of 122.5(7)°, while the other four angles are of 118.8(3)° (Fig. 1d). The angles are close to 120°, and C-C distances are quite similar indicating the sp^2 hybridisation of carbon atoms. In the ideal polyacene chain with ordered single- and double-order carbon-carbon bonds [58], the distribution of shorter and longer C-C contacts is incompatible with the experimental observations for γ-DyC_2 (and for HP-CaC_2 as well [28]). Similar C-C bond lengths within the hexagons in γ-DyC_2 (and HP-CaC_2) suggest a conjugated π-electron system in polyacene-like ribbons. The integrated crystal orbital bond indexes (ICOBI) [49] calculated for γ-DyC_2, HP-CaC_2, and isostructural YC_2 (Table S8) vary from ~0.7 to ~1.0. These values, being sufficiently close to 1, confirm strong covalent bonding between carbon atoms. The ELF maps for γ-DyC_2, HP-CaC_2, YC_2 (Fig. S5) also demonstrate localisation of electrons on C-C bonds in hexagons, and ionic bonding between Dy and C units. Calculated electron density of states (eDOSes) (Fig. S5) for these phases show the presence of carbon *p*-electrons at the Fermi level that agrees with the formation of the conducting conjugated π-electron system.

According to the experimental data, the length of common edges of hexagons in γ-DyC_2 and HP-CaC_2 is slightly (by ~0.05 Å) shorter than the length of non-shared edges. This agrees with the calculations for all three isostructural high-pressure carbides (DyC_2, CaC_2, and YC_2), which result in the shorter common edges by ~0.02-0.03 Å. This observation is in contrast with what is known for crystals of organic polyaromatic hydrocarbons (naphthalene, anthracene, tetracene, pentacene, pyrene [58–60]) where common edges of hexagon carbon rings are slightly longer (up to ~0.1 Å) than those with carbon connected to hydrogen. A similar effect is known, for example, for acetylene and acetylides [61]. The reason could be the strong electrostatic interaction between carbon and the metal ion: indeed, at ambient pressure, the difference in electronegativity of C and H is ~0.3 eV/e [62–64]. At 70 GPa, this difference significantly increases, reaching ~5.9 eV/e for C and Dy, ~17 eV/e – for C and Ca, and ~15.7 eV/e – for C and Y [63,64]. According to calculations and available experimental data, the average C-C distances in hexagons of γ-DyC_2 and YC_2 (~1.49 Å) are slightly longer than in HP-CaC_2 (~1.45 Å). This qualitatively aligns with some additional electron transfer from cation to carbon ribbons in rare earth carbides in comparison to HP-CaC_2: there is a small decrease of the C-C bond order and higher formal charges on Dy and Y in rare earth carbides than in HP-CaC_2.

According to SCXRD for Dy_5C_9 at ~70 GPa, the C-C distance in the carbon chains is of ~1.46 Å and the C-C-C angle is of ~132°. All atoms of the chain lie in the same plane, as the torsion angle is zero (Fig. 2e). The crystal structure is well reproduced by theoretical calculations (Table S4). According to the theory, both in Dy_5C_9 and in a hypothetical Y_5C_9 with the same structure, the lengths of C-C bonds are very similar (alternating lengths along the chain are of ~1.42 Å and ~1.44 Å at 70 GPa), and the angle between carbon atoms is of ~135°. That implies *cis*-polyacetylene type deprotonated carbon chains with predominantly sp^2-hybridized carbon and conjugated π-electron system. The ICOBI calculated for carbon atoms in the chains of Y_5C_9 and Dy_5C_9, are equal to ~0.7 and ~1.1 respectively. The presence of carbon's *p*-electrons at the Fermi level, as in the calculated eDOS (Fig. S6, Table S8) supports this assignment. Strong covalent bonding between carbon atoms in the chains, and the ionic nature of Dy and isolated C are evident from ELF maps (Fig. 2 and S6). At the same time, C-C distances are significantly longer than in *cis*-polyacetylene – 1.37 Å [65], and the bond angle is significantly larger than 120° expected for sp^2-hybridized carbon. Remarkably, in γ-Dy_4C_5 and γ-Y_4C_5 the geometry of $[C_3]$ groups (in γ-Dy_4C_5, C-C contact is of ~1.43 Å, bond angle – ~132°) is very similar to the geometry of elements forming *cis*-polyacetylene-type chains. Experimental and theoretical data on γ-Y_4C_5 [17] suggest that the bond order of carbon atoms in $[C_3]$ is ~1.31. Thus, carbon chains discovered in Dy_5C_9 can be considered as polymerised in *cis* conformation $[C_3]$ groups found in γ-Dy_4C_5 and γ-Y_4C_5.

As discussed above, the analysis of ELF maps (Fig. 1, 2, and S2-S4) suggests the ionic bonding between dysprosium and carbon species in γ-DyC_2, Dy_5C_9, γ-Dy_4C_5, and Dy_3C_2. that allows considering them, along with Dy_4C_3, as salt carbides [61]. In fact, the synthesis of all these compounds from elements also makes them similar to salt carbides, so that one can assign a formal charge to a carbon atom or to carbon groups.

There is a correlation between the formal charges of nitrogen and carbon dimers and their lengths. Recently we demonstrated this using as an example $[N_2]^{x-}$ dimers in the high-pressure $Na_3(N_2)_4$, $Ca_3(N_2)_4$, $Sr_3(N_2)_4$, and $Ba(N_2)_3$ compounds [3] and, for $[C_2]^{x-}$ dimers, in yttrium carbide γ-Y_4C_5 containing both $[C_2]$ and nonlinear $[C_3]$ units [17]. In the structures of the carbon compounds synthesised in this study, there are more complex carbon arrangements, including infinite ribbons of fused carbon rings, that imposed a necessity to introduce the effective bond order into consideration to comprehend the relationship between the C-C bond lengths and formal charges of individual carbon atoms or their groups. We have collected the literature data for a number of binary metal-carbon compounds featuring $[C_2]$ or $[C_3]$ units [17,29,53,66–83] with reported C-C interatomic distances. For each of these compounds, we

calculated the effective bond order (EBO) between the carbon atoms using two equations introduced below. For a compound containing both isolated "methanide"-type carbon atoms and carbon dimers, with the chemical formula $Me_n(C_2)_mC_k$ (*k* is number of isolated "methanide"-type carbon atoms, and *m* is the number of carbon dimers), the effective bond order (EBO) between carbon atoms is calculated as follows:

$$EBO = \frac{(2 \times 4m - nZ_{Me} + 4k)}{2m}, \quad (1)$$

where "4" is the number of valence electrons in a free carbon atom, Z_{Me} is the formal charge of the cation. Carbons' formal charge in dimers is *x=4-EBO*. For example, for barium acetylide, BaC_2, according to this formula, the effective bond order of carbon atoms is '3', and formal charge is '-1'. Similarly, for $Me_n(C_3)_mC_k$ carbides containing only $[C_3]$ units, we used the following equation:

$$EBO = \frac{(3 \times 4m - nZ_{Me} + 4k)}{4m}. \quad (2)$$

The results of our calculations for the binary metal-carbon compounds found in the literature [17,29,53,66–83] are presented in the graphical form in Fig. S7, showing a correlation between the C-C distances in $[C_2]$ and $[C_3]$ units, *d*(C-C), and the bond order in the pairs of C atoms (green and blue dots). The data points shown by green and blue dots in Fig. S7 were fitted by the linear equation: *EBO = 10.81 – 6.57×d(C-C)* (dashed line in Fig. S7).

With the linear equation obtained above, we determined the bond order for C-C bonds for all dysprosium carbides studied here, using the values of *d(C-C)* obtained experimentally from SCXRD. For Dy_3C_2 we found the bond order ~1 in dimers, implying it to be an ethanide featuring $[C_2]^{6-}$ units, which is in perfect agreement with the reasoning presented in reference [29]. In dimers of γ-Dy_4C_5, the EBO is of ~1.71 (implying the formal charge of the dimers as $[C_2]^{4.6-}$), whereas in trimers the EBO is of ~1.40, suggesting $[C_3]^{6.4-}$ units. For Dy_5C_9, all C-C bonds in the chains are similar, and the EBO is of ~1.22 (thus one-dimensionally infinite polyanions $^1_\infty[(C_4)^{6.2-}]$). For γ-DyC_2, possessing ribbons of fused hexagon rings, the estimated C-C EBO is of ~1.27 for shared hexagon edges and of ~0.90 for unshared ones. This gives a formal charge of ~ -3.0 for two carbons per formula unit. Remarkably, the same reasoning implies a formal charge of ~ -2.4 per two carbon atoms in HP-CaC_2 [28], that is about 1*e* less than expected for Ca^{2+} vs Dy^{3+}. Knowing the EBO (thus formal charges) of the carbon polyanions, we can estimate the oxidation state of dysprosium atoms in the studied compounds: dysprosium (III) in γ-DyC_2, Dy_5C_9, γ-Dy_4C_5, and Dy_4C_3, and dysprosium (II) in Dy_3C_2.

The Mulliken charges of dysprosium in the carbides at ~70 GPa were found to be 1.66 for Dy1 in γ-DyC_2; 1.88 for Dy1 and Dy2 in Dy_5C_9; 1.69 for Dy1, 1.75 for Dy2 and 1.55 for Dy3 in γ-Dy_4C_5; 1.01 for Dy1 and 1.13 for Dy2 in Dy_3C_2; and 1.64 for Dy in Dy_4C_3 (Table S9). The values for γ-DyC_2, Dy_5C_9, γ-Dy_4C_5, and Dy_4C_3 are consistent with the Mulliken charges reported for other dysprosium(III)-containing compounds [29,84,85]. The lower Mulliken charges of dysprosium in Dy_3C_2 are in agreement with the assessment of the cation in this compound as Dy^{2+} [29]. The model Y-C system shows similar results (Table S10).

Experimental studies of the equations of state of dysprosium carbides were beyond the scope of this work, however the pressure-volume relations were simulated and described with the second order Birch-Murnaghan equation of state (Table S11). The calculated bulk moduli decrease with the increase of dysprosium content: K_0(γ-DyC_2) = 189(2) GPa > K_0(Dy_5C_9) = 164(2) GPa > K_0(γ-Dy_4C_5) = 123.8(8) GPa > K_0(Dy_3C_2) = 96.7(9) GPa > K_0(Dy_4C_3) = 91.6(12) GPa (Table S11, Fig. S8). There is also an inverse correlation between the compressibility and the ratio $R=\langle d\rangle^3/(Z_{Dy}*Z_C)$ ($\langle d\rangle$ is the average Dy-C distance in the first coordination sphere; Z_{Dy} and Z_C are the formal charges of dysprosium and carbon) (Fig. S9a). For the studied compounds, with the increase of the *R* ratio the compressibility decreases (Fig. S9a), whereas for ionic and ionic-covalent compounds the correlation is known to be direct [3,86]. This indicates an unusual compression mechanism for the studied dysprosium carbides that is in line with the observation of the almost linear correlation between compressibility and the average bond order in carbon pairs (Fig. S9b).

Computations of phonon dispersion relations in harmonic approximation at 0 K show that at 70 GPa γ-DyC_2, Dy_5C_9, γ-Dy_4C_5 and Dy_4C_3 are dynamically stable (Fig. S10), while Dy_3C_2 shows tiny instability at 70 GPa (Fig. S10g) similar to that found previously for this compound at the synthesis pressure of 55 GPa [29]. γ-DyC_2, γ-Dy_4C_5 and Dy_4C_3 are predicted to be dynamically stable at 0 GPa (Fig. S10b, f, j) and thus potentially quenchable to ambient conditions, but one should consider this prediction with caution. Notably, γ-Y_4C_5 discovered earlier was found dynamically unstable at ambient conditions [17] in contrast to the isostructural γ-Dy_4C_5 from the current study (Fig. S10f).

The calculated convex hull diagram at 0 K and 70 GPa (Fig. 3) shows that according to the theory, γ-DyC_2, γ-Dy_4C_5 and Dy_3C_2 are thermodynamically stable at the synthesis pressure. Two dysprosium carbides, Dy_5C_9 and Dy_4C_3, lie above the convex hull by 70 and 16 meV per atom, respectively (Fig. 3). These differences in energy turn out to be smaller than k_BT (241 meV) at the synthesis temperature (~2800 K), thus suggesting that these phases might be metastable at ambient temperature and high pressures.

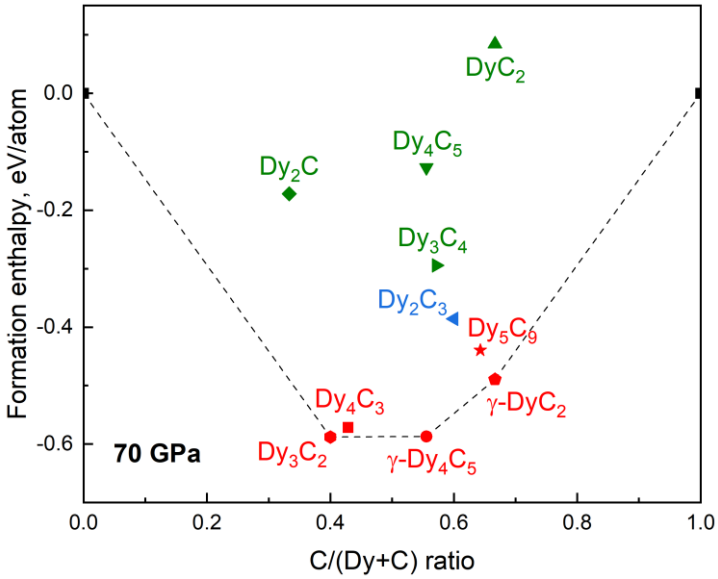

Fig. 3. Calculated convex hull diagram constructed for the Dy-C binary system at 70 GPa. Only known Dy-C phases are included. Dashed lines indicate the convex hull; carbides synthesized in this work are given in red; Dy_2C_3 (shown in blue) has been previously observed both at extreme [29] and ambient conditions [83]; carbides shown in green have been reported at ambient pressure (Dy_2C [87], Dy_4C_5 [72,88,89], Dy_3C_4 [90,91], and DyC_2 [53]).

4.2.5 Conclusion

To summarize, novel dysprosium carbides γ-DyC_2, Dy_5C_9, γ-Dy_4C_5, Dy_3C_2, and Dy_4C_3 were synthesized by the direct reaction of metallic dysprosium and carbon originated from diamond anvils upon laser heating to ~2800 K at ~70 GPa. Their crystal structures were studied *in situ*. The most notable features of the new carbides are polyacene-like ribbons in γ-DyC_2 and *cis*-polyacetylene-type chains in Dy_5C_9. This study demonstrates the drastic effect of high pressures on the chemistry of the Dy-C system with the general tendency to formation of carbides with complex polyanions.

4.2.6 Acknowledgements

The authors acknowledge the European Synchrotron Radiation Facility (ESRF) for the provision of beamtime at the ID15b and ID11 beamlines. Computations were performed at the Leibniz Supercomputing Center of the Bavarian Academy of Sciences and the Humanities, and the research center for scientific computing at the University of Bayreuth. F.I.A., N.D., and L.D. thank Gerd Steinle-Neumann (Bavarian Research Institute of Experimental Geochemistry and Geophysics (BGI), University of Bayreuth, 95440 Bayreuth, Germany) for the valuable discussions and advice regarding the theoretical calculations. N.D. and L.D. thank the Deutsche Forschungsgemeinschaft (DFG projects DU 954–11/1, DU 393–9/2, DU 393–13/1; DU

945/15-1) for financial support. N.D. also thanks the Swedish Government Strategic Research Area in Materials Science on Functional Materials at Linköping University (Faculty Grant SFO-Mat-LiU No. 2009 00971). M. B. acknowledges the support of Deutsche Forschungsgemeinschaft (DFG Emmy-Noether Program project BY112/2-1). Co-funded by the European Union (ERC, HIPMAT, 101077963). Views and opinions expressed are however those of the author(s) only and do not necessarily reflect those of the European Union or the European Research Council. Neither the European Union nor the granting authority can be held responsible for them. D.L. thanks the UKRI Future Leaders Fellowship (MR/V025724/1) for financial support.

4.2.7 References

[1] Y. Yin, A. Aslandukova, N. Jena, F. Trybel, I.A. Abrikosov, B. Winkler, et al., Unraveling the Bonding Complexity of Polyhalogen Anions: High-Pressure Synthesis of Unpredicted Sodium Chlorides Na2Cl3 and Na4Cl5 and Bromide Na4Br5, JACS Au 3 (2023) 1634–1641. https://doi.org/10.1021/jacsau.3c00090.

[2] W. Zhang, A.R. Oganov, A.F. Goncharov, Q. Zhu, S.E. Boulfelfel, A.O. Lyakhov, et al., Unexpected Stable Stoichiometries of Sodium Chlorides, Science (80-.). 342 (2013) 1502–1505. https://doi.org/10.1126/science.1244989.

[3] D. Laniel, B. Winkler, T. Fedotenko, A. Aslandukova, A. Aslandukov, S. Vogel, et al., High-pressure Na3(N2)4, Ca3(N2)4, Sr3(N2)4, and Ba(N2)3 featuring nitrogen dimers with noninteger charges and anion-driven metallicity, Phys. Rev. Mater. 6 (2022) 023402. https://doi.org/10.1103/PhysRevMaterials.6.023402.

[4] A. Aslandukov, F. Trybel, A. Aslandukova, D. Laniel, T. Fedotenko, S. Khandarkhaeva, et al., Anionic N18 Macrocycles and a Polynitrogen Double Helix in Novel Yttrium Polynitrides YN6 and Y2N11 at 100 GPa, Angew. Chemie Int. Ed. 61 (2022) 1–7. https://doi.org/10.1002/anie.202207469.

[5] M. Bykov, E. Bykova, G. Aprilis, K. Glazyrin, E. Koemets, I. Chuvashova, et al., Fe-N system at high pressure reveals a compound featuring polymeric nitrogen chains, Nat. Commun. 9 (2018) 1–8. https://doi.org/10.1038/s41467-018-05143-2.

[6] A. Aslandukov, A. Aslandukova, D. Laniel, S. Khandarkhaeva, Y. Yin, F.I. Akbar, et al., Stabilization of N6 and N8 anionic units and 2D polynitrogen layers in high-pressure scandium polynitrides, Nat. Commun. 15 (2024) 2244. https://doi.org/10.1038/s41467-

024-46313-9.

[7] B.A. Steele, E. Stavrou, J.C. Crowhurst, J.M. Zaug, V.B. Prakapenka, I.I. Oleynik, High-Pressure Synthesis of a Pentazolate Salt, Chem. Mater. 29 (2017) 735–741. https://doi.org/10.1021/acs.chemmater.6b04538.

[8] D. Laniel, F. Trybel, Y. Yin, T. Fedotenko, S. Khandarkhaeva, A. Aslandukov, et al., Aromatic hexazine [N6]4− anion featured in the complex structure of the high-pressure potassium nitrogen compound K9N56, Nat. Chem. 15 (2023) 641–646. https://doi.org/10.1038/s41557-023-01148-7.

[9] Y. Wang, M. Bykov, I. Chepkasov, A. Samtsevich, E. Bykova, X. Zhang, et al., Stabilization of hexazine rings in potassium polynitride at high pressure, Nat. Chem. 14 (2022) 794–800. https://doi.org/10.1038/s41557-022-00925-0.

[10] N.P. Salke, K. Xia, S. Fu, Y. Zhang, E. Greenberg, V.B. Prakapenka, et al., Tungsten Hexanitride with Single-Bonded Armchairlike Hexazine Structure at High Pressure, Phys. Rev. Lett. 126 (2021) 065702. https://doi.org/10.1103/PhysRevLett.126.065702.

[11] Y. Zhang, L. Wu, B. Wan, Y. Zhao, R. Gao, Z. Li, et al., Structural variety beyond appearance: High-pressure phases of CrB4 in comparison with FeB4, Phys. Chem. Chem. Phys. 18 (2016) 2361–2368. https://doi.org/10.1039/c5cp06745f.

[12] E. Bykova, E. Johansson, M. Bykov, S. Chariton, H. Fei, S. V. Ovsyannikov, et al., Novel Class of Rhenium Borides Based on Hexagonal Boron Networks Interconnected by Short B2Dumbbells, Chem. Mater. 34 (2022) 8138–8152. https://doi.org/10.1021/acs.chemmater.2c00520.

[13] A.P. Drozdov, P.P. Kong, V.S. Minkov, S.P. Besedin, M.A. Kuzovnikov, S. Mozaffari, et al., Superconductivity at 250 K in lanthanum hydride under high pressures, Nature 569 (2019) 528–531. https://doi.org/10.1038/s41586-019-1201-8.

[14] D. Laniel, B. Winkler, E. Bykova, T. Fedotenko, S. Chariton, V. Milman, et al., Novel sulfur hydrides synthesized at extreme conditions, Phys. Rev. B 102 (2020) 134109. https://doi.org/10.1103/PhysRevB.102.134109.

[15] V. V. Struzhkin, D.Y. Kim, E. Stavrou, T. Muramatsu, H.K. Mao, C.J. Pickard, et al., Synthesis of sodium polyhydrides at high pressures, Nat. Commun. 7 (2016) 1–8. https://doi.org/10.1038/ncomms12267.

[16] M. Miao, Y. Sun, E. Zurek, H. Lin, Chemistry under high pressure, Nat. Rev. Chem. 4 (2020) 508–527. https://doi.org/10.1038/s41570-020-0213-0.

[17] A. Aslandukova, A. Aslandukov, L. Yuan, D. Laniel, S. Khandarkhaeva, T. Fedotenko, et al., Novel High-Pressure Yttrium Carbide γ-Y4C5 Containing [C2] and Nonlinear

[C3] Units with Unusually Large Formal Charges, Phys. Rev. Lett. 127 (2021) 135501. https://doi.org/10.1103/PhysRevLett.127.135501.

[18] L. Wang, X. Dong, Y. Wang, H. Zheng, K. Li, X. Peng, et al., Pressure-Induced Polymerization and Disproportionation of Li2C2 Accompanied with Irreversible Conductivity Enhancement, J. Phys. Chem. Lett. 8 (2017) 4241–4245. https://doi.org/10.1021/acs.jpclett.7b01779.

[19] X. Dong, L. Wang, K. Li, H. Zheng, Y. Wang, Y. Meng, et al., Tailored Synthesis of the Narrowest Zigzag Graphene Nanoribbon Structure by Compressing the Lithium Acetylide under High Temperature, J. Phys. Chem. C 122 (2018) 20506–20512. https://doi.org/10.1021/acs.jpcc.8b04081.

[20] Y.L. Li, S.N. Wang, A.R. Oganov, H. Gou, J.S. Smith, T.A. Strobel, Investigation of exotic stable calcium carbides using theory and experiment, Nat. Commun. 6 (2015) 1–9. https://doi.org/10.1038/ncomms7974.

[21] C. Su, J. Zhang, G. Liu, X. Wang, H. Wang, Y. Ma, Catenation of carbon in LaC2 predicted under high pressure, Phys. Chem. Chem. Phys. 18 (2016) 14286–14291. https://doi.org/10.1039/c6cp01484d.

[22] Y. Guo, C. Yu, J. Lin, C. Wang, C. Ren, B. Sun, et al., Pressure-induced structural transformations and polymerization in ThC2, Sci. Rep. 7 (2017) 11. https://doi.org/10.1038/srep45872.

[23] X. Feng, S. Lu, C.J. Pickard, H. Liu, S.A.T. Redfern, Y. Ma, Carbon network evolution from dimers to sheets in superconducting ytrrium dicarbide under pressure, Commun. Chem. 1 (2018) 1–7. https://doi.org/10.1038/s42004-018-0085-0.

[24] J. Nylén, S. Konar, P. Lazor, D. Benson, U. Häussermann, Structural behavior of the acetylide carbides Li2C2 and CaC2 at high pressure, J. Chem. Phys. 137 (2012) 224507. https://doi.org/10.1063/1.4770268.

[25] M. Debessai, J.J. Hamlin, J.S. Schilling, D. Rosenmann, D.G. Hinks, H. Claus, Superconductivity for CaC6 to 32 GPa hydrostatic pressure, Phys. Rev. B - Condens. Matter Mater. Phys. 82 (2010) 3–5. https://doi.org/10.1103/PhysRevB.82.132502.

[26] A. Gauzzi, S. Takashima, N. Takeshita, C. Terakura, H. Takagi, N. Emery, et al., Enhancement of superconductivity and evidence of structural instability in intercalated graphite CaC6 under high pressure, Phys. Rev. Lett. 98 (2007) 15–18. https://doi.org/10.1103/PhysRevLett.98.067002.

[27] L. Zhang, Y. Xie, T. Cui, Y. Li, Z. He, Y. Ma, et al., Pressure-induced enhancement of electron-phonon coupling in superconducting Ca C6 from first principles, Phys. Rev. B

- Condens. Matter Mater. Phys. 74 (2006) 1–5. https://doi.org/10.1103/PhysRevB.74.184519.

[28] S. Khandarkhaeva, T. Fedotenko, A. Aslandukova, F.I. Akbar, M. Bykov, D. Laniel, et al., Extending carbon chemistry at high-pressure by synthesis of CaC2 and Ca3C7 with deprotonated polyacene- and para-poly(indenoindene)-like nanoribbons, Nat. Commun. 15 (2024) 2855. https://doi.org/10.1038/s41467-024-47138-2.

[29] F.I. Akbar, A. Aslandukova, A. Aslandukov, Y. Yin, F. Trybel, S. Khandarkhaeva, et al., High-pressure synthesis of dysprosium carbides, Front. Chem. 11 (2023) 1–9. https://doi.org/10.3389/fchem.2023.1210081.

[30] I. Kantor, V. Prakapenka, A. Kantor, P. Dera, A. Kurnosov, S. Sinogeikin, et al., BX90: A new diamond anvil cell design for X-ray diffraction and optical measurements, Rev. Sci. Instrum. 83 (2012) 125102. https://doi.org/10.1063/1.4768541.

[31] T. Fedotenko, L. Dubrovinsky, G. Aprilis, E. Koemets, A. Snigirev, I. Snigireva, et al., Laser heating setup for diamond anvil cells for in situ synchrotron and in house high and ultra-high pressure studies, Rev. Sci. Instrum. 90 (2019) 104501. https://doi.org/10.1063/1.5117786.

[32] P.I. Dorogokupets, A. Dewaele, Equations of state of MgO, Au, Pt, NaCl-B1, and NaCl-B2: Internally consistent high-temperature pressure scales, High Press. Res. 27 (2007) 431–446. https://doi.org/10.1080/08957950701659700.

[33] T. Sakai, E. Ohtani, N. Hirao, Y. Ohishi, Equation of state of the NaCl-B2 phase up to 304 GPa, J. Appl. Phys. 109 (2011) 084912. https://doi.org/10.1063/1.3573393.

[34] R. Hrubiak, J.S. Smith, G. Shen, Multimode scanning X-ray diffraction microscopy for diamond anvil cell experiments, Rev. Sci. Instrum. 90 (2019). https://doi.org/10.1063/1.5057518.

[35] Rigaku Oxford Diffraction, CrysAlisPro Software system (2015)., Rigaku Oxford Diffraction, CrysAlisPro Softw. Syst. (2015). (2015). https://doi.org/10.1063/1.2372734.

[36] A. Aslandukov, M. Aslandukov, N. Dubrovinskaia, L. Dubrovinsky, Domain Auto Finder (DAFi) program: the analysis of single-crystal X-ray diffraction data from polycrystalline samples, J. Appl. Crystallogr. 55 (2022) 1383–1391. https://doi.org/10.1107/s1600576722008081.

[37] O. V. Dolomanov, L.J. Bourhis, R.J. Gildea, J.A.K. Howard, H. Puschmann, OLEX2: a complete structure solution, refinement and analysis program, J. Appl. Crystallogr. 42 (2009) 339–341. https://doi.org/10.1107/S0021889808042726.

[38] G.M. Sheldrick, SHELXT – Integrated space-group and crystal-structure determination, Acta Crystallogr. Sect. A Found. Adv. 71 (2015) 3–8. https://doi.org/10.1107/S2053273314026370.

[39] G.M. Sheldrick, Crystal structure refinement with SHELXL, Acta Crystallogr. Sect. C Struct. Chem. 71 (2015) 3–8. https://doi.org/10.1107/S2053229614024218.

[40] K. Momma, F. Izumi, VESTA 3 for three-dimensional visualization of crystal, volumetric and morphology data, J. Appl. Crystallogr. 44 (2011) 1272–1276. https://doi.org/10.1107/S0021889811038970.

[41] J. Gonzalez-Platas, M. Alvaro, F. Nestola, R. Angel, EosFit7-GUI: A new graphical user interface for equation of state calculations, analyses and teaching, J. Appl. Crystallogr. 49 (2016) 1377–1382. https://doi.org/10.1107/S1600576716008050.

[42] G. Kresse, J. Furthmüller, Efficiency of ab-initio total energy calculations for metals and semiconductors using a plane-wave basis set, Comput. Mater. Sci. 6 (1996) 15–50. https://doi.org/10.1016/0927-0256(96)00008-0.

[43] P.E. Blöchl, Projector augmented-wave method, Phys. Rev. B 50 (1994) 17953–17979. https://doi.org/10.1103/PhysRevB.50.17953.

[44] J.P. Perdew, K. Burke, M. Ernzerhof, Generalized gradient approximation made simple, Phys. Rev. Lett. 77 (1996) 3865–3868. https://doi.org/10.1103/PhysRevLett.77.3865.

[45] H.J. Monkhorst, J.D. Pack, Special points for Brillonin-zone integrations, Phys. Rev. B 13 (1976) 5188–5192. https://doi.org/10.1103/PhysRevB.13.5188.

[46] A. Togo, I. Tanaka, First principles phonon calculations in materials science, Scr. Mater. 108 (2015) 1–6. https://doi.org/10.1016/j.scriptamat.2015.07.021.

[47] J. Rath, A.J. Freeman, Generalized magnetic susceptibilities in metals: Application of the analytic tetrahedron linear energy method to Sc, 11 (1975) 2109–2117. https://doi.org/10.1103/PhysRevB.11.2109.

[48] C. Friedrich, Tetrahedron integration method for strongly varying functions: Application to the GT self-energy, Phys. Rev. B 100 (2019) 075142(15). https://doi.org/10.1103/PhysRevB.100.075142.

[49] P.C. Müller, C. Ertural, J. Hempelmann, R. Dronskowski, Crystal Orbital Bond Index: Covalent Bond Orders in Solids, J. Phys. Chem. C 125 (2021) 7959–7970. https://doi.org/10.1021/acs.jpcc.1c00718.

[50] S. Maintz, V.L. Deringer, A.L. Tchougréeff, R. Dronskowski, LOBSTER: A tool to extract chemical bonding from plane-wave based DFT, J. Comput. Chem. 37 (2016) 1030–1035. https://doi.org/10.1002/jcc.24300.

[51] L. Pauling, The principles determining the structure of complex ionic crystals, J. Am. Chem. Soc. 51 (1929) 1010–1026. https://doi.org/10.1021/ja01379a006.

[52] M. Nespolo, B. Guillot, CHARDI2015: Charge distribution analysis of non-molecular structures, J. Appl. Crystallogr. 49 (2016) 317–321. https://doi.org/10.1107/S1600576715024814.

[53] G.Y. Adachi, Y. Shibata, K. Ueno, J. Shiokawa, Heats of the tetragonal-cubic transformation in rare earth dicarbides and mixed rare earth dicarbide solid solutions, J. Inorg. Nucl. Chem. 38 (1976) 1023–1026. https://doi.org/10.1016/0022-1902(76)80021-8.

[54] V. Babizhetskyy, B. Kotur, V. Levytskyy, H. Michor, Alloy Systems and Compounds Containing Rare Earth Metals and Carbon, Handb. Phys. Chem. Rare Earths 52 (2017) 1–263. https://doi.org/10.1016/bs.hpcre.2017.09.001.

[55] R. Vidhya, M.P. Antony, P.R. Vasudeva Rao, Enthalpy and Gibbs energy of formation of dysprosium dicarbide, J. Nucl. Mater. 350 (2006) 129–134. https://doi.org/10.1016/j.jnucmat.2005.12.001.

[56] H.P. Sarker, M.N. Huda, Role of f-electrons in determining insulator to metal phase transitions of Ca(La1−xCex)2S4 ($0 \leq x \leq 1$) solid solution: A DFT + U study, J. Appl. Phys. 130 (2021) 145102. https://doi.org/10.1063/5.0058096.

[57] N. Tateiwa, J. Pospíšil, Y. Haga, H. Sakai, T.D. Matsuda, E. Yamamoto, Itinerant ferromagnetism in actinide 5 f-electron systems: Phenomenological analysis with spin fluctuation theory, Phys. Rev. B 96 (2017) 035125. https://doi.org/10.1103/PhysRevB.96.035125.

[58] J.E. Anthony, The larger acenes: Versatile organic semiconductors, Angew. Chemie - Int. Ed. 47 (2008) 452–483. https://doi.org/10.1002/anie.200604045.

[59] R.E. Newnham, Properties of Materials: Anisotropy, Symmetry, Structure, 2005.

[60] Q. Ai, K. Jarolimek, S. Mazza, J.E. Anthony, C. Risko, Delimited Polyacenes: Edge Topology as a Tool to Modulate Carbon Nanoribbon Structure, Conjugation, and Mobility, Chem. Mater. 30 (2018) 947–957. https://doi.org/10.1021/acs.chemmater.7b04715.

[61] U. Ruschewitz, Binary and ternary carbides of alkali and alkaline-earth metals, Coord. Chem. Rev. 244 (2003) 115–136. https://doi.org/10.1016/S0010-8545(03)00102-4.

[62] X. Dong, A.R. Oganov, H. Cui, X.-F. Zhou, H.-T. Wang, Electronegativity and chemical hardness of elements under pressure, Proc. Natl. Acad. Sci. 119 (2022) 1–8. https://doi.org/10.1073/pnas.2117416119.

[63] M. Rahm, T. Zeng, R. Hoffmann, Electronegativity Seen as the Ground-State Average Valence Electron Binding Energy, J. Am. Chem. Soc. 141 (2019) 342–351. https://doi.org/10.1021/jacs.8b10246.

[64] M. Rahm, R. Cammi, N.W. Ashcroft, R. Hoffmann, Squeezing All Elements in the Periodic Table: Electron Configuration and Electronegativity of the Atoms under Compression, J. Am. Chem. Soc. 141 (2019) 10253–10271. https://doi.org/10.1021/jacs.9b02634.

[65] C.S. Yannoni, T.C. Clarke, Molecular geometry of cis- and trans-polyacetylene by nutation NMR spectroscopy, Phys. Rev. Lett. 51 (1983) 1191–1193. https://doi.org/10.1103/PhysRevLett.51.1191.

[66] V. Vohn, W. Kockelmann, U. Ruschewitz, On the synthesis and crystal structure of BaC2, J. Alloys Compd. 284 (1999) 132–137. https://doi.org/10.1016/S0925-8388(98)00957-8.

[67] V. Vohn, M. Knapp, U. Ruschewitz, Synthesis and crystal structure of SrC2, J. Solid State Chem. 151 (2000) 111–116. https://doi.org/10.1006/jssc.2000.8630.

[68] M. Atoji, Magnetic and crystal structures of CeC2, PrC2, NdC2, TbC2, and HoC2 at low temperatures, J. Chem. Phys. 46 (1967) 1891–1901. https://doi.org/10.1063/1.1840950.

[69] M. Atoji, Neutron diffraction study of Ce2C3 at low temperatures, J. Chem. Phys. 46 (1967) 4148–4149. https://doi.org/10.1063/1.1840499.

[70] Y. Yosida, Surface superconductivity and structural analysis of YC2 single crystals encapsulated in carbon nanocages, J. Appl. Phys. 92 (2002) 5494–5497. https://doi.org/10.1063/1.1510946.

[71] M.C. Krupka, A.L. Giorgi, N.H. Krikorian, E.G. Szklaizz, High-pressure synthesis of yttrium-thorium sesquicarbide: A new high-temeperature superconductor, J. Less-Common Met. 19 (1969) 113–119. https://doi.org/10.1016/0022-5088(69)90026-5.

[72] R. Czekalla, T. Hüfken, W. Jeitschko, R.D. Hoffmann, R. Pöttgen, The Rare Earth Carbides R4C5 with R=Y, Gd, Tb, Dy, and Ho, J. Solid State Chem. 132 (1997) 294–299. https://doi.org/10.1006/jssc.1997.7461.

[73] M. Atoji, K. Gschneidner, A.H. Daane, R.E. Rundle, F.H. Spedding, The Structures of Lanthanum Dicarbide and Sesquicarbide by X-Ray and Neutron Diffraction, J. Am. Chem. Soc. 80 (1958) 1804–1808. https://doi.org/10.1021/ja01541a008.

[74] R. Czekalla, W. Jeitschko, R.-D. Hoffmann, H. Rabeneck, Preparation, Crystal Structure, and Properties of the Lanthanoid Carbides Ln4C7 with Ln = Ho, Er, Tm, and

Lu, Zeitschrift Für Naturforsch. B 51 (1996) 646–654. https://doi.org/10.1515/znb-1996-0505.

[75] H. Ninomiya, T. Koshinuma, T. Nishio, H. Fujihisa, K. Kawashima, I. Hase, et al., Experimental and Computational Determination of Optimal Boron Content in Layered Superconductor Sc20C8-xBxC20, Inorg. Chem. 59 (2020) 14290–14295. https://doi.org/10.1021/acs.inorgchem.0c02090.

[76] T.W. Button, I.J. McColm, Reaction of carbon with lanthanide silicides IV: The Y5Si3-C system, J. Less-Common Met. 97 (1984) 237–244. https://doi.org/10.1016/0022-5088(84)90028-6.

[77] O. Reckeweg, A. Baumann, H.A. Mayer, J. Glaser, H.J. Meyer, On the coexistence of tetragonal and monoclinic CaC2: Structural and spectroscopic studies on alkaline earth metal acetylides, MC2 (M = Ca, Sr, Ba), Zeitschrift Fur Anorg. Und Allg. Chemie 625 (1999) 1686–1692. https://doi.org/10.1002/(sici)1521-3749(199910)625:10<1686::aid-zaac1686>3.3.co;2-o.

[78] K. Klöss, D. Hinz-Hübner, U. Ruschewitz, Über eine neue Modifikation des Na2C2, Zeitschrift Für Anorg. Und Allg. Chemie 628 (2002) 2701–2704. https://doi.org/https://doi.org/10.1002/1521-3749(200212)628:12<2701::AID-ZAAC2701>3.0.CO;2-%23.

[79] S. Hemmersbach, B. Zibrowius, U. Ruschewitz, Na2C2 und K2C2: Synthese, Kristallstruktur und spektroskopische Eigenschaften, Z. Anorg. Allg. Chem. 625 (1999) 1440–1446. https://doi.org/10.1002/(SICI)1521-3749(199909)625.

[80] H. Fjellvág, P. Karen, Crystal Structure of Magnesium Sesquicarbide, Inorg. Chem. 31 (1992) 3260–3263. https://doi.org/10.1021/ic00041a018.

[81] P. Karen, A. Kjekshus, Q. Huang, V.L. Karen, The crystal structure of magnesium dicarbide, J. Alloys Compd. 282 (1999) 72–75. https://doi.org/10.1016/S0925-8388(98)00828-7.

[82] V. Babizhetskyy, O. Jepsen, R.K. Kremer, A. Simon, B. Ouladdiaf, A. Stolovits, Structure and bonding of superconducting LaC2, J. Phys. Condens. Matter 26 (2014) 025701. https://doi.org/10.1088/0953-8984/26/2/025701.

[83] F.H. Spedding, K. Gschneidner Jr., A.H. Daane, The Crystal Structures of Some of the Rare Earth Carbides, J. Am. Chem. Soc. 80 (1958) 4499–4503. https://doi.org/10.1021/ja01550a017.

[84] T. Gupta, G. Velmurugan, T. Rajeshkumar, G. Rajaraman, Role of Lanthanide-Ligand bonding in the magnetization relaxation of mononuclear single-ion magnets: A case

study on Pyrazole and Carbene ligated LnIII(Ln=Tb, Dy, Ho, Er) complexes, J. Chem. Sci. 128 (2016) 1615–1630. https://doi.org/10.1007/s12039-016-1147-4.

[85] G. Ahuja, F. Science, U. Raj, Study of Electronic Properties of Dy2O3 using First Principles Calculations, Int. J. Pure Appl. Phys. 13 (2017) 123–126.

[86] R.M. Hazen, L.W. Finger, Bulk Modulus-Volume Relationship for Cation-Anion Polyhedra, J. Geophys. Res. 84 (1979) 6723–6728. https://doi.org/https://doi.org/10.1029/JB084iB12p06723.

[87] M. Atoji, Neutron-diffraction studies of Tb2C and Dy2C in the temperature range 4-296 K, J. Chem. Phys. 75 (1981) 1434–1441. https://doi.org/10.1063/1.442150.

[88] The Materials Project, Materials Data on Dy4C5 by Materials Project, United States (2020). https://doi.org/10.17188/1664795.

[89] V. Babizhetskyy, B. Kotur, V. Levytskyy, Phase Equilibria and Crystal Structure of the Ternary Compounds in Dy–B–C System at 1270 K, Proc. Shevchenko Sci. Soc. Chem. Sci. LVI (2019) 45–55. https://doi.org/10.37827/ntsh.chem.2019.56.045.

[90] T. Hüfken, W. Jeitschko, The high-temperature (β) modification of Y4C7 with Lu4C7 type and Dy3C4 with Sc3C4 type structure, J. Alloys Compd. 278 (1998) 161–164. https://doi.org/10.1016/S0925-8388(98)00541-6.

[91] The Materials Project, Materials Data on Dy3C4 by Materials Project, United States (2020). https://doi.org/10.17188/1665344.

4.2.8 Supporting information

Table S1. Summary of the high-pressure high-temperature (HPHT) experiments in diamond anvil cells (DACs). Pressure values, determined using the equation of state (EoS) for NaCl, which served as the pressure medium, correspond to the pressures measured at the center of the samples, with uncertainties arising from pressure gradients within the diamond anvil cells (DACs).

DAC number	Starting materials	Culet size (μm)	Pressure (GPa, ±5)	Temperature (K, ±200)	Reaction products
1	Dy in NaCl	80	70	2800	γ-DyC_2, Dy_5C_9, γ-Dy_4C_5, Dy_3C_2
2	Dy in NaCl	120	95	2800	Dy_4C_3

Table S2. Crystallographic information for carbides reported in this work. Pressures are given as determined from EoS of NaCl (pressure medium) for each of the phases with corresponding uncertainties arising for ±2μm area around the single-crystal X-ray diffraction (SCXRD) data collection positions.

Chemical formula	γ-DyC_2	Dy_5C_9	γ-Dy_4C_5	Dy_3C_2	Dy_4C_3
Pressure (GPa)	66(3)	68(3)	65(3)	68(3)	95(3)
Space group	*Immm*	*P4/mnc*	*Cmce*	*P4/mbm*	*I*-43*d*
Structure type			γ-Y_4C_5	U_3Si_2	anti-Th_3P_4
a (Å)	2.6355(12)	7.2218(7)	11.800(6)	5.8699(11)	6.6798(8)
b (Å)	5.707(3)		7.2291(15)		
c (Å)	6.737(3)	4.8618(4)	8.416(2)	3.3260(7)	
V ($Å^3$)	101.31(7)	253.56(5)	717.9(4)	114.60(5)	298.05(11)
Z	4	2	8	2	4
R_{int}	3.21%	3.80%	3.10%	4.02%	3.89%
R_1	2.30%	3.97%	3.92%	4.87%	2.50%

Table S3. Crystallographic information for a selected domain of γ-DyC_2 (*Immm*) at 66(3) GPa and the corresponding DFT-relaxed structure data. Simulated crystallographic data for isostructural CaC_2 (*Immm*) [1,2] and YC_2 (*Immm*) [3] are given for comparison. The carbon atoms of HP-CaC_2 in [2] are named in reverse order (C1 and C2 are given as “C2” and “C1”,

respectively). The full crystallographic dataset for γ-DyC_2 was deposited to the CCDC under the deposition number 2311064.

Chemical formula		γ-DyC_2 (experiment)	γ-DyC_2 (theory)	CaC_2 (theory)	YC_2 (theory)
Pressure (GPa)		66(3)	70	70	70
Crystal data					
Mr		186.52			
ρ (g/cm^3)		12.228			
Radiation type		X-ray, λ = 0.2846 Å			
μ (mm^{-1})		6.410			
Space group		*Immm*			
a (Å)		2.6355(12)	2.6362	2.5331	2.6331
b (Å)		5.707(3)	5.7420	5.8603	5.7458
c (Å)		6.737(3)	6.7298	6.4952	6.6956
V (Å^3)		101.31(7)	101.87	96.42	101.30
Z		4			
Atom / Wyck. site/ Fractional atomic coordinates (x; y; z)	Dy1/4*i* Ca1/4*i* Y1/4*i*	0 0 0.21614(12)	0 0 0.21630	0 0 0.20367	0 0 0.21607
	C1/4*h*	0 0.255(3) 0.5	0 0.25196 0.5	0 0.24459 0.5	0 0.25185 0.5
	C2/4*g*	0 0.371(2) 0	0 0.37221 0	0 0.37734 0	0 0.37226 0
Data collection					
No. of measured, independent and observed [I > 2σ(I)] reflections		212/104/95			
R_{int}		3.21%			
Refinement					
R_1		2.30%			
wR_2		5.03%			
GOF		1.020			
No. of reflections/No. of parameters		104/9			

Table S4. Crystallographic information for a selected domain of Dy_5C_9 (*P*4/*mnc*) at 68(3) GPa and the corresponding DFT-relaxed structure data. Simulated crystallographic data for isostructural and Y_5C_9 (*P*4/*mnc*) is given for comparison. The full crystallographic dataset for Dy_5C_9 was deposited to the CCDC under the deposition number 2311066.

Chemical formula		Dy_5C_9 (experiment)	Dy_5C_9 (theory)	Y_5C_9 (theory)
Pressure (GPa)		68(3)	70	70
Crystal data				
Mr		920.59		
ρ (g/cm^3)		12.058		
Radiation type		X-ray, λ = 0.4100 Å		
μ (mm^{-1})		17.031		
Space group		*P4/mnc*		
a (Å)		7.2218(7)	7.2921	7.2700
c (Å)		4.8618(4)	4.8717	4.8737
V (Å^3)		253.56(5)	259.05	257.58
Z		2		
Atom / Wyckoff site/ Fractional atomic coordinates (x; y; z)	Dy1/8*h* Y1/8*h*	0.10180(8) 0.28660(10) 0	0.101300 0.283330 0	0.10191 0.28295 0
	Dy2/2*b* Y2/2*b*	0 0 0.5	0 0 0.5	0 0 0.5
	C1/16*i*	0.2949(13) 0.0972(13) 0.350(2)	0.40162 0.19778 0.14592	0.40229 0.19712 0.14573
	C2/2*a*	0 0 0	0 0 0	0 0 0
Data collection				
No. of measured, independent and observed [I > 2σ(I)] reflections		532/175/148		
R_{int}		3.80%		
Refinement				
R_1		3.97%		
wR_2		10.00%		
GOF		1.099		
No. of reflections/No. of parameters		175/14		

Table S5. Crystallographic information for a selected domain of γ-Dy_4C_5 (*Cmce*) at 65(3) GPa and the corresponding DFT-relaxed structure data. The carbon and metal atoms of γ-Y_4C_5 in the study [4] are named in different order. The full crystallographic dataset for γ-Dy_4C_5 was deposited to the CCDC under the deposition number 2311067.

Chemical formula		γ-Dy_4C_5 (experiment)	γ-Dy_4C_5 (theory)
Pressure (GPa)		65(3)	70
Crystal data			
Mr		710.05	
ρ (g/cm^3)		13.139	
Radiation type		X-ray, λ = 0.2846 Å	
μ (mm^{-1})		7.224	
Space group		*Cmce*	
a (Å)		11.800(6)	11.9476
b (Å)		7.2291(15)	7.3318
c (Å)		8.416(2)	8.5736
V (Å^3)		717.9(4)	751.03
Z		8	
Atom / Wyck. site/ Fractional atomic coordinates (x; y; z)	Dy1/16*g*	0.14184(8) 0.12235(9) 0.35339(8)	0.14391 0.12535 0.35173
	Dy2/8*d*	0.15444(10) 0 0	0.1504 0 0
	Dy3/8*f*	0 0.28688(15) 0.12455(13)	0 0.30957 0.12164
	C1/8*f*	0 0.004(3) 0.183(2)	0 0.01342 0.1736
	C2/16*g*	0.1862(17) 0.297(2) 0.1256(18)	0.19369 0.30774 0.12106
	C3/8*f*	0 0.332(3) 0.389(3)	0 0.34167 0.39021
	C4/8*e*	0.25 0.382(3) 0.25	0.25 0.38263 0.25
Data collection			
No. of measured, independent and observed [I > 2σ(I)] reflections		1042/504/418	
R_{int}		3.10%	
Refinement			

R_1	3.92%	
wR_2	8.08%	
GOF	1.114	
No. of reflections/No. of parameters	504/33	

Table S6. Crystallographic information for a selected domain of Dy_3C_2 (*P*4/*mbm*) at 68(3) GPa and the corresponding DFT-relaxed structure data. The full crystallographic dataset for Dy_3C_2 was deposited to the CCDC under the deposition number 2311063.

Chemical formula		Dy_3C_2 (experiment)	Dy_3C_2 (theory)
Pressure (GPa)		68(3)	70
Crystal data			
Mr		511.52	
ρ (g/cm^3)		14.824	
Radiation type		X-ray, λ = 0.4100 Å	
μ (mm^{-1})		22.580	
Space group		*P4/mbm*	
a (Å)		5.8699(11)	5.9130
c (Å)		3.3260(7)	3.3702
V (Å^3)		114.60(5)	117.84
Z		2	
Atom / Wyck. site/ Fractional atomic coordinates (x; y; z)	Dy1/2*a*	0 0 0	0 0 0
	Dy2/4*h*	0.18337(19) 0.68337(19) 0.5	0.1816 0.6816 0.5
	C1/4*g*	0.590(3) 0.090(3) 0	0.587900 0.087900 0
Data collection			
No. of measured, independent and observed [I > 2σ(I)] reflections		246/89/84	
R_{int}		4.02%	
Refinement			
R_1		4.87%	
wR_2		13.16%	
GOF		1.060	

No. of reflections/No. of parameters	89/9	

Table S7. Crystallographic information for a selected domain of Dy_4C_3 (*I*-43*d*) at 95(3) GPa and the corresponding DFT-relaxed structure data. The full crystallographic dataset for Dy_4C_3 was deposited to the CCDC under the deposition number 2311065.

Chemical formula		Dy_4C_3 (experiment)	Dy_4C_3 (theory)
Pressure (GPa)		95(3)	95
Crystal data			
Mr		686.03	
ρ (g/cm^3)		15.288	
Radiation type		X-ray, λ = 0.2844 Å	
μ (mm^{-1})		8.998	
Space group		*I*-43*d*	
a (Å)		6.6798(8)	6.8027
V (Å^3)		298.05(11)	314.81
Z		4	4
Atom / Wyck. site/ Fractional atomic coordinates (x; y; z)	Dy1/16*c*	0.06665(7) 0.06665(7) 0.06665(7)	0.06906 0.06906 0.06906
	C1/12*a*	0.375 0 0.25	0.375 0 0.25
No. of measured, independent and observed [I > 2σ(I)] reflections		757/154/131	
R_{int}		3.89%	
Refinement			
R_1		2.50%	
wR_2		5.64%	
GOF		1.214	
data/parameters ratio		154/6	

Table S8. The crystal orbital bond indexes (ICOBI) for C-C bonds in carbides structures relaxed at 70 GPa.

	ICOBI for C-C in [C_2]	ICOBI for C-C in [C_3]	ICOBI for C-C in ribbons		ICOBI for C-C in chains	
γ-DyC_2			d(C1-C2) = 1.4985 Å	0.993		
			d(C2-C2) = 1.4676 Å	0.970		
HP-CaC_2			d(C1-C2) = 1.4542 Å	0.814		
			d(C2-C2) = 1.4376 Å	0.919		
YC_2			d(C1-C2) = 1.4973 Å	0.705		
			d(C2-C2) = 1.4679 Å	0.713		
Dy_5C_9					d(C1-C1) = 1.4218 Å	1.184
					d(C1-C1) = 1.4419 Å	1.101
Y_5C_9					d(C1-C1) = 1.4205 Å	0.707
					d(C1-C1) = 1.4415 Å	0.677
γ-Dy_4C_5	1.282	1.262				
Dy_3C_2	1.108					

Table S9. Results of charge distribution analysis using Mulliken charge calculations based on the computed charge density and charge analysis in the ionic approximation for γ-DyC_2, Dy_5C_9, γ-Dy_4C_5, Dy_3C_2, and Dy_4C_3 at synthesis conditions.

	Atom / Wyckoff site	Mulliken	CHARDI
γ-DyC_2	Dy1/4*i*	1.66	2.96
	C1/4*h*	-1.07	-1.82
	C2/4*g*	-0.59	-1.14
Dy_5C_9	Dy1/8*h*	1.88	3.39
	Dy2/2*b*	1.88	3.20
	C1/16*i*	-0.93	-1.61
	C2/2*a*	-1.97	-3.88

γ-Dy_4C_5	Dy1/16*g*	1.69	2.81
	Dy2/8*d*	1.75	2.82
	Dy3/8*f*	1.55	3.14
	C1/8*f*	-1.42	-2.42
	C2/16*g*	-1.43	-2.33
	C3/8*f*	-1.50	-2.47
	C4/8*e*	-0.89	-2.03
Dy_3C_2	Dy1/2*a*	1.01	1.46
	Dy2/4*h*	1.13	2.45
	C1/4*g*	-1.63	-3.18
Dy_4C_3	Dy/16*c*	1.64	2.91
	C/12*a*	-2.19	-3.88

Table S10. Results of charge distribution analysis using Mulliken charge calculations based on the computed charge density for the model Y-C system: γ-YC_2, Y_5C_9, γ-Y_4C_5, and Y_3C_2 at 70 GPa.

	Atom / Wyckoff site	Mulliken
γ-YC_2	Y1/4*i*	1.51
	C1/4*h*	-0.87
	C2/4*g*	-0.64
Y_5C_9	Y1/8*h*	1.65
	Y2/2*b*	1.98
	C1/16*i*	-0.95
	C2/2*a*	-0.98
γ-Y_4C_5	Y1/16*g*	1.51
	Y2/8*d*	1.64
	Y3/8*f*	1.11
	C1/8*f*	-1.18
	C2/16*g*	-1.11
	C3/8*f*	-1.24
	C4/8*e*	-1.13
Y_3C_2	Y1/2*a*	0.82
	Y2/4*h*	0.92
	C1/4*g*	-1.33

Y_4C_3	Y/16*c*	1.00
	C/12*a*	-1.33

Table S11. Parameters of the 2nd order Birch-Murnaghan equations of state for γ-DyC_2, Dy_5C_9, γ-Dy_4C_5, Dy_3C_2, and Dy_4C_3.

	2nd order Birch-Murnaghan EoS	
Compound	V_0 (Å^3)	K_0 (GPa)
γ-DyC_2	128.6(2)	189(2)
Dy_5C_9	334.6(8)	164(2)
γ-Dy_4C_5	1018.9(12)	123.8(8)
Dy_3C_2	168.1(3)	96.7(9)
Dy_4C_3	485.3(13)	91.6(12)

Table. S12. The C–C distances in [C_n] units in dysprosium carbides: γ-DyC_2, Dy_5C_9, γ-Dy_4C_5, and Dy_3C_2 - synthesized in this work.

	Pressure (GPa)	C-C distance in [C_n] units, Å (experiment)	C-C distance in [C_n] units, Å (theory, 70 GPa)
γ-DyC_2 (ribbons)	66(3)	C1-C2, 1.508(5)	C1-C2, 1.4985
		C2-C2, 1.451(9)	C2-C2, 1.4676
Dy_5C_9 (chains)	68(3)	1.459(5), 1.458(5)	1.4218, 1.4419
γ-Dy_4C_5 (dimers and trimers)	65(3)	C1-C3 in [C_2], 1.385(11)	C1-C3 in [C_2], 1.3729
		C2-C4 in [C_3], 1.432(6)	C2-C4 in [C_3], 1.4058
Dy_3C_2 (dimers)	68(3)	1.49(4)	1.4702

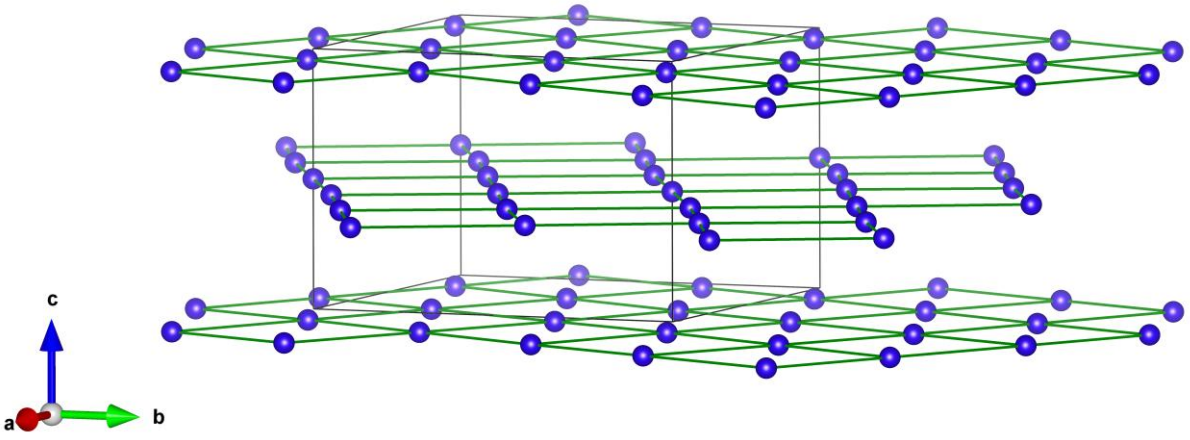

Fig. S1. Arrangement of parallel planes comprised of Dy atoms rotated relative to each other by ~40° in Dy_5C_9 at 68(3) GPa.

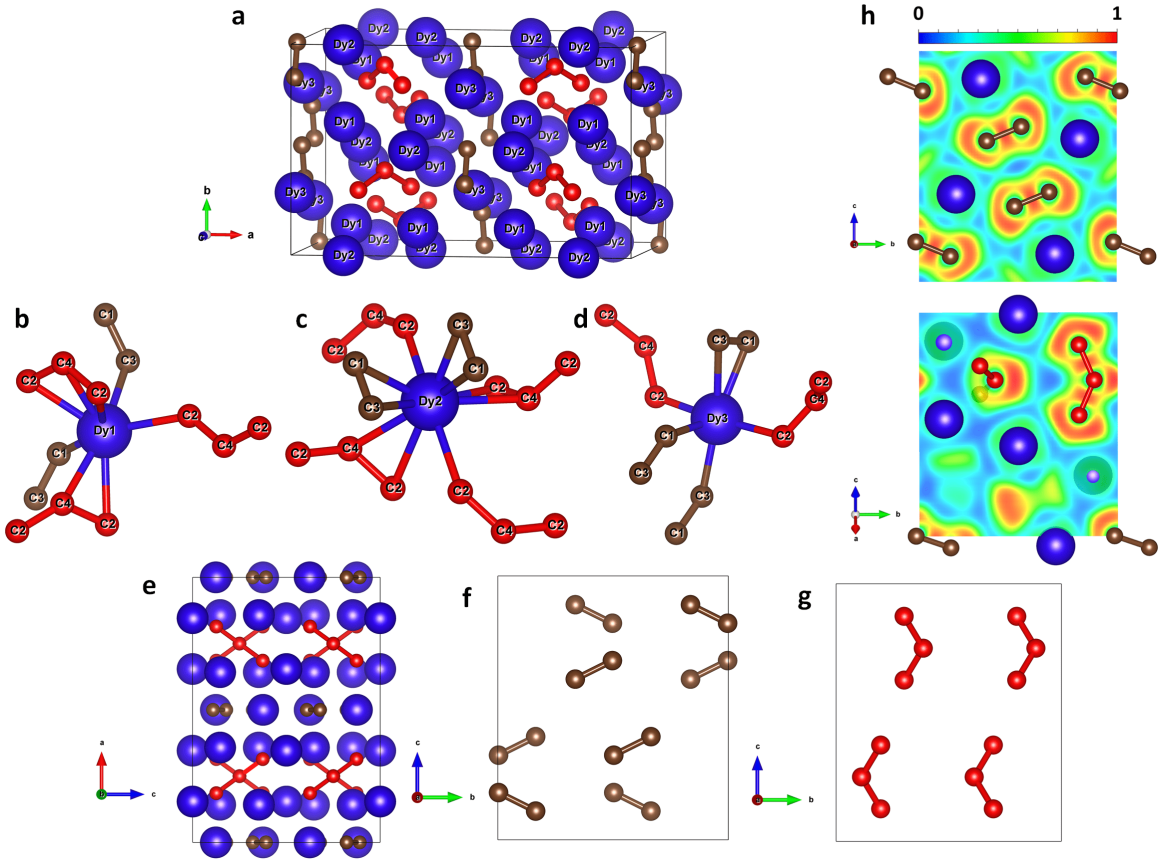

Fig. S2. Crystal structure of γ-Dy_4C_5. All Dy atoms are blue, brown balls represent carbon atoms of the dumbbells, red balls – carbon atoms forming trimers; grey thin lines outline the unit cell. (a) A general view of the crystal structure. (b)-(d) The coordination environment of the Dy1, Dy2 and Dy3 atoms. (e) The unit cell viewed along the *b* direction. (f) Arrangement of [C_2] units in the rows along the *b* direction (Dy atoms in the rows are not shown). (g) Arrangement of [C_3] units. (h) The electron localization function (ELF) calculated in the (1 0 0) plane containing carbon dumbbells [C_2] (top) and in the plane containing carbon trimers [C_3] (bottom).

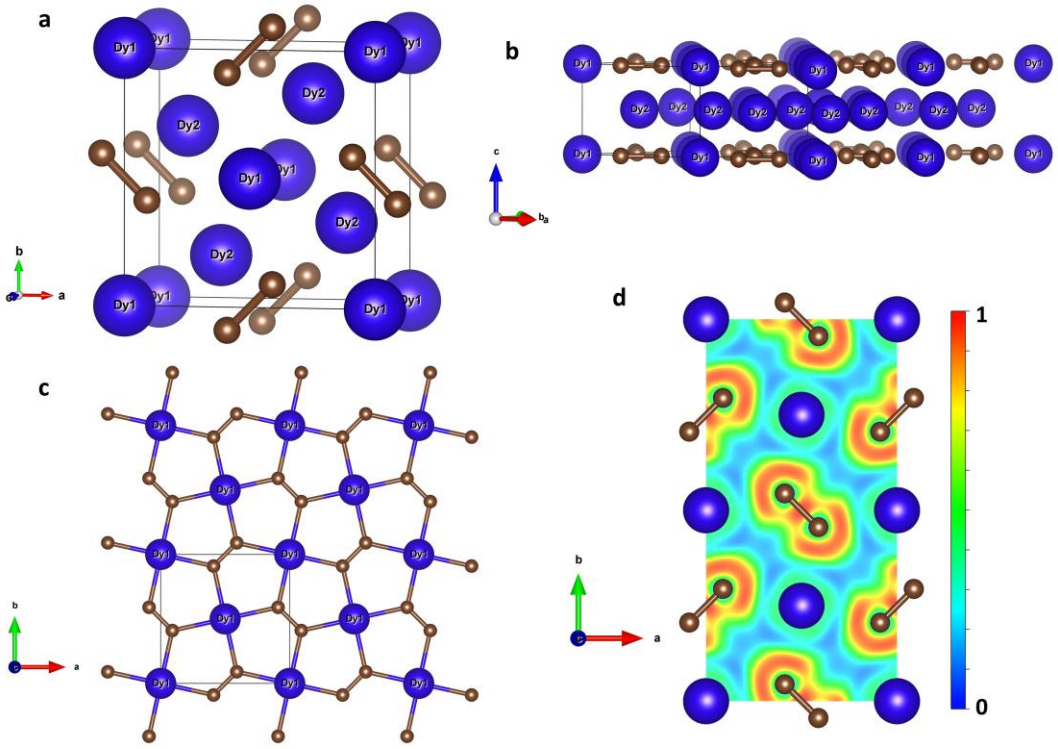

Fig. S3. Crystal structure and calculated properties of Dy_3C_2 at 68(3) GPa. All Dy atoms are blue, C atoms are brown; grey thin lines outline the unit cell. (a) A view of the unit cell. (b) A view of crystal structure representing the "Dy1-C" and "Dy2" layers alternating along the *c*-axis. (c) A view of the flat layer consisting of Dy1 and carbon atoms (along the *c*-axis). (d) The electron localization function calculated in the (0 0 1) plane containing carbon dumbbells [C_2].

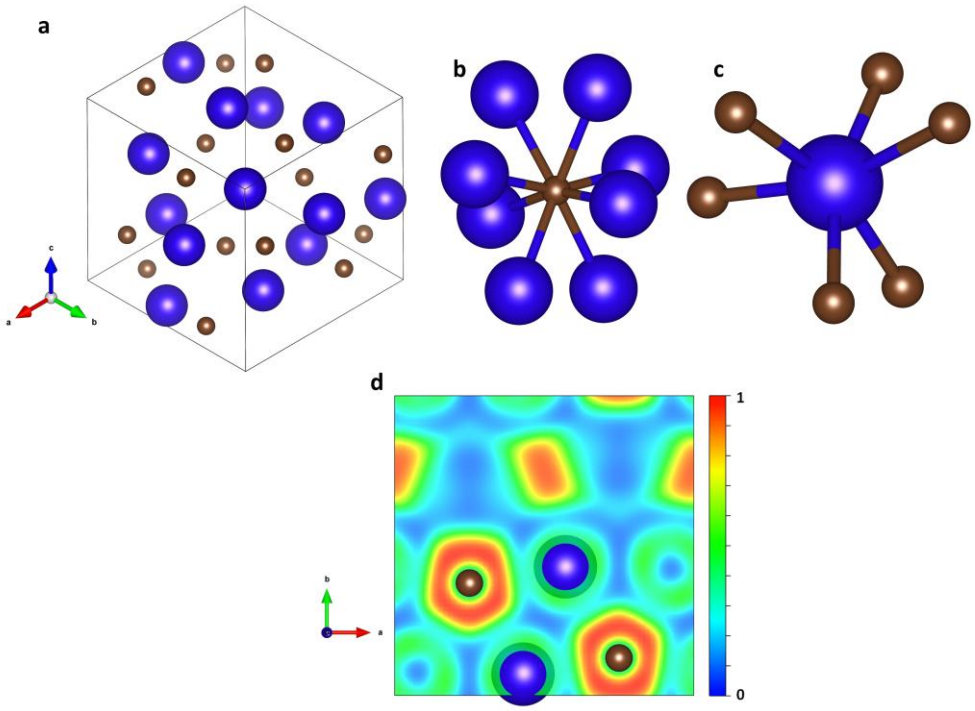

Fig. S4. Crystal structure and calculated properties of Dy_4C_3 at 95(3) GPa. Dy atoms are blue, C atoms are brown; grey thin lines outline the unit cell. (a) A view of the crystal structure along

the (1 1 1) direction. (b) The coordination environment of the Dy atom. (c) The coordination environment of the C atoms. (d) The electron localization function calculated in the (0 0 1) plane.

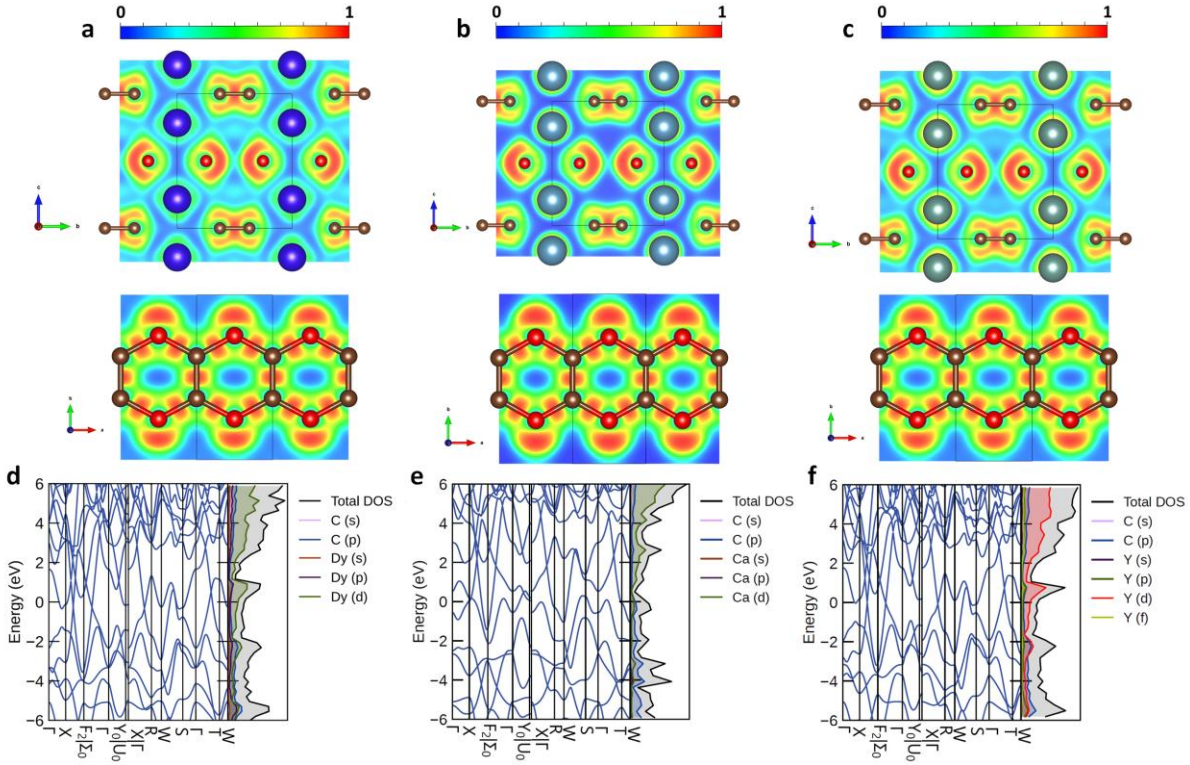

Fig. S5. Results of DFT-based calculations. The electron localization functions calculated in the (1 0 0) (top) or in the (0 0 1) plane containing carbon ribbons (bottom) for (a) γ-DyC_2, (b) HP-CaC_2, and (c) YC_2 relaxed at 70 GPa. The electron density of states and band structure along high-symmetry directions in the Brillouin zone for (d) γ-DyC_2 (in frozen-core approximation), (e) HP-CaC_2, and (f) YC_2 at 70 GPa.

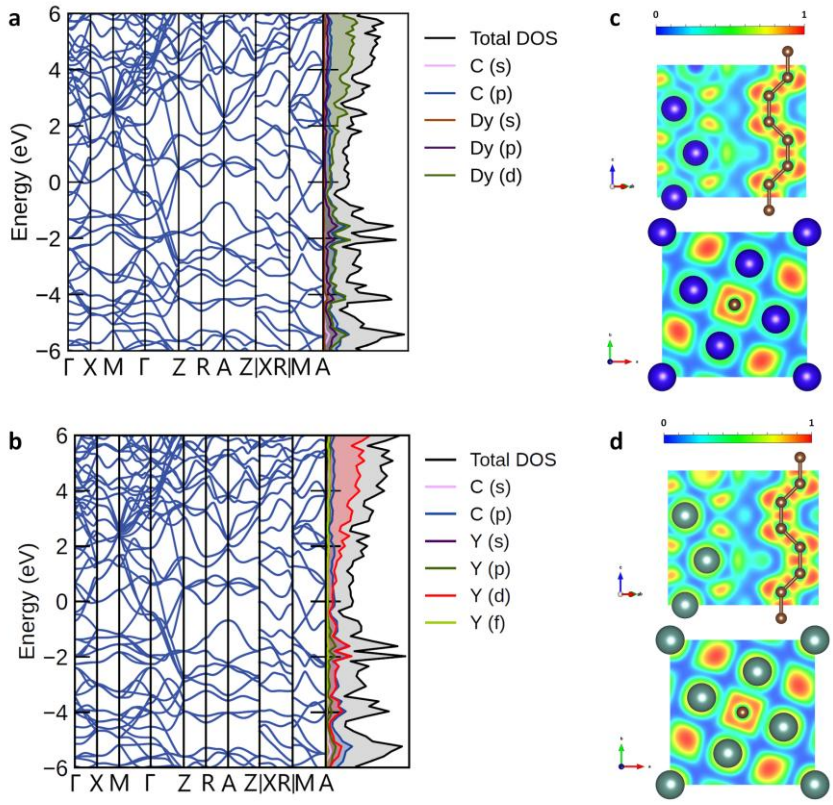

Fig. S6. Results of DFT-based calculations. The electron density of states and band structure along high-symmetry directions in the Brillouin zone for (a) Dy_5C_9 (in frozen-core approximation) and (b) Y_5C_9 at 70 GPa. The electron localization function calculated in the (-1 1 0) plane containing carbon chains (top) or in (0 0 1) (bottom) for (c) Dy_5C_9 and (d) Y_5C_9 relaxed at 70 GPa.

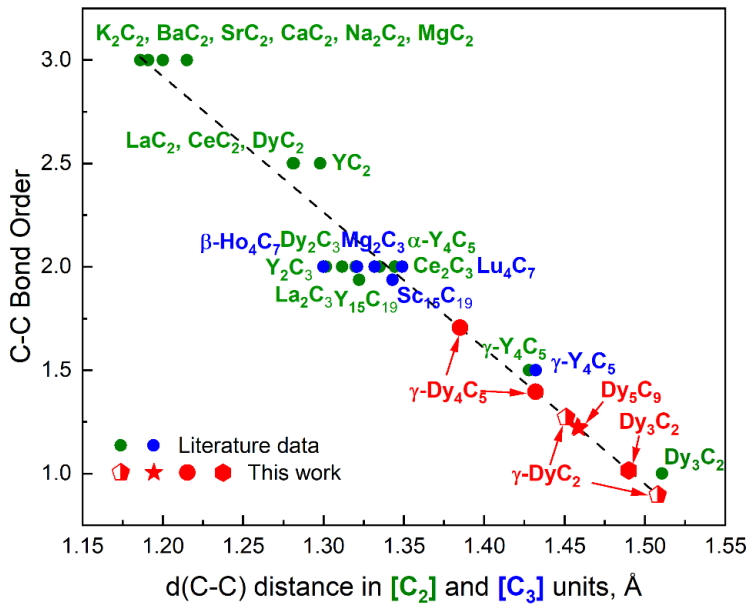

Fig. S7. Correlation between the C-C distances in $[C_2]$ and $[C_3]$ units, *d*(C-C), and their bond order in a number of binary metal-carbon compounds. Literature data are from experiments [5–

23], except for γ-Y_4C_5 [4] and for Dy_2C_3 and Dy_3C_2 [24] (DFT-computed structures were fully relaxed at 1 bar). Straight line is a result of the fit of literature data ("green" and "blue" data-points) and described by equation: *EBO = 10.81 – 6.57×d(C-C).*

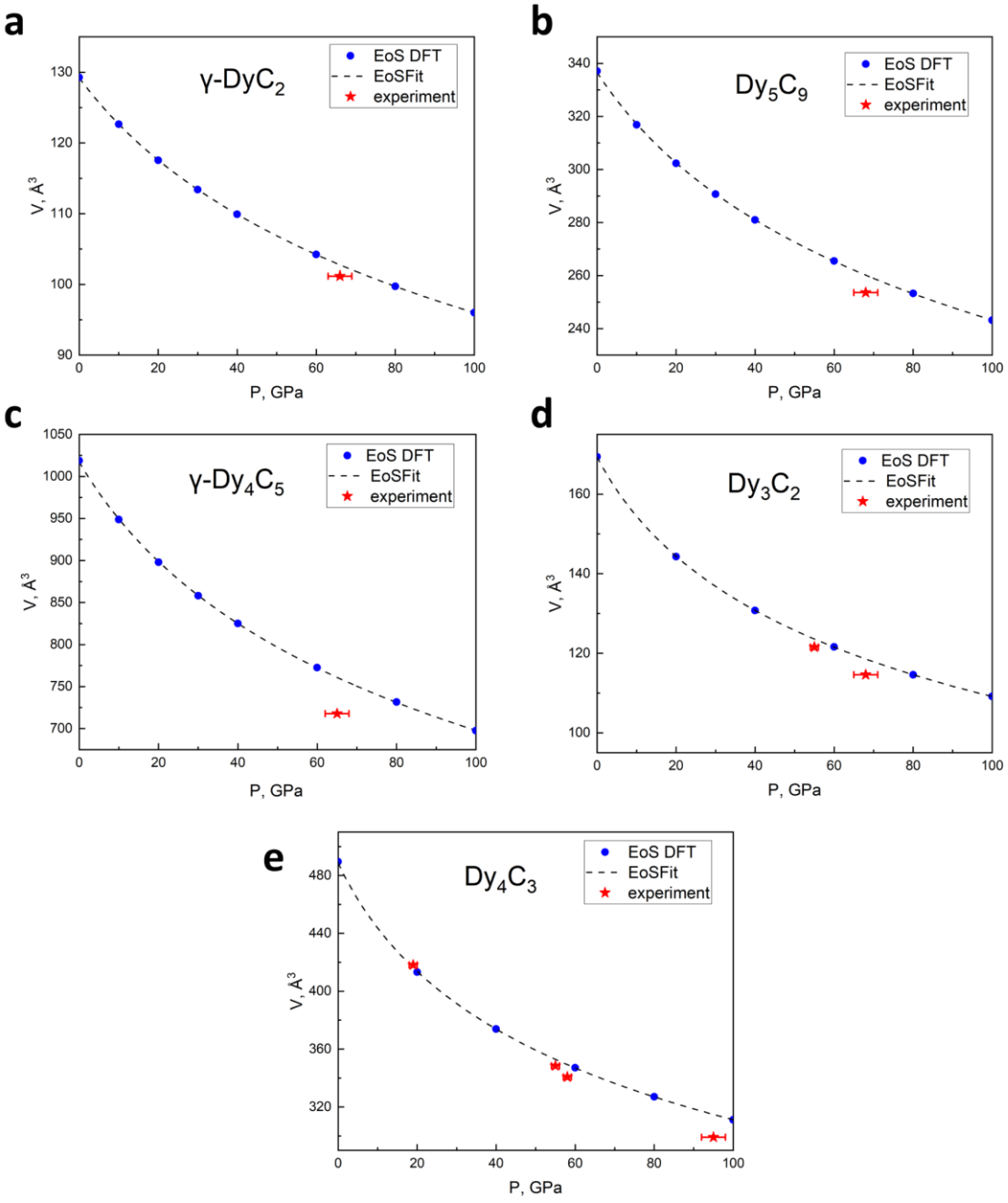

Fig. S8. Calculated P-V curves for relaxed (a) γ-DyC_2, (b) Dy_5C_9, (c) γ-Dy_4C_5, (d) Dy_3C_2, and (e) Dy_4C_3 structures in comparison with experimental data. The data for Dy_4C_3 at 19-58 GPa were obtained in previous study [24].

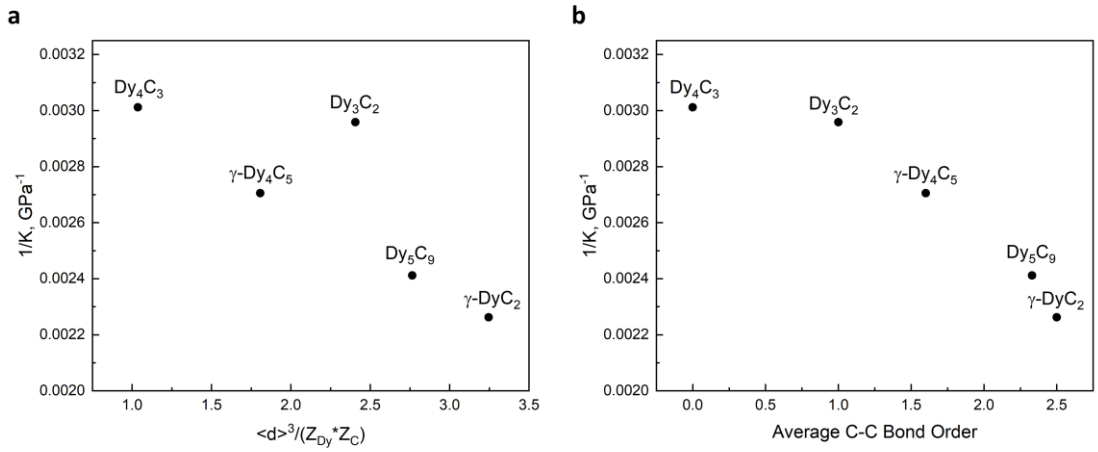

Fig. S9. (a) Correlation between compressibility and the ratio $<d>^3/(Z_{Dy}*Z_C)$ ($<d>$ is an average Dy-C distance in the first coordination sphere, Z_{Dy} and Z_C are the 'charges' of dysprosium and carbon, respectively). (b) Correlation between compressibility $1/K$ (K is the bulk modulus) and 'average bond order' of carbon atoms in synthesized compounds.

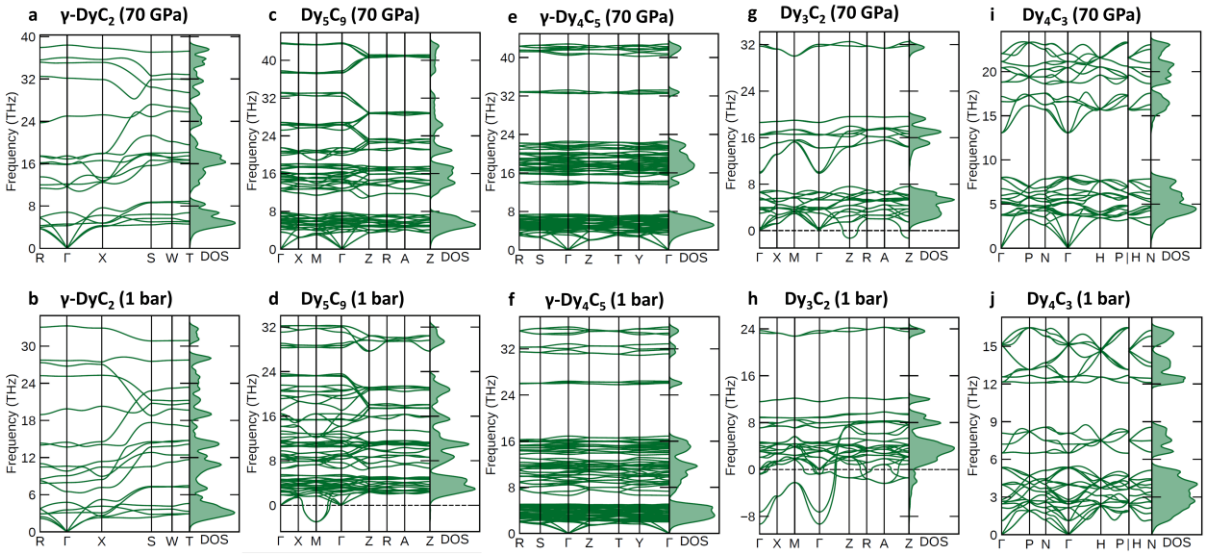

Fig. S10. Phonon dispersion curves along high-symmetry directions in the Brillouin zone and phonon density of states calculated for γ-DyC_2, Dy_5C_9, γ-Dy_4C_5, Dy_3C_2, and Dy_4C_3 at 70 GPa and 1 bar.

Supplementary References

[1] Y.L. Li, S.N. Wang, A.R. Oganov, H. Gou, J.S. Smith, T.A. Strobel, Investigation of exotic stable calcium carbides using theory and experiment, Nat. Commun. 6 (2015) 1–9. https://doi.org/10.1038/ncomms7974.

[2] S. Khandarkhaeva, T. Fedotenko, A. Aslandukova, F.I. Akbar, M. Bykov, D. Laniel, A. Aslandukov, U. Ruschewitz, C. Tobeck, B. Winkler, S. Chariton, V. Prakapenka, K.

Glazyrin, C. Giacobbe, E.L. Bright, M. Belov, N. Dubrovinskaia, L. Dubrovinsky, Extending carbon chemistry at high-pressure by synthesis of CaC2 and Ca3C7 with deprotonated polyacene- and para-poly(indenoindene)-like nanoribbons, Nat. Commun. 15 (2024) 2855. https://doi.org/10.1038/s41467-024-47138-2.

[3] X. Feng, S. Lu, C.J. Pickard, H. Liu, S.A.T. Redfern, Y. Ma, Carbon network evolution from dimers to sheets in superconducting ytrrium dicarbide under pressure, Commun. Chem. 1 (2018) 1–7. https://doi.org/10.1038/s42004-018-0085-0.

[4] A. Aslandukova, A. Aslandukov, L. Yuan, D. Laniel, S. Khandarkhaeva, T. Fedotenko, G. Steinle-Neumann, K. Glazyrin, N. Dubrovinskaia, L. Dubrovinsky, Novel High-Pressure Yttrium Carbide γ-Y4C5 Containing [C2] and Nonlinear [C3] Units with Unusually Large Formal Charges, Phys. Rev. Lett. 127 (2021) 135501. https://doi.org/10.1103/PhysRevLett.127.135501.

[5] O. Reckeweg, A. Baumann, H.A. Mayer, J. Glaser, H.J. Meyer, On the coexistence of tetragonal and monoclinic CaC2: Structural and spectroscopic studies on alkaline earth metal acetylides, MC2 (M = Ca, Sr, Ba), Zeitschrift Fur Anorg. Und Allg. Chemie 625 (1999) 1686–1692. https://doi.org/10.1002/(sici)1521-3749(199910)625:10<1686::aid-zaac1686>3.3.co;2-o.

[6] K. Klöss, D. Hinz-Hübner, U. Ruschewitz, Über eine neue Modifikation des Na2C2, Zeitschrift Für Anorg. Und Allg. Chemie 628 (2002) 2701–2704. https://doi.org/https://doi.org/10.1002/1521-3749(200212)628:12<2701::AID-ZAAC2701>3.0.CO;2-%23.

[7] M. Atoji, Neutron diffraction study of Ce2C3 at low temperatures, J. Chem. Phys. 46 (1967) 4148–4149. https://doi.org/10.1063/1.1840499.

[8] G.Y. Adachi, Y. Shibata, K. Ueno, J. Shiokawa, Heats of the tetragonal-cubic transformation in rare earth dicarbides and mixed rare earth dicarbide solid solutions, J. Inorg. Nucl. Chem. 38 (1976) 1023–1026. https://doi.org/10.1016/0022-1902(76)80021-8.

[9] Y. Yosida, Surface superconductivity and structural analysis of YC2 single crystals encapsulated in carbon nanocages, J. Appl. Phys. 92 (2002) 5494–5497. https://doi.org/10.1063/1.1510946.

[10] M.C. Krupka, A.L. Giorgi, N.H. Krikorian, E.G. Szklaizz, High-pressure synthesis of yttrium-thorium sesquicarbide: A new high-temeperature superconductor, J. Less-Common Met. 19 (1969) 113–119. https://doi.org/10.1016/0022-5088(69)90026-5.

[11] R. Czekalla, T. Hüfken, W. Jeitschko, R.D. Hoffmann, R. Pöttgen, The Rare Earth

Carbides R4C5 with R=Y, Gd, Tb, Dy, and Ho, J. Solid State Chem. 132 (1997) 294–299. https://doi.org/10.1006/jssc.1997.7461.

[12] M. Atoji, K. Gschneidner, A.H. Daane, R.E. Rundle, F.H. Spedding, The Structures of Lanthanum Dicarbide and Sesquicarbide by X-Ray and Neutron Diffraction, J. Am. Chem. Soc. 80 (1958) 1804–1808. https://doi.org/10.1021/ja01541a008.

[13] R. Czekalla, W. Jeitschko, R.-D. Hoffmann, H. Rabeneck, Preparation, Crystal Structure, and Properties of the Lanthanoid Carbides Ln4C7 with Ln = Ho, Er, Tm, and Lu, Zeitschrift Für Naturforsch. B 51 (1996) 646–654. https://doi.org/10.1515/znb-1996-0505.

[14] H. Ninomiya, T. Koshinuma, T. Nishio, H. Fujihisa, K. Kawashima, I. Hase, S. Ishida, H. Ogino, A. Iyo, Y. Yoshida, Y. Gotoh, H. Eisaki, Experimental and Computational Determination of Optimal Boron Content in Layered Superconductor Sc20C8-xBxC20, Inorg. Chem. 59 (2020) 14290–14295. https://doi.org/10.1021/acs.inorgchem.0c02090.

[15] T.W. Button, I.J. McColm, Reaction of carbon with lanthanide silicides IV: The Y5Si3-C system, J. Less-Common Met. 97 (1984) 237–244. https://doi.org/10.1016/0022-5088(84)90028-6.

[16] S. Hemmersbach, B. Zibrowius, U. Ruschewitz, Na2C2 und K2C2: Synthese, Kristallstruktur und spektroskopische Eigenschaften, Z. Anorg. Allg. Chem. 625 (1999) 1440–1446. https://doi.org/10.1002/(SICI)1521-3749(199909)625.

[17] H. Fjellvág, P. Karen, Crystal Structure of Magnesium Sesquicarbide, Inorg. Chem. 31 (1992) 3260–3263. https://doi.org/10.1021/ic00041a018.

[18] P. Karen, A. Kjekshus, Q. Huang, V.L. Karen, The crystal structure of magnesium dicarbide, J. Alloys Compd. 282 (1999) 72–75. https://doi.org/10.1016/S0925-8388(98)00828-7.

[19] V. Babizhetskyy, O. Jepsen, R.K. Kremer, A. Simon, B. Ouladdiaf, A. Stolovits, Structure and bonding of superconducting LaC2, J. Phys. Condens. Matter 26 (2014) 025701. https://doi.org/10.1088/0953-8984/26/2/025701.

[20] F.H. Spedding, K. Gschneidner Jr., A.H. Daane, The Crystal Structures of Some of the Rare Earth Carbides, J. Am. Chem. Soc. 80 (1958) 4499–4503. https://doi.org/10.1021/ja01550a017.

[21] V. Vohn, W. Kockelmann, U. Ruschewitz, On the synthesis and crystal structure of BaC2, J. Alloys Compd. 284 (1999) 132–137. https://doi.org/10.1016/S0925-8388(98)00957-8.

[22] V. Vohn, M. Knapp, U. Ruschewitz, Synthesis and crystal structure of SrC2, J. Solid

State Chem. 151 (2000) 111–116. https://doi.org/10.1006/jssc.2000.8630.

[23] M. Atoji, Magnetic and crystal structures of CeC2, PrC2, NdC2, TbC2, and HoC2 at low temperatures, J. Chem. Phys. 46 (1967) 1891–1901. https://doi.org/10.1063/1.1840950.

[24] F.I. Akbar, A. Aslandukova, A. Aslandukov, Y. Yin, F. Trybel, S. Khandarkhaeva, T. Fedotenko, D. Laniel, M. Bykov, E. Bykova, N. Dubrovinskaia, L. Dubrovinsky, High-pressure synthesis of dysprosium carbides, Front. Chem. 11 (2023) 1–9. https://doi.org/10.3389/fchem.2023.1210081.

4.3 High-Pressure Synthesis of Rare-Earth Metals Carbides Featuring Carbon Polyanions

Fariia Iasmin Akbar[1,2*], Alena Aslandukova[1], Andrey Aslandukov[1,2], Yuqing Yin[2,3], Elena Bykova[4], Maxim Bykov[5], Dominique Laniel[6], Pavel Milkin[7], Wenju Zhou[2], Timofey Fedotenko[8], Konstantin Glazyrin[8], Hanns-Peter Liermann[8], Eleanor Lawrence Bright[9], Jonathan Wright[9], Anna Pakhomova[9], Gaston Garbarino[9], Mohamed Mezouar[9], Stella Chariton[10], Vitali Prakapenka[10], Davide Comboni[9], Michael Hanfland[9], Natalia Dubrovinskaia[2,3], and Leonid Dubrovinsky[1*]

[1] Bavarian Research Institute of Experimental Geochemistry and Geophysics (BGI), University of Bayreuth, Univesitaetsstrasse 30, 95440 Bayreuth, Germany

[2] Material Physics and Technology at Extreme Conditions, Laboratory of Crystallography, University of Bayreuth, Univesitaetsstrasse 30, 95440 Bayreuth, Germany

[3] Department of Physics, Chemistry and Biology (IFM), Linköping University, SE-581 83, Linköping, Sweden

[4] Institute of Geosciences, Goethe University Frankfurt, Altenhöferallee 1, 60438 Frankfurt am Main, Germany

[5] Institute of Inorganic and Analytical Chemistry, Goethe University Frankfurt, Max-von-Laue-Straße 7, 60438 Frankfurt am Main, Germany

[6] Centre for Science at Extreme Conditions and School of Physics and Astronomy, University of Edinburgh, EH9 3FD Edinburgh, United Kingdom

[7] Faculty of Engineering Sciences, University of Bayreuth, Ludwig Thoma Str. 36A, Bayreuth 95447, Germany

[8] Deutsches Elektronen-Synchrotron DESY, Notkestrasse 85, 22607 Hamburg, Germany

[9] European Synchrotron Radiation Facility, CS 40220, 38043 Grenoble Cedex 9, France

[10] Center for Advanced Radiation Sources, University of Chicago Chicago, Illinois 60637, USA

***Corresponding authors:** Fariia Iasmin Akbar Fariia.Akbar@uni-bayreuth.de; Leonid Dubrovinsky Leonid.Dubrovinsky@Uni-Bayreuth.de

Keywords: high-pressure, diamond anvil cell, rare-earth carbides, carbides, rare-earth elements, lanthanides carbides.

To be submitted to *JACS*

4.3.1 Abstract

Studying the chemistry of materials under high pressure reveals new compounds and phenomena. In this investigation, rare-earth elements reacted with carbon in laser-heated diamond anvil cells at pressures up to 124 GPa and temperatures of 2500 K. *In situ* single-crystal synchrotron X-ray diffraction (XRD) analysis unveiled novel rare-earth carbides, such as β-LaC, γ-SmC, Nd_5C_7, La_3C_5, ε-LaC_2, δ-NdC_2, along with previously reported Dy_3C_2, Dy_4C_3, γ-Dy_4C_5, Dy_5C_9, and γ-DyC_2. Various rare-earth metal carbides yielded similar structures, suggesting regularities in their crystal chemistry under extreme conditions. γ-SmC and δ-NdC_2 feature infinite flat carbon *cis*-polyacetylene-type chains, while La_3C_5 and ε-LaC_2 consist of naphthalene-decalin-like entities, which have never been observed or predicted before. In the structures of β-LaC and Nd_5C_7, carbon atoms form dimers and non-linear trimers, respectively. Nd_5C_7 and γ-Sm_4C_5 (isostructural to γ-Dy_4C_5) were recovered to ambient conditions. Density functional theory calculations corroborate the findings and reveal conjugated π-electron systems in novel infinite carbon polyanions. This study sheds light on the regularities in high-pressure rare-earth metal carbides chemistry and shows the route for the synthesis of novel carbon species through direct reactions of carbon with metals.

4.3.2 Introduction

High pressure can significantly affect the chemistry of materials, making this topic of considerable interest. The synthesis of atypical compounds is highly intriguing, referring to those with compositions and structures deviating from those common at ambient conditions, and leading to the formation of polyanion arrangements in various systems, including polyhalides [1,2], polynitrides [3–10], polyborides [11,12], polyhydrides [13–16]. The phenomenon of homonuclear bond formation can be attributed to the increase in resonance integrals as pressure rises, leading to a larger gap between bonding and antibonding states, resulting in stronger bonds. This effect is relatively less pronounced for heteronuclear bonds, suggesting the existence of non-intuitive compounds featuring homonuclear bonds [16]. It dramatically enriches chemistry enabling the design of novel materials with peculiar properties for potential applications, such as one-dimensional materials in electronics, supercapacitors, membranes, catalysis, and sensors [17]. For instance, graphene's 1D conductive nanoribbon allotrope exhibits exceptional electronic properties and can be used in electronic devices due to its tunable band gap [18].

The polyanions in carbides formed at high-pressures occasionally exhibit similarities to motifs found in organic chemistry. Increasing pressure contributes to the formation of more complex arrangements, progressing from carbon dumbbells and trimers (Dy_3C_2 [19], Mg_2C_3 [20], γ-Y_4C_5 [21]) to carbon chains and ribbons (Dy_5C_9 and γ-DyC_2 [22], HP-CaC_2 and Ca_3C_7 [23], LiC_2 and Li_3C_4 [24], Li_2C_2 [25]).

Recently, several new structural types were discovered and characterized in the dysprosium-carbon system under extreme conditions [22]. The reproduction of the novel structure of γ-Y_4C_5 containing carbon dimers and trimers [21] by γ-Dy_4C_5 [22], the predicted *Immm*-YC_2 consisting of flat carbon ribbons [26] – by γ-DyC_2, and the predicted *P*4/*mbm*-Ca_3C_2 comprising carbon dumbbells [27] – by Dy_3C_2 [22] inspired further investigation of rare-earth carbides systematically.

Here we report the results of high-pressure high-temperature (HPHT) synthesis experiments using laser-heated DACs which revealed the systematic formation of novel rare-earth metals carbides of 13 structural types at pressures up to 124 GPa. The crystal structures of REE_xC_y (REE = Sc, Y, La, Nd, Sm, Gd, Dy, and Yb) carbides were determined and refined based on single-crystal synchrotron X-ray diffraction. In total, 32 novel compounds were synthesized. The synthesized Nd_5C_7 and γ-Sm_4C_5 (isostructural to the recently discovered γ-Y_4C_5 [21]) were found to be recoverable to ambient conditions.

4.3.3 Materials and methods

4.3.3.1 Nomenclature

For the sake of clarity for readers, in this paper we use simplified nomenclature of anionic units in the crystal structures of REE-C compounds (REE = Sc, Y, La, Nd, Sm, Gd, Dy, and Yb). In particular, unless otherwise specified, we mean completely deprotonated species; saying ‘ethanide’, we mean ethanehexaide C_2^{6-}; ‘polyacetylide’ – deprotonated polyacetylene poly-[ethene-1,2-diyl]; ‘polyacenide’ – deprotonated polyacene or poly(buta-1,3,-diene-1,4:3,2-tetrayl); ‘naphthalenide’ – deprotonated naphthalene or bicyclo[4.4.0]deca-1,3,5,7,9-pentaene; ‘decalinide’ – deprotonated decalin or decahydronaphthalene or bicyclo[4.4.0]decane.

4.3.3.2 Sample preparation

Diamond anvils with culet diameters of 250 μm and 120 μm were aligned in BX90-type diamond anvil cells (DACs) [28]. Rhenium gaskets with an initial thickness of 200 μm were indented down to ~28 μm and ~22 μm, respectively. Sample cavities with diameters of

105 μm and 55 μm, respectively, were laser-drilled at the indentations centers. Pure Sc, Y, La, Nd, Sm, Gd, and Yb (99.9% purity, Merc Inc.) flakes and a layer of dry sodium chloride (99.999% purity, ChemPUR) were placed between the diamond anvils. The sodium chloride served as a thermal insulator and pressure-transmitting medium [29], while the diamond anvils acted as a source of carbon. Three additional experiments were conducted with Sm loaded in argon at ~44, 103, and 117 GPa to check the influence of the pressure medium on the reaction between a metal and diamond. Argon is a weaker thermal insulator than NaCl which makes the laser heating procedure more complicated and requires higher laser beam energy, as observed experimentally during the heating of samples. Since argon is softer under high pressure than NaCl, the metal piece might move from the diamond surface during laser heating precluding direct reaction between the loaded metal and carbon form diamond anvil [30].

Samples were compressed to the desired pressure and laser-heated up to 2500(200) K. Laser heating of the samples was carried out using an *in house* double-sided YAG laser (1064 nm wavelength) heating setup. Thermal emission spectra from the heated area were collected using IsoPlane SCT 320 spectrometer with a 1024×2560 PI-MAX 4 camera [31]. The pressure was determined using the NaCl equation of states (EoS) [32,33].

4.3.3.3 X-ray diffraction

The reaction products were analyzed by single-crystal X-ray diffraction measurements at several synchrotron beamlines: P02.2 of DESY, Hamburg, Germany ($\lambda \approx 0.29$ Å, beam size ~ 2 × 2 μm^2) [34]; ID11 of ESRF, Grenoble, France ($\lambda \approx 0.2846$ Å, beam size ~ 0.75 × 0.75 μm^2); ID15B of ESRF, Grenoble, France ($\lambda \approx 0.41$ Å, beam size ~ 1.5 × 1.5 μm^2); ID27 of ESRF, Grenoble, France ($\lambda \approx 0.3738$ Å, beam size ~ 1.5 × 1.5 μm^2). Powder XRD images were collected upon continuous rotation of the sample in a range of ±20° around the vertical ω axis at DESY, and ±1° around the vertical ω axis at ESRF. During single-crystal data collection, the cell was rotated from –38° to +38° with narrow 0.5° steps. Creating maps with XDI software [35] helps to visualize the phases distribution within the pressure chamber and to locate areas where the step-scans were performed. The CrysAlis^{Pro} software package [36] was used for the analysis of the single-crystal XRD data (peak hunting, indexing, data integration, frame scaling, and absorption correction). To calibrate an instrumental model in the CrysAlis^{Pro} software, i.e. the sample-to-detector distance, detector's origin, offsets of the goniometer angles, and inclination of both the X-ray beam and detector with respect to the instrument axis, we used a single crystal of orthoenstatite [$(Mg_{1.93}Fe_{0.06})(Si_{1.93},Al_{0.06})O_6$, *Pbca* space group, a = 8.8117(2) Å, b = 5.18320(10) Å, and c = 18.2391(3) Å]. The DAFi program

was used to search for reflection's groups belonging to individual single crystal domains [37]. Using the OLEX2 software package [38], the structures were solved with the ShelXT structure solution program [39] using intrinsic phasing and refined with the ShelXL [40] refinement package using least-squares minimization. Crystal structure visualization was made with the VESTA software [41]. The equations of state were obtained by fitting the pressure-volume dependence data using the EoSFit7-GUI [42].

The properties of the synthesized compounds were determined through the first-principles calculations using the framework of density functional theory (DFT) as implemented in the VASP (Vienna ab initio simulation package) code [43] (see Supplemental materials).

4.3.4 Results and discussion

A summary of our experiments is presented in Table S1. High-pressure reactions between rare-earth metals and carbon in diamond anvil cells (DACs) at pressures of ~34-124 GPa and temperatures of ~2200-2500 K resulted in the formation of rare-earth carbides of 13 distinct structural types, among which 9 were previously unknown. In total, 32 novel compounds were discovered (Tables 1 and S1-S22, Fig. 1 and 2).

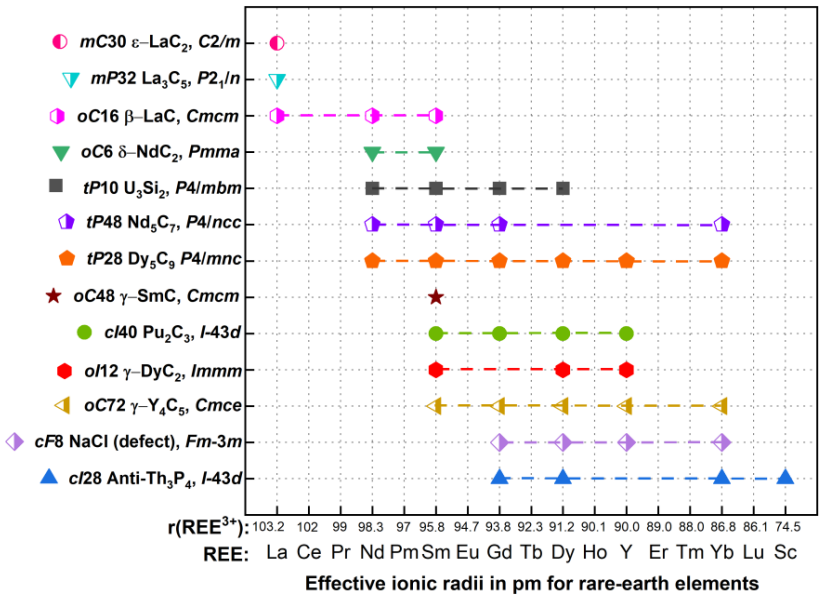

Figure 1. Summary of the high-pressure high-temperature experiments (ionic radii of rare-earth elements r(REE^{3+}) are from [44]). Yttrium carbides Y_2C_3 and γ-Y_4C_5 and dysprosium carbides Dy_3C_2, Dy_5C_9, Dy_2C_3, γ-DyC_2, γ-Dy_4C_5, and Dy_4C_3 were synthesized and characterized earlier in [19,21,22].

Table 1. List of compounds synthesized in this work and their crystallographic characteristics.

Structure type	Space group	Chemical formula	Synthesis pressure (GPa)
*mC*30 ε-LaC_2	*C*2/*m*	ε-LaC_2	45(1), 59(1), 67(1)
*mP*32 La_3C_5	$P2_1/n$	La_3C_5	45(1), 67(1)
*oC*16 β-LaC	*Cmcm*	β-LaC	41(1), 45(1), 59(1), 68(1)
		β-NdC	43(1), 57(1)
		β-SmC	51(1)
*oC*6 δ-NdC_2 (predicted in the La-C system [45])	*Pmma*	δ-NdC_2	43(1), 55(1)
		δ-SmC_2	44(1)
*tP*10 U_3Si_2	*P*4/*mbm*	Nd_3C_2	43(1), 57(1)
		Sm_3C_2	44(1)
		Gd_3C_2	45(1)
		Dy_3C_2 [19], [22]	55(1), 68(3)
*tP*48 Nd_5C_7	*P*4/*ncc*	Nd_5C_7	57(1)
		Sm_5C_7	42(1), 50(1)
		Gd_5C_7	45(1)
		Yb_5C_7	42(1), 60(1)
*tP*28 Dy_5C_9 [22]	*P*4/*mnc*	Y_5C_9	68(3)
		Nd_5C_9	57(1) (observed at 37(2) GPa during the decompression)
		Sm_5C_9	42(1), 44(1), 50(1), 62(1)
		Gd_5C_9	46(1), 58(1)
		Dy_5C_9 [22]	68(3)
		Yb_5C_9	43(1), 60(1)
*oC*48 γ-SmC	*Cmcm*	γ-SmC	103(4)
*cI*40 Pu_2C_3	*I*-43*d*	Y_2C_3 [21]	46(1)
		Sm_2C_3	42(1)
		Gd_2C_3	32(2), 44(1), 57(1)
		Dy_2C_3 [19]	19(1)
	Immm	γ-YC_2	94(3), 124(3)
		γ-SmC_2	62(1), 103(4), 117(4)

*oI*12 γ-DyC_2 (predicted in the Y-C system [26])		γ-DyC_2 [22]	66(3)
*oC*72 γ-Y_4C_5 [21]	*Cmce*	γ-Y_4C_5 [21]	44(1)
		γ-Sm_4C_5	42(1), 44(1)
		γ-Gd_4C_5	34(1), 45(1)
		γ-Dy_4C_5 [22]	65(3)
		γ-Yb_4C_5	42(1)
*cF*8 NaCl (defect)	*Fm*-3*m*	Y_xC	40(1)
		Gd_xC	34(2), 46(1)
		Dy_xC	43(1)
		Yb_xC	42(1)
*cI*28 Anti-Th_3P_4	*I*-43*d*	Sc_4C_3	64(1)
		Gd_4C_3	32(2), 34(2), 46(1)
		Dy_4C_3 [19], [22]	19(1), 55(1), 58(1), 95(3)
		Yb_4C_3	42(1)

* Dy_3C_2, Dy_5C_9, Dy_2C_3, γ-DyC_2, γ-Dy_4C_5, and Dy_4C_3 were synthesized in the previous studies [19,22], Y_2C_3 and γ-Y_4C_5 were synthesized in the work [21].

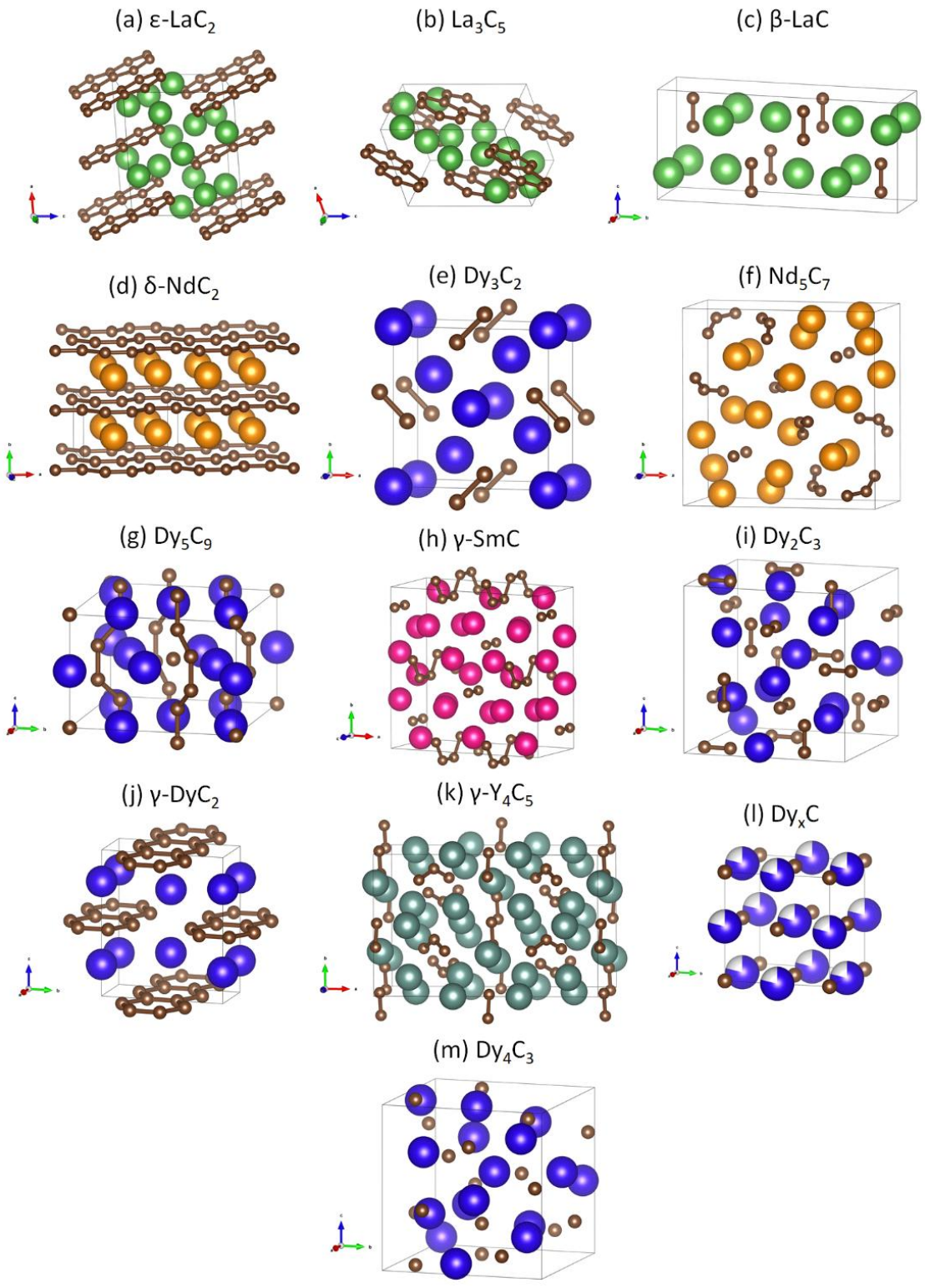

Figure 2. Crystal structures of rare-earth metals carbides synthesized under extreme conditions: (a) ε-LaC_2, (b) La_3C_5, (c) β-LaC (β-NdC, β-SmC), (d) δ-NdC_2 (δ-SmC_2), (e) Dy_3C_2 (Nd_3C_2, Sm_3C_2, Gd_3C_2), (f) Nd_5C_7 (Sm_5C_7, Gd_5C_7, Yb_5C_7), (g) Dy_5C_9 (Y_5C_9, Nd_5C_9, Sm_5C_9, Gd_5C_9, Yb_5C_9), (h) γ-SmC, (i) Dy_2C_3 (Y_2C_3, Sm_2C_3, Gd_2C_3), (j) γ-DyC_2 (γ-YC_2, γ-SmC_2), (k) γ-Y_4C_5 (γ-Sm_4C_5, γ-Gd_4C_5, γ-Dy_4C_5), (l) Dy_xC (Y_xC, Gd_xC, Yb_xC), (m) Dy_4C_3 (Sc_4C_3, Gd_4C_3, Yb_4C_3). Dy_3C_2, Dy_5C_9, Dy_2C_3, γ-DyC_2, γ-Dy_4C_5, and Dy_4C_3 were synthesized in the previous studies [19,22], Y_2C_3 and γ-Y_4C_5 were synthesized in the work [21].

4.3.4.1 Rare-earth metal carbides containing discrete carbon atoms

Carbides with the defect *cF*8 NaCl-type and *cI*28 anti-Th_3P_4-type structures were found as products of high-pressure high-temperature synthesis (Table 1, Fig. 1 and 2). These carbides contain single carbon atoms.

Anti-Th_3P_4-type structure has been known only for scandium carbide, *cI*28 Sc_4C_3, at ambient pressure [46,47], while the Dy_4C_3 was observed at 19 GPa in a DAC for the first time [19]. In the investigated rare-earth metals-carbon systems, carbides with the anti-Th_3P_4 structure type were synthesized for scandium, gadolinium and ytterbium at ~32-64 GPa (Tables 1, S1 and S2, Fig. 1 and 2). Rare-earth carbides REE_4C_3 (REE – rare-earth element) possess the cubic space group *I-43d*, #220 (*Z* = 4) with two occupied Wyckoff positions: 16*c*(REE1) and 12*a*(C1). Since their structure represents discrete carbon atoms assuming the formula $REE^{3+}{}_4C^{4-}{}_3$, these compounds can be classified as methanides [19]. Based on the previously demonstrated resemblance between Dy_4C_3 and known sesquicarbide Dy_2C_3 [19], the sites of discrete carbon atoms coincide with the positions of the centers of carbon dumbbells in known rare-earth sesquicarbides featuring a Pu_2C_3-type structure (Fig. S1). The combined experimental data for Dy_4C_3 synthesized at 19-95 GPa [19,22] are fitted using the 2nd order Birch-Murnaghan equation of state (BM2 EoS), as illustrated in Fig. S2.

Carbides of defect NaCl structure type are known at ambient conditions for Sc, Y and Sm-Lu [47]. In this study, carbides with variable stoichiometry REE_xC (REE = Y, Gd, Dy, Yb; x ~ 0.6-1) were formed at ~34-46 GPa (Tables 1 and S1, Fig. 1 and 2). Metal and carbon atoms occupy 4*b* and 4*a* Wyckoff positions, respectively. The full experimental crystallographic data of REE_xC carbides are provided in Tables S3-S6. The stoichiometry differs at distinct crystallographic domains. This variation is attributed to the uncontrollable metal-carbon ratio in the heated pressure chamber area, as observed in PdC_x [29].

4.3.4.2 Rare-earth metal carbides containing carbon [C_2] dimers

Carbides of *oC*16 β-LaC, *tP*10 U_3Si_2 and *cI*40 Pu_2C_3 structure types comprise carbon [C_2] units (Fig. 2c, e, i). Additionally, compounds of structural types *oC*48 γ-SmC and *oC*72 γ-Y_4C_5 [21] contain not only carbon dumbbells but also polycarbon anions (Fig. 2h, k). However, these carbides will be discussed later in this study.

Compounds β-REEC (REE = La, Nd, Sm) represent a new structural type *oC*16 β-LaC (space group *Cmcm*, #63, *Z* = 8) that has not been observed previously (Table 1, Fig. 1-3). The *oC*2 LaC (we call it "α-LaC") lanthanum carbide was observed in the earlier high-pressure experiments [48]. The crystal structures of β-REEC carbides are composed of two

crystallographically distinct positions of metal atoms 4*c* (REE1 and REE2) and one of the carbon atoms 8*f* (C1) (Table S7). The REE1 atoms have a coordination number (CN) of 6, with respect to the nearest carbon atoms, four of which belong to the two [C_2] dimers in a side-on orientation, and two more atoms come from the two end-on oriented [C_2] units (Fig. 3c). The REE2 atoms possess the highest coordination number, CN = 8, with the contribution of two carbon dumbbells [C_2] in a side-on orientation, and four atoms from the four end-on oriented [C_2] units (Fig. 3d). Dimers [C_2] are oriented along the *c*-axis (Fig. 3a, b). The bond length in [C_2] units is ~1.4 Å (Table S7) lying between C-C distances in ethane (~1.54 Å) and ethylene (~1.31 Å) at ambient pressure [49]. The C-C bond length in benzene is ~1.39 Å [49]. Consequently, C-C bond orders in the carbon dimers [C_2] are non-integer and should be in the range of 1.0-1.5. The representation of the formal charge formula can be given as $REE^{3+}{}_2[C_2]^{5-}\cdot 1e$ in the assumption of integer charges of [C_2] units and 3+ charge of metal atoms. The presence of delocalized valence electrons has been demonstrated for other compounds, e.g., for $Sc_3C_4 = Sc^{3+}{}_{30}[C_2]^{2-}{}_2[C_3]^{4-}{}_8C^{4-}{}_{12}\cdot 6e$ [50], $Li^{+}{}_6C^{4-}\cdot 2e$, $Zr^{4+}{}_6I^{-}{}_{12}C^{4-}\cdot 8e$, and $Ta^{5+}{}_2S^{2-}{}_2C^{4-}\cdot 2e$ [51].

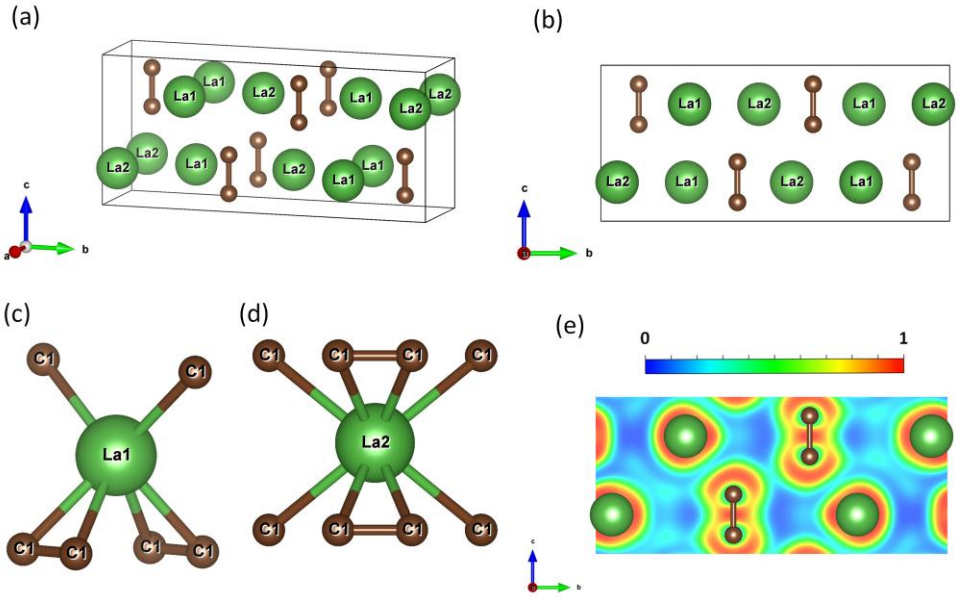

Figure 3. Crystal structure of orthorhombic β-LaC (*Cmcm*, *Z* = 8). Green and brown spheres represent lanthanum and carbon atoms, respectively. (a) A view of the crystal structure. (b) The structure viewed along the *a*-axis. (c) The coordination environment of La1 atoms. (d) The coordination environment of La2 atoms. (e) The electron localization function (ELF) calculated in the (1 0 0) plane containing carbon dumbbells.

The U_3Si_2-type structure (space group *P*4/*mbm*, #127, *Z* = 2), predicted for calcium carbide Ca_3C_2 [27], was observed for the first time in the Dy-C system under high pressure (Dy_3C_2 at 55 GPa [19]). The structure is known for silicides [52], borides [53], and intermetallides [54]. The synthesized Nd_3C_2 (43 and 57 GPa), Sm_3C_2 (44 GPa), Gd_3C_2

(45 GPa), and Dy_3C_2 (55 and 68 GPa [19,22]) contain two crystallographically distinct positions for metal atoms: 2*a* (CN(REE1) = 4) and 4*h* (CN(REE2) = 6), along with a single 4*g* Wyckoff position occupied by carbon atoms (Table S8, Fig. 2e and S3). Metal atoms situated in 2*a* positions, coupled with carbon dumbbells, form the pentagonal Cairo tiling within the *ab* plane [19]. This alternates along the *c*-axis with a parallel layer consisting of metal atoms at the 4*h* sites (Fig. S3) [19]. As previously shown, the C-C bond order is about 1, suggesting the formal charge formula $REE^{2+}{}_3[C_2]^{6-}$ (REE = Nd, Sm, Gd, Dy) [19]. The compounds can be called rare-earth metal (II) ethanides.

The DAC with samarium carbides synthesized in an argon pressure medium was decompressed to ambient pressure. On decompression, Sm_3C_2 was found to be stable down to ~20 GPa (Table S8).

Sesquicarbides REE_2C_3 (REE = Y, Sm, Gd, Dy), which are known at ambient conditions [47,55,56], were found as products of high-pressure high-temperature synthesis in a DAC at pressures of ~19-57 GPa (Tables 1 and S1, Fig. 1 and 2i) [19]. These compounds belong to the known structural type Pu_2C_3 characterized by cubic space group *I-43d*, #220 (*Z* = 8) (Table S9, Fig. S1). C-C distances in $[C_2]$ dimers correspond to $[C_2]^{4-}$ formal charge (Tables S9 and S23). Due to these comparisons and charge analysis provided in [19] for Dy_2C_3, the formal charge formula can be given as $REE^{3+}{}_4[C_2]^{4-}{}_3$ assuming it is a rare-earth metal (III) ethenide.

4.3.4.3 Rare-earth metal carbides containing carbon [C_3] trimers

The crystal structures of the carbides REE_5C_7 (REE = Nd, Sm, Gd, Yb) and γ-REE_4C_5 (REE = Y [21], Sm, Gd, Dy [22], Yb) represent a new structure type *tP*48 Nd_5C_7 and recently discovered *oC*72 γ-Y_4C_5 structure type [21] (Table 1, Fig. 1 and 2f, k). Beyond $[C_3]$ trimers, synthesized compounds demonstrate the presence of discrete carbon atoms in REE_5C_7 and dimers $[C_2]$ in γ-REE_4C_5, respectively.

New structural type *tP*48 Nd_5C_7 (space group *P*4/*ncc*, #130, *Z* = 4) has been discovered for Nd, Sm, Gd, and Yb carbides at ~42-60 GPa (Tables 1, S1, and S10, Fig. 1 and 4). There are two crystallographically non-equivalent metal atoms occupying Wyckoff positions 4*a* (REE1) and 16*g* (REE2) (REE = Nd, Sm, Gd, Yb). Three Wyckoff positions are occupied by carbon atoms: 16*g* (C1), 8*f* (C2), and 4*c* (C3), with C1 and C2 atoms forming $[C_3]$ trimers. The REE1 atoms are surrounded by ten nearest carbon atoms (CN = 10), where six atoms are contributed by two $[C_3]$ trimers in a side-on orientation and four more atoms are from the four end-on oriented $[C_3]$ units (Fig. 4c). The REE2 atoms are eight-fold coordinated (CN = 9) by

four differently oriented [C_3] trimers and two discrete carbon atoms (Fig. 4d). The C-C distance in trimers, equal to ~1.4 Å (Tables S10 and S24), supposes a non-integer bond order in the range of 1.0-1.5, analogously to γ-Y_4C_5 [21]. Considering the larger ∠C-C-C angle in carbon trimers for Nd_5C_7-type carbides in comparison with γ-Y_4C_5 [21] and the assumption of REE^{3+} (REE = Nd, Sm, Gd, Yb) oxidation state, formal charge formula might be represented as $REE^{3+}{}_5[C_3]^{5.5-}{}_2C^{4-}$ or $REE^{3+}{}_5[C_3]^{5-}{}_2C^{4-}\cdot 1e$.

Synthesized at 57(1) GPa Nd_5C_7 was recovered to ambient conditions. The decompression steps details are given in the Table S11. As seen from the experimental data (Table S11, Fig. S4), the symmetry changes to the monoclinic $P2_1/c$ at pressures below ~12 GPa. The decompression steps were fitted using the BM2 EoS (Fig. S4a).

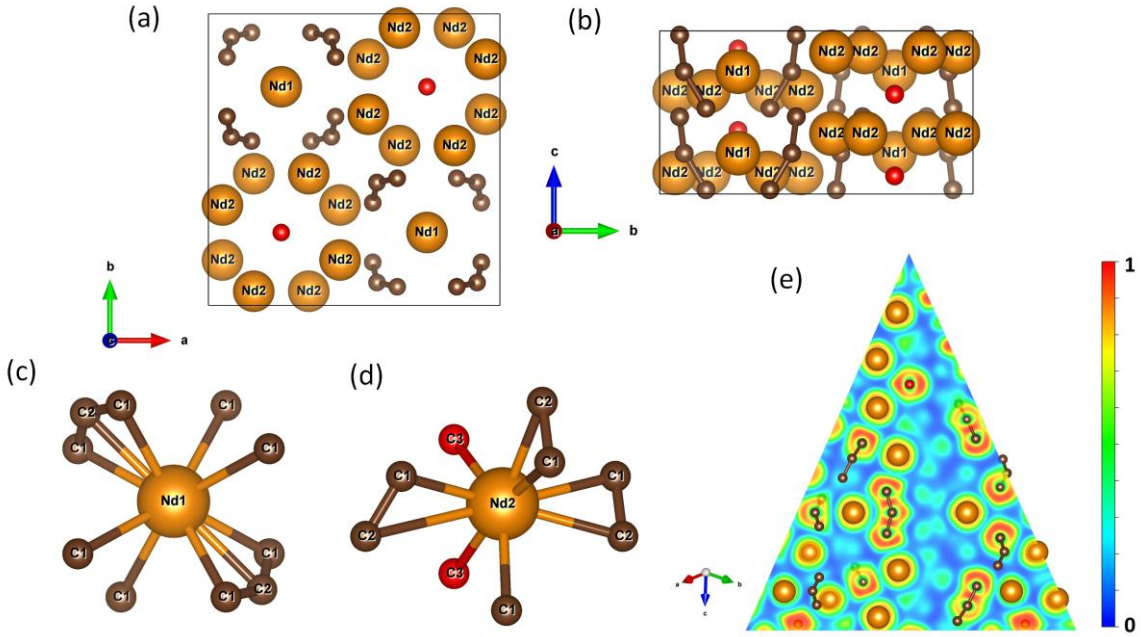

Figure 4. Crystal structure of tetragonal Nd_5C_7 (*P*4/*ncc*, *Z* = 4). The orange, red, and brown spheres represent neodymium, discrete carbon atoms, and carbon atoms forming trimers. (a) The unit cell in projection along the *c*-axis. (b) The view of the crystal structure along the *a*-axis. (c) The coordination environment of Nd1 atoms. (d) The coordination environment of Nd2 atoms. (e) The ELF calculated in the plane containing carbon trimers [C_3].

The recently discovered *oC*72 γ-Y_4C_5 structure type (space group *Cmce*, #64, *Z* = 8) [21] was observed through high-pressure high-temperature experiments at ~34-65 GPa involving several lanthanides: Sm, Gd, Dy [22] and Yb (Tables 1, S12-S14, Fig. 1, 2k, and S5). In these crystal structures, REE1, REE2, and REE3 are at the 16*g*, 8*d*, and 8*f*, and C1, C2, C3, and C4 are at the 8*f*, 16*g*, 8*f*, and 8*e* Wyckoff sites, respectively (REE = Sm, Gd, Dy [22], Yb). C1 and C3 atoms form [C_2] dimers lying in the *bc* plane, while C2 and C4 form [C_3] trimers [21,22]. Metal atoms are coordinated by carbon atoms from dimers and trimers with varying

orientations and have coordination numbers: CN(REE1) = 8, CN(REE2) = 10, CN(REE3) = 6. The bond lengths of [C_2] and [C_3] units in the newly synthesized carbides (Tables S12 and S24) are consistent with the C-C bond lengths in reported γ-Y_4C_5 [21] and γ-Dy_4C_5 [22], that suggests the nature of synthesized compounds is similar to the earlier considered yttrium and dysprosium carbides. Based on the charge analysis in [21] and [22], the formal charge formula of the synthesized carbides can be written as $REE^{3+}{}_4[C_2]^{5-}[C_3]^{6-}\cdot 1e$.

Synthesized at 44(1) GPa γ-Sm_4C_5 was decompressed to ambient pressure and quenched in air. Combined decompression steps in argon (Table S13) and single-crystal XRD measurements at 42(1) GPa for γ-Sm_4C_5 synthesized in NaCl pressure medium (Table S12) were fitted using the BM2 EoS (Fig. S6). Previously observed at 65(3) GPa γ-Dy_4C_5 [19] was decompressed to 12 GPa in NaCl pressure medium until the crystal diffraction became unavailable. The decompression steps (Table S14) were fitted using the BM2 EoS (Fig. S7).

4.3.4.4 Rare-earth metal carbides containing carbon chains

Carbon chains were identified in the carbides δ-NdC_2 and δ-SmC_2, γ-SmC, and several rare-earth metals carbides with the recently discovered Dy_5C_9-type structure [22]: Y_5C_9, Nd_5C_9, Sm_5C_9, Gd_5C_9, and Yb_5C_9 (Table 1, Fig. 1 and 2d, g, h). The novel dicarbides *oC*6 δ-NdC_2 and δ-SmC_2 crystallize in the orthorhombic space group *Pmma*, #51 (Z = 2). The unit cell parameters for δ-NdC_2 at 43(1) GPa are a = 4.9714(12) Å, b = 3.1475(5) Å and c = 3.8083(3) Å, while for δ-SmC_2 at 44(1) GPa, they are a = 4.9458(12) Å, b = 3.1468(3) Å and c = 3.7503(11) Å (Table S15). Meanwhile, lanthanum dicarbide LaC_2 of the same structure was theoretically predicted [45]. The neodymium dicarbide δ-NdC_2 was successfully synthesized at 55(1) GPa as well. In the δ-NdC_2 and δ-SmC_2, 2*f* and 4*i* Wyckoff sites are occupied by REE1 (REE = Nd, Sm) and C1 atoms, respectively. There are two distinct layers of metal atoms and carbon *cis*-polyacetylene-type chains, which are situated within the *ac* plane. These layers alternate along the *b*-axis (Fig. 5a, b). REE atoms are twelve-fold coordinated (CN = 12) by C atoms from the nearest carbon chains (Fig. 5c). The carbon atoms form flat chains along the *a*-axis, featuring alternating interatomic distances between carbon atoms of 1.41(2) Å and 1.501(17) Å, and the ∠C-C-C angle of 135.7(7)° in δ-NdC_2 at 43(1) GPa, while the C-C distance in δ-SmC_2 varies between 1.45(2) Å and 1.463(18) Å with the ∠C-C-C angle of 134.1(7)° at 44(1) GPa. In comparison to the literature on sp^3 and sp^2 hybridization in hydrocarbons [49,57,58], the C-C distances in δ-NdC_2 and δ-SmC_2 fall between the C-C bond lengths in benzene (~1.39 Å) and ethane (~1.54 Å) at ambient conditions. This proposes the C-C bond order within the range of 1.0-1.5. Since the planar

geometry of chains similar to the polyacetylene, the formal charge formula can be interpreted as $REE^{3+}[C_2]^{2-}\cdot 1e$.

Along with Sm_3C_2 obtained in an argon pressure medium, δ-SmC_2 synthesized at 44(1) GPa was observed down to 36(1) GPa. The crystal quality significantly deteriorated at the second pressure step, resulting in a higher value of R_{int} after data integration. This suggests the carbide's instability at lower pressures (Table S15).

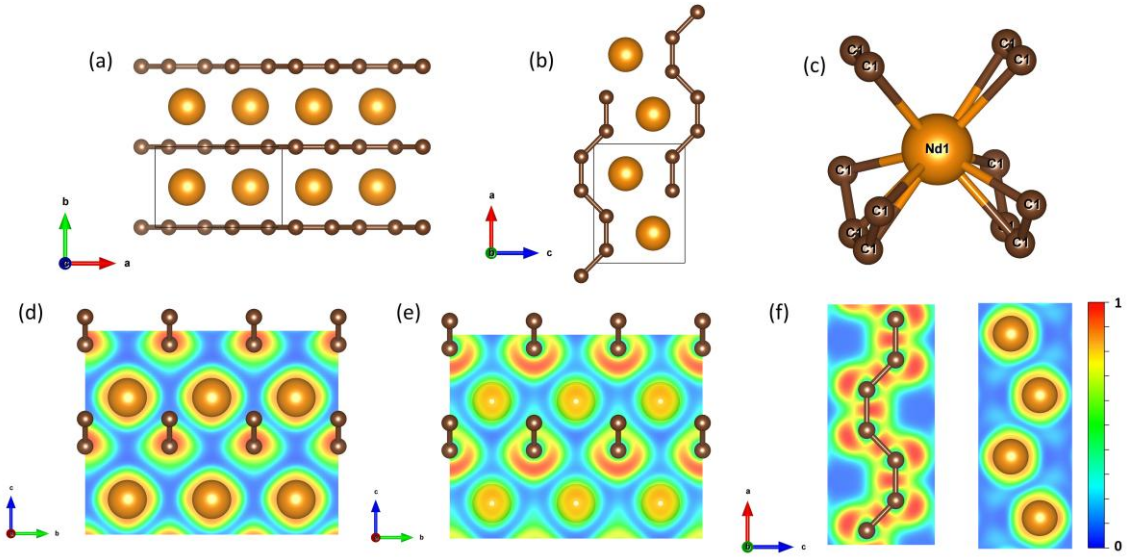

Figure 5. Crystal structure of orthorhombic δ-NdC_2 (*Pmma*, *Z* = 2). Neodymium atoms are given in orange, carbon atoms are shown in brown. (a) Projection of the unit cell along the *c*-axis emphasizing the layers arrangement in the [0 1 0] direction. (b) The view of the crystal structure along the *b*-axis. (c) The coordination environment of neodymium atoms. (d) The ELF calculated in the *bc* plane containing Nd atoms. (e) The ELF calculated in the *bc* plane containing C atoms. (f) The ELF calculated in the *ac* planes containing carbon chains and Nd atoms.

Newly found samarium carbide *oC*48 γ-SmC possesses the orthorhombic space group *Cmcm*, #63 (*Z* = 24). The unit cell parameters are *a* = 10.0193(14) Å, *b* = 9.897(9) Å, and *c* = 4.7921(5) Å at 103(4) GPa (Fig. 2h and 6, Table S16). Four Wyckoff positions 4*c*, 8*g*, 4*c*, and 8*g* are occupied by samarium atoms, whereas the 8*f* and 16*h* sites host carbon atoms. There are two types of carbon entities: carbon dimers formed by C1 atoms and 1D *cis*-polyacetylene-type deprotonated carbon chains with sp^2-hybridized C2 carbon atoms and conjugated π-electron system. These entities are oriented along the *c*-axis (Fig. 6a, b). The Sm1 atoms possess the highest coordination number, CN = 10, with respect to the nearest carbon atoms, two of which belong to the $[C_2]$ unit in a side-on orientation, while the remaining eight carbon atoms originate from the two carbon chains (Fig. 6c). The Sm2 atoms have an eight-fold coordination environment (CN = 8) comprised of one $[C_2]$ dimer in a side-on orientation, two C atoms from two $[C_2]$ dimers in an end-on orientation, and four C atoms from the nearby

carbon chain (Fig. 6d). The Sm3 atoms are six-fold coordinated (CN = 6) by two carbon atoms from two end-on oriented [C_2] dimers and four carbon atoms from two neighboring chains (Fig. 6e). The Sm4 atoms also have a CN of 6 with the coordination environment consisting of one side-on oriented [C_2] dumbbell and four C atoms from the two nearest carbon chains (Fig. 6f). At 103(4) GPa, the C-C bond length within carbon [C_2] dumbbells equals 1.360(18) Å, while the distance between carbon atoms in the *cis*-polyacetylene-type chains alternates between 1.50(4) Å and 1.511(14) Å (Tables S16 and S25). According to argumentation regarding the relationship between C-C distances and bond order provided above, C-C bond length in [C_2] dumbbells might correspond to a bond order of ~1.5 with a formal charge of 5-, whereas the geometry of *cis*-polyacetylene-like planar carbon chains supposes the [C_4] unit with a formal charge of 4- and a bond order of ~1.5. In the described polyhedral, the Sm1-C, Sm2-C, Sm3-C, and Sm4-C distances vary within the ranges of 2.361(14) Å to 2.88(3) Å, 2.340(12) Å to 2.490(7) Å, 2.31(3) Å to 2.390(14) Å, and 2.315(14) Å to 2.558(16) Å, respectively. Relying on the analysis of distances, coordination numbers, and charge distribution discussed for Dy_3C_2 [19] and γ-Y_4C_5 [21], similarly, the formal charge formula $Sm^{3+}Sm^{2+}{}_5[C_2]^{5-}[C_4]^{4-}\cdot 4e$ can be postulated. In this formula, only Sm1 atoms are presumed to adopt a formal charge of 3+, based on their higher coordination number (CN = 10) compared to Sm2, Sm3, and Sm4; the four extra valence electrons are delocalized in the conduction band and do not participate in the Sm-C or C-C bonding. Fluctuating between Sm^{2+} and Sm^{3+} oxidation states is known from the literature [59].

During the decompression of γ-SmC to 87(5) GPa, unusual behavior of the unit cell deformation was observed: while parameters *a* and *b* increase by ~2.32% and ~0.54%, respectively, parameter *c* slightly decreases by ~0.61%, suggesting potential phase transition. The unit cell parameters of decompressed γ-SmC at 87(3) GPa are *a* = 10.252(2) Å, *b* = 9.8369(15) Å, *c* = 4.818(4) Å (Table S16). As the sample was further decompressed, the crystal structure significantly deteriorated and diffraction from the compound became almost undetectable below 80 GPa.

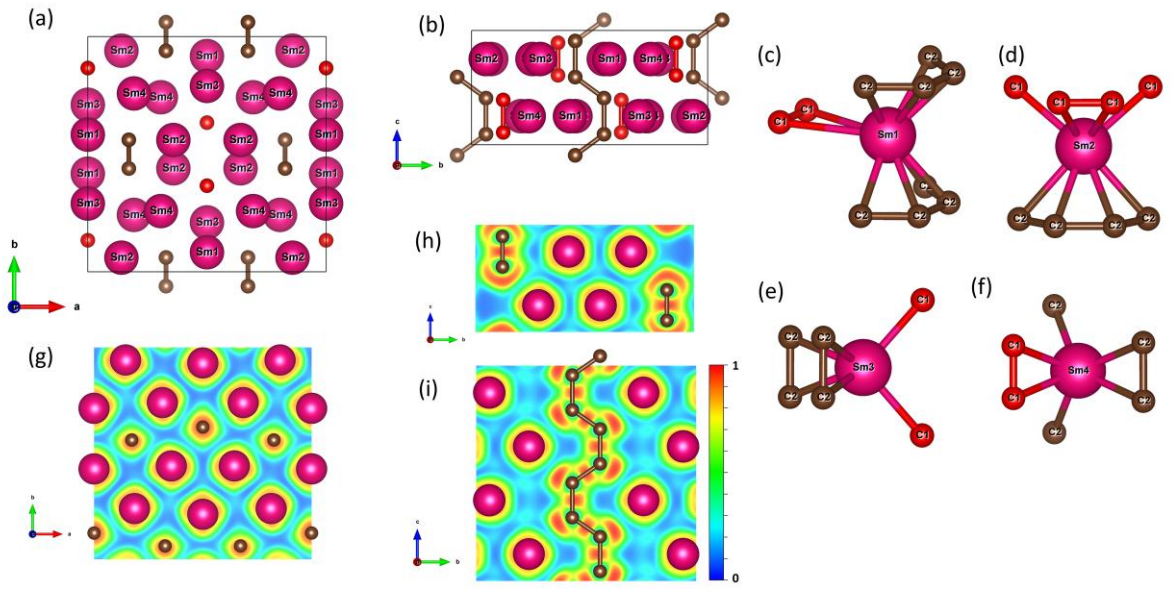

Figure 6. Crystal structure of orthorhombic γ-SmC (*Cmcm*, *Z* = 24). Samarium atoms are marked by pink, carbon atoms formed dimers are represented in red, carbon atoms formed chains are given in brown. (a) The unit cell in projection along the *c*-axis. (b) The view of the crystal structure along the *a*-axis. (c) The coordination environment of Sm1 atoms. (d) The coordination environment of Sm2 atoms. (e) The coordination environment of Sm3 atoms. (f) The coordination environment of Sm4 atoms. (g) The ELF calculated in the *ab* plane containing Sm atoms. (h) The ELF calculated in the *bc* plane containing carbon dumbbells [C_2]. (i) The ELF calculated in the *bc* plane containing carbon chains.

The *tP*28 Dy_5C_9 structure type, which was recently discovered [22], has also been identified as a product of high-pressure high-temperature synthesis in the Y-C, Nd-C, Sm-C, Gd-C, and Yb-C systems, leading to appearance of the novel compounds Y_5C_9, Nd_5C_9, Sm_5C_9, Gd_5C_9, and Yb_5C_9 at ~42-68 GPa (Fig. 1, 2g, and S8). The full crystallographic information is provided in Tables S17 and S18. The structures crystallize in the tetragonal space group *P*4/*mnc*, #128 (*Z* = 2) with two metal (REE) and two carbon (C) atoms at crystallographically distinct positions: 8*h* (REE1), 2*b* (REE2), 16*i* (C1), and 2*a* (C2) (REE = Y, Nd, Sm, Gd, Dy [22], Yb). The C1 atoms form 1D *cis*-polyacetylene-type chains along the *c*-axis, while C2 atoms are located at sites between REE2 atoms along the *c*-axis. The metal atoms are characterized by the coordination numbers CN(REE1) = 11 and CN(REE2) = 10. The interatomic distances in carbon chains are provided in the Table S25. In the chains, the C-C bond order lies within the range of 1.0-1.5 implying the formal charge formula $REE^{3+}{}_5C^{4-}[C_4]^{4-}[C_4]^{4-}\cdot 3e$ in accordance with the carbon chains flat geometry, as demonstrated in the previous study [22].

Synthesis in an argon pressure medium at 44(1) GPa resulted in the formation of $Sm_5C_{8.6}$ stoichiometry with Dy_5C_9-type structure, where discrete carbon atoms C2 at 2*a* Wyckoff sites have a partial occupancy of 0.6 (Table S18). The partial occupancy of C2 atoms

becomes apparent when comparing the unit cell volumes obtained in experiments in Ar and NaCl pressure media. Notably, the unit cell volume of $Sm_5C_{8.6}$ at 44(1) GPa is somewhat smaller than the volume of Sm_5C_9 at 50(1) GPa (Table S18). This confirms the observation of the partial occupancy in $Sm_5C_{8.6}$. The data collection details of the samarium carbide during the decompression are presented in Table S18. The single-crystal structure refinement at 36(1) GPa revealed a partial occupancy of discrete carbon atom C2 equal to 1, that points to the formation of variable carbon atom occupancy phase, denoted as 'Sm_5C_{8+x}', with Dy_5C_9-type structure under the experimental conditions employing argon as the pressure medium (Table S18). The phase recovered under ambient conditions, along with γ-Sm_4C_5, was characterized by an insufficient number of reflections suitable for single-crystal XRD. These reflections correspond to a unit cell with orthorhombic symmetry and unit cell parameters close to 'Sm_5C_{8+x}' at 1 GPa. This observation suggests the potential for a phase transition of this compound to a structure recoverable under ambient conditions.

4.3.4.5 Rare-earth metal carbides containing carbon ribbons

The novel structural type *oI*12 γ-DyC_2 (space group *Immm*, #71, Z = 4), initially uncovered for the rare-earth metal Dy in [22], has been successfully replicated in high-pressure experiments with two more rare-earth elements, Y and Sm (Tables 1 and S1, Fig. 1, 2j, and S9). Theoretically predicted γ-YC_2 [26] was synthesized for the first time at pressures of 94(3) and 124(3) GPa, whereas γ-SmC_2 was shown to be synthesizable at pressures starting from 62(1) GPa and extending up to 117(4) GPa (Tables S1 and S19). As far as the predicted pressure range of the γ-YC_2 phase stability is quite wide [26], the same scenario might be expected for γ-SmC_2 and γ-DyC_2 – especially in light of the similarity of rare-earth metals carbides chemistry revealed in the current research.

The dicarbides orthorhombic crystal structure is characterized by the alternating layers. One layer consists of metal atoms, while the next layer is composed of carbon nanoribbons formed by interconnected six-membered rings and oriented along the *a*-axis. These metal and carbon layers alternate along the *c*-axis (Fig. 2j and S9). Metal atoms occupy 4*i* Wyckoff site, while carbon atoms are located at two crystallographically different positions 4*h*(C1) and 4*g*(C2). Metal atoms are coordinated by the twelve nearest carbon atoms from nearby carbon ribbons (CN = 12). The full experimental crystallographic data, including the crystal structure, data collection, and refinement details of γ-YC_2 and γ-SmC_2, are provided in Table S19. Charge analysis carried out in [22] has shown that the formal charge formula of γ-DyC_2-type carbides is $REE^{3+}{}_2[C_4]^{4-}\cdot 2e$ (REE = Y, Sm).

Synthesized at 117(4) GPa γ-SmC_2 was decompressed to 67(5) GPa – until the crystal diffraction became undetectable (Table S20). The same procedure was performed for the γ-SmC_2 synthesized at 62(1) GPa (Table S19). Combined decompression steps and single-crystal XRD measurements at 62(1), 103(4), and 117(4) GPa were fitted using the BM2 EoS (Fig. S10). The previously discovered at 66(3) GPa γ-DyC_2 [22] was decompressed to 41(3) GPa until the crystal diffraction was no longer detectable (Table S20). The decompression steps were fitted by the BM2 EoS (Fig. S11).

4.3.4.6 Lanthanum naphthalenene-decalinides

Two compounds containing six-membered rings were synthesized in the La-C system in the pressure range of 45(1)-67(1) GPa (Tables 1 and S1, Fig. 1 and 2a, b). The novel lanthanum carbides ε-LaC_2 and La_3C_5 consist of naphthalene-decalin-like entities.

The structure of lanthanum dicarbide *mC*30 ε-LaC_2 has a monoclinic unit cell (space group *C*2/*m*, #12, $Z = 10$) with parameters $a = 7.883(3)$ Å, $b = 5.8534(6)$ Å, $c = 6.9388(5)$ Å, $\beta = 94.010(18)°$ at 45(1) GPa (Table S21, Fig. 7). It is composed of six crystallographically distinct atoms, La1, La2, La3, C1, C2, and C3, on the 2*d*, 4*i*, 4*i*, 8*j*, 4*g*, and 8*j* Wyckoff sites, respectively. Each of the three lanthanum atoms is twelve-fold coordinated by carbon atoms, CN(La) = 12 (Fig. 7c-e). The La-C distances within the La1 atom polyhedron range from 2.686(10) Å to 3.083(15) Å, while for the La2 atom polyhedron, the *d*(La-C) values are from 2.419(8) Å to 2.785(3) Å, and for the La3 atom polyhedron, the metal-carbon distances vary between 2.490(13) Å and 2.698(9) Å. In synthesized compound ε-LaC_2, the naphthalene-decalin-like rings are slightly bent and are not flat due to the minor deviation of angles from 180° within the six-membered rings, where the C-C bond lengths vary as follows: *d*(C1-C2) = 1.487(10) Å, *d*(C1-C3) = 1.429(13) Å, *d*(C2-C2) = 1.48(2) Å, and *d*(C3-C3) = 1.489(15) Å (Table S21, Fig. S12). These values lie between bond distances in naphthalene $C_{10}H_8$ [60] and decalin $C_{10}H_{18}$ [61], supposing the intermediate state of the carbon fragments. Correspondingly, the C-C bond orders are between 1.0 and 1.5. Therefore, considering a formal oxidation state 3+ of La atoms, the formula of the framework can be written as $La^{3+}{}_5[C_{10}]^{12-}\cdot 3e$ (see the paragraph below).

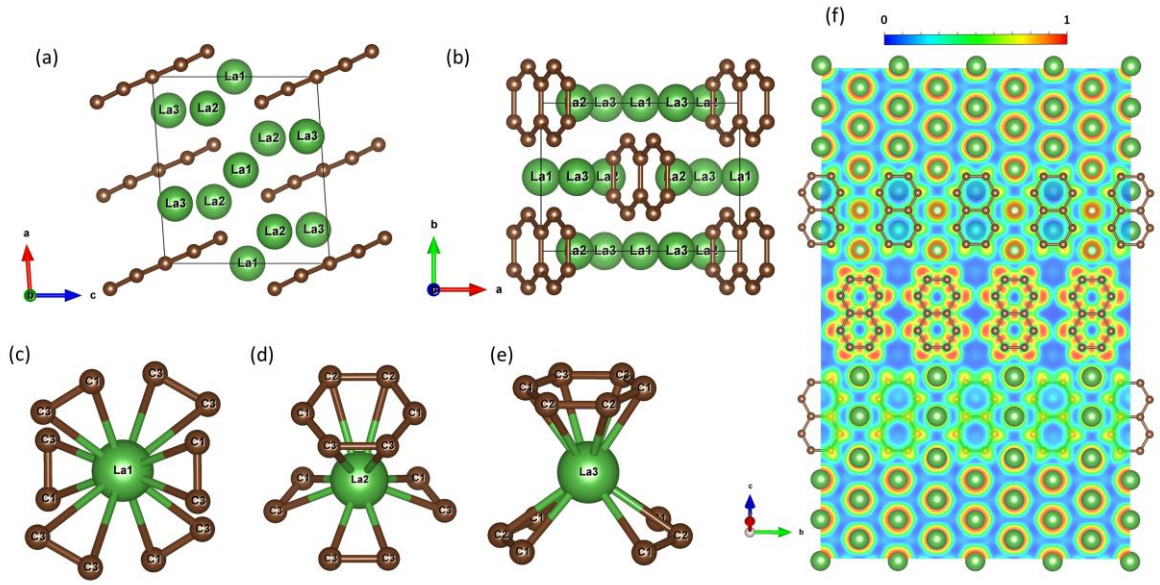

Figure 7. Crystal structure of monoclinic ε-LaC_2 (*C*2/*m*, *Z* = 10). Green and brown spheres represent lanthanum and carbon atoms, respectively. (a) The projection of the structure along the *b*-axis. (b) The structure viewed along *c* direction. (c) The coordination environment of La1 atoms. (d) The coordination environment of La2 atoms. (e) The coordination environment of La3 atoms. (f) The electron localization function (ELF) calculated in the plane containing carbon naphthalene-decalin-like rings.

The structure of *mP*32 La_3C_5 also has a monoclinic unit cell (space group $P2_1/n$, #14, *Z* = 4) with lattice parameters *a* = 4.869(12) Å, *b* = 10.846(5) Å, *c* = 7.366(4) Å, *β* = 107.79(13)° at 45(1) GPa (Table S22, Fig. 8). It consists of 8 crystallographically distinct atoms, three La and five C, all are at Wyckoff sites 4*e*. The lanthanum atoms have different coordination numbers: CN(La1) = 10, CN(La2) = 9, CN(La3) = 11 (Fig. 8c-e). The La-C distances within the polyhedra vary in the ranges: *d*(La1-C) = 2.46(3) – 2.754(19) Å, *d*(La2-C) = 2.594(19) – 2.86(5) Å, *d*(La3-C) = 2.46(5) – 2.83(5) Å. Like in the ε-LaC_2, naphthalene-decalin-like entities are bent in the La_3C_5 structure. The distortion of the naphthalene-decalin-like rings in this structure is slightly more pronounced due to the larger angle deviations and unequal C-C bond lengths: *d*(C1-C3) = 1.54(5) Å, *d*(C1-C5) = 1.47(3) Å, *d*(C2-C5) = 1.44(5) Å, *d*(C2-C4) = 1.44(5) Å, *d*(C3-C4) = 1.44(3) Å, *d*(C3-C3) = 1.45(6) Å (Table S22, Fig. S13). Therefore, based on the comparison with naphthalene $C_{10}H_8$ [60] and decalin $C_{10}H_{18}$ [61] geometry and assumption of a formal oxidation state 2+ of La atoms (due to the lower CN of La atoms in comparison with ε-LaC_2), the formal charge interpretation is $La^{2+}{}_6[C_{10}]^{12-}$. Considering the close geometry of the carbon rings in La_3C_5 and ε-LaC_2, the formal charge of the naphthalene-decalin-like fragments in ε-LaC_2 could also be assigned as 12- (see the paragraph above).

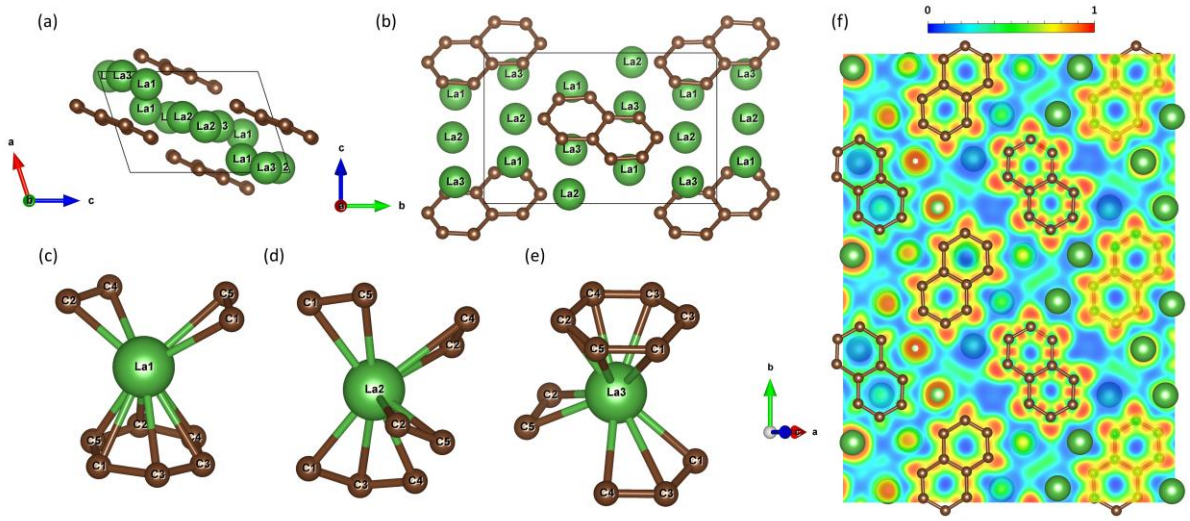

Figure 8. Crystal structure of monoclinic La_3C_5 ($P2_1/n$, $Z = 4$). Green and brown spheres represent lanthanum and carbon atoms, respectively. (a) The projection of the structure along the *b*-axis. (b) The structure viewed along *a*-axis. (c) The coordination environment of La1 atoms. (d) The coordination environment of La2 atoms. (e) The coordination environment of La3 atoms. (f) The electron localization function (ELF) calculated in the plane containing carbon naphthalene-decalin-like rings.

4.3.4.7 Discussion

Convex hull diagrams were generated for the La-C and Y-C systems at 40, 100, and 150 GPa, encompassing all synthesized structural types considered in the current study (Fig. S14) in order to identify and track the empirical trends within the rare-earth metals carbides system. Lanthanum high-pressure chemistry differs significantly from other rare-earth elements, that is seen from experimental results and plotted convex hull diagrams (Fig. 1 and S14). In the current research, only one lanthanum carbide structural type – *oC*16 β-LaC, observed at high pressures, was found to be reproducible for other lanthanides – Nd and Sm, while naphthalene-decalin-like carbon rings were observed only in La-C system. Meanwhile, yttrium demonstrated chemical properties that closely coincided with those of the lanthanides under extreme conditions. This can be inferred from Fig. 1 and the convex hull diagrams for the Y-C system in Fig. S14.

The element that prevails in the majority of high-pressure rare-earth metals carbides structural types is samarium (Fig. 1). Among the 13 structural types of carbides synthesized under extreme conditions in this study, samarium formed 9 of them. Following samarium, gadolinium and dysprosium are the second most common elements forming 8 of 13 structural types of carbides under extreme conditions. This observation is consistent with their intermediate positions in the list of lanthanides, as illustrated in Fig. 1. Such intermediate

characteristics correspond to the similarity of their chemical behavior with elements of both the first and second half of the lanthanide series.

For comparison of chemical properties of the synthesized isostructural carbides, their structures were relaxed at a fixed pressure using DFT (Tables S23-S27). The theoretical computations were performed in the frozen *f*-electrons approximation for lanthanides to provide an illustrative description of the synthesized compounds. This approach helps to determine the C-C distance values in the considered structures, while the experimental data yields high uncertainty for light atoms due to the electron density contribution from heavy atoms. A systematic increase in the length of C-C bonds in isostructural carbides correlates with the rising atomic number of a lanthanide, which is particularly notable for $[C_2]$ and $[C_3]$ units: for instance, $d(C\text{-}C)_{[C2]}$ = 1.4126 Å for Nd_3C_2 and $d(C\text{-}C)_{[C2]}$ = 1.4702 Å for Dy_3C_2, $d(C\text{-}C)_{[C3]}$ = 1.3983 Å for γ-Sm_4C_5 and $d(C\text{-}C)_{[C3]}$ = 1.4058 Å for γ-Dy_4C_5 (Tables S23 and S24).

The Nd_5C_7-type and γ-Y_4C_5-type carbides synthesized under high-pressure high-temperature conditions demonstrate the variability of hybridization and, correspondingly, charge of carbon atoms due to the different geometry of $[C_3]$ units, including the variability of the ∠C-C-C angle and C-C distance in carbon trimers, that are in good agreement with DFT calculations (Table S24). The assumed charge formulas align with this statement. Moreover, carbides of these structural types, Nd_5C_7 and γ-Sm_4C_5, were found to be recoverable to ambient conditions (Tables S11 and S13). In the case of Nd_5C_7, the phase transition occurs at pressures below ~12 GPa (Table S11, Fig. S4). Comparing the enthalpy values of the two phases, Nd_5C_7 (*P*4/*ncc*) and Nd_5C_7 ($P2_1/c$), indicates the phase transition at ~4.7 GPa (Fig. S4b).

The planar geometry of carbon chains and ribbons observed in the mentioned above carbides (δ-NdC_2-type, γ-SmC-type, Dy_5C_9-type, and γ-DyC_2-type) confirms the assumption of sp^2-hybridization of carbon atoms in the conjugated π-electron system and the suggested formal charges. The variation in C-C distances in described carbides compared to those in organic derivatives is caused by the presence of non-bonding electrons in the conduction band. The electron density becomes more concentrated around carbon atoms as a more electronegative element, resulting in a repulsive effect between adjacent carbon atoms in chains and ribbons. This repulsion leads to the elongation of C-C bond lengths.

In relaxed structures of HP-CaC_2 [27], γ-YC_2 and γ-DyC_2 [22], the C2-C2 bond length is shorter than the C1-C2 distance, where C2-C2 is the connecting bond between two adjacent six-membered rings in carbon ribbons (Fig. S9). The experimental results presented in the current research (Table S19) and in the previous work [22] are in good agreement with theoretical calculations (Table S26). The described polyacene-like carbon ribbons in the

synthesized dicarbides differ from polyacene [62] in their C-C distances: the bond lengths at the periphery are longer than those connecting rings within the nanoribbons [22]. This contradicts the C-C distances in standard polyacene [62]. The variation of C-C distances arises from the coordination of metal atoms with each carbon atom from the chains, while in polyacene, only the carbon atoms at the periphery are bonded to hydrogen atoms acting as electron density donors.

ε-LaC_2 and La_3C_5 demonstrate a more complex nature of bonding. Contrary to the observed carbon ribbons and chains, the ten-membered carbon fragments in the lanthanum carbides are non-planar, resembling the geometry of naphthalene and decalin molecules. These non-planar carbon rings suggest an intermediate state between the hybridization of carbon atoms in naphthalene and decalin.

According to the performed Mulliken charge analysis [63] of *oC*16 β-LaC, *tP*48 Nd_5C_7, *oC*72 γ-Y_4C_5, *oC*6 δ-NdC_2, *tP*28 Dy_5C_9, and *oI*12 γ-DyC_2 types carbides (Table S28), the calculated Mulliken charges of rare-earth elements' atoms correspond to the known values for the REE^{3+}-containing compounds in literature [59,64–69]. For the *tP*10 U_3Si_2-type carbides, the charges on metal atoms are lower than those for REE^{3+} and correspond to the REE^{2+} oxidation state as it was described in the previous study [19]. In the case of *oC*48 γ-SmC, the formal charge interpretation aligns well with the results of Mulliken charge analysis (Table S28). Specifically, Sm1 atom is assigned the highest Mulliken charge of 1.62, while charges 1.34, 1.32, and 1.37 are attributed to Sm2, Sm3, and Sm4 atoms, respectively, assuming 3+ oxidation state for Sm1 atoms and 2+ – for Sm2, Sm3, and Sm4, that supports the formal charge interpretation provided above. Presented results of charge distribution correlate with known Mulliken charges for compounds with 2+ or 3+ oxidation states of samarium [59,68,69]. Mulliken charge analysis indicates charges of 1.50 on La1, 1.55 on La2, and 1.42 on La3 in *mC*30 ε-LaC_2, while for the *mP*32 La_3C_5, the values are 1.17 on La1, 1.29 on La2, and 1.35 on La3 with similar charges on carbon atoms in both compounds (Table S28), that corresponds to the formal charges assumed above. Discrepancies between charges of metal atoms arise from variations in the La/C ratio and higher coordination numbers for La atoms in the ε-LaC_2 compared to the La_3C_5. The integrated crystal orbital bond indexes (ICOBI) [63] calculated for carbon chains in γ-SmC and carbon rings-membered arrangements in ε-LaC_2 and La_3C_5 vary in the range 0.89-0.95, close to 1, supporting strong covalent bonding between carbon atoms. Electron localization function (ELF) maps suggest the ionic bonding between metal and carbon species in the considered compounds (Fig. 3-8, S1, S3, S5, S8, S9), supposing them as salt carbides [70]. Calculated electron density of states (eDOS) (Fig. S15) of the novel phases ε-

LaC_2, La_3C_5, β-LaC, δ-NdC_2, Nd_5C_7, and γ-SmC shows the presence of carbon *p*-electrons at Fermi level that agree with formation conducting conjugated π-electron system in carbon polyanions like in other rare-earth metal carbides discussed earlier [19,22] and the assumption of the presence of excess electrons that do not participate in the C-C bonding in the synthesized carbides.

The known correlation between formal charges of the dimers and interatomic length for $[C_2]^{x-}$ [19,21] may be reformulated in terms of individual carbons' formal charges (or effective bond order, Fig. S16), as it was performed for dysprosium carbides [22]. Applying this approach to carbon species in carbides of samarium, one can estimate for Sm_3C_2 the C-C effective bond order (EBO) ~1 ($[C_2]^{6-}$ ethanide units like in the work [19]); for β-SmC, C-C bonds in dumbbells have EBO ~1.87 ($[C_2]^{4.3-}$ units) ($[C_2]^{4.6-}$ for β-LaC, $[C_2]^{4.5-}$ for β-NdC); carbon trimers in Sm_5C_7 are characterized by C-C EBO ~1.62 ($[C_3]^{5.5-}$ units); in γ-Sm_4C_5, for dimers EBO is ~1.48 ($[C_2]^{5-}$ units) and for trimers – ~1.61 ($[C_3]^{5.6-}$ units); for Sm_5C_9, all C-C bonds in the chains are approximately the same and have EBO ~1.19 (thus one-dimensionally infinite polyanions $^1_\infty[(C_4)^{6.5-}]$); C-C EBO in carbon chains of δ-SmC_2 is ~1.24 (one-dimensionally infinite polyanions $^1_\infty[(C_2)^{3.1-}]$); in γ-SmC, for dumbbells EBO is ~1.9 ($[C_2]^{4.2-}$ units) and for chains – ~0.91 (one-dimensionally infinite polyanions $^1_\infty[(C_4)^{8.7-}]$). Analogously to γ-DyC_2 [22], the formal charge for two carbon atoms per γ-SmC_2 formula unit is ~-3.0; for ε-LaC_2, the formal charge of naphthalene-decalin-like anion [C_{10}] is ~-14.1, and for La_3C_5, the [C_{10}]-anion has a formal charge of ~-14.0. Simple consideration suggests Sm (II) in Sm_3C_2 β-SmC, and γ-SmC (Sm1 atoms), La (II) in La_3C_5 and β-LaC, Nd (II) in β-NdC, Sm (III) in Sm_5C_7, γ-Sm_4C_5, Sm_5C_9, δ-SmC_2, γ-SmC (Sm2, Sm3, and Sm4 atoms), and γ-SmC_2, and and La (III) in ε-LaC_2.

Clear correlations exist with physical properties such as carbon-carbon distance and compressibility. Although the current study did not delve into experimental equations of state for rare-earth metals carbides, pressure-volume relations were simulated for all synthesized compounds and fitted using the BM2 EoS (see Table S29). The calculated bulk moduli indicate a tendency to increase with the decreasing of rare-earth element content: K_0(γ-SmC_2) = 179 GPa > K_0(δ-SmC_2) = 170.3 GPa > K_0(Sm_5C_9) = 150 GPa > K_0(Sm_2C_3) = 119 GPa ~ K_0(Sm_5C_7) = 123 GPa > K_0(γ-Sm_4C_5) = 106 GPa > K_0(β-SmC) = 113 GPa > K_0(γ-SmC) = 102 GPa > K_0(Sm_3C_2) = 93 GPa (Table S29). The minor inconsistency between two carbides, Sm_2C_3 and Sm_5C_7, closely related in terms of their metal/carbon ratio, might be related to the difference in carbon entities present in the

compounds. There is also correlation (Fig. S17a) between compressibility and ratio $R=<d>^3/(Z_{REE}*Z_C)$ ($<d>$ is an average REE-C distance in the first coordination sphere, Z_{REE} and Z_C are the charges on the rare-earth metal and carbon). An increase of bulk moduli with decreasing *R* is well-known for ionic and ionic-covalent compounds [3,71], and this trend is observed for carbides with anti-Th_3P_4-type, La_3C_5-type, and ε-LaC_2-type structures, establishing the ionic nature of the compressibility dependence on the *R* for these compounds. However, the trend for the carbides of γ-SmC, γ-Y_4C_5, Nd_5C_7, Pu_2C_3, Dy_5C_9, δ-NdC_2, and γ-DyC_2 structural types is opposite (Fig. S17a). This indicates an unusual compression mechanism for the studied carbides that is in line with the observation of the almost linear correlation between compressibility and the average bond order in carbon pairs (Fig. S17b).

Computations of phonon dispersion relations in harmonic approximation at 0 K show that novel carbides ε-LaC_2, La_3C_5, β-LaC, δ-NdC_2, and γ-SmC exhibit dynamic stability at the synthesis pressure (Fig. S18), while Nd_5C_7 shows tiny instability in Γ-points (Fig. S18i) similar to that in Z-points for Dy_3C_2 at synthesis pressure of 55 GPa reported previously [19]. Nevertheless, Nd_5C_7 is predicted to be dynamically stable at ambient pressure (Fig. S18j), which aligns with experimental observations during the phase quenching process under air in the current research.

4.3.5 Conclusions

Novel rare-earth carbides observed in this study were synthesized by direct reaction of the rare-earth metals and carbon from diamond anvils upon laser heating at pressures up to ~124 GPa. The pressure range most enriched with the variation of carbide types is ~30-70 GPa. Under pressures above ~80-100 GPa, carbon polyanions are predominantly formed which is consistent with the tendency of theoretical predictions. The diversity of their crystal structures indicates the drastic effect of high pressure on the chemistry of rare-earth elements-carbon systems. The most notable features of the novel carbides are polyacene-like ribbons in γ-YC_2, γ-SmC_2, and γ-DyC_2, *cis*-polyacetylene-type chains in Y_5C_9, Nd_5C_9, Sm_5C_{8+x}, Gd_5C_9, Dy_5C_9, Yb_5C_9, δ-NdC_2, δ-SmC_2, and γ-SmC, and naphthalene-decalin-like entities in ε-LaC_2 and La_3C_5. Experiments involving quenching of the synthesized carbides have shown that Nd_5C_7 and γ-Sm_4C_5 are recoverable to ambient conditions. These findings demonstrate the tendency for carbides with complex polyanions to form at high pressures and their potential to exist under ambient conditions. The systematic study of rare-earth metals carbides under extreme conditions has revealed regularities in their chemistry under high pressure.

4.3.6 References

[1] Y. Yin, A. Aslandukova, N. Jena, F. Trybel, I. A. Abrikosov, B. Winkler, S. Khandarkhaeva, T. Fedotenko, E. Bykova, D. Laniel, M. Bykov, A. Aslandukov, F. I. Akbar, K. Glazyrin, G. Garbarino, C. Giacobbe, E. L. Bright, Z. Jia, L. Dubrovinsky, N. Dubrovinskaia, Unraveling the Bonding Complexity of Polyhalogen Anions: High-Pressure Synthesis of Unpredicted Sodium Chlorides Na2Cl3 and Na4Cl5 and Bromide Na4Br5, *JACS Au* **3**, 1634–1641 (2023).

[2] W. Zhang, A. R. Oganov, A. F. Goncharov, Q. Zhu, S. E. Boulfelfel, A. O. Lyakhov, E. Stavrou, M. Somayazulu, V. B. Prakapenka, Z. Konôpková, Unexpected Stable Stoichiometries of Sodium Chlorides, *Science (80-.).* **342**, 1502–1505 (2013).

[3] D. Laniel, B. Winkler, T. Fedotenko, A. Aslandukova, A. Aslandukov, S. Vogel, T. Meier, M. Bykov, S. Chariton, K. Glazyrin, V. Milman, V. Prakapenka, W. Schnick, L. Dubrovinsky, N. Dubrovinskaia, High-Pressure Na3(N2)4, Ca3(N2)4, Sr3(N2)4, and Ba(N2)3 Featuring Nitrogen Dimers with Noninteger Charges and Anion-Driven Metallicity, *Phys. Rev. Mater.* **6**, 023402 (2022).

[4] A. Aslandukov, F. Trybel, A. Aslandukova, D. Laniel, T. Fedotenko, S. Khandarkhaeva, G. Aprilis, C. Giacobbe, E. Lawrence Bright, I. A. Abrikosov, L. Dubrovinsky, N. Dubrovinskaia, Anionic N18 Macrocycles and a Polynitrogen Double Helix in Novel Yttrium Polynitrides YN6 and Y2N11 at 100 GPa, *Angew. Chemie Int. Ed.* **61**, 1–7 (2022).

[5] M. Bykov, E. Bykova, G. Aprilis, K. Glazyrin, E. Koemets, I. Chuvashova, I. Kupenko, C. McCammon, M. Mezouar, V. Prakapenka, H. P. Liermann, F. Tasnádi, A. V. Ponomareva, I. A. Abrikosov, N. Dubrovinskaia, L. Dubrovinsky, Fe-N System at High Pressure Reveals a Compound Featuring Polymeric Nitrogen Chains, *Nat. Commun.* **9**, 1–8 (2018).

[6] A. Aslandukov, A. Aslandukova, D. Laniel, S. Khandarkhaeva, Y. Yin, F. I. Akbar, S. Chariton, V. Prakapenka, E. L. Bright, C. Giacobbe, J. Wright, D. Comboni, M. Hanfland, N. Dubrovinskaia, L. Dubrovinsky, M. Han, N. Dubrovinskaia, L. Dubrovinsky, Stabilization of N6 and N8 Anionic Units and 2D Polynitrogen Layers in High-Pressure Scandium Polynitrides, *Nat. Commun.* **15**, 2244 (2024).

[7] B. A. Steele, E. Stavrou, J. C. Crowhurst, J. M. Zaug, V. B. Prakapenka, I. I. Oleynik,

High-Pressure Synthesis of a Pentazolate Salt, *Chem. Mater.* **29**, 735–741 (2017).

[8] D. Laniel, F. Trybel, Y. Yin, T. Fedotenko, S. Khandarkhaeva, A. Aslandukov, G. Aprilis, A. I. Abrikosov, T. Bin Masood, C. Giacobbe, E. L. Bright, K. Glazyrin, M. Hanfland, J. Wright, I. Hotz, I. A. Abrikosov, L. Dubrovinsky, N. Dubrovinskaia, Aromatic Hexazine [N6]4− Anion Featured in the Complex Structure of the High-Pressure Potassium Nitrogen Compound K9N56, *Nat. Chem.* **15**, 641–646 (2023).

[9] Y. Wang, M. Bykov, I. Chepkasov, A. Samtsevich, E. Bykova, X. Zhang, S. Jiang, E. Greenberg, S. Chariton, V. B. Prakapenka, A. R. Oganov, A. F. Goncharov, Stabilization of Hexazine Rings in Potassium Polynitride at High Pressure, *Nat. Chem.* **14**, 794–800 (2022).

[10] N. P. Salke, K. Xia, S. Fu, Y. Zhang, E. Greenberg, V. B. Prakapenka, J. Liu, J. Sun, J.-F. Lin, Tungsten Hexanitride with Single-Bonded Armchairlike Hexazine Structure at High Pressure, *Phys. Rev. Lett.* **126**, 065702 (2021).

[11] Y. Zhang, L. Wu, B. Wan, Y. Zhao, R. Gao, Z. Li, J. Zhang, H. Gou, H. K. Mao, Structural Variety beyond Appearance: High-Pressure Phases of CrB4 in Comparison with FeB4, *Phys. Chem. Chem. Phys.* **18**, 2361–2368 (2016).

[12] E. Bykova, E. Johansson, M. Bykov, S. Chariton, H. Fei, S. V. Ovsyannikov, A. Aslandukova, S. Gabel, H. Holz, B. Merle, B. Alling, I. A. Abrikosov, J. S. Smith, V. B. Prakapenka, T. Katsura, N. Dubrovinskaia, A. F. Goncharov, L. Dubrovinsky, Novel Class of Rhenium Borides Based on Hexagonal Boron Networks Interconnected by Short B2Dumbbells, *Chem. Mater.* **34**, 8138–8152 (2022).

[13] A. P. Drozdov, P. P. Kong, V. S. Minkov, S. P. Besedin, M. A. Kuzovnikov, S. Mozaffari, L. Balicas, F. F. Balakirev, D. E. Graf, V. B. Prakapenka, E. Greenberg, D. A. Knyazev, M. Tkacz, M. I. Eremets, Superconductivity at 250 K in Lanthanum Hydride under High Pressures, *Nature* **569**, 528–531 (2019).

[14] D. Laniel, B. Winkler, E. Bykova, T. Fedotenko, S. Chariton, V. Milman, M. Bykov, V. Prakapenka, L. Dubrovinsky, N. Dubrovinskaia, Novel Sulfur Hydrides Synthesized at Extreme Conditions, *Phys. Rev. B* **102**, 134109 (2020).

[15] V. V. Struzhkin, D. Y. Kim, E. Stavrou, T. Muramatsu, H. K. Mao, C. J. Pickard, R. J. Needs, V. B. Prakapenka, A. F. Goncharov, Synthesis of Sodium Polyhydrides at High

Pressures, *Nat. Commun.* **7**, 1–8 (2016).

[16] M. Miao, Y. Sun, E. Zurek, H. Lin, Chemistry under High Pressure, *Nat. Rev. Chem.* **4**, 508–527 (2020).

[17] S. Shang, C. Du, Y. Liu, M. Liu, X. Wang, W. Gao, Y. Zou, J. Dong, Y. Liu, J. Chen, A One-Dimensional Conductive Metal-Organic Framework with Extended π-d Conjugated Nanoribbon Layers, *Nat. Commun.* **13**, (2022).

[18] Z. Chen, A. Narita, K. Müllen, Graphene Nanoribbons: On-Surface Synthesis and Integration into Electronic Devices, *Adv. Mater.* **32**, 1–26 (2020).

[19] F. I. Akbar, A. Aslandukova, A. Aslandukov, Y. Yin, F. Trybel, S. Khandarkhaeva, T. Fedotenko, D. Laniel, M. Bykov, E. Bykova, N. Dubrovinskaia, L. Dubrovinsky, High-Pressure Synthesis of Dysprosium Carbides, *Front. Chem.* **11**, 1–9 (2023).

[20] T. A. Strobel, O. O. Kurakevych, D. Y. Kim, Y. Le Godec, W. Crichton, J. Guignard, N. Guignot, G. D. Cody, A. R. Oganov, Synthesis of β-Mg2C3: A Monoclinic High-Pressure Polymorph of Magnesium Sesquicarbide, *Inorg. Chem.* **53**, 7020–7027 (2014).

[21] A. Aslandukova, A. Aslandukov, L. Yuan, D. Laniel, S. Khandarkhaeva, T. Fedotenko, G. Steinle-Neumann, K. Glazyrin, N. Dubrovinskaia, L. Dubrovinsky, Novel High-Pressure Yttrium Carbide γ-Y4C5 Containing [C2] and Nonlinear [C3] Units with Unusually Large Formal Charges, *Phys. Rev. Lett.* **127**, 135501 (2021).

[22] F. I. Akbar, A. Aslandukova, Y. Yin, A. Aslandukov, D. Comboni, M. Hanfland, N. Dubrovinskaia, High-Pressure Dysprosium Carbides Containing Carbon Dimers, Trimers, Chains, and Ribbons, *Submitt. to Carbon* (2024).

[23] S. Khandarkhaeva, T. Fedotenko, A. Aslandukova, F. I. Akbar, M. Bykov, D. Laniel, A. Aslandukov, U. Ruschewitz, C. Tobeck, B. Winkler, S. Chariton, V. Prakapenka, K. Glazyrin, C. Giacobbe, E. L. Bright, M. Belov, N. Dubrovinskaia, L. Dubrovinsky, Extending Carbon Chemistry at High-Pressure by Synthesis of CaC2 and Ca3C7 with Deprotonated Polyacene- and Para-Poly(Indenoindene)-like Nanoribbons, *Nat. Commun.* **15**, 2855 (2024).

[24] X. Dong, L. Wang, K. Li, H. Zheng, Y. Wang, Y. Meng, H. Shu, H. K. Mao, S. Feng, C. Jin, Tailored Synthesis of the Narrowest Zigzag Graphene Nanoribbon Structure by Compressing the Lithium Acetylide under High Temperature, *J. Phys. Chem. C* **122**,

20506–20512 (2018).

[25] L. Wang, X. Dong, Y. Wang, H. Zheng, K. Li, X. Peng, H. K. Mao, C. Jin, Y. Meng, M. Huang, Z. Zhao, Pressure-Induced Polymerization and Disproportionation of Li2C2 Accompanied with Irreversible Conductivity Enhancement, *J. Phys. Chem. Lett.* **8**, 4241–4245 (2017).

[26] X. Feng, S. Lu, C. J. Pickard, H. Liu, S. A. T. Redfern, Y. Ma, Carbon Network Evolution from Dimers to Sheets in Superconducting Ytrrium Dicarbide under Pressure, *Commun. Chem.* **1**, 1–7 (2018).

[27] Y. L. Li, S. N. Wang, A. R. Oganov, H. Gou, J. S. Smith, T. A. Strobel, Investigation of Exotic Stable Calcium Carbides Using Theory and Experiment, *Nat. Commun.* **6**, 1–9 (2015).

[28] I. Kantor, V. Prakapenka, A. Kantor, P. Dera, A. Kurnosov, S. Sinogeikin, N. Dubrovinskaia, L. Dubrovinsky, BX90: A New Diamond Anvil Cell Design for X-Ray Diffraction and Optical Measurements, *Rev. Sci. Instrum.* **83**, 125102 (2012).

[29] T. Fedotenko, L. Dubrovinsky, S. Khandarkhaeva, S. Chariton, E. Koemets, I. Koemets, M. Hanfland, N. Dubrovinskaia, Synthesis of Palladium Carbides and Palladium Hydride in Laser Heated Diamond Anvil Cells, *J. Alloys Compd.* **844**, 6 (2020).

[30] G. Aprilis, I. Kantor, I. Kupenko, V. Cerantola, A. Pakhomova, I. E. Collings, R. Torchio, T. Fedotenko, S. Chariton, M. Bykov, E. Bykova, E. Koemets, D. M. Vasiukov, C. McCammon, L. Dubrovinsky, N. Dubrovinskaia, Comparative Study of the Influence of Pulsed and Continuous Wave Laser Heating on the Mobilization of Carbon and Its Chemical Reaction with Iron in a Diamond Anvil Cell, *J. Appl. Phys.* **125**, (2019).

[31] T. Fedotenko, L. Dubrovinsky, G. Aprilis, E. Koemets, A. Snigirev, I. Snigireva, A. Barannikov, P. Ershov, F. Cova, M. Hanfland, N. Dubrovinskaia, Laser Heating Setup for Diamond Anvil Cells for in Situ Synchrotron and in House High and Ultra-High Pressure Studies, *Rev. Sci. Instrum.* **90**, 104501 (2019).

[32] P. I. Dorogokupets, A. Dewaele, Equations of State of MgO, Au, Pt, NaCl-B1, and NaCl-B2: Internally Consistent High-Temperature Pressure Scales, *High Press. Res.* **27**, 431–446 (2007).

[33] T. Sakai, E. Ohtani, N. Hirao, Y. Ohishi, Equation of State of the NaCl-B2 Phase up to

304 GPa, *J. Appl. Phys.* **109**, 084912 (2011).

[34] H. P. Liermann, Z. Konôpková, W. Morgenroth, K. Glazyrin, J. Bednarčik, E. E. McBride, S. Petitgirard, J. T. Delitz, M. Wendt, Y. Bican, A. Ehnes, I. Schwark, A. Rothkirch, M. Tischer, J. Heuer, H. Schulte-Schrepping, T. Kracht, H. Franz, The Extreme Conditions Beamline P02.2 and the Extreme Conditions Science Infrastructure at PETRA III, *J. Synchrotron Radiat.* **22**, 908–924 (2015).

[35] R. Hrubiak, J. S. Smith, G. Shen, Multimode Scanning X-Ray Diffraction Microscopy for Diamond Anvil Cell Experiments, *Rev. Sci. Instrum.* **90**, (2019).

[36] *Rigaku Oxford Diffraction, CrysAlisPro Software System (2015).*, Rigaku Oxford Diffraction, CrysAlisPro Software system (2015).

[37] A. Aslandukov, M. Aslandukov, N. Dubrovinskaia, L. Dubrovinsky, Domain Auto Finder (DAFi) Program: The Analysis of Single-Crystal X-Ray Diffraction Data from Polycrystalline Samples, *J. Appl. Crystallogr.* **55**, 1383–1391 (2022).

[38] O. V. Dolomanov, L. J. Bourhis, R. J. Gildea, J. A. K. Howard, H. Puschmann, OLEX2: A Complete Structure Solution, Refinement and Analysis Program, *J. Appl. Crystallogr.* **42**, 339–341 (2009).

[39] V. Petrícek, M. Dušek, L. Palatinus, Crystallographic Computing System JANA2006: General Features, *Zeitschrift Fur Krist.* **229**, 345–352 (2014).

[40] G. M. Sheldrick, Crystal Structure Refinement with SHELXL, *Acta Crystallogr. Sect. C Struct. Chem.* **71**, 3–8 (2015).

[41] K. Momma, F. Izumi, VESTA 3 for Three-Dimensional Visualization of Crystal, Volumetric and Morphology Data, *J. Appl. Crystallogr.* **44**, 1272–1276 (2011).

[42] J. Gonzalez-Platas, M. Alvaro, F. Nestola, R. Angel, EosFit7-GUI: A New Graphical User Interface for Equation of State Calculations, Analyses and Teaching, *J. Appl. Crystallogr.* **49**, 1377–1382 (2016).

[43] G. Kresse, J. Furthmüller, Efficiency of Ab-Initio Total Energy Calculations for Metals and Semiconductors Using a Plane-Wave Basis Set, *Comput. Mater. Sci.* **6**, 15–50 (1996).

[44] N. N. Greenwood, A. Earnshaw, *Chemistry of the Elements (2nd Edition)* (Butterworth-

Heinemann, 1997).

[45] C. Su, J. Zhang, G. Liu, X. Wang, H. Wang, Y. Ma, Catenation of Carbon in LaC2 Predicted under High Pressure, *Phys. Chem. Chem. Phys.* **18**, 14286–14291 (2016).

[46] G.-Y. Adachi, N. Imanaka, Z. Fuzhong, *Rare Earth Carbides*, in *Handbook on the Physics and Chemistry of Rare Earths*, Vol. 15 (1991), pp. 61–189.

[47] V. Babizhetskyy, B. Kotur, V. Levytskyy, H. Michor, Alloy Systems and Compounds Containing Rare Earth Metals and Carbon, *Handb. Phys. Chem. Rare Earths* **52**, 1–263 (2017).

[48] D. Laniel, F. Trybel, B. Winkler, F. Knoop, T. Fedotenko, S. Khandarkhaeva, A. Aslandukova, T. Meier, S. Chariton, K. Glazyrin, V. Milman, V. Prakapenka, I. A. Abrikosov, L. Dubrovinsky, N. Dubrovinskaia, High-Pressure Synthesis of Seven Lanthanum Hydrides with a Significant Variability of Hydrogen Content, *Nat. Commun.* **13**, 1–9 (2022).

[49] J. E. Gready, The Value of the π-Bond Order–Bond Length Relationship in Geometry Prediction and Chemical Bonding Interpretation, *J. Comput. Chem.* **5**, 411–426 (1984).

[50] R. Pöttgen, W. Jeitschko, Sc3C4, a Carbide with C3 Units Derived from Propadiene, *Inorg. Chem.* **30**, 427–431 (1991).

[51] A. Simon, Clusters of Valence Electron Poor Metals-Structure, Bonding, and Properties**, *Angew. Chem. Int. Ed. Engl.* **27**, 159–183 (1988).

[52] W. H. Zachariasen, Crystal Chemical Studies of the 5f-Series of Elements. I. New Structure Types, *Acta Crystallogr.* **1**, 265–268 (1948).

[53] A. B. Riabov, V. A. Yartys, B. C. Hauback, P. W. Guegan, G. Wiesinger, I. R. Harris, Hydrogenation Behaviour, Neutron Diffraction Studies and Microstructural Characterization of Boron Oxide-Doped Zr-V Alloys, *J. Alloys Compd.* **293**, 93–100 (1999).

[54] P. Chai, J. D. Corbett, Two New Compounds, β-ScTe and Y3Au2, and a Reassessment of Y2Au, *Acta Crystallogr. Sect. C Cryst. Struct. Commun.* **67**, 53–55 (2011).

[55] H. Rassaerts, H. Nowotny, G. Vinek, F. Benesovsky, Zum System Scandium-Kohlenstoff, 1. Mitt.:, *Monatshefte Für Chemie* **98**, 460–468 (1967).

[56] T. Mochiku, T. Nakane, H. Kito, H. Takeya, S. Harjo, T. Ishigaki, T. Kamiyama, T. Wada, K. Hirata, Crystal Structure of Yttrium Sesquicarbide, *Phys. C Supercond. Its Appl.* **426**–**431**, 421–425 (2005).

[57] J. Clayden, N. Greeves, S. Warren, *Organic Chemistry (Second Edition)*.

[58] A. C. T. Van Duin, S. Dasgupta, F. Lorant, W. A. Goddard, ReaxFF: A Reactive Force Field for Hydrocarbons, *J. Phys. Chem. A* **105**, 9396–9409 (2001).

[59] W. L. Li, C. Ertural, D. Bogdanovski, J. Li, R. Dronskowski, Chemical Bonding of Crystalline LnB6 (Ln = La-Lu) and Its Relationship with Ln2B8 Gas-Phase Complexes, *Inorg. Chem.* **57**, 12999–13008 (2018).

[60] D. W. J. Cruickshank, R. A. Sparks, Experimental and Theoretical Determinations of Bond Lengths in Naphthalene, Anthracene and Other Hydrocarbons, *Proc. R. Soc. London. Ser. A. Math. Phys. Sci.* **258**, 270–285 (1960).

[61] S. Eibl, A. Fitch, M. Brunelli, A. D. Evans, P. Pattison, M. Plazanet, M. R. Johnson, C. Alba-Simionesco, H. Schober, Tarns-Decahydronaphthalene (Decalin) from Powder Diffraction Data, *Acta Crystallogr. Sect. C Cryst. Struct. Commun.* **C65**, 278–280 (2009).

[62] Q. Ai, K. Jarolimek, S. Mazza, J. E. Anthony, C. Risko, Delimited Polyacenes: Edge Topology as a Tool to Modulate Carbon Nanoribbon Structure, Conjugation, and Mobility, *Chem. Mater.* **30**, 947–957 (2018).

[63] P. C. Müller, C. Ertural, J. Hempelmann, R. Dronskowski, Crystal Orbital Bond Index: Covalent Bond Orders in Solids, *J. Phys. Chem. C* **125**, 7959–7970 (2021).

[64] V. Louis-Achille, L. De Windt, M. Defranceschi, Electronic Structure of Minerals: The Apatite Group as a Relevant Example, *Int. J. Quantum Chem.* **77**, 991–1006 (2000).

[65] V. V. Korochentsev, A. V. Elovskii, V. I. Vovna, I. S. Os'mushko, A. G. Mirochnik, I. V. Kalinovskaya, Electronic Structure of Adducts of Nd(III) Carboxylate Complexes Determined by DFT and XPS Methods, *J. Struct. Chem.* **58**, 1120–1128 (2017).

[66] H. Wu, H. Yan, G. Zhao, S. Qiu, X. Qiu, X. Zhou, T. Qiu, Influence of Impurities on Adsorption of Hydrated Y3+ Ions on the Kaolinite (001) Surface, *Colloids Surfaces A Physicochem. Eng. Asp.* **653**, 129961 (2022).

[67] N. Claiser, M. Souhassou, C. Lecomte, B. Gillon, C. Carbonera, A. Caneschi, A. Dei, D. Gatteschi, A. Bencini, Y. Pontillon, E. Lelièvre-Berna, Combined Charge and Spin Density Experimental Study of the Yttrium(III) Semiquinonato Complex Y(HBPz3)2(DTBSQ) and DFT Calculations, *J. Phys. Chem. B* **109**, 2723–2732 (2005).

[68] W. Huang, W. H. Xu, W. H. E. Schwarz, J. Li, On the Highest Oxidation States of Metal Elements in MO4 Molecules (M = Fe, Ru, Os, Hs, Sm, and Pu), *Inorg. Chem.* **55**, 4616–4625 (2016).

[69] S. Labouille, C. Clavaguéra, F. Nief, Theoretical Insights into the Nature of Divalent Lanthanide-Ligand Interactions, *Organometallics* **32**, 1265–1271 (2013).

[70] U. Ruschewitz, Binary and Ternary Carbides of Alkali and Alkaline-Earth Metals, *Coord. Chem. Rev.* **244**, 115–136 (2003).

[71] R. M. Hazen, L. W. Finger, Bulk Modulus-Volume Relationship for Cation-Anion Polyhedra, *J. Geophys. Res.* **84**, 6723–6728 (1979).

4.3.7 Supporting information

Theoretical calculations

The properties of the synthesized compounds were determined through the first-principles calculations using the framework of density functional theory (DFT) as implemented in the VASP (Vienna ab initio simulation package) code [1]. To expand the electronic wave function in plane waves we used the Projector-Augmented-Wave (PAW) method [2]. The Generalized Gradient Approximation (GGA) functional was used for calculating the exchange-correlation energies, as proposed by Perdew–Burke–Ernzerhof (PBE) [3]. The PAW potentials with the following valence configurations of 5*s*5*p*6*s*5*d* for lanthanides, 4*s*4*p*5*s*4*d* for Y, and 2*s*2*p* for C were used to describe the interaction between the core and the valence electrons in frozen f-electrons approximation for lanthanides [1]. Convergence tests with a threshold of 2 meV per atom in energy led to an energy cutoff for the plane wave expansion of 750 eV for all phases and a Monkhorst-Pack [4] k-point grid of 5 × 7 × 6 for ε-LaC_2 and 'ε-YC_2', 9 × 4 × 6 for La_3C_5 and 'Y_3C_5', 12 × 3 × 7 for β-LaC, β-NdC, β-SmC and 'β-YC', 8 × 12 × 10 for 'δ-LaC_2', δ-NdC_2, δ-SmC_2 and 'δ-YC_2', 3 × 3 × 6 for 'La_5C_7', Nd_5C_7, Sm_5C_7, Gd_5C_7, Yb_5C_7 and 'Y_5C_7', 6 × 6 × 11 for 'La_3C_2', Nd_3C_2, Sm_3C_2, Gd_3C_2, Dy_3C_2 and 'Y_3C_2', 4 × 4 × 8 for 'γ-LaC', γ-SmC and 'γ-YC', 15 × 7 × 6 for 'γ-LaC_2', γ-SmC_2, γ-DyC_2 and γ-YC_2, 4 × 4 × 4 for 'La_2C_3', Sm_2C_3, Gd_2C_3, Dy_2C_3, and Y_2C_3, 3 × 5 × 4 for 'γ-La_4C_5', γ-Sm_4C_5, γ-Gd_4C_5, γ-Dy_4C_5, Yb_4C_5 and γ-Y_4C_5, 4 × 4 × 6 for 'La_5C_9', Nd_5C_9, Sm_5C_9, Gd_5C_9, Dy_5C_9, Yb_5C_9 and Y_5C_9, and 4 × 4 × 4 for 'La_4C_3', Gd_4C_3, Dy_4C_3, Yb_4C_3,'Y_4C_3' and Sc_4C_3. Computations were performed for eight volumes that cover the pressure range of 0-100 GPa. Harmonic lattice dynamics calculations were performed with the PHONOPY software [5] using the finite displacement method for 2 × 2 × 2 (ε-LaC_2), 2 × 3 × 2 (La_3C_5), 2 × 2 × 2 (β-LaC), 2 × 2 × 2 (δ-NdC_2), and 6 × 6 × 6 (Nd_5C_7) supercells with respectively adjusted k-points. The tetrahedron method was used for Brillouin zone integrations, employing a mesh of 15 × 15 × 11 k-points for ε-LaC_2, 18 × 8 × 12 k-points for La_3C_5, 12 × 12 × 14 k-points for β-LaC, 16 × 25 × 21 k-points for δ-NdC_2, and 8 × 8 × 15 k-points for Nd_5C_7 [6,7]. The integrated values of the crystal orbital bond index (ICOBI) [8] and Mulliken charges were calculated using LOBSTER v4.1.0 software [9]. The charge distribution in the ionic approximation based on a generalization of Pauling's concept of bond strength [10] was made using CHARDI2015 [11]. In our calculations, temperature, configurational entropy, and the entropy contribution due to lattice vibrations were neglected.

Table S1. Summary of the high-pressure high-temperature experiments in diamond anvil cells.

DAC number	Starting materials	Culet size (μm)	Pressure (GPa)	Temperature (K, ±200)	Reaction products
YY01	Y in NaCl	250	40(1)	2500	Y_xC
LA04	Dy in NaCl	250	43(1)	2500	Dy_xC
LA06	La in NaCl	250	41(1)	2500	β-LaC
LA09	Sc in NaCl	250	64(1)	2500	Sc_4C_3
LA11	Gd in NaCl	250	34(2)	2500	Gd_4C_3, Gd_xC, γ-Gd_4C_5, Gd_2C_3
			45(1)	2500	Gd_3C_2, Gd_4C_3, Gd_xC, γ-Gd_4C_5, Gd_5C_7, Gd_2C_3, Gd_5C_9
			58(1)	2500	Gd_2C_3, Gd_5C_9
LA14	Sm in NaCl	250	42(1)	2500	γ-Sm_4C_5, Sm_5C_7, Sm_2C_3, Sm_5C_9
			50(1)	2500	β-SmC, Sm_5C_7, Sm_5C_9
			62(1)	2500	γ-SmC_2, Sm_5C_9
LA15	La in NaCl	250	45(1)	2500	β-LaC, La_3C_5, ε-LaC_2
			59(1)	2500	β-LaC, ε-LaC_2
			67(1)	2500	β-LaC, La_3C_5, ε-LaC_2
LA17	Nd in NaCl	250	37(2)	(Observed during the decompression)	Nd_5C_9
			43(1)	2500	Nd_3C_2, β-NdC, δ-NdC_2
			56(2)	2500	Nd_3C_2, β-NdC, Nd_5C_7, δ-NdC_2
LA18	Yb in NaCl	250	42(1)	2500	Yb_4C_3, Yb_xC, γ-Yb_4C_5, Yb_5C_7, Yb_5C_9
			60(1)	2500	Yb_5C_7, Yb_5C_9
LA19	Sm in Ar	120	103(4)	2300	γ-SmC, γ-SmC_2
			117(4)	2300	γ-SmC_2
LA23	Sm in Ar	250	44(1)	2200	Sm_3C_2, γ-Sm_4C_5, $Sm_5C_{8.6}$, δ-SmC_2

ALA33	Y in NaCl	120	68(3)	2500	Y_5C_9
			94(3)	2500	γ-YC_2
			124(3)	2500	γ-YC_2

Table S2. Structure refinement details and crystallographic data of Sc_4C_3 at 64(1) GPa, Gd_4C_3 at 32(2), 34(2) and 46(1) GPa, Yb_4C_3 at 42(1) GPa. The full crystallographic datasets deposited to the CCDC are available under the deposition numbers: 2346565 (Sc_4C_3 at 64(1) GPa), 2346566 (Gd_4C_3 at 32(2) GPa), 2346567 (Gd_4C_3 at 34(2) GPa), 2346568 (Gd_4C_3 at 46(2) GPa), 2346569 (Yb_4C_3 at 42(1) GPa).

Chemical formula	Sc_4C_3	Gd_4C_3			Yb_4C_3
Pressure (GPa)	64(1)	32(2)	34(2)	46(1)	42(1)
Crystal data					
Mr	215.87	665.03			728.19
ρ (g/cm^3)	5.095	11.117	11.172	11.899	14.018
Radiation type	X-ray, λ = 0.3738 Å	X-ray, λ = 0.3738 Å	X-ray, λ = 0.2901 Å	X-ray, λ = 0.2846 Å	X-ray, λ = 0.2846 Å
Space group	*I*-43*d*				
a (Å)	6.5531(2)	7.352(2)	7.3397(4)	7.187(2)	7.0138(11)
V (Å^3)	281.41(3)	397.3(4)	395.40(6)	371.2(3)	345.03(16)
Z	4				
CN of REE1	6				
REE1-C distances in first coordination sphere (Å)	2.1411(8), 2.4073(8)	2.3862(17), 2.7202(17)	2.3830(7), 2.7147(7)	2.3492(11), 2.6390(11)	2.2750(10), 2.5969(10)
Atom / Wyck. site/ Fractional atomic coordinates (x; y; z)					
REE1/16*c*	0.06454(11) 0.06454(11) 0.06454(11)	0.0623(2) 0.0623(2) 0.0623(2)	0.06241(9) 0.06241(9) 0.06241(9)	0.06468(11) 0.06468(11) 0.06468(11)	0.06208(12) 0.06208(12) 0.06208(12)
C1/12*a*	0.375 0 0.25	0.375 0 0.25	0.375 0 0.25	0.375 0 0.25	0.375 0 0.25
Data collection					
No. of measured, independent and observed [I > 2σ(I)] reflections	305/110/100	189/99/76	789/234/176	679/145/119	522/138/113
R_{int}	1.94%	3.99%	3.22%	5.47%	2.97%
Refinement					
R_1	2.72%	4.78%	3.63%	3.12%	3.34%
wR_2	6.98%	12.91%	8.98%	7.27%	8.04%
GOF	1.198	1.094	1.060	1.094	1.088
No. of reflections/No. of parameters	110/6	99/7	234/7	145/6	138/7

Table S3. Structure refinement details and crystallographic data of Y_xC at 40(1) GPa. The full crystallographic dataset of $Y_{0.79}C$ was deposited to the CCDC under the deposition number 2346650.

Chemical formula	$Y_{0.6}C$	$Y_{0.65}C$	$Y_{0.66}C$	$Y_{0.68}C$	$Y_{0.79}C$
REE_xC, x =	0.60(13)	0.65(7)	0.66(8)	0.68(10)	0.79(4)
Pressure (GPa)	40(1)				
Crystal data					
Mr	64.91	69.13	70.25	72.25	82.03
ρ (g/cm^3)	4.484	4.823	4.842	4.975	5.804
Radiation type	X-ray, λ = 0.41015 Å	X-ray, λ = 0.41015 Å	X-ray, λ = 0.41015 Å	X-ray, λ = 0.41015 Å	X-ray, λ = 0.41015 Å
Space group	*Fm*-3*m*				
a (Å)	4.5813(6)	4.5661(7)	4.5847(3)	4.5861(5)	4.5448(9)
V (Å^3)	96.15(4)	95.20(4)	96.37(2)	96.45(3)	93.87(5)
Z	4				
CN of Y1	6				
Y1-C distances in first coordination sphere (Å)	2.2906(4)	2.2831(4)	2.29235(16)	2.2931(3)	2.2724(5)
Atom / Wyck. site/ Fractional atomic coordinates (x; y; z)					
Y1/4*b*	0.5 0.5 0.5				
C1/4*a*	0 0 0				
Data collection					
No. of measured, independent and observed [I > 2σ(I)] reflections	56/21/21	74/22/22	62/22/22	67/22/22	66/22/22
R_{int}	6.49%	5.16%	4.45%	8.20%	4.11%
Refinement					
R_1	6.20%	3.14%	3.84%	4.38%	2.01%
wR_2	16.06%	7.90%	9.29%	10.44%	3.68%
GOF	1.198	1.377	1.339	1.275	1.330
No. of reflections/No. of parameters	21/4	22/4	22/4	22/4	22/4

Table S4. Structure refinement details and crystallographic data of Gd_xC at 34(2) and 46(1) GPa. The full crystallographic datasets of $Gd_{0.73}C$ at 34(2) GPa and $Gd_{0.71}C$ at 46(1) GPa

were deposited to the CCDC under the deposition numbers 2346651 and 2346652, respectively.

Chemical formula	$Gd_{0.73}C$	$Gd_{0.78}C$	$Gd_{0.68}C$	$Gd_{0.71}C$	$Gd_{0.82}C$
REE_xC, x =	0.73(4)	0.78(7)	0.68(5)	0.71(6)	0.82(17)
Pressure (GPa)	34(2)		46(1)		
Crystal data					
Mr	126.41	135.06	118.94	123.66	141.35
ρ (g/cm^3)	7.952	8.496	7.862	8.070	9.291
Radiation type	X-ray, λ = 0.2901 Å	X-ray, λ = 0.2901 Å	X-ray, λ = 0.2846 Å	X-ray, λ = 0.2846 Å	X-ray, λ = 0.2846 Å
Space group	*Fm*-3*m*				
a (Å)	4.7264(5)	4.7264(5)	4.6491(5)	4.6690(14)	4.6578(17)
V ($Å^3$)	105.58(3)	105.58(3)	100.49(3)	101.78(9)	101.05(11)
Z	4				
CN of Gd1	6				
Gd1-C distances in first coordination sphere (Å)	2.3632(3)	2.3632(3)	2.3245(3)	2.3345(8)	2.3289(9)
Atom / Wyck. site/ Fractional atomic coordinates (x; y; z)					
Gd1/4*b*	0.5 0.5 0.5				
C1/4*a*	0 0 0				
Data collection					
No. of measured, independent and observed [I > 2σ(I)] reflections	130/35/35	132/36/36	147/36/33	164/43/41	98/25/25
R_{int}	3.58%	2.98%	5.40%	4.43%	7.26%
Refinement					
R_1	2.60%	2.57%	3.75%	3.11%	5.03%
wR_2	3.86%	5.37%	5.53%	5.71%	11.23%
GOF	1.122	1.120	1.138	1.065	1.424
No. of reflections/No. of parameters	35/4	36/4	36/4	43/4	25/4

Table S5. Structure refinement details and crystallographic data of Dy_xC at 43(1) GPa. The full crystallographic dataset of $Dy_{0.79}C$ was deposited to the CCDC under the deposition number 2346653.

Chemical formula	$Dy_{0.59}C$	$Dy_{0.62}C$	$Dy_{0.67}C$	$Dy_{0.75}C$	$Dy_{0.79}C$
REE_xC, x =	0.59(6)	0.62(9)	0.67(8)	0.75(4)	0.79(9)
Pressure (GPa)	43(1)				

Crystal data					
Mr	108.29	113.17	120.48	133.07	139.57
ρ (g/cm^3)	7.523	7.848	8.361	9.239	9.695
Radiation type	X-ray, λ = 0.2905 Å	X-ray, λ = 0.2905 Å	X-ray, λ = 0.2905 Å	X-ray, λ = 0.2905 Å	X-ray, λ = 0.2905 Å
Space group	*Fm*-3*m*				
a (Å)	4.5728(15)	4.5754(17)	4.5742(13)	4.5736(12)	4.573(2)
V (Å^3)	95.62(10)	95.78(11)	95.71(8)	95.67(8)	95.62(14)
Z	4				
CN of Dy1	6				
Dy1-C distances in first coordination sphere (Å)	2.2864(8)	2.2877(9)	2.2871(7)	2.2868(7)	2.2865(10)
Atom / Wyck. site/ Fractional atomic coordinates (x; y; z)					
Dy1/4*b*	0.5 0.5 0.5				
C1/4*a*	0 0 0				
Data collection					
No. of measured, independent and observed [I > 2σ(I)] reflections	85/32/32	88/33/33	119/35/35	120/33/33	109/34/33
R_{int}	2.16%	2.97%	2.12%	4.19%	2.99%
Refinement					
R_1	3.20%	3.60%	2.90%	2.09%	2.79%
wR_2	7.66%	8.57%	7.46%	3.58%	6.15%
GOF	1.412	1.194	1.432	1.357	1.119
No. of reflections/No. of parameters	32/4	33/4	35/4	33/5	34/4

Table S6. Structure refinement details and crystallographic data of Yb_xC at 42(1) GPa. The full crystallographic dataset of $Yb_{0.59}C$ was deposited to the CCDC under the deposition number 2346654.

Chemical formula	$Yb_{0.59}C$	$Yb_{0.6}C$	$Yb_{0.68}C$	$Yb_{0.84}C$	$Yb_{0.85}C$	$Yb_{0.9}C$	YbC
REE_xC, x =	0.59(2)	0.60(6)	0.68(5)	0.84(9)	0.85(3)	0.90(4)	1
Pressure (GPa)	42(1)						
Crystal data							
Mr	113.67	116.70	129.24	158.23	159.53	167.75	185.05
ρ (g/cm^3)	8.168	8.372	9.308	11.358	11.486	12.075	13.331

Radiation type	X-ray, λ = 0.2905 Å	X-ray, λ = 0.2905 Å	X-ray, λ = 0.2905 Å	X-ray, λ = 0.2905 Å	X-ray, λ = 0.2905 Å	X-ray, λ = 0.2905 Å	X-ray, λ = 0.2905 Å
Space group	*Fm*-3*m*						
a (Å)	4.5214(5)	4.5240(7)	4.5181(8)	4.5230(5)	4.5184(7)	4.5188(6)	4.5177(9)
V (Å^3)	92.43(3)	92.59(4)	92.23(5)	92.53(3)	92.25(4)	92.27(4)	92.20(5)
Z	4						
CN of Yb1	6						
Yb1-C distances in first coordination sphere (Å)	2.2607(3)	2.2620(4)	2.2590(5)	2.2615(3)	2.2592(4)	2.2594(4)	2.2589(5)
Atom / Wyck. site/ Fractional atomic coordinates (x; y; z)							
Yb1/4*b*	0.5 0.5 0.5						
C1/4*a*	0 0 0						
Data collection							
No. of measured, independent and observed [I > 2σ(I)] reflections	109/26/25	119/32/31	117/30/30	119/25/25	119/32/32	120/32/32	115/31/31
R_{int}	7.86%	4.15%	3.58%	4.07%	2.58%	2.69%	3.81%
Refinement							
R_1	1.87%	3.49%	1.66%	2.29%	1.32%	1.27%	1.82%
wR_2	2.76%	5.94%	3.98%	5.05%	2.02%	2.18%	4.75%
GOF	1.229	1.124	1.191	1.336	1.034	1.075	1.255
No. of reflections/No. of parameters	26/4	32/4	30/4	25/4	32/4	32/4	31/5

Table S7. Structure refinement details and crystallographic data of β-LaC at 41(1)-68(1) GPa, β-NdC at 43(1) and 57(1) GPa, and β-SmC at 51(1) GPa. The full crystallographic datasets deposited to the CCDC are available under the deposition numbers: 2346664 (β-LaC at 41(1) GPa), 2346665 (β-LaC at 45(1) GPa), 2346666 (β-LaC at 59(1) GPa), 2346667 (β-LaC at 68(1) GPa), 2346668 (β-NdC at 43(1) GPa), 2346669 (β-NdC at 57(1) GPa), 2346670 (β-SmC at 51(1) GPa).

Chemical formula	β-LaC				β-NdC		β-SmC
Pressure (GPa)	41(1)	45(1)	59(1)	68(1)	43(1)	57(1)	51(1)
Crystal data							
Mr	150.92				156.25		162.36
ρ (g/cm^3)	9.363	9.472	9.966	10.259	10.503	11.095	11.444

Radiation type	X-ray, λ = 0.2844 Å	X-ray, λ = 0.2901 Å	X-ray, λ = 0.2905 Å	X-ray, λ = 0.28457 Å	X-ray, λ = 0.2904 Å	X-ray, λ = 0.2846 Å	X-ray, λ = 0.29521 Å
Space group	*Cmcm*						
a (Å)	3.2858(8)	3.2966(9)	3.2079(5)	3.1635(13)	3.2242(6)	3.1782(9)	3.1897(19)
b (Å)	12.0825(19)	11.997(4)	11.8700(11)	11.87(4)	11.698(3)	11.399(12)	11.48(2)
c (Å)	5.3937(12)	5.3520(9)	5.2833(19)	5.204(3)	5.2398(16)	5.1641(8)	5.1459(19)
V ($Å^3$)	214.13(8)	211.66(10)	201.18(8)	195.4(7)	197.63(8)	187.1(2)	188.5(4)
Z	8						
CN of REE1	6						
CN of REE2	8						
REE1-C distances in first coordination sphere (Å)	2.507(5), 2.600(7)	2.513(8), 2.588(10)	2.462(6), 2.554(9)	2.45(6), 2.50(6)	2.447(6), 2.522(9)	2.415(14), 2.466(14)	2.395(14), 2.444(17)
REE2-C distances in first coordination sphere (Å)	2.589(5), 2.696(6)	2.575(8), 2.674(8)	2.533(6), 2.636(8)	2.54(6), 2.56(3)	2.519(6), 2.614(8)	2.479(14), 2.555(8)	2.501(15), 2.562(13)
C-C distance in [C_2] units (Å)	1.387(15)	1.39(2)	1.36(3)	1.43(6)	1.38(2)	1.387(17)	1.41(4)
Atom / Wyck. site/ Fractional atomic coordinates (x; y; z)							
REE1/4*c*	0 0.74567(4) 0.25	0 0.74592(7) 0.25	0 0.74549(4) 0.25	0 0.7460(5) 0.25	0 0.74639(5) 0.25	0 0.74588(14) 0.25	0 0.74715(10) 0.25
REE2/4*c*	0 0.04679(4) 0.25	0 0.04733(7) 0.25	0 0.04713(4) 0.25	0 0.0481(5) 0.25	0 0.04693(5) 0.25	0 0.04868(15) 0.25	0 0.04640(11) 0.25
C1/8*f*	0 0.3915(5) 0.1214(13)	0 0.3930(8) 0.1199(18)	0 0.3921(5) 0.1217(19)	0 0.392(6) 0.113(5)	0 0.3923(6) 0.1184(19)	0 0.3933(16) 0.1157(16)	0 0.3902(16) 0.113(3)
Data collection							
No. of measured, independent and observed [$I > 2\sigma(I)$] reflections	672/376/289	548/267/221	556/250/196	192/76/66	444/232/ 195	576/222/172	265/127/110
R_{int}	4.02%	1.40%	2.55%	5.25%	1.83%	2.18%	1.25%
Refinement							
R_1	3.08%	3.60%	2.73%	3.93%	3.54%	4.21%	2.23%
wR_2	7.36%	9.23%	4.94%	8.68%	9.10%	10.03%	6.30%
GOF	1.045	1.092	1.013	1.098	1.096	1.001	1.129
No. of reflections/	376/12	267/15	250/12	76/12	232/12	222/12	127/12

No. of parameters							

Table S8. Structure refinement details and crystallographic data of Nd_3C_2 synthesized at 43(1) and 57(1) GPa, Sm_3C_2 synthesized at 44(1) GPa and decompressed to 20(1) GPa, and Gd_3C_2 synthesized at 45(1) GPa. The full crystallographic datasets deposited to the CCDC are available under the deposition numbers: 2346814 (Nd_3C_2 at 43(1) GPa), 2346815 (Nd_3C_2 at 57(1) GPa), 2346816 (Sm_3C_2 at 44(1) GPa), 2346817 (Sm_3C_2 at 36(1) GPa), 2346818 (Gd_3C_2 at 45(1) GPa).

Chemical formula	Nd_3C_2		Sm_3C_2			Gd_3C_2
Pressure (GPa)	43(1)	57(1)	44(1)	Decompression		45(1)
				36(1)	20(1)	
Crystal data						
Mr	456.74		475.07			495.77
ρ (g/cm^3)	11.084	11.793	12.027	11.634	10.738	12.626
Radiation type	X-ray, λ = 0.2904 Å	X-ray, λ = 0.2846 Å	X-ray, λ = 0.2900 Å	X-ray, λ = 0.4100 Å	X-ray, λ = 0.4100 Å	X-ray, λ = 0.2904 Å
Space group	*P4/mbm*					
a (Å)	6.1889(7)	6.0437(17)	6.118(2)	6.2166(17)	6.3594(16)	6.0969(6)
c (Å)	3.573(5)	3.521(3)	3.5052(10)	3.509(3)	3.633(2)	3.5082(6)
V (Å^3)	136.85(19)	128.63(14)	131.18(10)	135.62(14)	146.93(12)	130.41(3)
Z	2					
CN of REE1	4					
CN of REE2	6					
REE1-C distances in first coordination sphere (Å)	2.633(5)	2.584(19)	2.582(13)	2.648(13)	2.73(4)	2.582(7)
REE2-C distances in first coordination sphere (Å)	2.511(4), 2.714(5)	2.468(13), 2.665(14)	2.482(9), 2.648(10)	2.490(9), 2.708(10)	2.54(3), 2.82(3)	2.462(5), 2.670(5)
C-C distance in [C_2] units (Å)	1.446(10)	1.37(4)	1.51(3)	1.44(3)	1.40(8)	1.468(13)
Atom / Wyck. site/ Fractional atomic coordinates (x; y; z)						
REE1/2*a*	0 0 0	0 0 0	0 0 0	0 0 0	0 0 0	0 0 0

REE2/4*h*	0.18390(5) 0.68390(5) 0.5	0.1859(2) 0.6859(2) 0.5	0.18355(12) 0.68355(12) 0.5	0.18340(12) 0.68340(12) 0.5	0.18200(18) 0.68200(18) 0.5	0.18148(5) 0.68148(5) 0.5
C1/4*g*	0.5826(8) 0.0826(8) 0	0.580(3) 0.080(3) 0	0.587(2) 0.087(2) 0	0.582(2) 0.082(2) 0	0.578(6) 0.078(6) 0	0.5851(10) 0.0851(10) 0
Data collection						
No. of measured, independent and observed [I > 2σ(I)] reflections	649/125/110	534/165/139	245/122/120	320/109/101	306/128/113	609/200/187
R_{int}	4.17%	3.92%	1.19%	1.91%	2.35%	1.94%
Refinement						
R_1	1.81%	7.49%	3.37%	4.08%	8.84%	2.41%
wR_2	3.89%	21.90%	8.27%	10.46%	22.13%	5.46%
GOF	1.080	1.154	1.172	1.120	1.150	1.089
No. of reflections/ No. of parameters	125/9	165/11	122/11	109/11	128/9	200/11

Table S9. Structure refinement details and crystallographic data of Sm_2C_3 at 42(1) GPa and Gd_2C_3 at 32(2), 44(1) and 57(1) GPa. The full crystallographic datasets deposited to the CCDC are available under the deposition numbers: 2346869 (Sm_2C_3 at 42(1) GPa), 2346870 (Gd_2C_3 at 32(2) GPa), 2346871 (Gd_2C_3 at 44(1) GPa), 2346872 (Gd_2C_3 at 57(1) GPa).

Chemical formula	Sm_2C_3	Gd_2C_3		
Pressure (GPa)	42(1)	32(2)	44(1)	57(1)
Crystal data				
Mr	336.73	350.53		
ρ (g/cm^3)	9.199	9.779	10.039	10.434
Radiation type	X-ray, λ = 0.3738 Å	X-ray, λ = 0.2901 Å	X-ray, λ = 0.2904 Å	X-ray, λ = 0.4100 Å
Space group	*I*-43*d*			
a (Å)	7.8637(16)	7.8090(5)	7.7409(10)	7.6420(5)
V (Å^3)	486.3(3)	476.19(9)	463.85(18)	446.29(9)
Z	8			
CN of REE1	9			
REE1-C distances in first coordination sphere (Å)	2.418(4) – 2.73(3)	2.3940(11) – 2.692(11)	2.3687(7) – 2.671(6)	2.3421(11) – 2.624(14)
C-C distance in [C_2] units (Å)	1.42(12)	1.33(5)	1.33(3)	1.25(7)
Atom / Wyck. site/ Fractional atomic coordinates (x; y; z)				

REE1/16*c*	0.05243(10) 0.05243(10) 0.05243(10)	0.05191(7) 0.05191(7) 0.05191(7)	0.05139(4) 0.05139(4) 0.05139(4)	0.05192(8) 0.05192(8) 0.05192(8)
C1/24*d*	0.285(7) 0 0.25	0.290(3) 0 0.25	0.2888(15) 0 0.25	0.293(4) 0 0.25
Data collection				
No. of measured, independent and observed [I > 2σ(I)] reflections	390/172/133	1000/206/172	874/214/186	486/160/143
R_{int}	6.56%	5.09%	2.93%	4.48%
Refinement				
R_1	4.97%	3.03%	2.16%	3.38%
wR_2	9.80%	6.70%	5.36%	7.80%
GOF	1.087	1.163	1.081	1.134
No. of reflections/No. of parameters	172/9	206/6	214/9	160/9

Table S10. Structure refinement details and crystallographic data of Nd_5C_7 at 57(1) GPa, Sm_5C_7 at 42(1) and 50(1) GPa, Gd_5C_7 at 45(1) GPa, and Yb_5C_7 at 42(1) and 60(1) GPa. The full crystallographic datasets deposited to the CCDC are available under the deposition numbers: 2347285 (Nd_5C_7 at 57(1) GPa), 2347286 (Sm_5C_7 at 42(1) GPa), 2347287 (Sm_5C_7 at 50(1) GPa), 2347288 (Gd_5C_7 at 45(1) GPa), 2347289 (Yb_5C_7 at 42(1) GPa), 2347290 (Yb_5C_7 at 60(1) GPa).

Chemical formula	Nd_5C_7	Sm_5C_7		Gd_5C_7	Yb_5C_7	
Pressure (GPa)	57(1)	42(1)	50(1)	45(1)	42(1)	60(1)
Crystal data						
Mr	805.27	835.82		870.32	949.27	
ρ (g/cm^3)	9.649	9.659	9.900	10.494	12.358	12.936
Radiation type	X-ray, λ = 0.2846 Å	X-ray, λ = 0.3738 Å	X-ray, λ = 0.2846 Å	X-ray, λ = 0.2904 Å	X-ray, λ = 0.2905 Å	X-ray, λ = 0.4100 Å
Space group	*P*4/*ncc*					
a (Å)	10.2129(17)	10.342(2)	10.2733(9)	10.145(2)	9.8772(11)	9.7188(13)
c (Å)	5.3143(14)	5.3744(9)	5.3134(5)	5.3522(17)	5.2299(19)	5.160(2)
V (Å^3)	554.3(2)	574.8(3)	560.78(11)	550.8(3)	510.2(2)	487.4(2)
Z	4					
CN of REE1	10					
CN of REE2	9					
REE1-C distances in first	2.474(10) – 2.619(10)	2.498(17) – 2.698(17)	2.490(11) – 2.638(10)	2.439(18) – 2.593(18)	2.38(4) – 2.49(4)	2.42(3) – 2.51(5)

coordination sphere (Å)						
REE2-C distances in first coordination sphere (Å)	2.361(9) – 3.077(9)	2.370(17) – 3.137(16)	2.366(11) – 3.100(8)	2.304(19) – 3.063(18)	2.28(4) – 3.02(3)	2.20(4) – 2.98(3)
C-C distance in [C_3] units (Å)	1.392(11)	1.366(16)	1.403(11)	1.43(2)	1.44(4)	1.45(6)
∠C-C-C in [C_3] units (°)	146.9(10)	144(2)	147.3(11)	146(3)	141(4)	146(4)
Atom / Wyck. site/ Fractional atomic coordinates (x; y; z)						
REE1/4*a*	0.75 0.25 0.25	0.75 0.25 0.25	0.75 0.25 0.25	0.75 0.25 0.25	0.75 0.25 0.25	0.75 0.25 0.25
REE2/16*g*	0.04836(7) 0.15564(6) 0.12915(12)	0.04630(8) 0.15389(8) 0.12891(11)	0.04691(5) 0.15433(5) 0.12825(8)	0.04598(10) 0.15353(10) 0.1280(3)	0.04655(11) 0.15264(11) 0.1258(3)	0.04670(17) 0.15245(18) 0.1239(6)
C1/16*g*	0.5638(9) 0.1478(8) 0.0263(18)	0.5627(18) 0.1457(16) 0.036(2)	0.5620(10) 0.1496(10) 0.0268(17)	0.5633(18) 0.1546(18) 0.027(3)	0.566(3) 0.153(3) 0.019(7)	0.556(3) 0.154(4) 0.016(12)
C2/8*f*	0.4217(8) 0.5783(8) 0.25	0.4244(15) 0.5756(15) 0.25	0.4214(7) 0.5786(7) 0.25	0.4205(18) 0.5795(18) 0.25	0.425(3) 0.575(3) 0.25	0.426(3) 0.574(3) 0.25
C3/4*c*	0.25 0.25 0.389(4)	0.25 0.25 0.386(4)	0.25 0.25 0.384(3)	0.25 0.25 0.382(10)	0.25 0.25 0.37(2)	0.25 0.25 0.30(3)
Data collection						
No. of measured, independent and observed [$I > 2\sigma(I)$] reflections	1315/380/ 312	399/280/209	1902/503/ 399	486/225/173	853/211/161	319/153/104
R_{int}	3.65%	1.34%	3.26%	3.36%	4.93%	4.65%
Refinement						
R_1	3.42%	5.10%	3.76%	3.86%	4.32%	5.84%
wR_2	8.06%	13.29%	10.42%	9.32%	9.63%	14.78%
GOF	1.107	1.074	1.056	1.216	1.112	1.066
No. of reflections/ No. of parameters	380/30	280/30	503/30	225/21	211/21	153/14

Table S11. Structure refinement details and crystallographic data of Nd_5C_7 synthesized at 67(1) GPa in NaCl, decompressed to 2.5 GPa, opened and closed in the glovebox in inert atmosphere, and quenched at ambient conditions in air (according to the EoS of NaCl-B1, NaCl pressure medium kept stresses leading to the detected pressure of ~1.5 GPa). The full

crystallographic datasets deposited to the CCDC are available under the deposition numbers: 2347672 (Nd_5C_7 at 2.5(2) GPa) and 2347673 (Nd_5C_7 at 1.5(1.5) GPa).

Chemical formula	Nd_5C_7						
Pressure (GPa)	57(1)	49(1)	37(1)	24(1)	12(1)	2.5(2)	1.5(1.5)
Crystal data							
Mr	805.27						
ρ (g/cm^3)	9.649	9.462	9.053	8.537	7.891	7.296	7.214
Radiation type	X-ray, λ = 0.2846 Å	X-ray, λ = 0.4099 Å					
Space group	*P4/ncc*					*P*2$_1$/*c*	
a (Å)	10.2129(17)	10.295(4)	10.448(3)	10.629(5)	11.010(5)	11.122(6)	11.179(6)
b (Å)	10.2129(17)	10.295(4)	10.448(3)	10.629(5)	11.010(5)	11.259(5)	11.284(6)
c (Å)	5.3143(14)	5.334(2)	5.413(3)	5.546(4)	5.592(7)	5.861(8)	5.885(9)
β (°)	90	90	90	90	90	92.77(7)	92.80(9)
V (Å^3)	554.3(2)	565.3(5)	590.9(4)	626.5(8)	677.8(10)	733.1(11)	741.5(13)
Z	4						
Data collection							
No. of measured, independent and observed [I > 2σ(I)] reflections	1315/380/ 312	447/184/ 130	851/417/ 257	414/254/ 174	846/281/ 206	1858/1147/ 762	843/601/ 438
R_{int}	3.65%	4.82%	6.11%	3.66%	6.35%	3.66%	2.38%
Refinement							
R_1	3.42%	12.24%	5.35%	5.19%	9.11%	13.85%	8.90%
wR_2	8.06%	35.36%	14.59%	13.49%	25.67%	34.61%	21.92%
GOF	1.107	1.486	0.975	0.997	1.047	1.282	1.023
No. of reflections/ No. of parameters	380/30	184/21	417/30	254/21	281/21	1147/49	601/74

Table S12. Structure refinement details and crystallographic data of γ-Sm_4C_5 at 42(1) GPa, γ-Gd_4C_5 at 34(1) and 45(1) GPa, and γ-Yb_4C_5 at 42(1) GPa. The full crystallographic datasets deposited to the CCDC are available under the deposition numbers: 2347325 (γ-Sm_4C_5 at 42(1) GPa), 2347326 (γ-Gd_4C_5 at 34(1) GPa), 2347327 (γ-Gd_4C_5 at 45(1) GPa), 2347328 (γ-Yb_4C_5 at 42(1) GPa).

Chemical formula	γ-Sm_4C_5	γ-Gd_4C_5		γ-Yb_4C_5
Pressure (GPa)	42(1)	34(1)	45(1)	42(1)

Crystal data				
Mr	661.45	689.05		752.21
ρ (g/cm^3)	10.147	10.540	11.018	12.918
Radiation type	X-ray, λ = 0.3738 Å	X-ray, λ = 0.3738 Å	X-ray, λ = 0.2846 Å	X-ray, λ = 0.2846 Å
Space group	*Cmce*			
a (Å)	12.427(3)	12.499(4)	12.451(6)	12.0074(6)
b (Å)	7.724(3)	7.6957(14)	7.585(2)	7.4694(11)
c (Å)	9.022(7)	9.029(8)	8.7969(13)	8.6251(8)
V (Å^3)	866.0(7)	868.5(8)	830.7(5)	773.57(14)
Z	8			
CN of REE1	8			
CN of REE2	10			
CN of REE3	6			
REE1-C distances in first coordination sphere (Å)	2.487(18) – 2.60(4)	2.47(4) – 2.66(6)	2.446(10) – 2.561(8)	2.370(7) – 2.503(6)
REE2-C distances in first coordination sphere (Å)	2.41(3) – 2.73(4)	2.42(4) – 2.756(11)	2.406(7) – 2.684(5)	2.351(6) – 2.631(3)
REE3-C distances in first coordination sphere (Å)	2.28(6) – 2.49(6)	2.35(8) – 2.45(7)	2.295(12) – 2.419(13)	2.172(9) – 2.318(5)
C-C distance in [C_2] units (Å)	1.42(6)	1.38(8)	1.377(17)	1.417(13)
C-C distance in [C_3] units (Å)	1.40(4)	1.34(5)	1.398(11)	1.416(7)
∠C-C-C in [C_3] units (°)	136(4)	137(4)	135.1(13)	133.9(8)
Atom / Wyck. site/ Fractional atomic coordinates (x; y; z)				
REE1/16*g*	0.14434(9) 0.37657(14) 0.14338(19)	0.14490(13) 0.12479(17) 0.3536(3)	0.14471(5) 0.12580(5) 0.35283(4)	14444(2) 0.12330(4) 0.35428(3)
REE2/8*d*	0.15178(11) 0 0	0.14967(18) 0 0	0.14986(7) 0 0	0.14784(2) 0 0
REE3/8*f*	0 0.2111(2) 0.3677(3)	0 0.3010(3) 0.1240(4)	0 0.30478(9) 0.12243(6)	0 0.29049(5) 0.13011(4)
C1/8*f*	0 0.003(4) 0.179(5)	0 0.002(7) 0.180(10)	0 0.0079(15) 0.1726(12)	0 0.0053(12) 0.1791(9)

C2/16*g*	0.309(2) 0.188(4) 0.132(4)	0.195(3) 0.312(4) 0.135(6)	0.1942(10) 0.3106(12) 0.1261(8)	0.1926(4) 0.3083(8) 0.1218(6)
C3/8*f*	0 0.159(5) 0.095(6)	0 0.345(5) 0.393(7)	0 0.3425(16) 0.3920(12)	0 0.3348(13) 0.3930(9)
C4/8*e*	0.25 0.120(3) 0.25	0.25 0.375(4) 0.25	0.25 0.3810(17) 0.25	0.25 0.3826(11) 0.25
Data collection				
No. of measured, independent and observed [I > 2σ(I)] reflections	653/287/231	575/275/220	1747/697/510	2312/1102/907
R_{int}	3.28%	2.66%	4.68%	2.26%
Refinement				
R_1	4.15%	5.45%	2.65%	2.63%
wR_2	10.16%	15.90%	5.33%	6.26%
GOF	0.998	1.127	0.923	0.956
No. of reflections/No. of parameters	287/33	275/33	697/33	1102/47

Table S13. Structure refinement details and crystallographic data of γ-Sm_4C_5 synthesized at 44(1) GPa in Ar, decompressed to 1 GPa and quenched at ambient conditions in air. The full crystallographic datasets deposited to the CCDC are available under the deposition numbers: 2347330 (γ-Sm_4C_5 at 1(1) GPa) and 2347331 (γ-Sm_4C_5 at 1 bar).

Chemical formula	γ-Sm_4C_5				
Pressure (GPa)	44(1)	36(1)	20(1)	1(1)	0
Crystal data					
Mr	661.45				
ρ (g/cm^3)	-	9.965	9.319	8.085	8.122
Radiation type	X-ray, λ = 0.2900 Å	X-ray, λ = 0.4100 Å	X-ray, λ = 0.4100 Å	X-ray, λ = 0.4100 Å	X-ray, λ = 0.4100 Å
Space group	*Cmce*				
a (Å)	12.480(18)	12.509(5)	12.669(8)	13.434(4)	13.3848(18)
b (Å)	7.725(2)	7.813(3)	7.935(3)	8.3805(15)	8.311(5)
c (Å)	8.976(2)	9.023(4)	9.38(4)	9.654(10)	9.7252(19)
V (Å^3)	865(1)	881.8(6)	943(4)	1086.9(12)	1081.9(6)
Z	8				
Data collection					

No. of measured, independent and observed [I > 2σ(I)] reflections	212	262/220/169	289/240/138	509/368/269	393/341/244
R_{int}	-	5.50%	9.27%	1.83%	2.31%
Refinement					
R_1	-	7.96%	16.06%	4.94%	6.01%
wR_2	-	19.99%	40.63%	13.94%	14.65%
GOF	-	1.063	1.410	0.991	0.975
No. of reflections/No. of parameters	-	220/33	240/31	368/33	341/33

Table S14. Structure refinement details and crystallographic data of γ-Dy_4C_5 synthesized at 65(3) GPa in the work [12] and decompressed to 12 GPa. The full crystallographic dataset of γ-Dy_4C_5 at 12(3) GPa was deposited to the CCDC under the deposition number: 2347451.

Chemical formula	γ-Dy_4C_5					
Pressure (GPa)	65(3) [12]	59(3)	53(3)	41(3)	30(3)	12(3)
Crystal data						
Mr	710.05					
ρ (g/cm^3)	13.139	13.017	12.759	12.370	11.929	10.999
Radiation type	X-ray, λ = 0.2846 Å	X-ray, λ = 0.2846 Å				
Space group	*Cmce*					
a (Å)	11.800(6)	11.839(6)	11.947(2)	12.186(3)	12.465(7)	12.642(4)
b (Å)	7.2291(15)	7.309(6)	7.332(3)	7.3692(16)	7.503(3)	7.696(2)
c (Å)	8.416(2)	8.374(3)	8.4400(12)	8.491(6)	8.455(13)	8.815(5)
V (Å^3)	717.9(4)	724.6(8)	739.3(3)	762.5(6)	790.7(14)	857.6(6)
Z	8					
Data collection						
No. of measured, independent and observed [I > 2σ(I)] reflections	1042/504/ 418	592/269/ 237	1381/641/ 557	1333/564/452	585/250/178	770/319/235
R_{int}	3.10%	3.01%	2.28%	2.52%	11.76%	5.32%
Refinement						
R_1	3.92%	3.53%	4.06%	4.45%	9.28%	6.06%

wR_2	8.08%	7.70%	9.93%	11.75%	26.34%	15.61%
GOF	1.114	1.095	1.085	1.070	1.151	1.045
No. of reflections/ No. of parameters	504/33	269/33	641/47	564/33	250/33	319/33

Table S15. Structure refinement details and crystallographic data of δ-NdC_2, synthesized at 43(1) and 55(1) GPa and decompressed to 10(2) GPa, and δ-SmC_2, synthesized at 44(1) GPa and decompressed to 36(1) GPa. The full crystallographic datasets deposited to the CCDC are available under the deposition numbers: 2347471 (δ-NdC_2 at 43(1) GPa), 2347472 (δ-NdC_2 at 55(1) GPa), 2347473 (δ-NdC_2 at 10(2) GPa), 2347474 (δ-SmC_2 at 44(1) GPa).

Chemical formula	δ-NdC_2						δ-SmC_2	
Pressure (GPa)	43(1)	55(1)	Decompression				44(1)	Decompression
			48(2)	33(2)	24(2)	10(2)		36(1)
Crystal data								
Mr	168.26						174.37	
ρ (g/cm^3)	9.377	9.750	9.519	9.188	8.956	8.841	9.922	9.707
Radiation type	X-ray, λ = 0.2904 Å	X-ray, λ = 0.2846 Å	X-ray, λ = 0.4099 Å				X-ray, λ = 0.2900 Å	X-ray, λ = 0.4100 Å
Space group	*Pmma*							
a (Å)	4.9714(12)	4.901(9)	4.9574(8)	5.044(3)	5.022(8)	5.047(2)	4.9458(12)	4.983(6)
b (Å)	3.1475(5)	3.0887(6)	3.1278(9)	3.177(2)	3.216(14)	3.195(6)	3.1468(3)	3.1524(9)
c (Å)	3.8083(3)	3.7860(10)	3.7858(9)	3.795(14)	3.863(2)	3.920(4)	3.7503(11)	3.798(2)
V (Å^3)	59.590(17)	57.31(11)	58.70(2)	60.8(2)	62.4(3)	63.21(13)	58.37(2)	59.66(8)
Z	2							
CN of REE1	12							
REE1-C distances in first coordination sphere (Å)	2.508(8) – 2.607(6)	2.461(18) – 2.583(9)	2.494(19) – 2.611(16)	2.47(6) – 2.72(6)	2.527(14) – 2.706(14)	2.556(13) – 2.699(16)	2.473(8) – 2.594(7)	-
C-C distance in carbon chains (Å)	1.41(2), 1.501(17)	1.44(5), 1.44(4)	1.44(5)	1.29(12), 1.53(8)	1.43(4), 1.45(5)	1.43(4), 1.49(4)	1.45(2), 1.463(18)	-
∠C-C-C in carbon chains (°)	135.7(7)	134.7(15)	136.2(18)	140(6)	138.2(15)	136.9(14)	134.1(7)	-
Atom / Wyck. site/ Fractional atomic coordinates (x; y; z)								
REE1/2*f*	0.25 0.5 0.65090(13)	0.25 0.5 0.64752(18)	0.25 0.5 0.6506(4)	0.25 0.5 0.656(2)	0.25 0.5 0.65443(17)	0.25 0.5 0.6541(3)	0.25 0.5 0.65466(19)	-

C1/4*i*	0.108(2) 0 0.1377(16)	0.103(5) 0 0.1348(17)	0.105(5) 0 0.132(5)	0.098(7) 0 0.11(2)	0.106(4) 0 0.123(4)	0.108(3) 0 0.130(5)	0.103(2) 0 0.140(2)	-
Data collection								
No. of measured, independent and observed [I > 2σ(I)] reflections	282/139/131	304/113/106	92/71/67	117/70/67	126/69/67	131/81/75	316/131/119	83/57/57
R_{int}	1.59%	1.59%	1.02%	5.41%	1.40%	3.51%	2.08%	13.58%
Refinement								
R_1	2.73%	2.73%	4.91%	13.64%	4.39%	3.61%	2.97%	-
wR_2	6.86%	6.86%	11.98%	29.83%	10.58%	9.78%	6.57%	-
GOF	1.162	1.162	1.173	1.352	1.185	1.258	1.059	-
No. of reflections/ No. of parameters	139/8	113/11	71/8	70/6	69/8	81/11	131/11	-

Table S16. Structure refinement details and crystallographic data of γ-SmC at 103(4) and 87(3) GPa. The full crystallographic datasets deposited to the CCDC are available under the deposition numbers: 2347674 (γ-SmC at 103(4) GPa) and 2347675 (γ-SmC at 87(5) GPa).

Chemical formula	γ-SmC	
Pressure (GPa)	103(4)	87(5) (decompression)
Crystal data		
Mr	162.36	
ρ (g/cm^3)	13.617	13.318
Radiation type	X-ray, λ = 0.2846 Å	X-ray, λ = 0.4100 Å
Space group	*Cmcm*	
a (Å)	10.0193(14)	10.252(2)
b (Å)	9.897(9)	9.8369(15)
c (Å)	4.7921(5)	4.818(4)
V (Å^3)	475.2(4)	485.8(4)
Z	24	
CN of Sm1	10	
CN of Sm2	8	
CN of Sm3	6	
CN of Sm4	6	
Sm1-C distances in first coordination sphere (Å)	2.361(14) – 2.88(3)	2.36(3) – 2.90(4)

Sm2-C distances in first coordination sphere (Å)	2.340(12) – 2.490(7)	2.31(4) – 2.52(4)
Sm3-C distances in first coordination sphere (Å)	2.31(3) – 2.390(14)	2.26(5) – 2.46(3)
Sm4-C distances in first coordination sphere (Å)	2.315(14) – 2.558(16)	2.36(3) – 2.61(4)
C-C distance in [C_2] units (Å)	1.360(18)	1.51(10)
C-C distance in carbon chains (Å)	1.50(4), 1.511(14)	1.46(9), 1.46(7)
∠C-C-C in carbon chains (°)	126.2(10)	131(3)
Atom / Wyck. site/ Fractional atomic coordinates (x; y; z)		
Sm1/4*c*	0 0.4170(2) 0.25	0 0.4180(3) 0.25
Sm2/8*g*	0.35903(6) 0.43982(15) 0.25	0.3575(2) 0.43968(19) 0.25
Sm3/4*c*	0 0.7099(2) 0.25	0 0.7104(3) 0.25
Sm4/8*g*	0.19352(6) 0.24185(15) 0.25	0.19154(19) 0.24152(18) 0.25
C1/8*f*	0 0.134(3) 0.1081(18)	0 0.133(3) 0.093(10)
C2/16*h*	0.3280(7) 0.061(2) 0.0923(14)	0.325(3) 0.056(2) 0.099(9)
Data collection		
No. of measured, independent and observed [$I > 2\sigma(I)$] reflections	1425/441/320	471/233/169
R_{int}	3.45%	4.73%
Refinement		
R_1	3.33%	5.30%
wR_2	7.79%	13.91%
GOF	0.975	1.072
No. of reflections/No. of parameters	441/33	233/27

Table S17. Structure refinement details and crystallographic data of Y_5C_9 at 68(3) GPa, Gd_5C_9 at 46(1) and 58(1) GPa, and Yb_5C_9 at 43(1) and 60(1) GPa. The full crystallographic datasets deposited to the CCDC are available under the deposition numbers: 2347575 (Y_5C_9 at 68(3) GPa), 2347576 (Nd_5C_9 at 37(2) GPa), 2347577 (Gd_5C_9 at 46(1) GPa), 2347578 (Gd_5C_9 at 58(1) GPa), 2347579 (Yb_5C_9 at 43(1) GPa), 2347580 (Yb_5C_9 at 60(1) GPa).

Chemical formula	Y_5C_9	Nd_5C_9	Gd_5C_9		Yb_5C_9	
Pressure (GPa)	68(3)	37(2)	46(1)	58(1)	43(1)	60(1)
Crystal data						
Mr	552.64	829.29	894.34		973.29	
ρ (g/cm^3)	7.190	9.214	10.644	11.031	12.500	13.082
Radiation type	X-ray, λ = 0.2904 Å	X-ray, λ = 0.4099 Å	X-ray, λ = 0.2905 Å	X-ray, λ = 0.4100 Å	X-ray, λ = 0.2905 Å	X-ray, λ = 0.4100 Å
Space group	*P4/mnc*					

a (Å)	7.2266(13)	7.742(3)	7.4869(7)	7.4008(10)	7.2387(4)	7.1107(6)
c (Å)	4.8882(18)	4.986(2)	4.978(7)	4.916(4)	4.935(5)	4.8868(10)
V ($Å^3$)	255.28(13)	298.9(3)	279.1(4)	269.2(2)	258.6(3)	247.09(7)
Z	2					
CN of REE1	11					
CN of REE2	10					
REE1-C distances in first coordination sphere (Å)	2.2136(11) – 2.615(9)	2.3371(17) – 2.727(18)	2.2802(10) – 2.71(3)	2.2460(7) – 2.655(14)	2.1821(4) – 2.640(14)	2.1449(6) – 2.571(8)
REE2-C distances in first coordination sphere (Å)	2.384(8), 2.4441(9)	2.4930(10) – 2.578(16)	2.436(15), 2.489(4)	2.436(9), 2.458(3)	2.362(8), 2.467(3)	2.340(7), 2.4434(6)
C-C distance in carbon chains (Å)	1.441(18), 1.47(2)	1.43(4), 1.49(4)	1.36(7), 1.57(6)	1.47(4), 1.47(3)	1.38(4), 1.54(3)	1.444(16), 1.50(2)
∠C-C-C in carbon chains (°)	132.7(8)	134.9(15)	135.8(19)	132.1(12)	135.0(11)	131.0(7)
Atom / Wyck. site/ Fractional atomic coordinates (x; y; z)						
REE1/8*h*	0.28889(14) 0.10182(15) 0	0.09741(19) 0.28572(17) 0	0.09968(11) 0.28778(12) 0	0.28644(7) 0.10027(7) 0	0.28391(5) 0.10133(5) 0	0.28381(7) 0.10217(6) 0
REE2/2*b*	0 0 0.5	0 0 0.5	0 0 0.5	0 0 0.5	0 0 0.5	0 0 0.5
C1/16*i*	0.0983(12) 0.2981(10) 0.350(2)	0.3003(19) 0.1073(19) 0.351(4)	0.3989(14) 0.2045(14) 0.137(7)	0.0979(9) 0.2980(8) 0.350(4)	0.2036(7) 0.4025(8) 0.140(4)	0.0945(8) 0.2972(9) 0.347(2)
C2/2*a*	0 0 0	0 0 0	0 0 0	0 0 0	0 0 0	0 0 0
Data collection						
No. of measured, independent and observed [I > 2σ(I)] reflections	628/169/133	474/209/127	725/130/112	523/196/159	1194/222/186	396/201/186
R_{int}	3.59%	4.46%	4.24%	2.86%	2.46%	1.49%
Refinement						
R_1	4.77%	5.27%	3.82%	3.27%	2.54%	3.08%
wR_2	11.48%	14.75%	10.17%	7.93%	6.29%	7.96%

GOF	1.124	0.966	1.116	0.998	1.098	1.055
No. of reflections/ No. of parameters	169/13	209/20	130/14	196/14	222/14	201/14

Table S18. Structure refinement details and crystallographic data of Sm_5C_9 at 42(1), 50(1) and 62(1) GPa, $Sm_5C_{8.6}$ at 44(1) GPa, and the decompression in Ar details. The full crystallographic datasets deposited to the CCDC are available under the deposition numbers: 2347618 (Sm_5C_9 at 42(1) GPa), 2347619 (Sm_5C_9 at 50(1) GPa), 2347620 (Sm_5C_9 at 62(1) GPa), 2347621 ($Sm_5C_{8.6}$ at 44(1) GPa), 2347622 (Sm_5C_9 at 36(1) GPa), 2347623 ($Sm_5C_{8.6}$ at 20(1) GPa).

Chemical formula	Sm_5C_9			$Sm_5C_{8.6}$	Sm_5C_9	$Sm_5C_{8.6}$	Sm_5C_{8+x}	Sm_5C_{8+x}
					Decompression			
Pressure (GPa)	42(1)	50(1)	62(1)	44(1)	36(1)	20(1)	1(1)	0
Crystal data								
Mr	859.84			854.50	859.84	854.62	-	-
ρ (g/cm^3)	9.845	10.040	10.612	10.017	9.812	9.466	-	-
Radiation type	X-ray, λ = 0.3738 Å	X-ray, λ = 0.2846 Å	X-ray, λ = 0.3738 Å	X-ray, λ = 0.2900 Å	X-ray, λ = 0.4100 Å			
Space group	*P4/mnc*							*Symmetry: oP*
a (Å)	7.6307(19)	7.5851(10)	7.4167(6)	7.5523(7)	7.6371(14)	7.689(2)	7.776(5)	5.12(2)
b (Å)	7.6307(19)	7.5851(10)	7.4167(6)	7.5523(7)	7.6371(14)	7.689(2)	7.776(5)	7.742(8)
c (Å)	4.9812(13)	4.9435(10)	4.8920(6)	4.9670(14)	4.990(2)	5.072(2)	5.121(3)	7.959(7)
V (Å^3)	290.04(16)	284.42(9)	269.10(5)	283.30(9)	291.02(16)	299.8(2)	309.7(3)	316(1)
Z	2							
CN of Sm1	11							
CN of Sm2	10							
Sm1-C distances in first coordination sphere (Å)	2.3163(9) – 2.718(9)	2.3041(5) – 2.696(5)	2.2560(8) – 2.630(10)	2.3011(6) – 2.694(11)	2.3246(11) – 2.716(12)	2.3433(14) – 2.754(18)	-	-
Sm2-C distances in first coordination sphere (Å)	2.4906(7), 2.515(9)	2.4718(6), 2.494(5)	2.433(9), 2.4460(4)	2.472(8), 2.4835(8)	2.4950(10), 2.519(11)	2.495(15), 2.5360(10)	-	-
C-C distance in carbon chains (Å)	1.46(2), 1.481(19)	1.473(10)	1.446(19), 1.48(2)	1.47(3), 1.49(3)	1.47(3), 1.50(3)	1.46(5), 1.57(4)	-	-

∠C-C-C in carbon chains (°)	133.9(8)	132.7(4)	132.0(8)	132.8(10)	132.9(10)	133.3(14)	-	-
Atom / Wyck. site/ Fractional atomic coordinates (x; y; z)								
Sm1/8*h*	0.09810(7) 0.28726(9) 0	0.09837(5) 0.28740(5) 0	0.09919(10) 0.28755(9) 0	0.09816(8) 0.28844(7) 0	0.09835(7) 0.28806(13) 0	0.09740(16) 0.28877(15) 0	-	-
Sm2/2*b*	0 0 0.5	0 0 0.5	0 0 0.5	0 0 0.5	0 0 0.5	0 0 0.5	-	-
C1/16*i*	0.2979(11) 0.1032(10) 0.353(2)	0.2972(6) 0.1018(5) 0.3510(10)	0.2953(11) 0.1023(13) 0.349(2)	0.2954(8) 0.1020(10) 0.352(3)	0.2978(13) 0.1026(9) 0.350(3)	0.2930(18) 0.102(2) 0.356(4)	-	-
C2/2*a*	0 0 0	0 0 0	0 0 0	0 0 0	0 0 0	0 0 0	-	-
Data collection								
No. of measured, independent and observed [$I > 2\sigma(I)$] reflections	403/219/ 183	1553/614/ 489	551/284/ 211	801/202/ 174	332/224/ 199	276/174/ 117	47	73
R_{int}	2.06%	2.48%	2.25%	2.57%	2.21%	5.44%	-	-
Refinement								
R_1	3.92%	3.67%	3.90%	2.79%	6.38%	5.85%	-	-
wR_2	11.09%	9.77%	10.33%	6.81%	18.64%	14.31%	-	-
GOF	1.066	1.072	1.051	1.183	1.191	1.030	-	-
No. of reflections/ No. of parameters	219/14	614/20	284/20	202/15	224/20	174/15	-	-

Table S19. Structure refinement details and crystallographic data of γ-YC_2 at 94(3) and 124(3) GPa, and γ-SmC_2 at 62(1), 103(4) and 117(4) GPa. γ-SmC_2 synthesized at 62(1) GPa was decompressed to 28(3) GPa. The full crystallographic datasets deposited to the CCDC are available under the deposition numbers: 2347599 (γ-YC_2 at 94(3) GPa), 2347600 (γ-YC_2 at 124(3) GPa), 2347601 (γ-SmC_2 at 62(1) GPa), 2347602 (γ-SmC_2 at 103(4) GPa), 2347603 (γ-SmC_2 at 117(4) GPa).

Chemical formula	γ-YC_2		γ-SmC_2				
Pressure (GPa)	94(3)	124(3)	62(1)	Decompression		103(4)	117(4)
				39(3)	28(3)		
Crystal data							
Mr	112.93		174.37				
ρ (g/cm^3)	7.877	8.247	10.802	10.148	10.042	11.688	11.987

Radiation type	X-ray, λ = 0.2846 Å	X-ray, λ = 0.2900 Å	X-ray, λ = 0.3738 Å	X-ray, λ = 0.4099 Å		X-ray, λ = 0.2846 Å	X-ray, λ = 0.2905 Å
Space group	*Immm*						
a (Å)	2.5981(19)	2.566(2)	2.6462(4)	2.6783(18)	2.6973(3)	2.5977(5)	2.5693(4)
b (Å)	5.6282(8)	5.5123(13)	5.8241(7)	6.045(6)	5.997(4)	5.5945(11)	5.557(13)
c (Å)	6.5126(10)	6.4306(14)	6.957(2)	7.050(5)	7.1301(17)	6.8187(8)	6.7674(11)
V (Å^3)	95.23(7)	90.95(9)	107.22(4)	114.14(16)	115.34(8)	99.10(3)	96.6(2)
Z	4						
CN of REE1	12						
REE1-C distances in first coordination sphere (Å)	2.339(4) – 2.499(5)	2.306(7) – 2.453(14)	2.453(11) – 2.63(2)	2.49(4) – 2.76(5)	2.50(6) – 2.69(7)	2.399(5) – 2.552(6)	2.378(14) – 2.521(15)
C2-C2 distance in carbon ribbons (Å)	1.494(11)	1.47(4)	1.50(5)	1.43(11)	1.57(17)	1.415(15)	1.43(4)
C1-C2 distance in carbon ribbons (Å)	1.467(4)	1.449(10)	1.491(14)	1.59(5)	1.50(6)	1.477(6)	1.455(14)
∠C1-C2-C2 in carbon ribbons (°)	117.7(3)	117.7(7)	117.4(10)	123(3)	116(5)	118.4(4)	118.0(10)
∠C2-C1-C2 in carbon ribbons (°)	124.6(5)	124.7(14)	125(2)	115(5)	128(10)	123.1(8)	124(2)
Atom / Wyck. site/ Fractional atomic coordinates (x; y; z)							
REE1/4*i*	0 0 0.21570(8)	0 0 0.2158(2)	0 0 0.21436(19)	0 0 0.2146(3)	0 0 0.2141(3)	0 0 0.21479(4)	0 0 0.21437(4)
C1/4*h*	0 0.2539(9) 0.5	0 0.255(2) 0.5	0 0.247(3) 0.5	0 0.260(9) 0.5	0 0.240(17) 0.5	0 0.2522(15) 0.5	0 0.252(4) 0.5
C2/4*g*	0 0.3673(9) 0	0 0.367(3) 0	0 0.371(4) 0	0 0.382(9) 0	0 0.369(14) 0	0 0.3735(13) 0	0 0.371(3) 0
Data collection							
No. of measured, independent and observed [I > 2σ(I)] reflections	346/140/127	145/53/46	129/86/79	111/64/59	117/65/54	292/152/144	238/85/84
R_{int}	3.70%	4.01%	2.42%	2.07%	3.56%	1.28%	1.10%
Refinement							
R_1	2.91%	2.64%	3.16%	6.66%	8.34%	2.25%	1.36%

wR_2	4.45%	6.41%	7.57%	18.01%	18.66%	5.65%	3.28%
GOF	1.080	1.185	1.068	1.199	1.028	1.073	1.300
No. of reflections/ No. of parameters	140/13	53/9	86/9	64/9	65/7	152/13	85/9

Table S20. Structure refinement, decompression details, and crystallographic data of γ-SmC_2 synthesized at 117(4) GPa and γ-DyC_2 synthesized at 66(3) GPa [12].

Chemical formula	γ-SmC_2				γ-DyC_2			
Pressure (GPa)	117(4)	Decompression			66(3) [12]	Decompression		
		110(5)	87(5)	67(5)		59(3)	53(3)	41(3)
Crystal data								
Mr	174.37				186.52			
ρ (g/cm^3)	11.987	11.729	11.455	11.061	12.228	11.880	11.688	-
Radiation type	X-ray, λ = 0.2905 Å	X-ray, λ = 0.4100 Å			X-ray, λ = 0.2846 Å			
Space group	*Immm*							
a (Å)	2.5693(4)	2.5865(14)	2.6007(19)	2.6226(7)	2.6355(12)	2.645(3)	2.665(6)	2.647(5)
b (Å)	5.557(13)	5.6437(11)	5.6516(11)	5.743(5)	5.707(3)	5.815(4)	5.830(3)	5.894(6)
c (Å)	6.7674(11)	6.765(12)	6.879(5)	6.951(6)	6.737(3)	6.779(2)	6.823(7)	6.903(4)
V (Å^3)	96.6(2)	98.75(19)	101.10(10)	104.71(13)	101.31(7)	104.28(13)	106.0(2)	107.7(3)
Z	4							
Data collection								
No. of measured, independent and observed [I > 2σ(I)] reflections	238/85/84	72/47/47	137/69/65	102/68/59	212/104/95	148/106/90	265/142/ 92	50
R_{int}	1.10%	3.14%	4.61%	6.18%	3.21%	2.27%	10.14%	-
Refinement								
R_1	1.36%	6.09%	4.07%	5.43%	2.30%	4.83%	11.87%	-
wR_2	3.28%	13.62%	10.02%	14.02%	5.03%	11.05%	27.14%	-
GOF	1.300	1.311	1.249	1.095	1.020	1.122	1.030	-
No. of reflections/ No. of parameters	85/9	47/7	69/9	68/9	104/9	106/9	142/7	-

Table S21. Structure refinement details and crystallographic data of ε-LaC_2 at 45(1), 59(1) and 67(1) GPa. The full crystallographic datasets deposited to the CCDC are available under the deposition numbers: 2347644 (ε-LaC_2 at 45(1) GPa), 2347645 (ε-LaC_2 at 59(1) GPa), 2347646 (ε-LaC_2 at 67(1) GPa).

Chemical formula	ε-LaC_2		
Pressure (GPa)	45(1)	59(1)	67(1)
Crystal data			
Mr	162.93		
ρ (g/cm^3)	8.471	8.822	9.073
Radiation type	X-ray, λ = 0.2901 Å	X-ray, λ = 0.2905 Å	X-ray, λ = 0.28457 Å
Space group	*C*2/*m*		
a (Å)	7.883(3)	7.817(4)	7.7253(18)
b (Å)	5.8534(6)	5.7214(11)	5.6918(17)
c (Å)	6.9388(5)	6.883(13)	6.802(2)
β (°)	94.010(18)	94.94(10)	94.43(2)
V (Å^3)	319.39(13)	306.7(6)	298.19(15)
Z	10		
CN of La1/La2/La3	12		
La1-C distances in first coordination sphere (Å)	2.686(10) – 3.083(15)	2.623(19) – 3.019(18)	2.625(10) – 2.987(10)
La2-C distances in first coordination sphere (Å)	2.419(8) – 2.785(3)	2.38(4) – 2.751(7)	2.373(11) – 2.718(5)
La3-C distances in first coordination sphere (Å)	2.490(13) – 2.698(9)	2.458(16) – 2.666(14)	2.421(10) – 2.630(14)
C1-C2 distance in carbon arrangements (Å)	1.487(10)	1.47(3)	1.471(13)
C1-C3 distance in carbon arrangements (Å)	1.429(13)	1.44(5)	1.422(15)
C2-C2 distance in carbon arrangements (Å)	1.48(2)	1.42(4)	1.43(4)
C3-C3 distance in carbon arrangements (Å)	1.489(15)	1.49(3)	1.45(2)
Atom / Wyck. site/ Fractional atomic coordinates (x; y; z)			
La1/2*d*	0 0.5 0.5	0 0.5 0.5	0 0.5 0.5
La2/4*i*	0.16989(19) 0 0.67789(10)	0.1683(2) 0 0.6805(4)	0.16995(11) 0 0.68104(15)
La3/4*i*	0.3196(2) 0 0.08555(10)	0.3200(2) 0 0.0867(4)	0.32030(10) 0 0.08499(15)
C1/8*j*	0.065(2) 0.2460(13) 0.1792(11)	0.069(2) 0.2482(18) 0.177(5)	0.0670(11) 0.2511(18) 0.1793(15)
C2/4*g*	0 0.1263(17) 0	0 0.124(3) 0	0 0.126(3) 0
C3/8*j*	0.136(2) 0.1272(12) 0.3458(11)	0.138(2) 0.1302(18) 0.351(5)	0.1391(12) 0.1275(17) 0.3480(16)

Data collection			
No. of measured, independent and observed [I > 2σ(I)] reflections	856/472/389	724/249/189	656/411/324
R_{int}	1.42%	3.94%	1.79%
Refinement			
R_1	5.51%	3.76%	3.64%
wR_2	15.44%	9.08%	9.19%
GOF	1.098	1.093	1.018
No. of reflections/No. of parameters	472/27	249/27	411/40

Table S22. Structure refinement details and crystallographic data of La_3C_5 at 45(1) and 67(1) GPa. The full crystallographic dataset of La_3C_5 at 45(1) GPa was deposited to the CCDC under the deposition number 2347647.

Chemical formula	La_3C_5	
Pressure (GPa)	45(1)	67(1)
Crystal data		
Mr	476.78	
ρ (g/cm^3)	8.550	9.111
Radiation type	X-ray, λ = 0.2846 Å	X-ray, λ = 0.28457 Å
Space group	$P2_1/n$	
a (Å)	4.869(12)	4.82(2)
b (Å)	10.846(5)	10.558(9)
c (Å)	7.366(4)	7.143(9)
β (°)	107.79(13)	107.0(3)
V (Å^3)	370.4(10)	347.6(18)
Z	4	
CN of La1	10	
CN of La2	9	
CN of La3	11	
La1-C distances in first coordination sphere (Å)	2.46(3) - 2.754(19)	-
La2-C distances in first coordination sphere (Å)	2.594(19) – 2.86(5)	-
La3-C distances in first coordination sphere (Å)	2.46(5) – 2.83(5)	-
C1-C3 distance in carbon arrangements (Å)	1.54(5)	-
C1-C5 distance in carbon arrangements (Å)	1.47(3)	-

C2-C4 distance in carbon arrangements (Å)	1.44(5)	-
C2-C5 distance in carbon arrangements (Å)	1.44(5)	-
C3-C3 distance in carbon arrangements (Å)	1.45(6)	-
C3-C4 distance in carbon arrangements (Å)	1.44(3)	-
Atom / Wyck. site/ Fractional atomic coordinates (x; y; z)		
La1/4*e*	0.1282(5) 0.87689(11) 0.72381(13)	-
La2/4*e*	0.0468(5) 0.63486(10) 0.93841(13)	-
La3/4*e*	0.0439(5) 0.12512(11) 0.85757(14)	-
C1/4*e*	0.163(9) 0.5445(17) 0.296(2)	-
C2/4*e*	0.027(9) 0.7421(17) 0.438(2)	-
C3/4*e*	0.042(9) 0.4664(18) 0.428(2)	-
C4/4*e*	0.063(9) 0.3339(19) 0.431(3)	-
C5/4*e*	0.146(8) 0.6793(16) 0.307(2)	-
Data collection		
No. of measured, independent and observed [I > 2σ(I)] reflections	1466/732/491	209/150/93
R_{int}	3.64%	3.74%
Refinement		
R_1	7.01%	-
wR_2	19.78%	-
GOF	1.014	-
No. of reflections/No. of parameters	732/48	-

Table S23. C-C distances in [C_2] units in the synthesized carbides and calculated C-C distances in the relaxed structures at fixed pressure by DFT.

Structure type	Chemical formula	Pressure (GPa)	C-C distance in [C_2] units (Å)	DFT	
				Pressure (GPa)	C-C distance in [C_2] units (Å)
*oC*16 β-LaC	β-LaC	41(1)	1.387(15)	70	1.3818
	β-NdC	43(1)	1.38(2)	70	1.3935
	β-SmC	51(1)	1.41(4)	70	1.3996
*tP*10 U_3Si_2	Nd_3C_2	43(1)	1.446(10)	70	1.4126
	Sm_3C_2	44(1)	1.51(3)	70	1.4270
	Gd_3C_2	45(1)	1.468(13)	70	1.4474

	Dy_3C_2 [12,13]	55(1)	1.51(3)	70	1.4702
*cI*40 Pu_2C_3	Y_2C_3 [14]	46(1)	1.32(1)	20	1.3313
	Sm_2C_3	42(1)	1.42(12)	20	1.3273
	Gd_2C_3	44(1)	1.33(3)	20	1.3100
	Dy_2C_3 [13]	19(1)	1.269(12)	20	1.3324

Table S24. C-C distances in the synthesized [C_3] trimers-containing carbides and calculated C-C distances in the relaxed structures at 70 GPa.

Structure type	Chemical formula	Pressure (GPa)	C-C distance in [C_3] (Å)	C-C-C bond angle in [C_3] (°)	C-C distance in [C_2] (Å)	DFT (70 GPa)		
						C-C distance in [C_3] units (Å)	C-C-C bond angle in [C_3] units (°)	C-C distance in [C_2] units (Å)
*tP*48 Nd_5C_7	Nd_5C_7	57(1)	1.392(11)	146.9(10)		1.3617	150.73	
	Sm_5C_7	50(1)	1.403(11)	147.3(11)		1.3662	149.36	
	Gd_5C_7	45(1)	1.43(2)	146(3)		1.3707	148.21	
	Yb_5C_7	42(1)	1.44(4)	141(4)		1.3803	145.39	
*oC*72 γ-Y_4C_5 [14]	γ-Y_4C_5 [14]	44(1)	1.43(1)	134.4(2)	1.40(2)	1.4055	134.27	1.3723
	γ-Sm_4C_5	42(1)	1.40(4)	136(4)	1.42(6)	1.3983	134.86	1.3621
	γ-Gd_4C_5	45(1)	1.398(11)	135.1(13)	1.377(17)	1.4017	134.37	1.3678
	γ-Dy_4C_5 [12]	65(3)	1.432(6)	132(3)	1.385(11)	1.4058	134.02	1.3730
	γ-Yb_4C_5	42(1)	1.416(7)	133.9(8)	1.417(13)	1.4103	134.27	1.3804

Table S25. C-C distances in the synthesized carbides containing carbon chains and C-C distances in the relaxed structures at fixed pressure by DFT.

Structure type	Chemical formula	Pressure (GPa)	C-C distance in chains (Å)	C-C distance in [C_2] units (Å)	DFT		
					Pressure (GPa)	C-C distance in carbon chains (Å)	C-C distance in [C_2] units (Å)
*oC*6 δ-NdC_2	NdC_2	43(1)	1.41(2), 1.501(17)		70	1.4219, 1.4611	
	SmC_2	44(1)	1.45(2), 1.463(18)		70	1.4203, 1.4552	
*oC*48 γ-SmC	γ-SmC	103(4)	1.50(4), 1.511(14)	1.360(18)	103	1.5224, 1.5710	1.3707
	Y_5C_9	68(3)	1.441(18), 1.47(2)		70	1.4205, 1.4415	

*tP*28 Dy_5C_9 [12]	Nd_5C_9	37(2)	1.43(4), 1.49(4)		70	1.4161, 1.4494	
	Sm_5C_9	62(1)	1.446(19), 1.48(2)		70	1.4168, 1.4452	
	Gd_5C_9	58(1)	1.47(3), 1.47(4)		70	1.4207, 1.4435	
	Dy_5C_9 [12]	68(3)	1.459(5), 1.458(5)		70	1.4218, 1.4419	
	Yb_5C_9	60(1)	1.444(16), 1.50(2)		70	1.4240, 1.4396	

Table S26. C-C distances in the synthesized carbides containing carbon ribbons and C-C distances in the relaxed structures at 70 GPa.

Structure type	Chemical formula	Pressure (GPa)	C-C bond	C-C distance (Å)	C-C distance (Å) at 70 GPa
*oI*12 γ-DyC_2 [12]	γ-YC_2	94(3)	C1-C2	1.467(4)	1.4973
			C2-C2	1.494(11)	1.4679
	γ-SmC_2	62(1)	C1-C2	1.491(14)	1.5083
			C2-C2	1.50(5)	1.4636
	γ-DyC_2 [12]	66(3)	C1-C2	1.508(5)	1.4985
			C2-C2	1.451(9)	1.4676

Table S27. C-C distances in the synthesized carbides containing carbon naphthalene-decalin-like rings and C-C distances in the relaxed structures at fixed pressure by DFT.

Structure type	Chemical formula	Pressure (GPa)	C-C bond	C-C distance in naphthalene-decalin-like rings (Å)	DFT	
					Pressure (GPa)	C-C distance in carbon chains (Å)
*mC*30 ε-LaC_2	ε-LaC_2	45(1)	C1-C2	1.487(10)	45	1.4784
			C1-C3	1.429(13)		1.4223
			C2-C2	1.48(2)		1.4653
			C3-C3	1.489(15)		1.4694
*mP*32 La_3C_5	La_3C_5	45(1)	C1-C3	1.54(5)	45	1.4871
			C1-C5	1.47(3)		1.4369
			C2-C4	1.44(5)		1.4507
			C2-C5	1.44(5)		1.4477
			C3-C3	1.45(6)		1.4808
			C3-C4	1.44(3)		1.4703

Table S28. Results of Mulliken charge analysis for observed carbides containing [C_n] units. The crystal orbital bond indexes (ICOBI) are given only for C-C bonds in [C_2] and [C_3] units, carbon chains, ribbons and naphthalene-decalin like carbon arrangements.

Phase	Atom / Wyckoff site	Coordination number (CN)	Mulliken	Type of the [C_n] units	ICOBI for C-C bond in [C_n] units	
*oC*16 β-LaC	La1/4*c*	6	0.94	[C_2]	d(C1-C1) = 1.3818 Å	1.140
	La2/4*c*	8	1.04			
	C1/8*f*		0.99			
*oC*16 β-NdC	Nd1/4*c*	6	1.35	[C_2]	d(C1-C1) = 1.3935 Å	1.292
	Nd2/4*c*	8	1.45			
	C1/8*f*		-1.40			
*oC*16 β-SmC	Sm1/4*c*	6	1.41	[C_2]	d(C1-C1) = 1.3996 Å	1.282
	Sm2/4*c*	8	1.61			
	C1/8*f*		-1.51			
*tP*10 Nd_3C_2	Nd1/2*a*	4	0.48	[C_2]	d(C1-C1) = 1.4126 Å	1.281
	Nd2/4*h*	6	1.25			
	C1/4*g*		-1.49			
*tP*10 Sm_3C_2	Sm1/2*a*	4	0.58	[C_2]	d(C1-C1) = 1.4270 Å	1.249
	Sm2/4*h*	6	1.34			
	C1/4*g*		-1.63			
*tP*10 Gd_3C_2	Gd1/2*a*	4	0.42	[C_2]	d(C1-C1) = 1.4474 Å	1.111
	Gd2/4*h*	6	0.48			
	C1/4*g*		0.69			
*tP*10 Dy_3C_2 [12,13]	Dy1/2*a*	4	1.01	[C_2]	d(C1-C1) = 1.4702 Å	1.108
	Dy2/4*h*	6	1.13			
	C1/4*g*		-1.63			
*tP*48 Nd_5C_7	Nd1/4*a*	10	1.62	[C_3]	d(C1-C2) = 1.3617 Å	1.418
	Nd2/16*g*	9	1.88			
	C1/16*g*		-1.43			
	C2/8*f*		-0.73			
	C3/4*c*		-1.96			
*tP*48 Sm_5C_7	Sm1/4*a*	10	1.70	[C_3]	d(C1-C2) = 1.3662 Å	1.441
	Sm2/16*g*	9	1.97			
	C1/16*g*		-1.50			

	C2/8*f*		-0.77			
	C3/4*c*		-2.04			
*tP*48 Gd_5C_7	Gd1/4*a*	10	0.89	$[C_3]$	d(C1-C2) = 1.3707 Å	1.277
	Gd2/16*g*	9	0.84			
	C1/16*g*		-0.64			
	C2/8*f*		-0.38			
	C3/4*c*		-0.92			
*tP*48 Yb_5C_7	Yb1/4*a*	10	1.85	$[C_3]$	d(C1-C2) = 1.3803 Å	1.356
	Yb2/16*g*	9	1.91			
	C1/16*g*		-1.48			
	C2/8*f*		-0.83			
	C3/4*c*		-1.91			
*oC*72 γ-Y_4C_5 [12,14]	Y1/16*g*	8	1.51	$[C_2]$	d(C1-C3) = 1.3723 Å	0.602
	Y2/8*d*	10	1.64			
	Y3/8*f*	6	1.11			
	C1/8*f*		-1.18	$[C_3]$	d(C2-C4) = 1.4055 Å	0.693
	C2/16*g*		-1.11			
	C3/8*f*		-1.24			
	C4/8*e*		-1.13			
*oC*72 γ-Sm_4C_5	Sm1/16*g*	8	1.74	$[C_2]$	d(C1-C3) = 1.3621 Å	1.392
	Sm2/8*d*	10	2.12			
	Sm3/8*f*	6	1.45			
	C1/8*f*		-1.52	$[C_3]$	d(C2-C4) = 1.3983 Å	1.360
	C2/16*g*		-1.53			
	C3/8*f*		-1.59			
	C4/8*e*		-0.88			
*oC*72 γ-Gd_4C_5	Gd1/16*g*	8	0.80	$[C_2]$	d(C1-C3) = 1.3678 Å	1.316
	Gd2/8*d*	10	0.86			
	Gd3/8*f*	6	0.58			
	C1/8*f*		-0.59	$[C_3]$	d(C2-C4) = 1.4017 Å	1.223
	C2/16*g*		-0.69			
	C3/8*f*		-0.65			
	C4/8*e*		-0.42			

*oC*72 γ-Dy_4C_5 [12]	Dy1/16*g*	8	1.69	[C_2]	d(C1-C3) = 1.3730 Å	1.282
	Dy2/8*d*	10	1.75			
	Dy3/8*f*	6	1.55			
	C1/8*f*		-1.42	[C_3]	d(C2-C4) = 1.4058 Å	1.262
	C2/16*g*		-1.43			
	C3/8*f*		-1.50			
	C4/8*e*		-0.89			
*oC*72 γ-Yb_4C_5	Yb1/16*g*	8	1.75	[C_2]	d(C1-C3) = 1.3804 Å	1.300
	Yb2/8*d*	10	1.88			
	Yb3/8*f*	6	1.59			
	C1/8*f*		-1.50	[C_3]	d(C2-C4) = 1.4103 Å	1.310
	C2/16*g*		-1.48			
	C3/8*f*		-1.60			
	C4/8*e*		-0.91			
*oC*6 δ-NdC_2	Nd1/2*f*	12	1.84	Carbon chains	d(C1-C1) = 1.4219 Å	1.249
	C1/4*i*		-0.92		d(C1-C1) = 1.4611 Å	1.097
*oC*6 δ-SmC_2	Sm1/2*f*	12	1.96	Carbon chains	d(C1-C1) = 1.4203 Å	1.249
	C1/4*i*		-0.98		d(C1-C1) = 1.4552 Å	1.109
*oC*48 γ-SmC	Sm1/4*c*	10	1.62	[C_2]	d(C1-C1) = 1.3707 Å	1.179
	Sm2/8*g*	8	1.34			
	Sm3/4*c*	6	1.32	Carbon chains	d(C2-C2) = 1.5224 Å	0.947
	Sm4/8*g*	6	1.37			
	C1/8*f*		-1.60		d(C2-C2) = 1.5710 Å	0.917
	C2/16*h*		-1.28			
*tP*28 Y_5C_9	Y1/8*h*	11	1.65	Carbon chains	d(C1-C1) = 1.4205 Å	0.707
	Y2/2*b*	10	1.98			
	C1/16*i*		-0.95		d(C1-C1) = 1.4415 Å	0.677
	C2/2*a*		-0.98			
*tP*28 Nd_5C_9	Nd1/8*h*	11	1.82	Carbon chains	d(C1-C1) = 1.4161 Å	1.250
	Nd2/2*b*	10	2.26			
	C1/16*i*		-0.92			1.130

	C2/2*a*		-2.18		d(C1-C1) = 1.4494 Å	
*tP*28 Sm_5C_9	Sm1/8*h*	11	1.97	Carbon chains	d(C1-C1) = 1.4168 Å	1.253
	Sm2/2*b*	10	2.26			
	C1/16*i*		-0.98		d(C1-C1) = 1.4452 Å	1.139
	C2/2*a*		-2.26			
*tP*28 Gd_5C_9	Gd1/8*h*	11	0.83	Carbon chains	d(C1-C1) = 1.4207 Å	1.082
	Gd2/2*b*	10	0.91			
	C1/16*i*		-0.44		d(C1-C1) = 1.4435 Å	1.002
	C2/2*a*		-0.71			
*tP*28 Dy_5C_9 [12]	Dy1/8*h*	11	1.88	Carbon chains	d(C1-C1) = 1.4218 Å	1.184
	Dy2/2*b*	10	1.88			
	C1/16*i*		-0.93		d(C1-C1) = 1.4419 Å	1.101
	C2/2*a*		-1.97			
*tP*28 Yb_5C_9	Yb1/8*h*	11	2.00	Carbon chains	d(C1-C1) = 1.4240 Å	1.204
	Yb2/2*b*	10	1.98			
	C1/16*i*		-0.98		d(C1-C1) = 1.4396 Å	1.109
	C2/2*a*		-2.14			
*oI*12 γ-YC_2	Y1/4*i*	12	1.51	Carbon ribbons	d(C1-C2) = 1.4973 Å	0.705
	C1/4*h*		-0.87		d(C2-C2) = 1.4679 Å	0.713
	C2/4*g*		-0.64			
*oI*12 γ-SmC_2	Sm1/4*i*	12	1.76	Carbon ribbons	d(C1-C2) = 1.5083 Å	1.023
	C1/4*h*		-1.16		d(C2-C2) = 1.4636 Å	1.009
	C2/4*g*		-0.60			
*oI*12 γ-DyC_2 [12]	Dy1/4*i*	12	1.66	Carbon ribbons	d(C1-C2) = 1.4985 Å	0.993
	C1/4*h*		-1.07			
	C2/4*g*		-0.59		d(C2-C2) = 1.4676 Å	0.970
*mC*30 ε-LaC_2	La1/2*d*	12	1.50	Naphthalene -decalin-like fragment	d(C1-C2) = 1.4784 Å	0.892
	La2/4*i*	12	1.55		d(C1-C3) = 1.4223 Å	0.948
	La3/4*i*	12	1.42			0.888

	C1/8*j*		-0.85		d(C2-C2) = 1.4653 Å	
	C2/4*g*		-0.42		d(C3-C3) = 1.4694 Å	0.893
	C3/8*j*		-0.80			
*mP*32 La_3C_5	La1/4*e*	10	1.17	Naphthalene-decalin-like fragment	d(C1-C3) = 1.4871 Å	0.889
	La2/4*e*	8	1.29		d(C1-C5) = 1.4369 Å	0.923
	La3/4*e*	11	1.34		d(C2-C4) = 1.4507 Å	0.892
	C1/4*e*		-0.84		d(C2-C5) = 1.4477 Å	0.870
	C2/4*e*		-0.84			
	C3/4*e*		-0.41		d(C3-C3) = 1.4808 Å	0.915
	C4/4*e*		-0.87		d(C3-C4) = 1.4703 Å	0.903
	C5/4*e*		-0.84			

Table S29. Parameters of the 2nd order Birch-Murnaghan equations of state calculated for observed under extreme conditions carbides.

Structural type	Compound	2nd order Birch-Murnaghan EoS	
		V_0 (Å^3)	K_0 (GPa)
*mC*30 ε-LaC_2	ε-LaC_2	400.4(13)	126(2)
*mP*32 La_3C_5	La_3C_5	461.7(5)	115.6(7)
*oC*16 β-LaC	β-LaC	277.3(4)	94.9(7)
	β-NdC	267.1(18)	103(4)
	β-SmC	255.0(19)	113(4)
*oC*6 δ-NdC_2	δ-NdC_2	74.07(15)	165(2)
	δ-SmC_2	71.12(13)	170.3(19)
*tP*48 Nd_5C_7	Nd_5C_7	745.2(5)	114.2(4)
	Sm_5C_7	708.4(5)	123.2(5)
	Gd_5C_7	674.8(3)	132.0(4)
	Yb_5C_7	607.1(3)	150.3(4)
*tP*10 U_3Si_2	Nd_3C_2	189.5(13)	91(3)
	Sm_3C_2	180.9(10)	93(2)
	Gd_3C_2	173.7(6)	94.7(17)
	Dy_3C_2	168.1(3)	96.7(9)

*oC*48 γ-SmC	γ-SmC	758(5)	102(3)
*oI*12 γ-DyC_2	γ-SmC_2	137.5(3)	179(2)
	γ-DyC_2	128.6(2)	189(2)
	γ-YC_2	128.70(20)	181.0(19)
*cI*40 Pu_2C_3	Sm_2C_3	605.2(5)	119.0(6)
	Gd_2C_3	577.0(6)	126.5(7)
	Dy_2C_3	555.6(6)	131.7(9)
	Y_2C_3	558.7(3)	124.9(4)
*oC*72 γ-Y_4C_5 [14]	γ-Y_4C_5 [14]	1023(2)	122(2)
	γ-Sm_4C_5	1112.5(20)	106.4(10)
	γ-Gd_4C_5	1061(2)	115.1(13)
	γ-Dy_4C_5	1018.9(12)	123.8(8)
	γ-Yb_4C_5	951.6(5)	137.3(4)
*tP*28 Dy_5C_9	Nd_5C_9	375.6(11)	149(3)
	Sm_5C_9	361.7(16)	150(4)
	Gd_5C_9	346.1(11)	158(3)
	Dy_5C_9	334.6(8)	164(2)
	Y_5C_9	334.9(6)	157.7(18)
	Yb_5C_9	315.9(5)	173.9(18)
*cI*28 Anti-Th_3P_4	Gd_4C_3	503(2)	88.8(18)
	Dy_4C_3	485.3(13)	91.6(12)
	Yb_4C_3	451.4(8)	101.2(9)
	Sc_4C_3	376.1(4)	122.1(7)

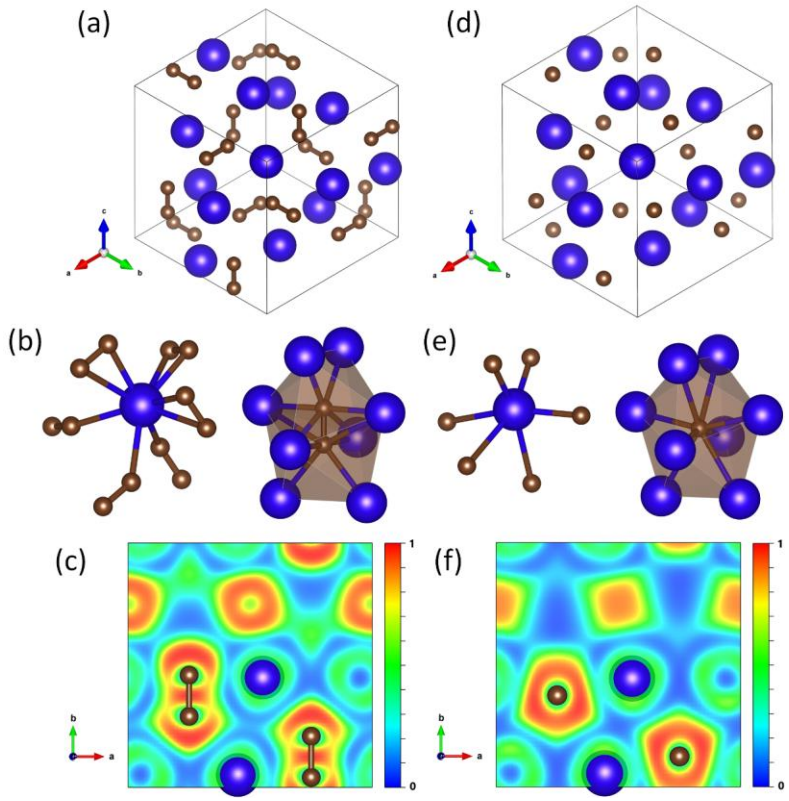

Figure S1. Crystal structure and calculated properties of Dy_2C_3 and Dy_4C_3 at 19 GPa. Dy atoms are blue, C atoms are brown; grey thin lines outline the unit cell. (a) A view of the Dy_2C_3 crystal structure along (1 1 1) direction. (b) The coordination environments of the Dy atom and carbon dumbbell [C_2] in Dy_2C_3. (c) The electron localization function of Dy_2C_3 calculated in (0 0 1). (d) A view of the Dy_4C_3 crystal structure along (1 1 1) direction. (e) The coordination environments of the Dy and C atoms in Dy_4C_3. (f) The electron localization function of Dy_4C_3 calculated in (0 0 1).

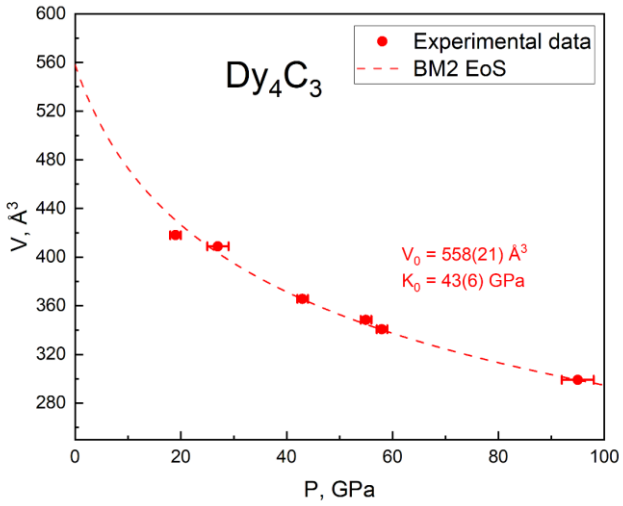

Figure S2. The pressure dependence of the unit cell volume of the synthesized Dy_4C_3 [12,13].

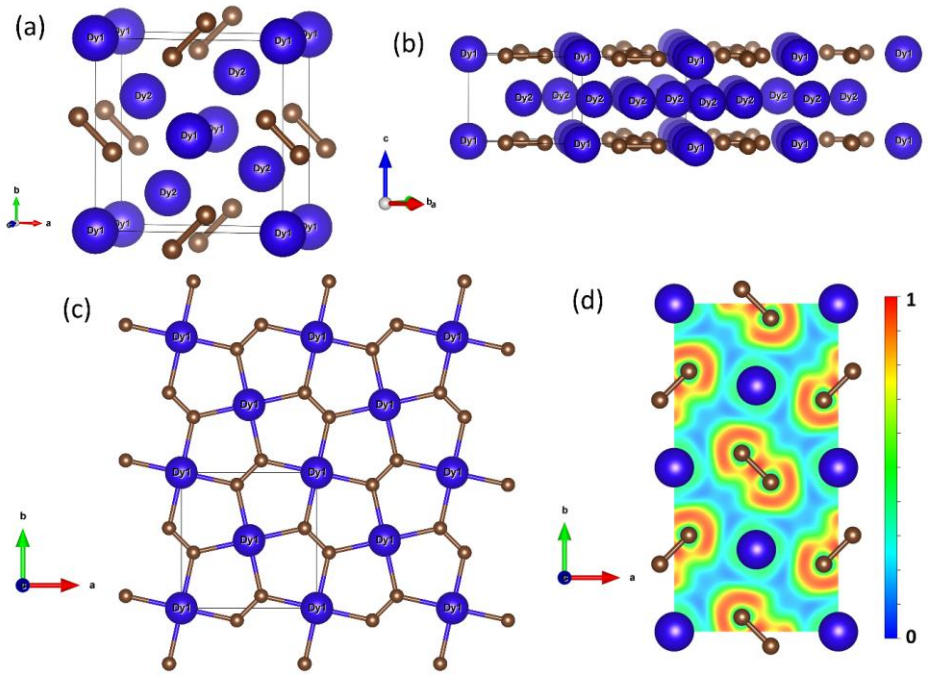

Figure S3. Crystal structure and calculated properties of Dy_3C_2 at 70 GPa. All Dy atoms are blue, C atoms are brown; grey thin lines outline the unit cell. (a) A view of the unit cell. (b) A view of crystal structure representing the "Dy1-C" and "Dy2" layers alternation along *c*-axis. (c) A view of the flat layer consisted of Dy1 and carbon atoms (along *c*-axis). (d) The electron localization function calculated in (0 0 1) plane containing carbon dumbbells [C_2].

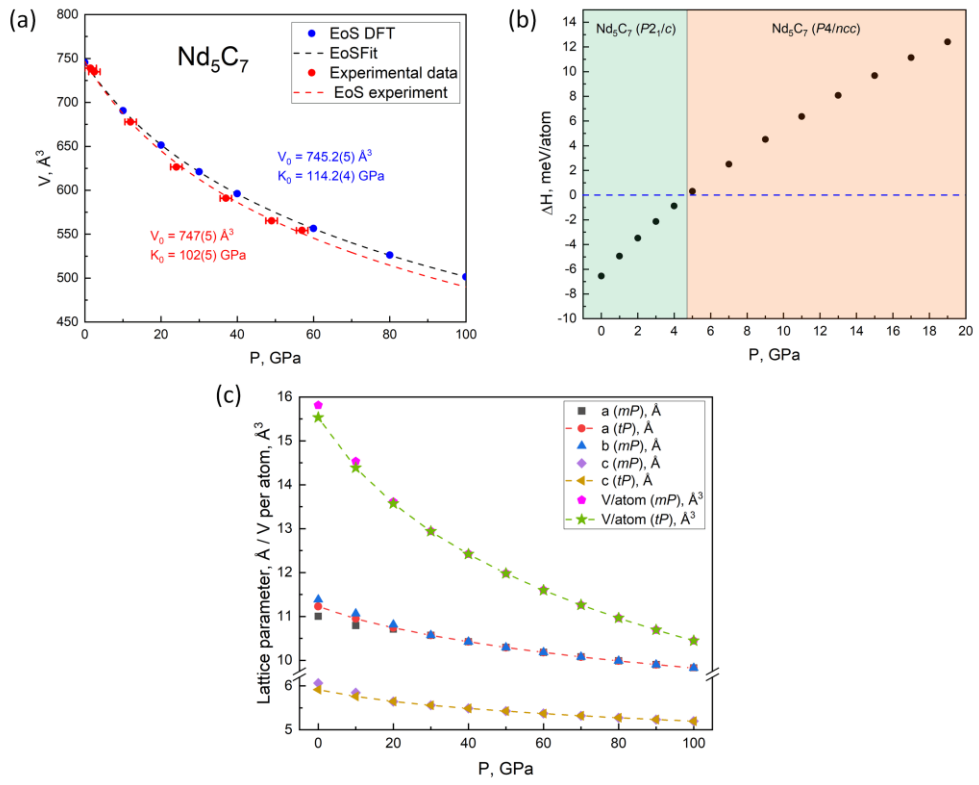

Figure S4. (a) The pressure dependence of the unit cell volume of the synthesized and recovered at ambient conditions Nd_5C_7. (b) The calculated difference in enthalpy per atom

(ΔH=H($P2_1/c$ Nd_5C_7)-H($P4/ncc$ Nd_5C_7)) as a function of pressure. (c) Pressure dependence of the lattice parameters and the unit cell volumes for the monoclinic Nd_5C_7 ($P2_1/c$) and tetragonal Nd_5C_7 ($P4/ncc$).

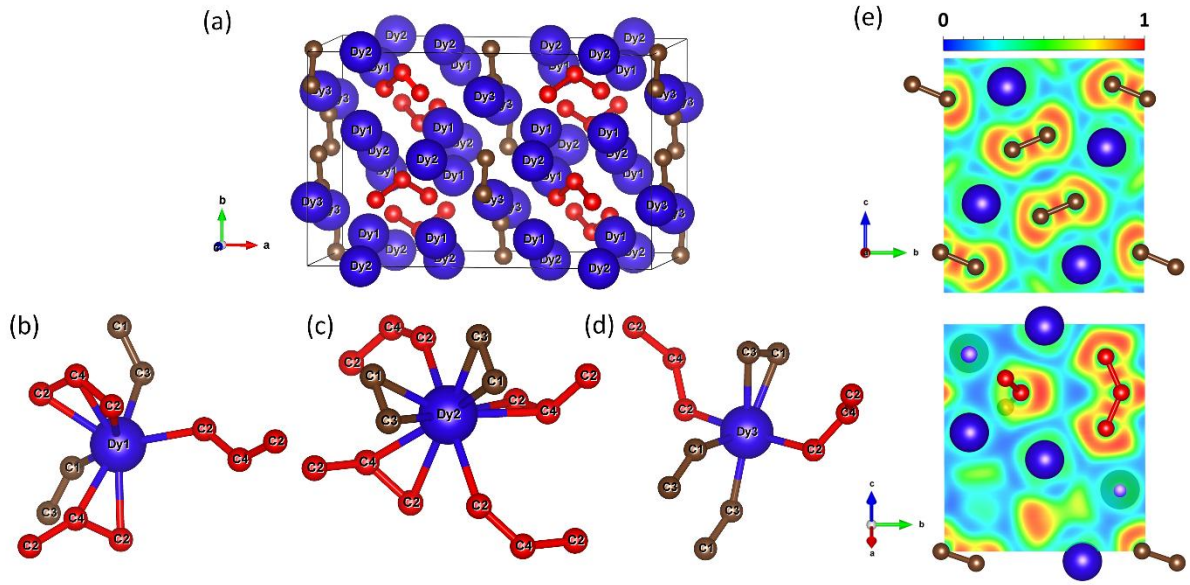

Figure S5. Crystal structure and calculated properties of γ-Dy_4C_5 at 70 GPa. All Dy atoms are blue, brown balls represent carbon atoms of the dumbbells, red balls – carbon atoms that form trimers; grey thin lines outline the unit cell. (a) A view of the crystal structure. (b)-(d) The coordination environment of the Dy1, Dy2 and Dy3 atoms. (e) The ELF calculated in (1 0 0) plane containing carbon dumbbells [C_2] (upper figure) or in plane containing carbon trimers [C_3] (bottom figure).

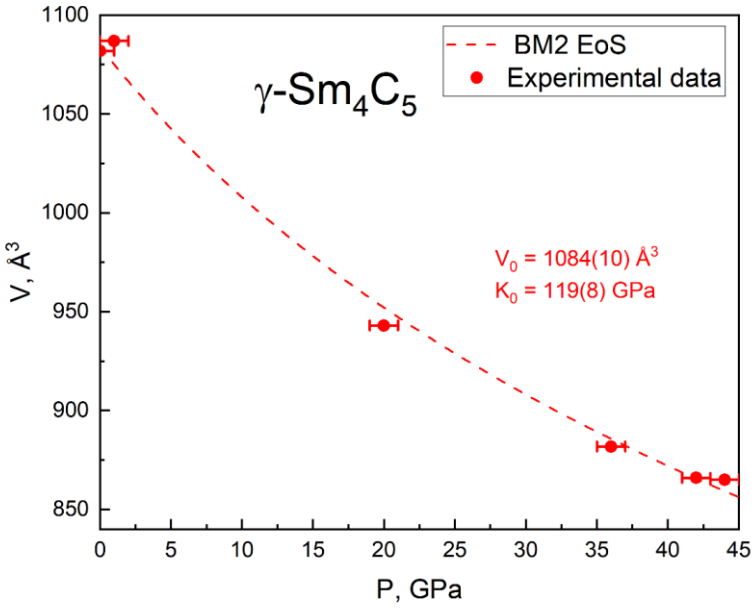

Figure S6. The pressure dependence of the unit cell volume of the synthesized γ-Sm_4C_5.

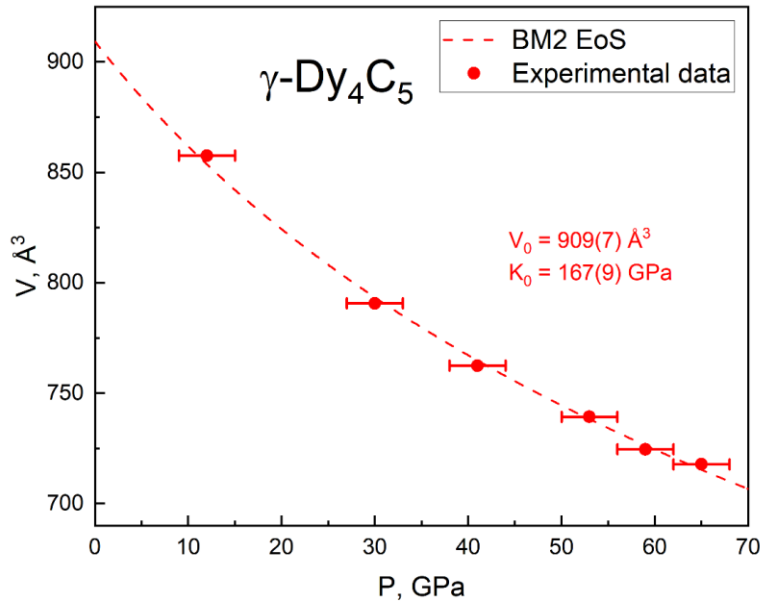

Figure S7. The pressure dependence of the unit cell volume of the synthesized γ-Dy_4C_5 [12].

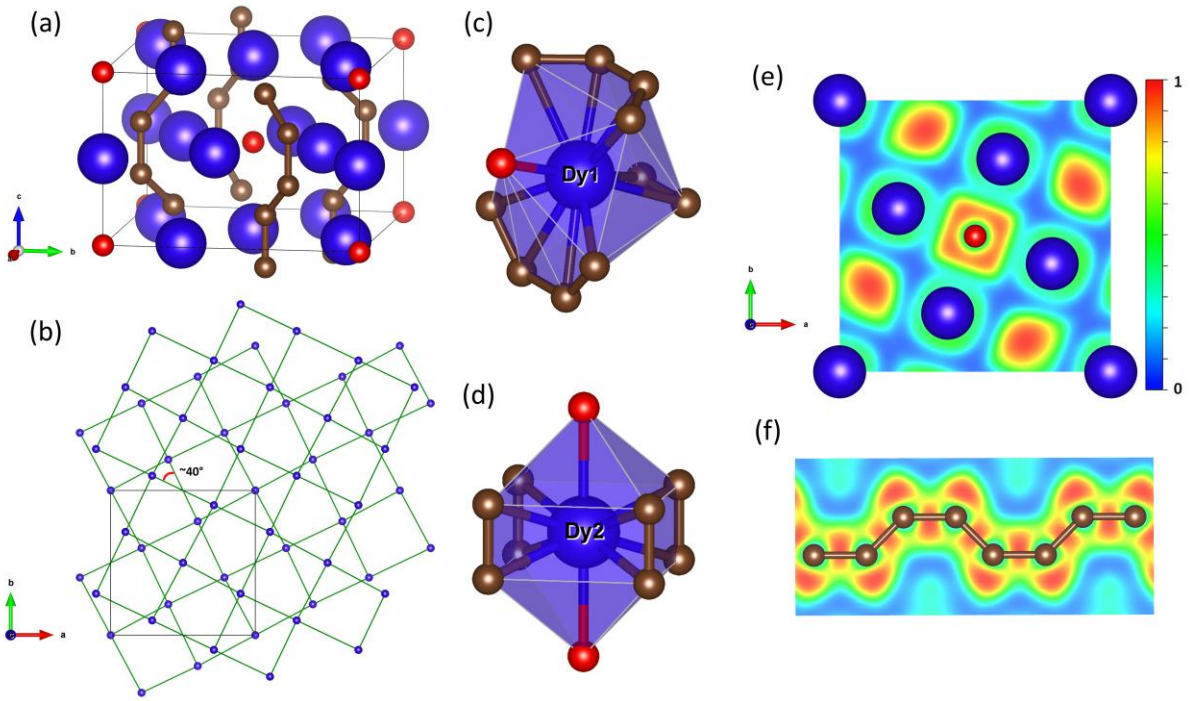

Figure S8. Crystal structure and calculated properties of Dy_5C_9 at 70 GPa. All Dy atoms are blue, C atoms formed chains are brown, discrete C atoms are red; grey thin lines outline the unit cell. (a) A view of the crystal structure. (b) Arrangement of parallel planes comprised of Dy atoms rotated relative to each other by ~40°. (c) and (d) The coordination environment of the Dy1 and Dy2 atoms. (e) The ELF calculated in (0 0 2). (f) The ELF calculated in plane containing carbon chain.

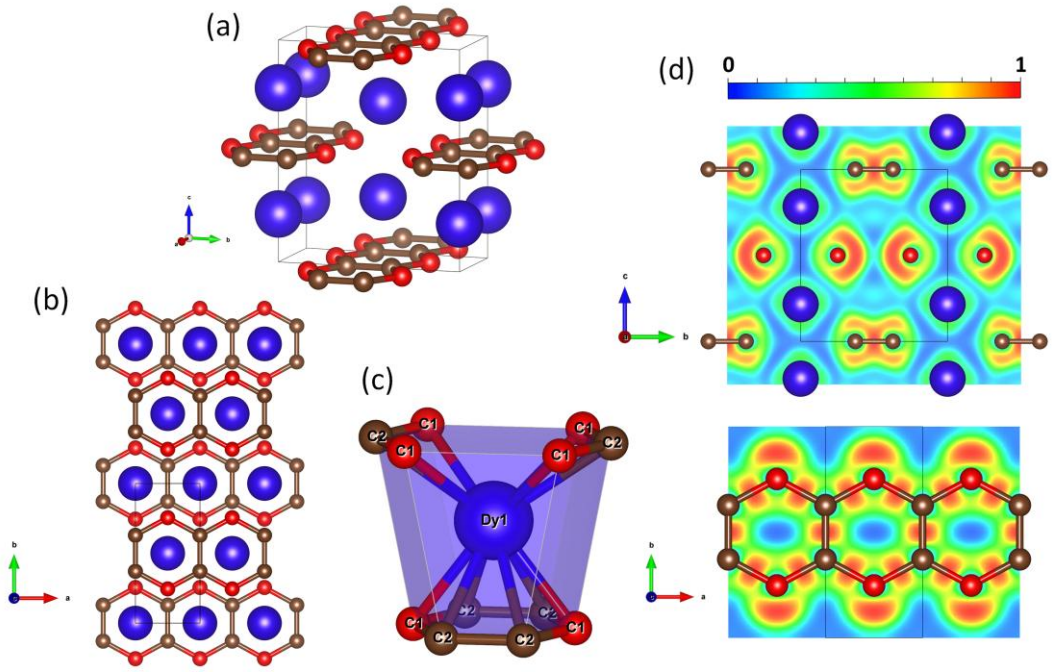

Figure S9. Crystal structure and calculated properties of γ-DyC_2 at 70 GPa. Dy1 atoms are blue, C1 atoms are red, C2 atoms are brown; grey thin lines outline the unit cell. (a) A view of the crystal structure. (b) The crystal structure along *c*-axis. (c) The coordination environment

of the dysprosium atom. (d) The ELF calculated in (1 0 0) (upper figure) or in (0 0 1) plane containing carbon ribbons (bottom figure).

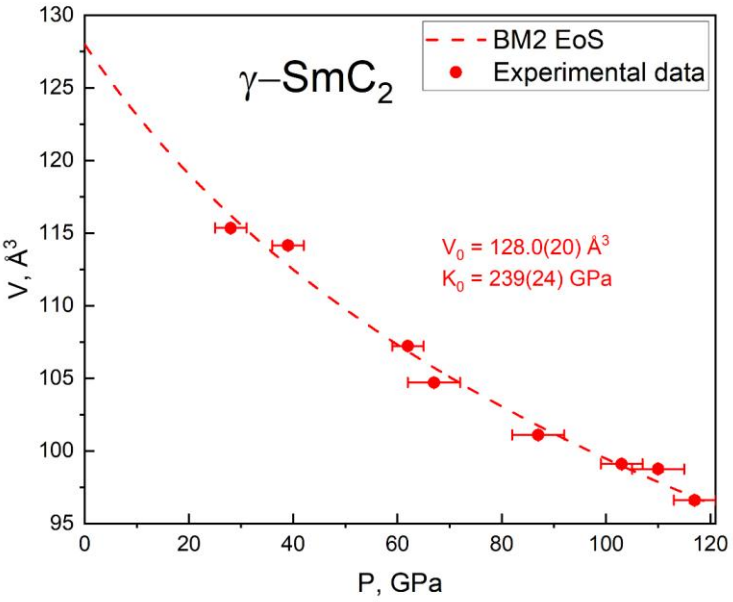

Figure S10. The pressure dependence of the unit cell volume of the synthesized γ-SmC_2.

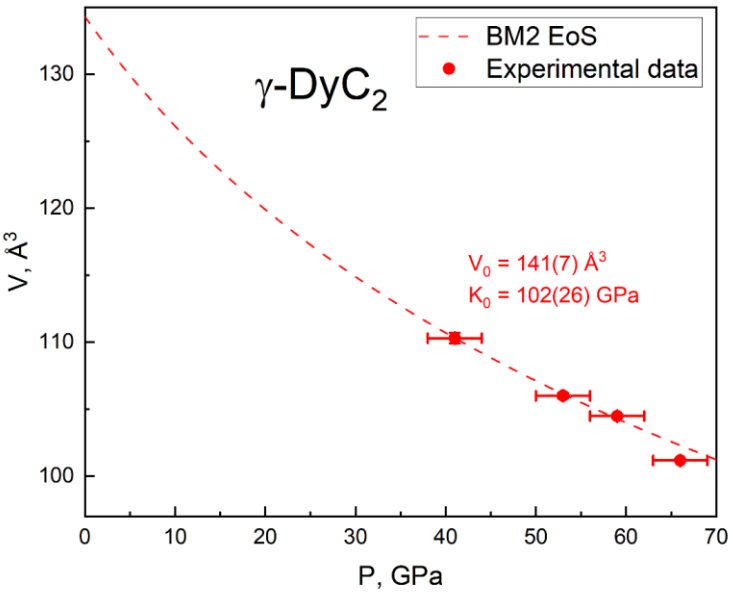

Figure S11. The pressure dependence of the unit cell volume of the synthesized γ-DyC_2 [12].

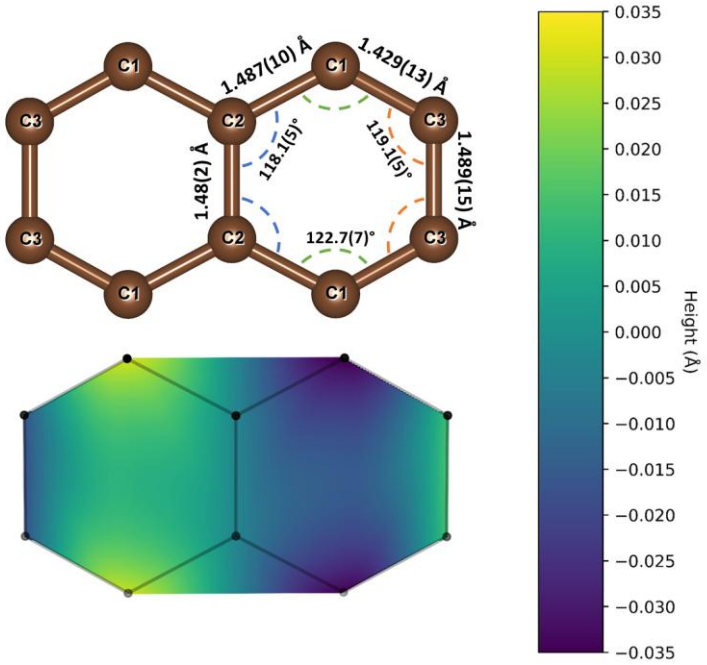

Figure S12. Naphthalene entities in synthesized *mC*30 ε-LaC_2 at 45(1) GPa. The maximum deviation from the averaging plane is ~0.032 Å. High error values are associated with the weak diffraction of the crystal and the fact that crystallites of this phase have the property of decomposing under a synchrotron beam during single-crystal XRD data collection.

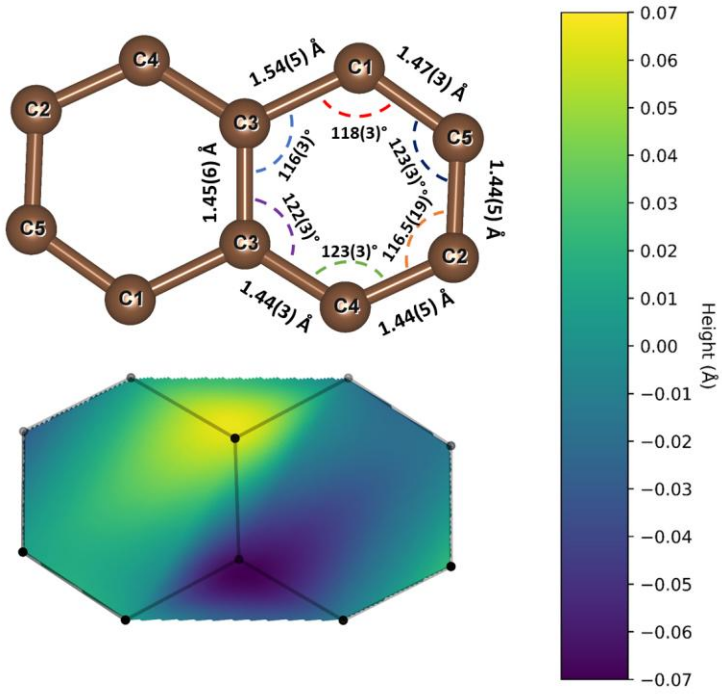

Figure S13. Naphthalene entities in synthesized *mP*32 La_3C_5 at 45(1) GPa. The maximum deviation from the averaging plane is ~0.068 Å. High error values are associated with the weak

diffraction of the crystal and the fact that crystallites of this phase have the property of decomposing under a synchrotron beam during single-crystal XRD data collection.

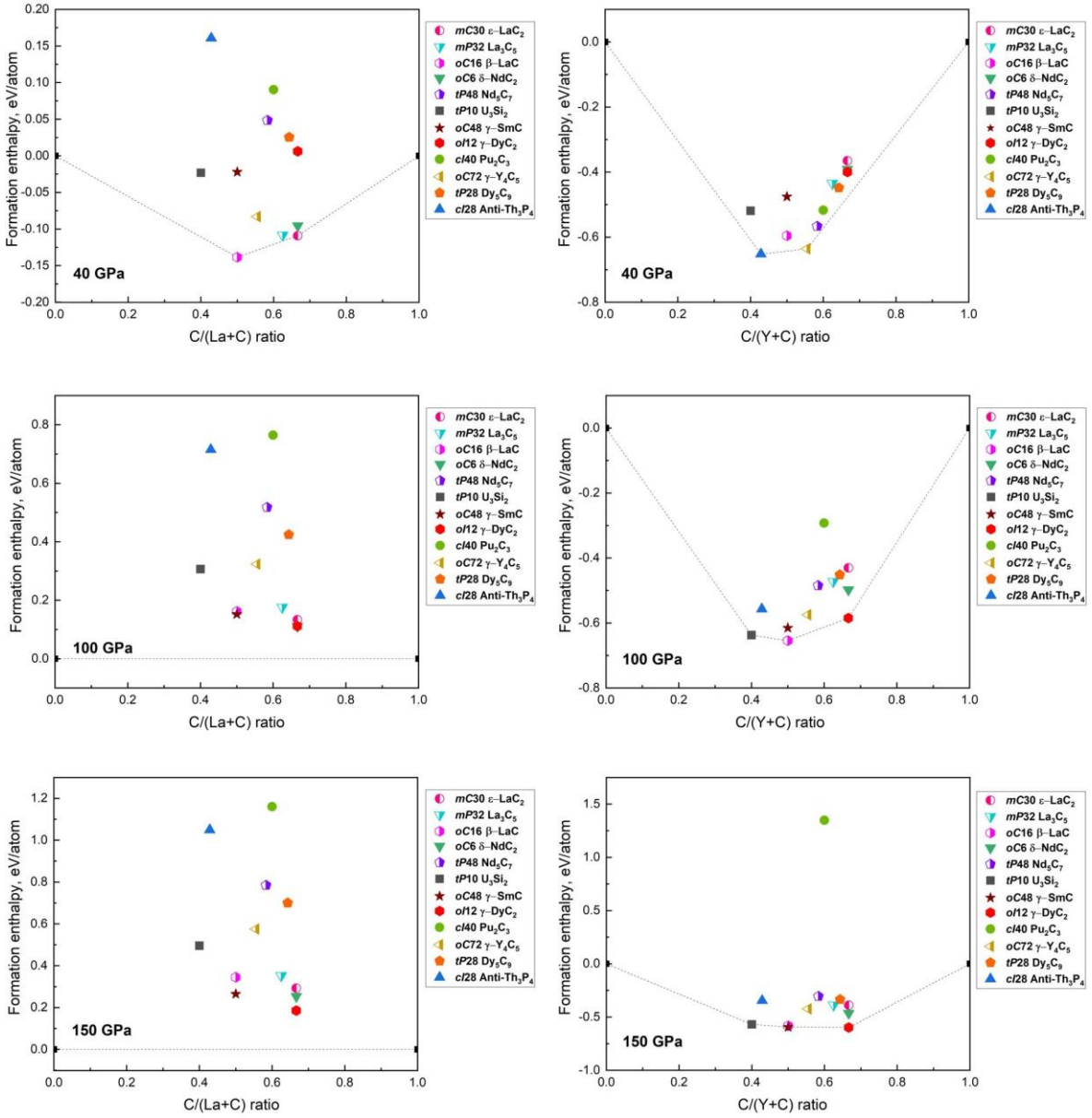

Figure S14. Calculated convex hull diagrams of the Y-C and La-C binary systems for all observed structural types at 40, 100, and 150 GPa. Dashed lines indicate the convex hulls.

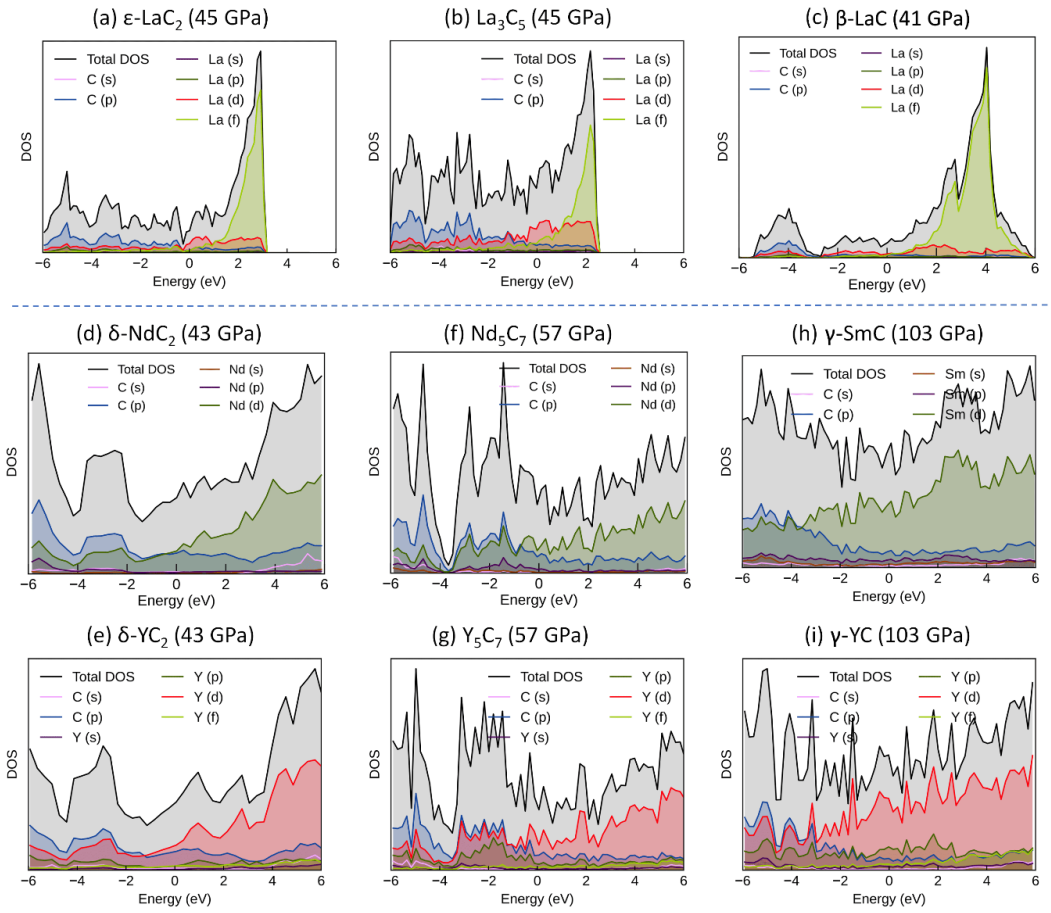

Figure S15. The electron density of states (eDOS) for (a) ε-LaC_2 at 45 GPa, (b) La_3C_5 at 45 GPa, (c) β-LaC at 41 GPa, (d) δ-NdC_2 at 43 GPa, (e) δ-YC_2 at 43 GPa, (f) Nd_5C_7 at 57 GPa, (g) Y_5C_7 at 57 GPa, (h) γ-SmC at 103 GPa, and (i) γ-YC at 103 GPa.

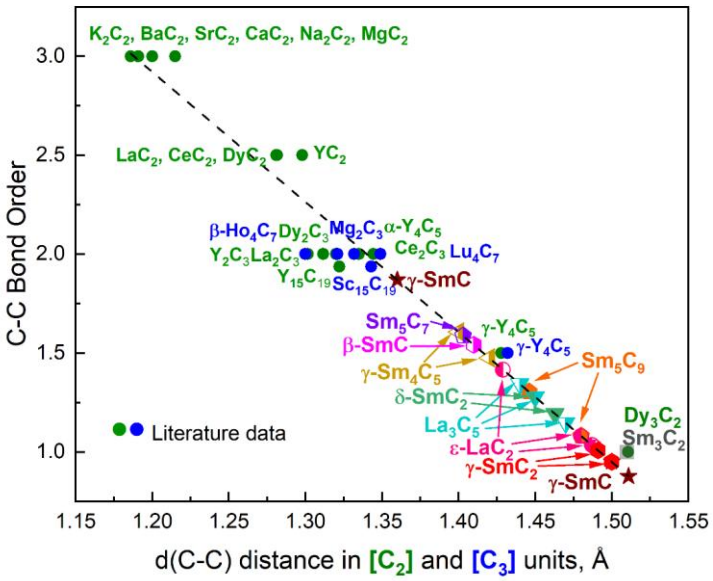

Figure S16. Correlation between the C-C distances in $[C_2]$ and $[C_3]$ units, *d*(C-C), and their bond order in a number of binary metal-carbon compounds. Literature data are from

experiments [15–33], except for γ-Y_4C_5 [14] and for Dy_2C_3 and Dy_3C_2 [13] (DFT-computed structures were fully relaxed at 1 bar). Straight line is a result of the fit of literature data ("green" and "blue" data-points) and described by equation: *EBO = 10.81 – 6.57×d(C-C).*

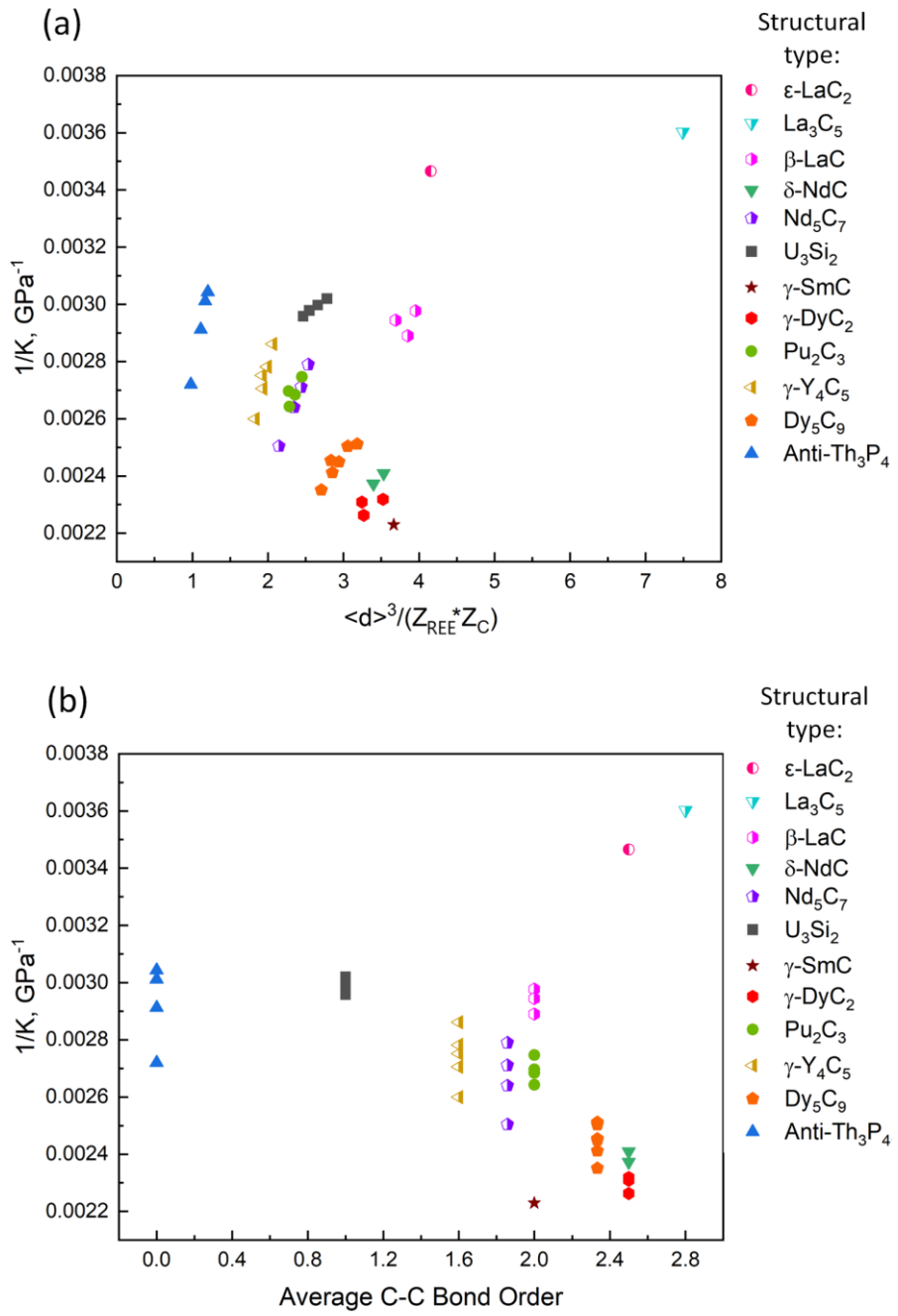

Figure S17. (a) Correlation between compressibility and ratio $R=\langle d\rangle^3/(Z_{REE}*Z_C)$ ($\langle d\rangle$ is an average REE-C distance in first coordination sphere, Z_{REE} and Z_C are the 'charges' on the rare-earth metal and carbon). (b) Correlation between compressibility and 'average bond order' of carbon atoms in synthesized compounds.

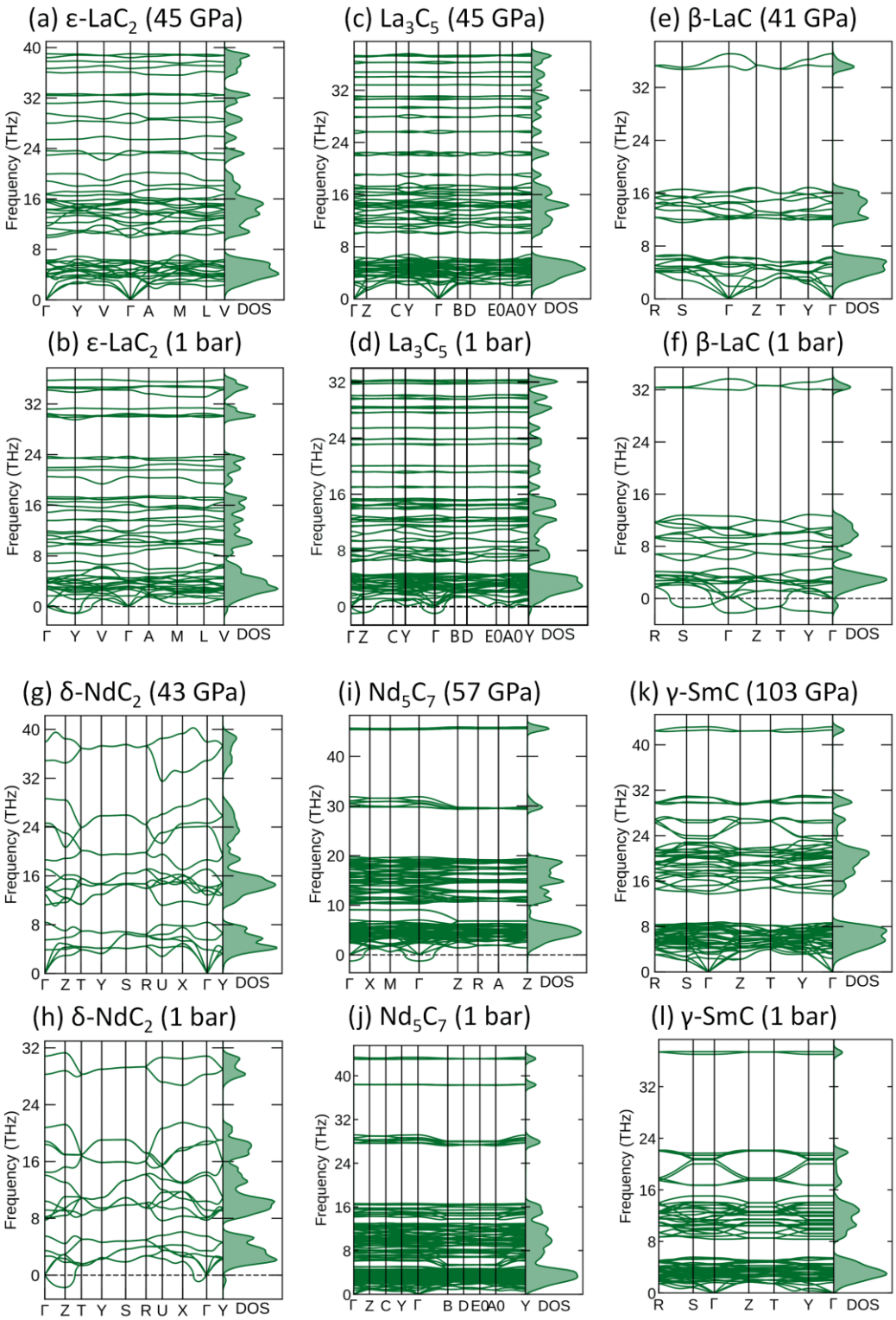

Figure S18. Calculated properties of ε-LaC_2, La_3C_5, β-LaC, δ-NdC_2, and Nd_5C_7. Phonon dispersion curves along high-symmetry directions in the Brillouin zone and phonon density of states: ε-LaC_2 at (a) 45 GPa and (b) ambient pressure, La_3C_5 at (c) 45 GPa and (d) ambient pressure, β-LaC at (e) 41 GPa and (f) ambient pressure, δ-NdC_2 at (g) 43 GPa and (h) ambient pressure, Nd_5C_7 at (i) 57 GPa and (j) ambient pressure, and γ-SmC at (k) 103 GPa and (l) ambient pressure.

Supplementary References

[1] G. Kresse, J. Furthmüller, Efficiency of Ab-Initio Total Energy Calculations for Metals and Semiconductors Using a Plane-Wave Basis Set, *Comput. Mater. Sci.* **6**, 15–50 (1996).

[2] P. E. Blöchl, Projector Augmented-Wave Method, *Phys. Rev. B* **50**, 17953–17979 (1994).

[3] J. P. Perdew, K. Burke, M. Ernzerhof, Generalized Gradient Approximation Made Simple, *Phys. Rev. Lett.* **77**, 3865–3868 (1996).

[4] H. J. Monkhorst, J. D. Pack, Special Points for Brillonin-Zone Integrations, *Phys. Rev. B* **13**, 5188–5192 (1976).

[5] A. Togo, I. Tanaka, First Principles Phonon Calculations in Materials Science, *Scr. Mater.* **108**, 1–6 (2015).

[6] J. Rath, A. J. Freeman, Generalized Magnetic Susceptibilities in Metals: Application of the Analytic Tetrahedron Linear Energy Method to Sc, **11**, 2109–2117 (1975).

[7] C. Friedrich, Tetrahedron Integration Method for Strongly Varying Functions: Application to the GT Self-Energy, *Phys. Rev. B* **100**, 075142(15) (2019).

[8] P. C. Müller, C. Ertural, J. Hempelmann, R. Dronskowski, Crystal Orbital Bond Index: Covalent Bond Orders in Solids, *J. Phys. Chem. C* **125**, 7959–7970 (2021).

[9] S. Maintz, V. L. Deringer, A. L. Tchougréeff, R. Dronskowski, LOBSTER: A Tool to Extract Chemical Bonding from Plane-Wave Based DFT, *J. Comput. Chem.* **37**, 1030–1035 (2016).

[10] L. Pauling, The Principles Determining the Structure of Complex Ionic Crystals, *J. Am. Chem. Soc.* **51**, 1010–1026 (1929).

[11] M. Nespolo, B. Guillot, CHARDI2015: Charge Distribution Analysis of Non-Molecular Structures, *J. Appl. Crystallogr.* **49**, 317–321 (2016).

[12] F. I. Akbar, A. Aslandukova, Y. Yin, A. Aslandukov, D. Comboni, M. Hanfland, N. Dubrovinskaia, High-Pressure Dysprosium Carbides Containing Carbon Dimers, Trimers, Chains, and Ribbons, *Submitt. to Chem. Eng. J.* (2024).

[13] F. I. Akbar, A. Aslandukova, A. Aslandukov, Y. Yin, F. Trybel, S. Khandarkhaeva, T. Fedotenko, D. Laniel, M. Bykov, E. Bykova, N. Dubrovinskaia, L. Dubrovinsky, High-Pressure Synthesis of Dysprosium Carbides, *Front. Chem.* **11**, 1–9 (2023).

[14] A. Aslandukova, A. Aslandukov, L. Yuan, D. Laniel, S. Khandarkhaeva, T. Fedotenko, G. Steinle-Neumann, K. Glazyrin, N. Dubrovinskaia, L. Dubrovinsky, Novel High-

Pressure Yttrium Carbide γ-Y4C5 Containing [C2] and Nonlinear [C3] Units with Unusually Large Formal Charges, *Phys. Rev. Lett.* **127**, 135501 (2021).

[15] O. Reckeweg, A. Baumann, H. A. Mayer, J. Glaser, H. J. Meyer, On the Coexistence of Tetragonal and Monoclinic CaC2: Structural and Spectroscopic Studies on Alkaline Earth Metal Acetylides, MC2 (M = Ca, Sr, Ba), *Zeitschrift Fur Anorg. Und Allg. Chemie* **625**, 1686–1692 (1999).

[16] K. Klöss, D. Hinz-Hübner, U. Ruschewitz, Über Eine Neue Modifikation Des Na2C2, *Zeitschrift Für Anorg. Und Allg. Chemie* **628**, 2701–2704 (2002).

[17] M. Atoji, Neutron Diffraction Study of Ce2C3 at Low Temperatures, *J. Chem. Phys.* **46**, 4148–4149 (1967).

[18] G. Y. Adachi, Y. Shibata, K. Ueno, J. Shiokawa, Heats of the Tetragonal-Cubic Transformation in Rare Earth Dicarbides and Mixed Rare Earth Dicarbide Solid Solutions, *J. Inorg. Nucl. Chem.* **38**, 1023–1026 (1976).

[19] Y. Yosida, Surface Superconductivity and Structural Analysis of YC2 Single Crystals Encapsulated in Carbon Nanocages, *J. Appl. Phys.* **92**, 5494–5497 (2002).

[20] M. C. Krupka, A. L. Giorgi, N. H. Krikorian, E. G. Szklaizz, High-Pressure Synthesis of Yttrium-Thorium Sesquicarbide: A New High-Temeperature Superconductor, *J. Less-Common Met.* **19**, 113–119 (1969).

[21] R. Czekalla, T. Hüfken, W. Jeitschko, R. D. Hoffmann, R. Pöttgen, The Rare Earth Carbides R4C5 with R=Y, Gd, Tb, Dy, and Ho, *J. Solid State Chem.* **132**, 294–299 (1997).

[22] M. Atoji, K. Gschneidner, A. H. Daane, R. E. Rundle, F. H. Spedding, The Structures of Lanthanum Dicarbide and Sesquicarbide by X-Ray and Neutron Diffraction, *J. Am. Chem. Soc.* **80**, 1804–1808 (1958).

[23] R. Czekalla, W. Jeitschko, R.-D. Hoffmann, H. Rabeneck, Preparation, Crystal Structure, and Properties of the Lanthanoid Carbides Ln4C7 with Ln = Ho, Er, Tm, and Lu, *Zeitschrift Für Naturforsch. B* **51**, 646–654 (1996).

[24] H. Ninomiya, T. Koshinuma, T. Nishio, H. Fujihisa, K. Kawashima, I. Hase, S. Ishida, H. Ogino, A. Iyo, Y. Yoshida, Y. Gotoh, H. Eisaki, Experimental and Computational Determination of Optimal Boron Content in Layered Superconductor Sc20C8-XBxC20, *Inorg. Chem.* **59**, 14290–14295 (2020).

[25] T. W. Button, I. J. McColm, Reaction of Carbon with Lanthanide Silicides IV: The Y5Si3-C System, *J. Less-Common Met.* **97**, 237–244 (1984).

[26] S. Hemmersbach, B. Zibrowius, U. Ruschewitz, Na2C2 Und K2C2: Synthese,

Kristallstruktur Und Spektroskopische Eigenschaften, *Z. Anorg. Allg. Chem.* **625**, 1440–1446 (1999).

[27] H. Fjellvág, P. Karen, Crystal Structure of Magnesium Sesquicarbide, *Inorg. Chem.* **31**, 3260–3263 (1992).

[28] P. Karen, A. Kjekshus, Q. Huang, V. L. Karen, The Crystal Structure of Magnesium Dicarbide, *J. Alloys Compd.* **282**, 72–75 (1999).

[29] V. Babizhetskyy, O. Jepsen, R. K. Kremer, A. Simon, B. Ouladdiaf, A. Stolovits, Structure and Bonding of Superconducting LaC2, *J. Phys. Condens. Matter* **26**, 025701 (2014).

[30] F. H. Spedding, K. Gschneidner Jr., A. H. Daane, The Crystal Structures of Some of the Rare Earth Carbides, *J. Am. Chem. Soc.* **80**, 4499–4503 (1958).

[31] V. Vohn, W. Kockelmann, U. Ruschewitz, On the Synthesis and Crystal Structure of BaC2, *J. Alloys Compd.* **284**, 132–137 (1999).

[32] V. Vohn, M. Knapp, U. Ruschewitz, Synthesis and Crystal Structure of SrC2, *J. Solid State Chem.* **151**, 111–116 (2000).

[33] M. Atoji, Magnetic and Crystal Structures of CeC2, PrC2, NdC2, TbC2, and HoC2 at Low Temperatures, *J. Chem. Phys.* **46**, 1891–1901 (1967).

4.4 Synthesis of rare-earth metal compounds through enhanced reactivity of alkali halides at high pressures

Yuqing Yin[1,2*], Fariia I. Akbar[1,3], Elena Bykova[3,4], Alena Aslandukova[3], Dominique Laniel[5], Andrey Aslandukov[1,3], Maxim Bykov[6], Michael Hanfland[7], Gaston Garbarino[7], Zhitai Jia[2], Leonid Dubrovinsky[3], Natalia Dubrovinskaia[1,8]

[1]Material Physics and Technology at Extreme Conditions, Laboratory of Crystallography, University of Bayreuth, 95440 Bayreuth, Germany

[2]State Key Laboratory of Crystal Materials, Shandong University, Jinan 250100, China

[3]Bayerisches Geoinstitut, University of Bayreuth, 95440 Bayreuth, Germany

[4]Earth and Planets Laboratory, Carnegie Institution for Science, 5241 Broad Branch Road, NW, Washington DC, 20015, USA

[5]Centre for Science at Extreme Conditions and School of Physics and Astronomy, University of Edinburgh, EH9 3FD Edinburgh, United Kingdom

[6]Institute of Inorganic Chemistry, University of Cologne, Greinstrasse 6, 50939 Cologne, Germany

[7]European Synchrotron Radiation Facility, B.P.220, F-38043 Grenoble Cedex, France

[8]Department of Physics, Chemistry and Biology (IFM), Linköping University, SE-581 83 Linköping, Sweden

***Corresponding author:** Yuqing.Yin@uni-bayreuth.de

Commun. Chem. **5**, 8–13 (2022), DOI: 10.1038/s42004-022-00736-x

4.4.1 Abstract

Chemical stability of the alkali halides NaCl and KCl has allowed for their use as inert media in high-pressure high-temperature experiments. Here we demonstrate the unexpected reactivity of the halides with metals (Y, Dy, and Re) and iron oxide (FeO) in a laser-heated diamond anvil cell, thus providing a synthetic route for halogen-containing binary and ternary compounds. So far unknown chlorides, Y_2Cl and DyCl, and chloride carbides, Y_2ClC and Dy_2ClC, were synthesized at ~40 GPa and 2000 K and their structures were solved and refined using *in situ* single-crystal synchrotron X-ray diffraction. Also, $FeCl_2$ with the HP-PdF_2-type structure, previously reported at 108 GPa, was synthesized at ~160 GPa and 2100 K. The

results of our *ab initio* calculations fully support experimental findings and reveal the electronic structure and chemical bonding in these compounds.

4.4.2 Introduction

Alkali halides, particularly sodium and potassium chlorides, are chemically very stable and are usually not considered as precursors for the synthesis of new compounds in high-pressure (HP) studies. Indeed, NaCl and KCl were thought to be chemically inert over wide pressure (up to 200 GPa) and temperature (up to 3000 K) ranges[1]. Therefore, they have often been used as pressure calibrants[2], pressure transmitting media[3], and electrical and thermal insulators in HP experiments[3–5]. Recent experimental and theoretical studies[6–8] suggest, however, that the behavior of the Na-Cl and K-Cl systems at HP is complex, and several compounds with an unusual stoichiometry (like $NaCl_3$,Na_3Cl, Na_2Cl, and KCl_3) have been reported. Still, NaCl and KCl are considered to be chemically stable under HP, as in the absence of ionization-promoting species[9,10], reactions are found in the presence of extra chlorine or sodium/potassium in a diamond anvil cell (DAC)[7,8].

Being formed by highly electropositive and electronegative elements, NaCl and KCl, having a stable electron configuration, are not expected to react with transition or rare-earth metals. In the present work we have shown that it is not the case under pressure, as our experiments, originally designed to study the HP behavior of metals (Y, Dy, Re, and Ag) in an "inert" pressure medium (NaCl) in a laser-heated diamond anvil cell (LHDAC), resulted in the synthesis of previously unknown chlorides, Y_2Cl and DyCl, and chloride carbides, Y_2ClC and Dy_2ClC, at about 40 GPa and 2000 K. An iron chloride, $FeCl_2$, with the HP-PdF_2-type structure, was found to be a product of a chemical reaction between FeO and KCl in a LHDAC at about 160 GPa and 2100 K.

Here we report the crystal structures of the chloride phases, Y_2Cl and DyCl, and chloride carbides Y_2ClC and Dy_2ClC, as well as the structure of iron chloride, $FeCl_2$. The structures were solved and refined using *in situ* high-pressure synchrotron single-crystal X-ray diffraction in a DAC. Our *ab initio* calculations are in good agreement with the experimental results.

4.4.3 Results and discussion

4.4.3.1 Reactivity of alkali halides and heavy metals at high pressures

To conduct the experiments, pieces of metals (Y, Dy, Re, or Ag) or FeO were loaded into a DAC between two layers of dried sodium or potassium chlorides. All experiments were

performed in BX90-type DACs equipped with Boehler-Almax type diamond anvils with culets of 250 or 120 μm[11]. NaCl or KCl served as pressure-transmitting media and turned out to also act as reactants. To facilitate a chemical reaction, the samples were laser-heated using YAG lasers with the metals serving as the absorbers.

Supplementary Table 1 provides information on all experiments carried out in this work. Silver was not found to react with NaCl after heating up to ~1950 K at ~44 GPa (Supplementary Fig. 1). Experiments with other metals, for example upon heating Dy in NaCl at ~40 GPa (Supplementary Fig. 2), optical observations provided early signs of chemical reactions. Raman spectroscopy was also helpful in some cases in giving a clear indication of a sample change after heating, like in the experiment with Re laser-heated in NaCl at ~38 GPa (Supplementary Fig. 3). However quite often Raman spectra did not yield any information on the phonon modes of the newly formed solids because of strong luminescence signals coming from the laser-heated spots.

The most reliable and accurate data on chemical reactions were obtained from XRD studies, when a chemical alteration of the sample is manifested in changes in the diffraction pattern and the products of the reactions, their chemical composition and structures, can be characterized using single-crystal X-ray diffraction data. Figure 1 shows powder diffraction patterns of the Y-NaCl sample before and after laser-heating up to ~2000 K at ~41 GPa. The pattern obtained before laser-heating displays only the presence of *hcp*-Y and B2-NaCl in the sample. After heating, additionally to the *hcp*-Y in B2-NaCl reflections, extra diffraction lines were observed (Fig. 1). The 2D XRD patterns in the insert in Fig. 1 show the appearance of numerous diffraction spots after laser heating, characteristic of single crystals. We used our approach to the high-pressure XRD data analysis[12–16] and the DAFi program[17], which we specially developed to process single-crystal XRD data from microcrystals. Processing these data revealed the formation of the previously known *fcc*-YC compound[18], a new HP phase of Y_3C_4 (to be published elsewhere), and new yttrium chloride and yttrium chloride carbide (Y_2Cl and Y_2ClC), which are discussed in detail in this work. Similarly, chemical reactions were detected in the Dy-NaCl, FeO-KCl, and Re-NaCl systems (Supplementary Table 1 and Supplementary Figs. 1–3), and the new phases, DyCl, Dy_2ClC, and $FeCl_2$, were identified. Unfortunately, despite all our efforts, the new phases in the Re-NaCl system could not be recognized, although we observed the signs of chemical reactions both in Raman spectra and the XRD data (Supplementary Fig. 3). The crystal structures, solved and refined at HP for all phases detected in the Y-NaCl, Dy-NaCl, and FeO-KCl systems after laser heating, are described in detail below.

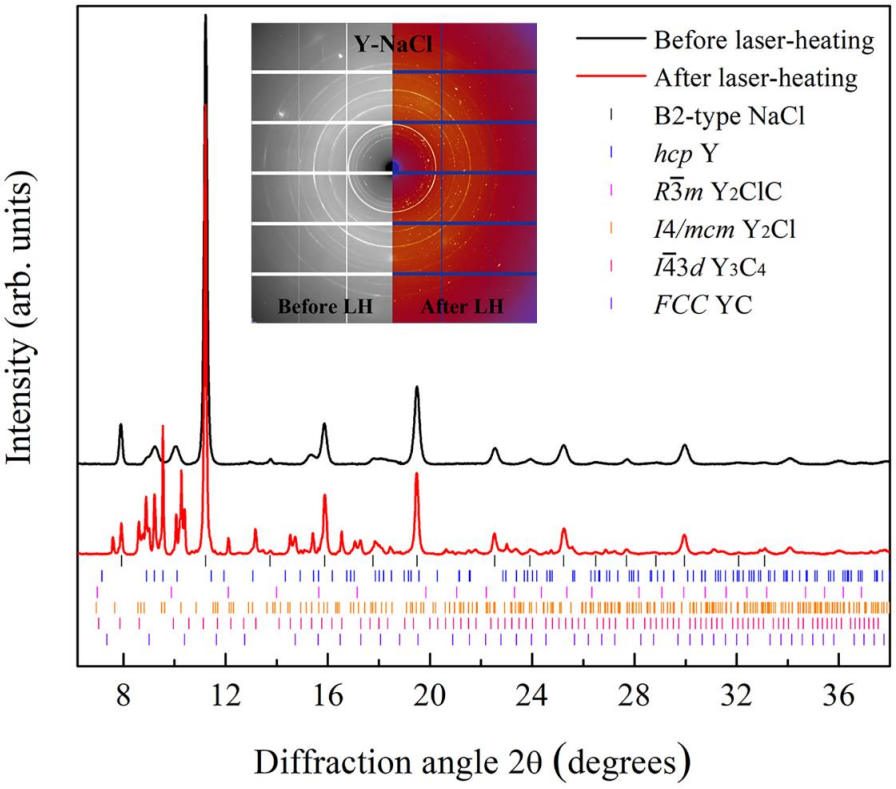

Fig. 1. Chemical reactions between yttrium and NaCl detected from X-ray diffraction. Powder X-ray diffraction patterns of the Y-NaCl sample before (black) and after (red) laser-heating at ~2000 K and 41 GPa. Insert shows 2D XRD patterns of the same sample before and after laser heating. The previously known (fcc-YC) and unknown (Y_2Cl, Y_2ClC, and Y_3C_4) compounds were identified using single-crystal XRD data; the ticks here are added according to their calculated powder XRD patterns.

4.4.3.2 Structures of chlorides Y_2Cl, DyCl, and $FeCl_2$

The yttrium-chlorine compound, Y_2Cl, synthesized at ~41 GPa and ~2000 K (Supplementary Table 1) crystallizes in a structure with the tetragonal space group *I*4/*mcm* (#140). Y atoms occupy the 8*h* Wyckoff site with the atomic coordinates (0.659(7) 0.159(7) 1/2) while the Cl atoms occupy the 4*a* (0 0 1/4) site (Fig. 2a, see also the CIF deposited at CSD 2184741 and Supplementary Data 1). The lattice parameters are a = 6.128(3) Å and c = 5.405(7) Å at 41(1) GPa. The full experimental crystallographic data, including the crystal structure, data collection and refinement details of Y_2Cl at 41(1) GPa are provided in Supplementary Table 2.

Yttrium atoms form $3^2.4.3.4$ nets in the *ab* plane (Fig. 2b). The nets are stacked along the *c* direction with a ½ period and rotated by 90° from one another (Fig. 2b). The chlorine atoms are located in the centers of square antiprisms formed between the layers of Y atoms (Fig. 2c). The Y-Cl distances within the antiprisms (~2.67 Å) are compatible with those known

for other yttrium chlorides at ambient conditions (YCl[19,20], Y_2Cl_3[21], YCl_3[22] – 2.70–2.75 Å). The striking difference is in the Cl-Cl and Y-Y distances (~2.70 Å and ~2.75 Å, correspondingly) of Y_2Cl compared to the known yttrium chlorides with predominantly ionic bonding between Y and Cl and metal-metal bonding within metal frameworks (for example, 3.30–3.72 Å for Cl-Cl and 3.27–3.96 Å for Y-Y in YCl and Y_2Cl_3)[21,23]. This indicates that the "metallic radius"[24] in Y_2Cl is different (smaller) from those in other yttrium chlorides. This might contribute to the reduction in enthalpy, making Y_2Cl a favored phase at HP. In fact, the Y_2Cl compound was predicted to be metallic at 20 GPa[25], and in metallic *hcp* yttrium at 40 GPa[26] the unit cell volume per atom is ~19.9 $Å^3$ that allows one to calculate the shortest Y-Y contact to be ~2.7 Å, which matches our measurements. Our ab initio calculations (Methods section) well reproduced the experimental crystal structure of Y_2Cl at 40 GPa (Supplementary Table 2) and confirmed its dynamical stability (Supplementary Fig. 4).

The structure of dysprosium chloride, DyCl, has a hexagonal unit cell with the lattice parameters a = 3.079(19) Å and c = 7.621(5) Å at 40(1) GPa (Fig. 2d, e, see also the CIF deposited at CSD 2184740 and Supplementary Data 2), and the space group symmetry $P6_3/mmc$ (#194) with the Dy atoms occupying the 2*a* Wyckoff site (0 0 1/2), and Cl atoms occupying the 2*c* site (1/3 2/3 3/4) (Table S3). In this NiAs (B8) type structure, the Cl atoms form a hexagonal close packing (*hcp*), in which Dy atoms occupy the centers of the edge-sharing octahedra. Although there are other rare-earth (REE) chlorides known at atmospheric pressure (REE = Sc, Y, Gd, and La)[23,27,28], they possess ZrCl-type structure, which is different from that of the HP Dy and Y chlorides.

The calculated structural parameters are in good agreement with the experimental results (Supplementary Table 3). DyCl is dynamically stable at our experimental pressure (~40 GPa) and its metallic nature at 40 GPa is confirmed with the Dy-*d* electrons dispersed at the Fermi level due to Dy-Dy metallic bonding (Supplementary Fig. 5).

The HP phase of $FeCl_2$ crystalized at 160(1) GPa in the HP-PdF_2 type structure with the $Pa\bar{3}$ (#205) space group and the lattice parameter a = 4.829(11) Å (Fig. 2f). Fe atoms occupy the 4*b* Wyckoff site, while Cl atoms occupy the 8*c* site, and form vertex-sharing Cl_6 octahedra with Fe atoms in the centers. The Fe-Fe, Fe-Cl, and Cl-Cl distances at 160(1) GPa are 3.41 Å, 1.98 Å, and 2.61 Å, respectively.

Our theoretical calculations reproduced the experimental crystal structure of $FeCl_2$ at 150 GPa (Supplementary Table 4) and confirmed its dynamical stability down to a pressure of 90 GPa (Supplementary Fig. 6). The measured unit cell volume and the pressure-volume points from theoretical calculations are shown in Supplementary Fig. 7. The calculated bulk modulus

of K_0 = 96.9(14) GPa (K' = 4.45(2); V_0 = 185.5(4) Å^3) was determined by fitting the third-order Birch-Murnaghan equation of state to the calculated P-V data (Supplementary Fig. 7). The calculated band structure along specific high-symmetry directions suggests that the cubic $FeCl_2$ phase is a typical example of normal semimetals[29], in which electron and hole pockets coexist on the Fermi surface (Supplementary Fig. 8).

It is worth mentioning that at ambient conditions $FeCl_2$ (phase I) possesses the layered $CdCl_2$-type structure ($R\bar{3}m$, #166), in which the chlorine atoms form a cubic close packing (*ccp*). Fe atoms, which fill ½ of its octahedral voids, are "sandwiched" between the two sheets of chlorine atoms[30], producing Cl-Fe-Cl layers separated from each other. At low pressures (~0.6 GPa) phase I undergoes a structural transition to phase II with the hexagonal CdI_2-like structure ($P\bar{3}m1$, #164), which is similar to that of phase I, but in phase II the chlorine atoms form a hexagonal close packing (*hcp*). This structure persists to 65 GPa[31]. At 108 GPa and 2000 K Yuan et al.[9] synthesized a $FeCl_2$ phase with the same HP-PdF_2 type structure, which we observed in this work at 160 GPa, but the synthesis was realized through hydrous systems to force the ionization of NaCl.

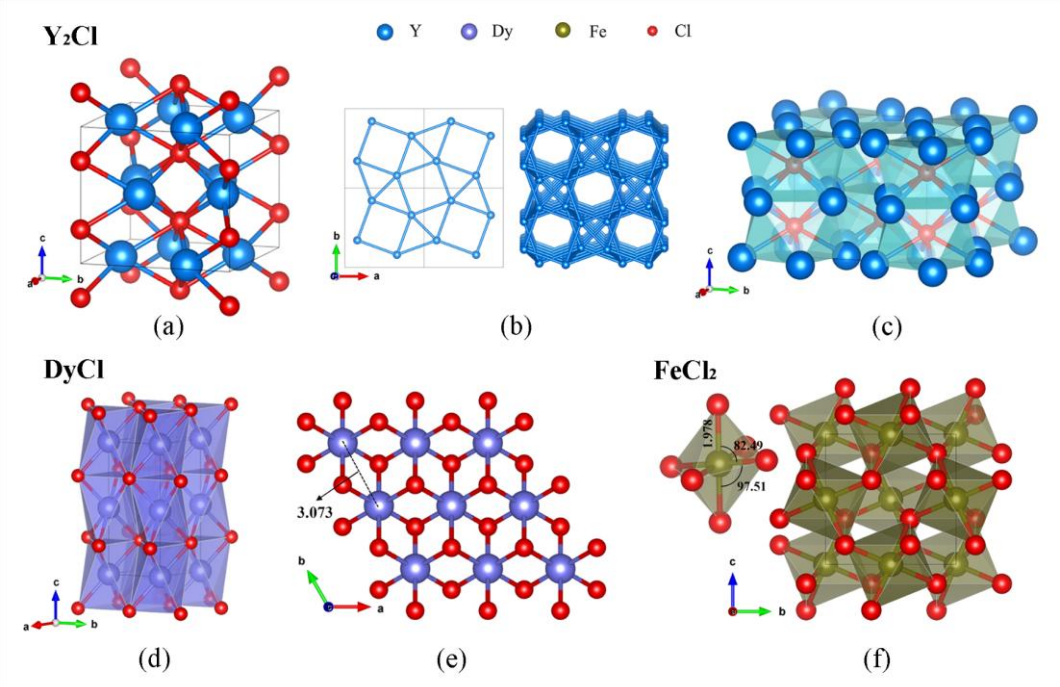

Fig. 2. Crystal structures of novel chlorides of Y, Dy, and Fe. (a) Stick-and-ball model of Y_2Cl structure at 41(1) GPa; (b) view of the Y metal framework in Y_2Cl along the *c*-direction; (c) square antiprisms geometry around the Cl center in Y_2Cl. (d) Polyhedral model of the crystal structure of DyCl at 40(1) GPa built of YCl_6 octahedra; (e) view of the structure along the *c*-direction: Cl atoms form hexagonal close packing (*hcp*) and Y atoms occupy the space in between. (f) Polyhedral model of $FeCl_2$ at 160(1) GPa. Y, Dy, Fe, and Cl atoms are shown in blue, purple, tan, and red colors, respectively.

4.4.3.3 Structures of novel chloride carbides Y_2ClC and Dy_2ClC

As shown in previous work[32], carbon from diamond anvils, being mobilized upon laser heating, can participate in chemical reactions. In this work, this phenomenon has led to the synthesis of previously unknown ternary compounds, Y_2ClC and Dy_2ClC, which are isostructural (space group $R\bar{3}m$, #166) and with similar lattice parameters. Y and Dy atoms occupy the Wyckoff site 6*c*, Cl atoms occupy the 3*a* site, and C atoms occupy the 3*b* site. The full experimental crystallographic data, including the crystal structure, data collection, and refinement details for these phases are provided in Supplementary Tables 5 and 6 (see also the CIF deposited at CSD 2184739 and 2184742) (Supplementary Data 3 for Y_2ClC and Supplementary Data 4 for Dy_2ClC).

In the structure of the novel chloride carbides, the rare-earth atoms (Y and Dy) form a distorted cubic close packing (*ccp*) (Fig. 3). If one considers Cl and C as equal-size spheres, the alternating close-packed layers of C and Cl also form a distorted *ccp*. Thus, the structure can be described as one derived from NaCl (B1) type with carbon and chlorine atoms forming the *ccp*, whose octahedral voids are occupied by the rare-earth atoms. Each rare-earth atom is connected to three Cl and three C atoms (Fig. 3d). As shown in Fig. 3e, the metal-C contacts (Y-C ~2.30 Å, and Dy-C ~2.29 Å) are significantly shorter than the metal-Cl ones (Y-Cl ~2.59 Å, and Dy-Cl ~2.60 Å), as expected due to the smaller ionic radius for C atoms. But the Y-Y and Dy-Dy contacts between layers AB, CA, and BC (Fig. 3b) are relatively short (~3.15 Å), and this distance is close to that of Dy-Dy in DyCl with a metallic bonding character, as discussed above.

To gain a deeper insight into the properties of Y_2ClC and Dy_2ClC, we performed calculations based on density functional theory (DFT). The relaxed structural parameters (Supplementary Tables 5 and 6) closely reproduce the corresponding experimental values at 40 GPa. Harmonic phonon dispersion calculations using the Phonopy software[33] show no imaginary frequencies, demonstrating the dynamical stability of $R\bar{3}m$ Y_2ClC at both 40 GPa and 1 bar (Supplementary Fig. 9). Ohmer et al.[34] predicted the stability of a Y_2ClC solid with a $P6_3/mmc$ space group (#194), which is considered to be a MAX-type ($M_{n+1}AX_n$)[35,36] compound. By comparing the enthalpy values of the two phases (Supplementary Table 7), we suggest that Y_2ClC will have a phase transition from $R\bar{3}m$ to $P6_3/mmc$ when the pressure is reduced to 10GPa (Supplementary Fig. 9c). No competing phase was found for $R\bar{3}m$ Dy_2ClC, and its dynamical stability at 40 GPa is demonstrated in Supplementary Fig. 10.

Considering that Y_2ClC and Dy_2ClC are isostructural, the computed total and projected electron densities of states (TDOS and PDOS) are illustrated in Fig. 4a taking Y_2ClC as an example. At 40 GPa, Y_2ClC is a metal, as it shows a non-zero density of states at the Fermi level, and the main contribution at the Fermi level comes from the yttrium *d*-states. Interestingly, the calculated electron localization function (ELF) of Y_2ClC at 40 GPa not only gives evidence of ionic bonding between the Y-Cl and Y-C atoms but features weak ELF values in the centers of the Y_4 tetrahedra (Fig. 4b–d), forming bridges connecting the C atoms (see the highlighted red dashed lines in Fig. 4b, d). One can speculate from the ELF values that these ELF bridges are caused by the hybridization of the Y-*d* orbitals (for ELF < 0.5, the metal bonding is undoubtedly more pronounced[37]). To confirm this conclusion, additional DFT calculations were performed with the C atoms removed, resulting in a stable Y_2Cl electride with a more localized ELF attractor at the center of the Y_4 tetrahedra and anionic electrons localized at the centers of Y_6 octahedra (Supplementary Fig. 11). The introduction of C atoms causes a charge loss in the Y_4 tetrahedra and a charge gain in the Y_6 octahedra (Supplementary Fig. 11g) resulting in the weak ELF bridges in Fig. 4b. The PDOS of Y-*d* orbitals and the partial charge density map further confirmed the Y-*d* orbital overlapping in the Y_4 tetrahedra of Y_2ClC (Supplementary Fig. 11f). Detailed information and further discussion of the electronic properties of Y_2ClC and Dy_2ClC can be found in Supplementary Discussion, Supplementary Fig. 11–13 and Supplementary Table 9.

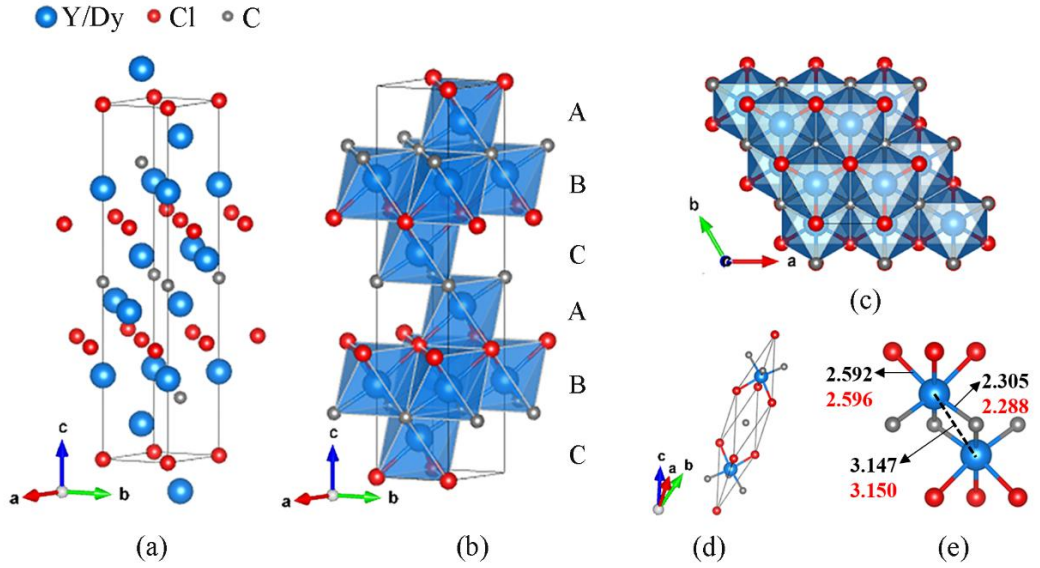

Fig. 3. Crystal structure of Y_2ClC and Dy_2ClC synthesized at ~ 40 GPa. (a) Ball model in a hexagonal setting. (b) Polyhedral model built of (YC_3Cl_3) octahedra; A, B, C letters highlight the *ccp* formed by Y/Dy atoms. (c) View of the structure along the *c*-direction; C and Cl atoms together formed the *ccp*. (d) Crystal structure in the rhombohedral setting. (e)

Interatomic distances (in Å) in Y_2ClC (black numbers) and Dy_2ClC (red numbers). Y/Dy, Cl, and C atoms are shown in blue, red, and grey colors.

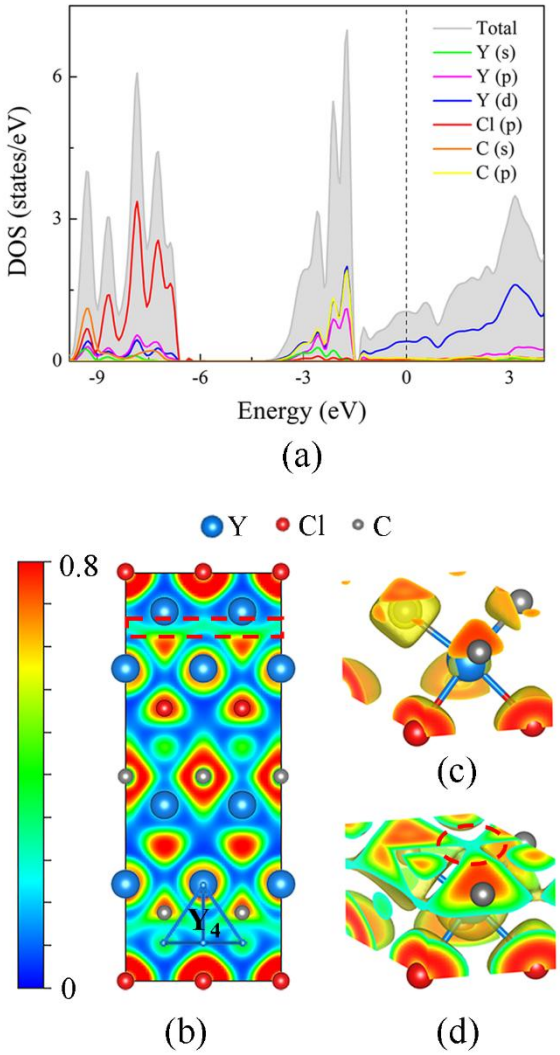

Fig. 4. Results of theoretical calculations. (a) The total and projected densities of states (TDOS and PDOS) curves of Y_2ClC at 40 GPa; the Fermi energy level was set to 0 eV. (b) The 2D electron localization function (ELF) map of Y_2ClC in the (1 0 0) plane; (c), (d) ELF with the isosurfaces value set as (c) 0.7 and (d) 0.25. Y, Cl, and C atoms are shown in blue, red, and grey colors. One Y_4 tetrahedron is highlighted in (b), and the weak ELF value in its center is highlighted with the red dashed circle in (d). These weak ELF values in the centers of the Y_4 tetrahedra form bridges connecting the C atoms (highlighted with the red dashed square in (b)).

4.4.4 Conclusions

To summarize, the chemical reactions between NaCl and Y, Dy, and Re at ~40 GPa and KCl and FeO at ~160 GPa, observed in the present work under HP, were unexpected. They led to the synthesis of hitherto unknown chlorides, Y_2Cl and DyCl, and chloride carbides, Y_2ClC and Dy_2ClC. Although these results limit the application of alkali halides as thermal

insulators and pressure media in LHDACs, as reactants, they provide a surprisingly simple route for the preparation of halogen-containing compounds.

4.4.5 Methods

Sample preparation. One stack of halide (NaCl or KCl) thin (3-5 μm) plate was first loaded on one of the diamond anvils, with a culet diameter of 250 μm (for DAC 1-4) or 120 μm (for DAC 5; Supplementary Table 1). A piece of pure flake of metal (Y/Dy/Re/Ag) or FeO of typically about $5 \times 5 \times 5$ μm^3 in size was positioned on the halide layer. Then we placed another stack of halide (NaCl or KCl) thin (3–5 μm) plate on the other diamond anvil so that the samples were loaded as sandwiches. Rhenium was used as the gasket material. NaCl and KCl powders were dried on a heating table at 220°C for 48 h before loading to avoid any presence of water. The *in situ* pressure was measured using the first-order Raman mode of the stressed diamond anvils[38]. Double-sided sample laser-heating was performed at our home laboratory at the Bayerisches Geoinstitut[39]. Detailed information of pressure and the heating temperature can be found in Supplementary Table 1.

X-ray diffraction. Synchrotron X-ray diffraction measurements of the compressed samples were performed at ID15 (λ = 0.41015 Å, beam size ~5.0 × 5.0 μm^2) and ID27 (λ = 0.3738 Å, beam size ~2.0 × 2.0 μm^2) of the EBS-ESRF. In order to determine the sample position for single-crystal X-ray diffraction data acquisition, a full X-ray diffraction mapping of the pressure chamber was performed. The sample positions displaying the greatest number of single-crystal reflections belonging to the phases of interest were chosen, and step-scans of 0.5° from −36° to +36° ω were performed. The CrysAlisPro software[40] was utilized for the single-crystal data analysis. To calibrate the instrumental model in the CrysAlisPro software, i.e. the sample-to-detector distance, detector's origin, offsets of the goniometer angles, and rotation of both the X-ray beam and detector around the instrument axis, we used a single crystal of orthoenstatite [$(Mg_{1.93}Fe_{0.06})$ $(Si_{1.93},Al_{0.06})O_6$, *Pbca* space group, a = 8.8117(2) Å, b = 5.1832(10) Å, and c = 18.2391(3) Å]. The DAFi program[17] was used for the search of reflections' groups belonging to individual single-crystal domains. The crystal structures were then solved and refined using the OLEX2[41] and JANA2006 software[42]. The crystallite sizes were estimated from X-ray maps. The crystallographic information is available in Supplementary Tables 2–6.

Density functional theory calculations. First-principles calculations were performed using the framework of density functional theory (DFT) as implemented in the Vienna Ab initio Simulation Package (VASP)[43]. The Projector-Augmented-Wave (PAW) method[44,45] was used to expand the electronic wave function in plane waves. The Generalized Gradient Approximation (GGA) functional was used for calculating the exchange-correlation energies, as proposed by Perdew–Burke–Ernzerhof (PBE)[46]. The PAW potentials with following valence configurations of 4*s*4*p*5*s*4*d* for Y, 4*f*6*s* for Dy, 3*p*4*s*3*d* for Fe, 3*s*3*p* for Cl, and 2*s*2*p* for C were used. The plane-wave kinetic energy cutoff was set to 600 eV. The crystal structure, ELF, and charge density maps visualization were made with the VESTA software[47]. The finite displacement method, as implemented in PHONOPY[33], was used to calculate phonon frequencies and phonon band structures.

4.4.6 Data availability

All data generated or analyzed during this study are included in this published article (and its Supplementary information files). The X-ray crystallographic coordinates for structures reported in this article have been deposited at the Cambridge Crystallographic Data Centre (CCDC), under deposition number CSD-2184739, CSD 2184740, CSD 2184741 and 2184742. These data can be obtained free of charge from The Cambridge Crystallographic Data Centre via www.ccdc.cam.ac.uk/data_request/cif.

4.4.7 Acknowledgements

The authors acknowledge the European Synchrotron Radiation Facility (ESRF) for provision of beamtime at the ID15b and ID27 beamlines. Y.Y. acknowledges the financial support provided by the China Scholarship Council (CSC) during her visit to the University of Bayreuth. N.D. and L.D. thank the Federal Ministry of Education and Research, Germany (BMBF, grant no. 05K19WC1) and the Deutsche Forschungsgemeinschaft (DFG; projects DU 954–11/1, DU 393–9/2, DU 393–13/1) for financial support. N.D. also thanks the Swedish Government Strategic Research Area in Materials Science on Functional Materials at Linköping University (Faculty Grant SFO-Mat-LiU No. 2009 00971). M.B. acknowledges the support of Deutsche Forschungsgemeinschaft (DFG Emmy-Noether project BY112/2-1). D.L. thanks the UKRI Future Leaders Fellowship (MR/V025724/1) for financial support. For the purpose of open access, the author has applied a Creative Commons Attribution (CC BY) licence to any Author Accepted Manuscript version arising from this submission.

4.4.8 References

1. Dorogokupets, P. I. & Dewaele, A. Equations of state of MgO, Au, Pt, NaCl-B1, and NaCl-B2: Internally consistent high-temperature pressure scales. *High Press. Res.* **27**, 431–446 (2007).
2. Decker, D. L. Equation of State of NaCl and Its Use as a Pressure Gauge in High-Pressure Research. *J. Appl. Phys.* **36**, 157–161 (1965).
3. Hu, J. *et al.* X-ray diffraction and laser heating: Application of a moissanite anvil cell. *J. Phys. Condens. Matter* **14**, 10479–10481 (2002).
4. Armentrout, M. & Kavner, A. High pressure, high temperature equation of state for Fe2SiO4 ringwoodite and implications for the Earth's transition zone. *Geophys. Res. Lett.* **38**, 1–4 (2011).
5. Langerome, B. *et al.* Probing NaCl at High Pressure through Optical Studies and Ab Initio Calculations. *J. Phys. Chem. C* **123**, 15724–15728 (2019).
6. Redeker, F. A., Beckers, H. & Riedel, S. Matrix-isolation and comparative far-IR investigation of free linear [Cl3]- and a series of alkali trichlorides. *Chem. Commun.* **53**, 12958–12961 (2017).
7. Zhang, W. *et al.* Stability of numerous novel potassium chlorides at high pressure. *Sci. Rep.* **6**, 1–6 (2016).
8. Zhang, W. *et al.* Unexpected stable stoichiometries of sodium chlorides. *Science (80-.).* **342**, 1502–1505 (2013).
9. Yuan, H., Man, L., Kim, D. Y., Popov, D. & Meng, Y. HP-PdF2-type FeCl2 as a potential Cl-carrier in the deep Earth. *Am. Miner.* **107**, 313–317 (2022).
10. Koemets, E. *et al.* Interaction between FeOOH and NaCl at extreme conditions: Synthesis of novel Na2FeCl4OHx compound. *Minerals* **10**, 1–7 (2020).
11. Kantor, I. *et al.* BX90: A new diamond anvil cell design for X-ray diffraction and optical measurements. *Rev. Sci. Instrum.* **83**, 125102 (2012).
12. Laniel, D. *et al.* Synthesis of magnesium-nitrogen salts of polynitrogen anions. *Nat. Commun.* **10**, 1–7 (2019).
13. Bykova, E. *et al.* Metastable silica high pressure polymorphs as structural proxies of deep Earth silicate melts. *Nat. Commun.* **9**, 1–8 (2018).
14. Bykov, M. *et al.* High-Pressure Synthesis of Dirac Materials: Layered van der Waals Bonded BeN4 Polymorph. *Phys. Rev. Lett.* **126**, 175501 (2021).

15. Bykov, M. *et al.* Stabilization of Polynitrogen Anions in Tantalum–Nitrogen Compounds at High Pressure. *Angew. Chemie - Int. Ed.* **60**, 9003–9008 (2021).
16. Bykov, M. *et al.* High-Pressure Synthesis of a Nitrogen-Rich Inclusion Compound ReN8·x N2 with Conjugated Polymeric Nitrogen Chains. *Angew. Chemie - Int. Ed.* **57**, 9048–9053 (2018).
17. Aslandukov, A., Aslandukov, M., Dubrovinskaia, N. & Dubrovinsky, L. Domain Auto Finder (DAFi) program: the analysis of single-crystal X-ray diffraction data from polycrystalline samples. *J. Appl. Crystallogr.* **55**, 1383–1391 (2022).
18. Aliakbari, A. & Amiri, P. Structural, elastic, electronic, thermal, and phononic properties of yttrium carbide: First-principles calculations. *Mater. Chem. Phys.* **270**, 124744 (2021).
19. Ford, J. E. & Corbett, J. D. Alkali-Metal Intercalates of Layered Yttrium Chloride Oxide and Their Hydration Reactions. *Inorg. Chem.* **24**, 4120–4128 (1985).
20. Ford, J. E., Meyer, G. & Corbett, J. D. Lithium Intercalation Compounds of Yttrium and Gadolinium Monochloride: Synthesis and Structure. *Inorg. Chem.* **23**, 2094–2098 (1984).
21. Mattausch, H., Eger, R., Simon, A., Hendricks, J. B. & Corbett, J. D. Reduced halides of yttrium with strong metal-metal bonding: Yttrium monochloride, monobromide, sesquichloride, and sesquibromide. *Inorg. Chem.* **19**, 2128–2132 (1980).
22. Templeton, D. H. & Carter, G. F. The crystal structure of yttrium trichloride and similar compounds. *J. Phys. Chem.* **58**, 940–944 (1954).
23. Wan, B. *et al.* Identifying quasi-2D and 1D electrides in yttrium and scandium chlorides via geometrical identification. *npj Comput. Mater.* **4**, 1–9 (2018).
24. Pearson, W. B. *The Crystal Chemistry and Physics of Metals and Alloys*. *Wiley-Inter-science* (1972).
25. Yu, H. & Chen, Y. Pressure-induced electrides and metallic phases in the Y-Cl system. *J. Phys. Condens. Matter* **33**, 215401 (2021).
26. Pace, E. J. *et al.* Structural phase transitions in yttrium up to 183 GPa. *Phys. Rev. B* **102**, 094104 (2020).
27. Simon, A., Mattausch, H. & Holzer, N. Monochloride von Lanthanoiden: GdCl und TbCl. *Angew. Chemie* **88**, 685–686 (1976).
28. Araujo, R. E. & Corbett, J. D. Lanthanum Monochloride and Lanthanum Sesquichloride. *Inorg. Chem.* **20**, 3082–3086 (1981).

29. Shekhar, C. *et al.* Extremely large magnetoresistance and ultrahigh mobility in the topological Weyl semimetal candidate NbP. *Nat. Phys.* **11**, 645–649 (2015).
30. Pasternak, A. Lattice dynamics of FeCl2. *J. Phys. C Solid State Phys.* **9**, 2987–2995 (1976).
31. Rozenberg, G. K. *et al.* Pressure-induced structural, electronic, and magnetic phase transitions in FeCl2 studied by x-ray diffraction and resistivity measurements. *Phys. Rev. B - Condens. Matter Mater. Phys.* **79**, 214105 (2009).
32. Khandarkhaeva, S. *et al.* Novel Rhenium Carbides at 200 GPa. *Eur. J. Inorg. Chem.* **2020**, 2186–2190 (2020).
33. Togo, A., Oba, F. & Tanaka, I. First-principles calculations of the ferroelastic transition between rutile-type and CaCl2-type SiO2 at high pressures. *Phys. Rev. B - Condens. Matter Mater. Phys.* **78**, 134106 (2008).
34. Ohmer, D., Qiang, G., Opahle, I., Singh, H. K. & Zhang, H. High-throughput design of 211- M2AX compounds. *Phys. Rev. Mater.* **3**, 053803 (2019).
35. Fashandi, H. *et al.* Synthesis of Ti3AuC2, Ti3Au2C2 and Ti3IrC2 by noble metal substitution reaction in Ti3SiC2 for high-temperature-stable Ohmic contacts to SiC. *Nat. Mater.* **16**, 814–818 (2017).
36. Sokol, M., Natu, V., Kota, S. & Barsoum, M. W. On the Chemical Diversity of the MAX Phases. *Trends Chem.* **1**, 210–223 (2019).
37. Savin, A., Nesper, R., Wengert, S. & Fässler, T. ELF: The Electron Localization Function. *Angew. Chem., Int. Ed. Engl.* **36**, 1808–1832 (1997).
38. Akahama, Y. & Kawamura, H. Pressure calibration of diamond anvil Raman gauge to 310 GPa. *J. Appl. Phys.* **100**, 043516 (2006).
39. Meng, Y., Hrubiak, R., Rod, E., Boehler, R. & Shen, G. New developments in laser-heated diamond anvil cell with in situ synchrotron x-ray diffraction at High Pressure Collaborative Access Team. *Rev. Sci. Instrum.* **86**, (2015).
40. Rigaku Oxford Diffraction Ltd. *Rigaku OD and CryAlis PRO* (2018).
41. Dolomanov, O. V., Bourhis, L. J., Gildea, R. J., Howard, J. A. K. & Puschmann, H. OLEX2: a complete structure solution, refinement and analysis program. *J. Appl. Crystallogr.* **42**, 339–341 (2009).
42. Petrícek, V., Dušek, M. & Palatinus, L. Crystallographic computing system JANA2006: General features. *Zeitschrift für Krist. - Cryst. Mater.* **229**, 345–352 (2014).
43. Kresse, G. & Furthmüller, J. Efficiency of ab-initio total energy calculations for metals and semiconductors using a plane-wave basis set. *Comput. Mater. Sci.* **6**, 15–50 (1996).

44. Blöchl, P. E. Projector augmented-wave method. *Phys. Rev. B* **50**, 17953–17979 (1994).
45. Kresse, G. & Joubert, D. From ultrasoft pseudopotentials to the projector augmented-wave method. *Phys. Rev. B - Condens. Matter Mater. Phys.* **59**, 1758–1775 (1999).
46. Perdew, J. P., Burke, K. & Ernzerhof, M. Generalized gradient approximation made simple. *Phys. Rev. Lett.* **77**, 3865–3868 (1996).
47. Momma, K. & Izumi, F. VESTA: A three-dimensional visualization system for electronic and structural analysis. *J. Appl. Crystallogr.* **41**, 653–658 (2008).

4.4.9 Supplementary Information

Supplementary Tables

Supplementary Table 1. Summary of the experiments on high-pressure high-temperature synthesis in a diamond anvil cell.

DAC number	Starting materials	Pressure (GPa, ±1)	Measured temperature (K, ±200)	Reaction products
1	Y and NaCl	41	2000	Y_2ClC^* + Y_2Cl + YC + Y_3C_4
2	Dy and NaCl	40	2000	Dy_2ClC^* + DyCl + Dy_3C_4
3	Re and NaCl	38	2100	Reaction was observed, but the products were not identified
4	Ag and NaCl	44	1950	No reaction observed
5	FeO and KCl	160	2100	$FeCl_2$

*Carbon in the products of the reactions originates from diamond anvils.

Supplementary Table 2. Crystal structure, data collection and refinement details of Y_2Cl at 41(1) GPa in comparison to the corresponding DFT-relaxed structure.

Crystal data		**DFT results**
Chemical formula	Y_2Cl	Y_2Cl
M_r	213.27	
Crystal system, space group	Tetragonal, *I*4/*mcm*	Tetragonal, *I*4/*mcm*
Temperature (K)	293	
Pressure (GPa)	41(1)	40
a, *c* (Å)	6.1279 (3), 5.405 (7)	6.1480, 5.4205
V (Å^3)	202.96 (3)	204.88
Z	4	4
Radiation type	Synchrotron, λ = 0.41015 Å	
μ (mm^{-1})	13.77	
Crystal size (mm)	0.001 × 0.001 × 0.001	
Data collection		

Diffractometer			ESRF ID15b, EIGER2 X 9M CdTe detector				
Absorption correction (essentially for absorption in diamonds and pressure medium)			Multi-scan *CrysAlis PRO* 1.171.40.67a (Rigaku Oxford Diffraction, 2019) Empirical absorption correction using spherical harmonics, implemented in SCALE3 ABSPACK scaling algorithm.				
T_{min}, T_{max}			0.547, 1				
No. of measured, independent and observed [$I > 2\sigma(I)$] reflections			284, 104, 99				
R_{int}			0.026				
$(\sin\theta/\lambda)_{max}$ (Å^{-1})			0.887				
Refinement							
$R[F^2 > 2\sigma(F^2)]$, $wR(F^2)$, S			0.038, 0.100, 1.16				
No. of reflections			104				
No. of parameters			7				
$\Delta\rho_{max}$, $\Delta\rho_{min}$ (e Å^{-3})			2.42, -2.10				
Crystal Structure							
Atom			Wyckoff Site	Coordinates (x, y, z)	U_{iso} (Å^2)		Coordinates (x y z)
Y1			8*h*	0.6586(7) 0.1586(7) 1/2	0.0090(4)		0.65855 0.15855 1/2
Cl1			4*a*	0 0 1/4	0.0095(5)		0 0 1/4
Anisotropic displacement parameters							
Atom	U_{11} (Å^2)	U_{22} (Å^2)	U_{33} (Å^2)	U_{12} (Å^2)	U_{13} (Å^2)	U_{23} (Å^2)	
Y1	0.0056(4)	0.0056(4)	0.0157(7)	0.00025(10)	0	0	
Cl1	0.0063(6)	0.0063(6)	0.0158(14)	0	0	0	

Supplementary Table 3. Crystal structure, data collection and refinement details of DyCl at 40(1) GPa in comparison to the corresponding DFT-relaxed structure.

Crystal data		**DFT results**
Chemical formula	DyCl	DyCl
M_r	197.95	
Crystal system, space group	Hexagonal, *P*6$_3$/*mmc*	Hexagonal, *P*6$_3$/*mmc*
Temperature (K)	293	
Pressure (GPa)	40(1)	40
a, *c* (Å)	3.0787 (19), 7.621 (5)	3.0922, 7.6267
V (Å^3)	62.56 (9)	63.15
Z	2	2
Radiation type	Synchrotron, λ = 0.3738 Å	
μ (mm^{-1})	11.32	
Crystal size (mm)	0.001 × 0.001 × 0.001	
Data collection		
Diffractometer	ESRF ID27, EIGER2 X CdTe 9M detector	
Absorption correction (essentially for absorption in diamonds and pressure medium)	Multi-scan *CrysAlis PRO* 1.171.41.120a (Rigaku Oxford Diffraction, 2021) Empirical absorption correction using spherical harmonics, implemented in SCALE3 ABSPACK scaling algorithm.	
T_{min}, T_{max}	0.617, 1	
No. of measured, independent and observed [$I > 2\sigma(I)$] reflections	90, 44, 41	
R_{int}	0.018	
$(\sin\theta/\lambda)_{max}$ (Å^{-1})	0.689	
Refinement		
$R[F^2 > 2\sigma(F^2)]$, $wR(F^2)$, *S*	0.045, 0.104, 1.24	
No. of reflections	44	
No. of parameters	5	
$\Delta\rho_{max}$, $\Delta\rho_{min}$ (e Å^{-3})	2.23, -5.92	

Crystal Structure							
	Wyckoff Site	Coordinates (x, y, z)	U_{iso} (Å^2)	Coordinates (x y z)			
Dy1	2*a*	0 0 1/2	0.0091(8)	0 0 1/2			
Cl1	2*c*	1/3 2/3 3/4	0.0115(10)	1/3 2/3 3/4			
Anisotropic displacement parameters							
Atom	U_{11} (Å^2)	U_{22} (Å^2)	U_{33} (Å^2)	U_{12} (Å^2)	U_{13} (Å^2)	U_{23} (Å^2)	
Dy1	0.0103(9)	0.0103(9)	0.0066(12)	0.0052(5)	0	0	
Cl1	0.0127(13)	0.0127(13)	0.0090(17)	0.0064(7)	0	0	

Supplementary Table 4. Crystal structure details of $FeCl_2$ at 160(1) GPa in comparison to the corresponding DFT-relaxed structure.

Crystal data		**DFT results**
Chemical formula	$FeCl_2$	$FeCl_2$
M_r	126.75	
Crystal system, space group	Cubic, $Pa\bar{3}$	Cubic, $Pa\bar{3}$
Temperature (K)	293	
Pressure (GPa)	160(1)	150
a (Å)	4.8289 (11)	4.8280
V (Å^3)	112.60 (8)	112.54
Z	4	4
No. of measured, independent and observed [$I > 2\sigma(I)$] reflections	288, 91, 84	
R_{int}	0.023	
$(\sin\theta/\lambda)_{max}$ (Å^{-1})	0.879	
$R[F^2 > 2\sigma(F^2)]$, $wR(F^2)$, *S*	0.038, 0.103, 1.23	
No. of reflections	91	
No. of parameters	6	
$\Delta\rho_{max}$, $\Delta\rho_{min}$ (e Å^{-3})	1.15, -0.94	
Crystal Structure		

	Wyckoff Site	Coordinates (x, y, z)	U_{iso} (Å^2)	Coordinates (x y z)
Fe1	4*b*	0 1/2 0	0.0080(4)	0 1/2 0
Cl1	8*c*	0.14803(15) 0.14803(15) 0.14803(15)	0.0080(4)	0.14731 0.14731 0.14731

Supplementary Table 5. Crystal structure, data collection and refinement details of Y_2ClC at 41(1) GPa in comparison to the corresponding DFT-relaxed structure.

Crystal data		**DFT results**
Chemical formula	Y_2ClC	Y_2ClC
M_r	225.28	
Crystal system, space group	Trigonal, $R\bar{3}m$	Trigonal, $R\bar{3}m$
Temperature (K)	293	
Pressure (GPa)	41(1)	40
a, *c* (Å)	3.3690 (7), 17.703 (6)	3.3842, 17.8335
V (Å^3)	174.01 (10)	176.88
Z	3	3
Radiation type	Synchrotron, λ = 0.41015 Å	
μ (mm^{-1})	12.06	
Crystal size (mm)	0.001 × 0.001 × 0.001	
Data collection		
Diffractometer	ESRF ID15b, EIGER2 X 9M CdTe detector	
Absorption correction (essentially for absorption in diamonds and pressure medium)	Multi-scan *CrysAlis PRO* 1.171.40.67a (Rigaku Oxford Diffraction, 2019) Empirical absorption correction using spherical harmonics, implemented in SCALE3 ABSPACK scaling algorithm.	
T_{min}, T_{max}	0.299, 1	
No. of measured, independent and observed [$I > 2\sigma(I)$] reflections	117, 53, 51	
R_{int}	0.042	
$(\sin\theta/\lambda)_{max}$ (Å^{-1})	0.713	

Refinement							
$R[F^2 > 2\sigma(F^2)]$, $wR(F^2)$, S	0.050, 0.125, 1.20						
No. of reflections	53						
No. of parameters	8						
$\Delta\rho_{max}$, $\Delta\rho_{min}$ (e Å^{-3})	1.93, -1.74						
Crystal Structure							
	Wyckoff Site	Coordinates (x, y, z)	U_{iso} (Å^2)	Coordinates (x y z)			
Y1	6*c*	0 0 0 0.23654(9)	0.0140(9)	0 0 0.23619			
Cl1	3*a*	0 0 0	0.0148(16)	0 0 0			
C1	3*b*	0 0 1/2	0.006(5)	0 0 1/2			
Anisotropic displacement parameters							
Atom	U_{11} (Å^2)	U_{22} (Å^2)	U_{33} (Å^2)	U_{12} (Å^2)	U_{13} (Å^2)	U_{23} (Å^2)	
Y1	0.0140(11)	0.0140(11)	0.0142(13)	0.0070(5)	0	0	
Cl1	0.014(2)	0.014(2)	0.016(4)	0.0071(10)	0	0	
C1	0.007(7)	0.007(7)	0.005(11)	0.003(3)	0	0	

Supplementary Table 6. Crystal structure, data collection and refinement details of Dy_2ClC at 40(1) GPa in comparison to the corresponding DFT-relaxed structure.

Crystal data		**DFT results**
Chemical formula	Dy_2ClC	Dy_2ClC
M_r	372.46	
Crystal system, space group	Trigonal, $R\bar{3}m$	Trigonal, $R\bar{3}m$
Temperature (K)	293	
Pressure (GPa)	40(1)	40
a, *c* (Å)	3.3193 (7), 18.004 (10)	3.3743, 18.0156
V (Å^3)	171.79 (12)	177.64
Z	3	3
Radiation type	Synchrotron, λ = 0.3738 Å	

μ (mm^{-1})	11.80						
Crystal size (mm)	0.003 × 0.003 × 0.003						
Data collection							
Diffractometer	ESRF ID27, EIGER2 X CdTe 9M detector						
Absorption correction (essentially for absorption in diamonds and pressure medium)	Multi-scan *CrysAlis PRO* 1.171.41.120a (Rigaku Oxford Diffraction, 2021) Empirical absorption correction using spherical harmonics, implemented in SCALE3 ABSPACK scaling algorithm.						
T_{min}, T_{max}	0.64, 1						
No. of measured, independent and observed [$I > 2\sigma(I)$] reflections	121, 121, 120						
R_{int}	0.015						
$(\sin\theta/\lambda)_{max}$ ($Å^{-1}$)	0.893						
Refinement							
$R[F^2 > 2\sigma(F^2)]$, $wR(F^2)$, S	0.037, 0.095, 1.16						
No. of reflections	121						
No. of parameters	8						
$\Delta\rho_{max}$, $\Delta\rho_{min}$ (e $Å^{-3}$)	2.87, -2.34						
Crystal Structure							
	Wyckoff Site	Coordinates (x, y, z)	U_{iso} ($Å^2$)	Coordinates (x y z)			
Dy1	6*c*	0 0 0.23608(7)	0.0108(5)	0 0 0.23595			
Cl1	3*a*	0 0 0	0.0115(15)	0 0 0			
C1	3*b*	0 0 1/2	0.010(5)	0 0 1/2			
Anisotropic displacement parameters							
Atom	U_{11} ($Å^2$)	U_{22} ($Å^2$)	U_{33} ($Å^2$)	U_{12} ($Å^2$)	U_{13} ($Å^2$)	U_{23} ($Å^2$)	
Dy1	0.0125(5)	0.0125(5)	0.0074(12)	0.0063(2)	0	0	
Cl1	0.0152(18)	0.0152(18)	0.004(6)	0.0076(9)	0	0	

Supplementary Table 7. Calculated enthalpies (eV) per Y atom of the $R\bar{3}m$ and $P6_3/mmc$[1] Y_2ClC.

Pressure	ΔH/Y atom ($R\bar{3}m$ Y_2ClC) (eV/atom)	ΔH/Y atom ($P6_3/mmc$ Y_2ClC) (eV/atom)
0	-14.2021	-14.2110
2	-13.7204	-13.7279
4	-13.2503	-13.2561
6	-12.7906	-12.7944
8	-12.3403	-12.3418
10	-11.8982	-11.8973
20	-9.7887	-9.7751
30	-7.8089	-7.7829
40	-5.9272	-5.8899

Supplementary Table 8. Unit cell parameters of the phases observed after laser-heating of Re and NaCl at 38(1) GPa (DAC 3, see Table S1).

Domain number	*a b c* (Å)	*α β γ* (°)	*V* (Å^3)
1	2.689(12) 9.225(14) 3.531(6)	90 90 90	87.58(4)
2	8.091(12) 7.138(11) 12.925(15)	90 95.05(3) 90	743.60(9)
3	4.803(7) 4.803(7) 4.803(7)	90 90 90	110.81(3)

Supplementary Table 9. Comparison of unit cell parameters (in hexagonal setting) and some bond lengths of $R\bar{3}m$ Y_2ClC, $R\bar{3}m$ Y_2Cl, $R\bar{3}m$ Dy_2ClC, and $R\bar{3}m$ Dy_2Cl at 40 GPa.

DFT model	Y_2ClC	Y_2Cl	DFT model	Dy_2ClC	Dy_2Cl
Space group	$R\bar{3}m$	$R\bar{3}m$	Space group	$R\bar{3}m$	$R\bar{3}m$
a (Å)	3.38	3.10	*a* (Å)	3.37	3.08
c (Å)	17.83	19.17	*c* (Å)	18.02	19.37
V (Å^3)	176.88	159.91	*V* (Å^3)	177.64	159.42
Y1-Y1 (Å)	3.157	3.057	Dy1-Dy1 (Å)	3.166	3.059
Y1-Y2 (Å)	3.384	3.104	Dy1-Dy2 (Å)	3.374	3.083
Y1-Y3 (Å)	3.978	4.304	Dy1-Dy3 (Å)	4.013	4.35

Y1-Cl1 (Å)	2.611	2.653	Dy1-Cl1 (Å)	2.622	2.666
Y1-C1 (Å)	2.314	-	Dy1-C1 (Å)	2.314	-
Y1-e^- (Å)*	-	2.178	Dy1-e^- (Å)*	-	2.171

*indicates that the position of e^- is the center of anionic electrons.

Supplementary Figures

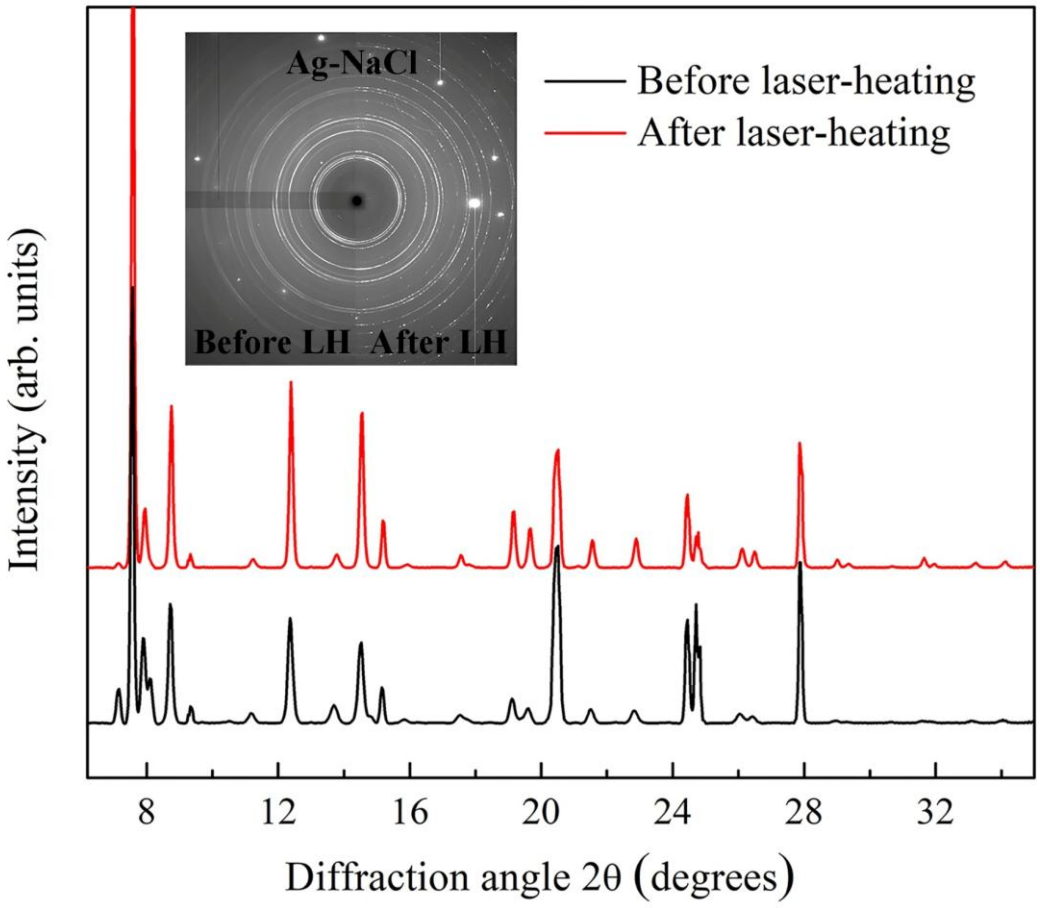

Supplementary Figure 1. Powder X-ray diffraction patterns of the Ag-NaCl sample before (black) and after (red) laser-heating at ~1950 K and 44 GPa. The patterns are similar, giving no indication of a chemical reaction. 2D XRD patterns in the inset show that the sample re-crystallized after laser heating, the single-crystal data we obtained from the laser-heated area are only of the cubic Ag and B2-NaCl.

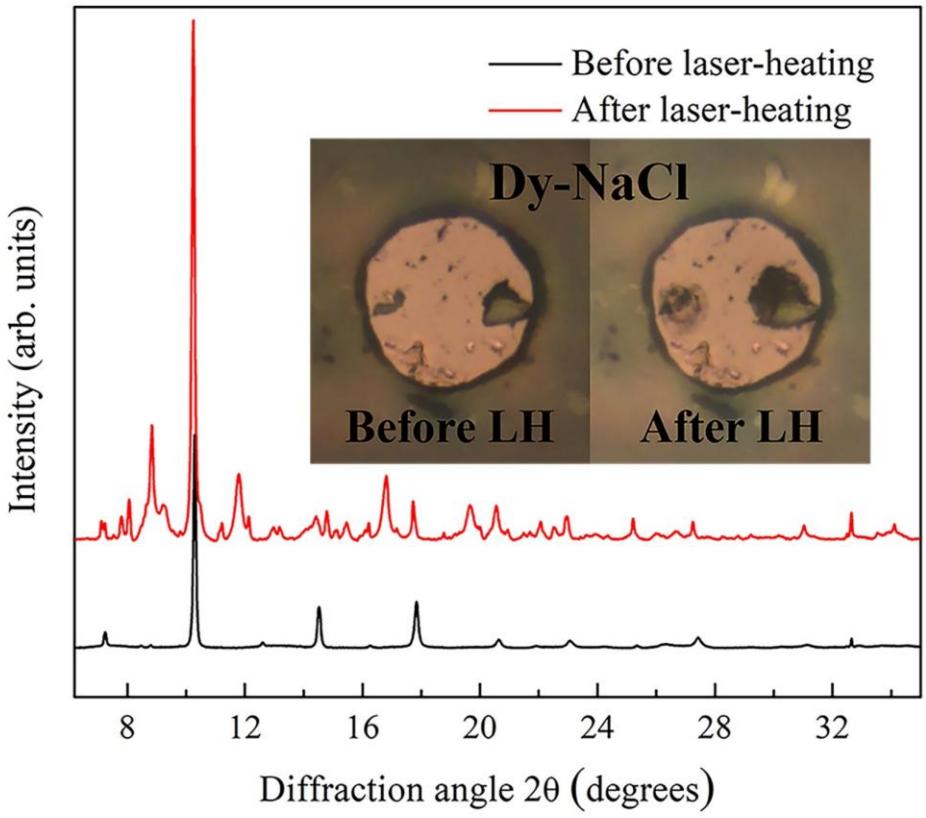

Supplementary Figure 2. Powder X-ray diffraction patterns of the Dy-NaCl sample before (black) and after (red) laser-heating at ~2000 K and 40 GPa. Inserts are optical photographs of the Dy-NaCl sample, demonstrating the production of additional products around the laser-heated area.

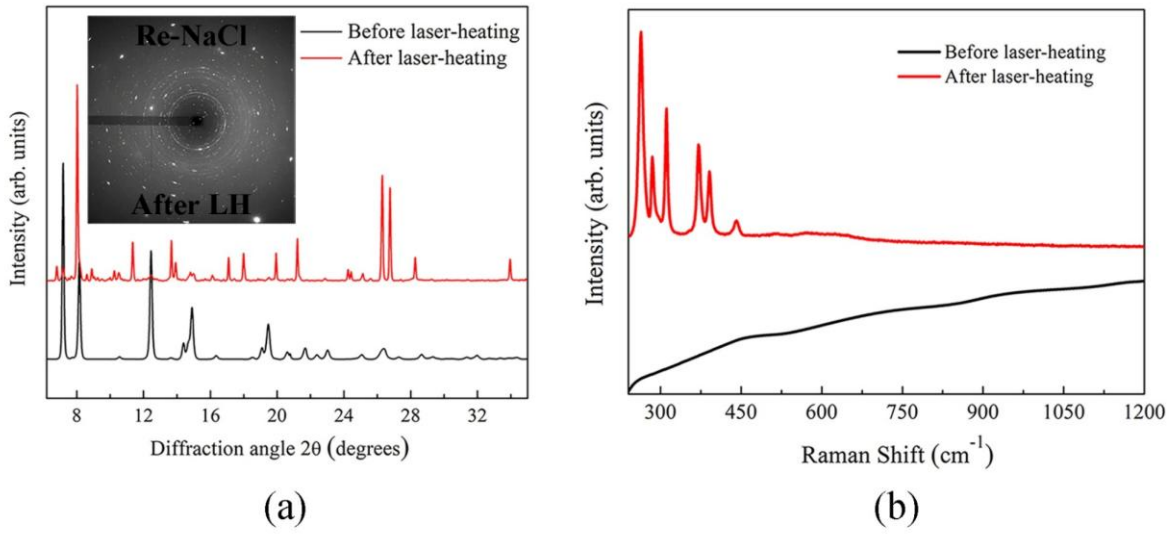

Supplementary Figure 3. (a) Powder X-ray diffraction patterns of the Re-NaCl sample before (black) and after (red) laser-heating at ~2100 K and 38 GPa. Insert shows a 2D XRD pattern

of the sample after its laser heating. (b) Raman spectrum of the Re-NaCl sample before and after laser-heating. Both the XRD pattern and the Raman spectrum give evidence of the chemical alteration of the sample. Using single-crystal X-ray diffraction data, we were able to determine the unit cell parameters of the new phases (see Supplementary Table 8). However, no reliable structural solutions were obtained.

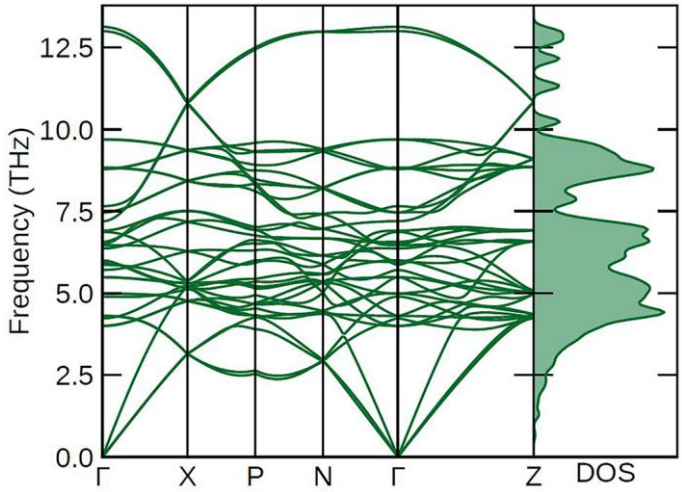

Supplementary Figure 4. Phonon dispersion curves along high-symmetry directions in the Brillouin zone and phonon density of states for Y_2Cl calculated at 40 GPa.

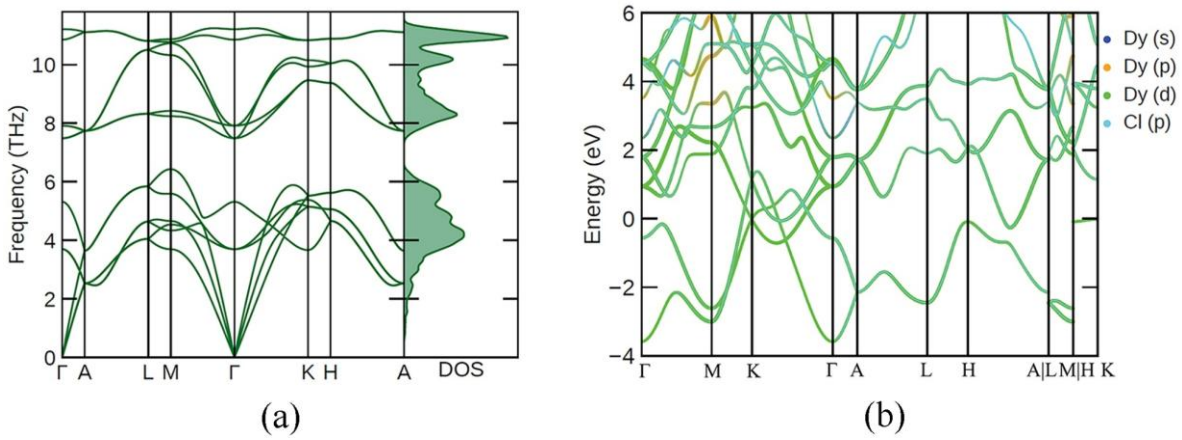

Supplementary Figure 5. (a) Phonon dispersion curves along high-symmetry directions in the Brillouin zone and phonon density of states for DyCl calculated at 40 GPa; (b) Calculated band structure of DyCl at 40 GPa. The Fermi energy level was set to 0 eV.

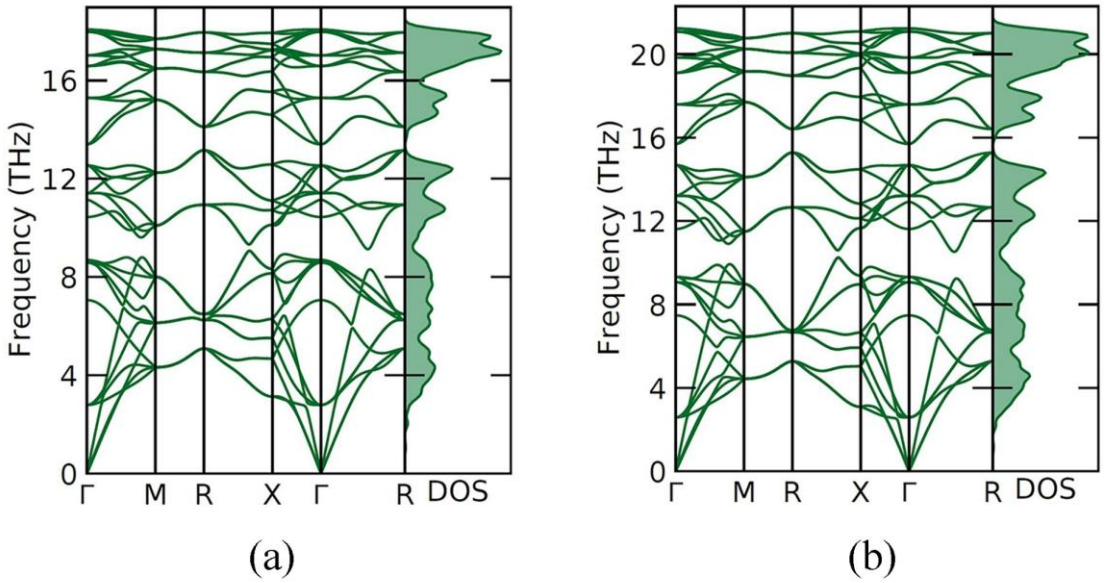

Supplementary Figure 6. Phonon dispersion curves along high-symmetry directions in the Brillouin zone and phonon density of states for $FeCl_2$ calculated at (a) 90 GPa and (b) 150 GPa.

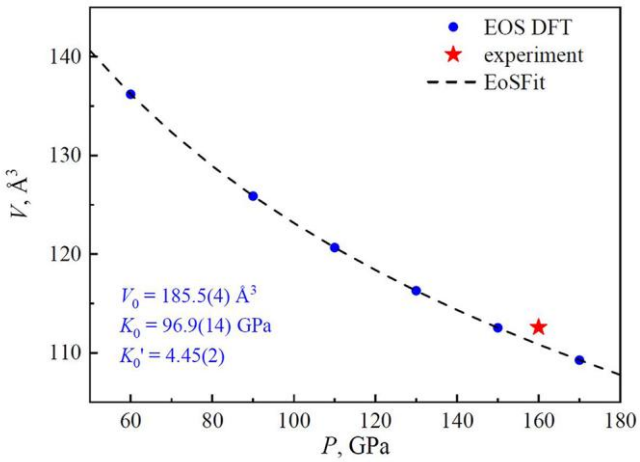

Supplementary Figure 7. Calculated (blue) and experimental (red) pressure-volume dependence of $Pa\bar{3}$ $FeCl_2$. Dashed lines represent the third-order Birch Murnaghan fit of the results.

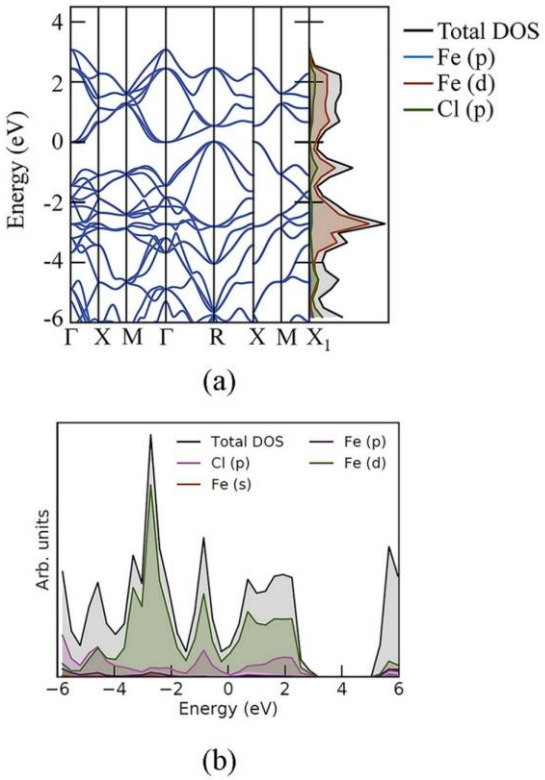

Supplementary Figure 8. (a) Calculated band structure and electron density of states of $FeCl_2$ at 150 GPa; (b) TDOS and PDOS curves of $FeCl_2$ at 150 GPa. The Fermi energy level was set to 0 eV.

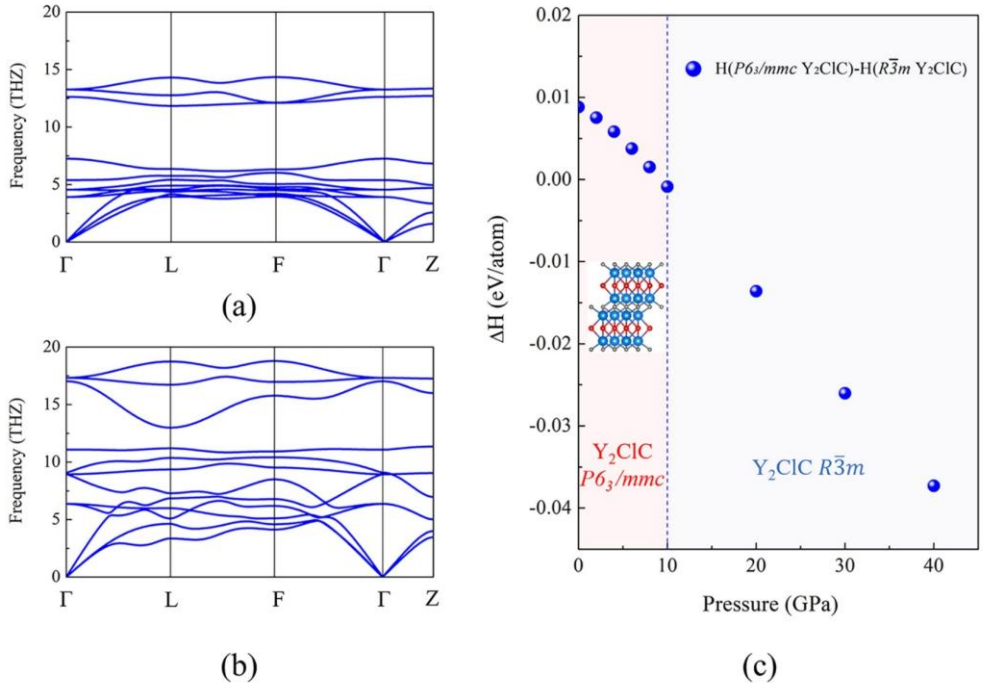

Supplementary Figure 9. Phonon dispersion curves along high-symmetry directions in the Brillouin zone for $R\bar{3}m$ Y_2ClC calculated at (a) 0 GPa and (b) 40 GPa. (c) The calculated difference in enthalpy per Y atom (ΔH=H($P6_3/mmc$ Y_2ClC)-H($R\bar{3}m$ Y_2ClC)) as a function of pressure.

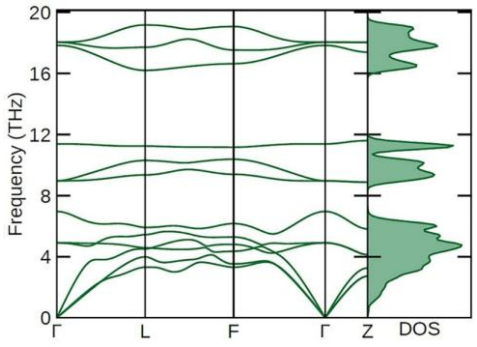

Supplementary Figure 10. Phonon dispersion curves along high-symmetry directions in the Brillouin zone and phonon density of states for $R\bar{3}m$ Dy_2ClC calculated at 40 GPa.

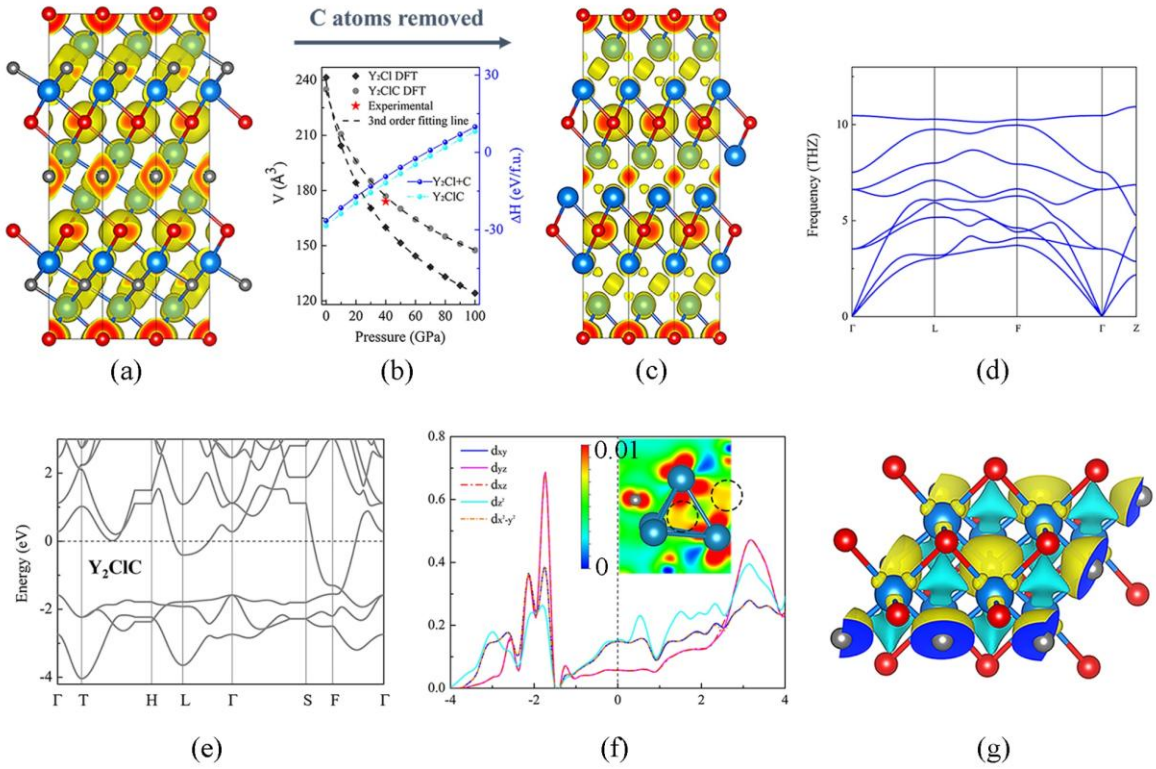

Supplementary Figure 11. (a) The electron localization function (ELF) of Y_2ClC with the isosurfaces value of 0.6; (b) The pressure dependence of the unit cell volume of $R\bar{3}m$ Y_2Cl and Y_2ClC (with left axis) and the calculated enthalpies per formula unit (f.u.) of the reactants and products of reaction $Y_2Cl + C \rightarrow Y_2ClC$ (with right axis); (c) ELF of $R\bar{3}m$ Y_2Cl with the isosurfaces value of 0.6; (d) Phonon dispersion curves along high-symmetry directions in the Brillouin zone and phonon density of states for $R\bar{3}m$ Y_2Cl calculated at 40 GPa; (e) Calculated band structure of $R\bar{3}m$ Y_2ClC at 40 GPa. The Fermi energy level was set to 0 eV. (f) The PDOS curves of the Y-*d* orbitals. The Fermi energy level was set to 0 eV. Insert shows theY_4 tetrahedron and the partial charge density map in the (1 0 -1) plane (rhombohedral setting) around the Fermi level (-1 eV < E-E_F < 0 eV). The black circles emphasize the Y-*d* orbital overlapping in the Y_4 tetrahedron. (g) Charge density difference for C atoms inserted in $R\bar{3}m$ Y_2Cl. Yellow indicates regions of charge gain and blue indicates regions of charge loss.

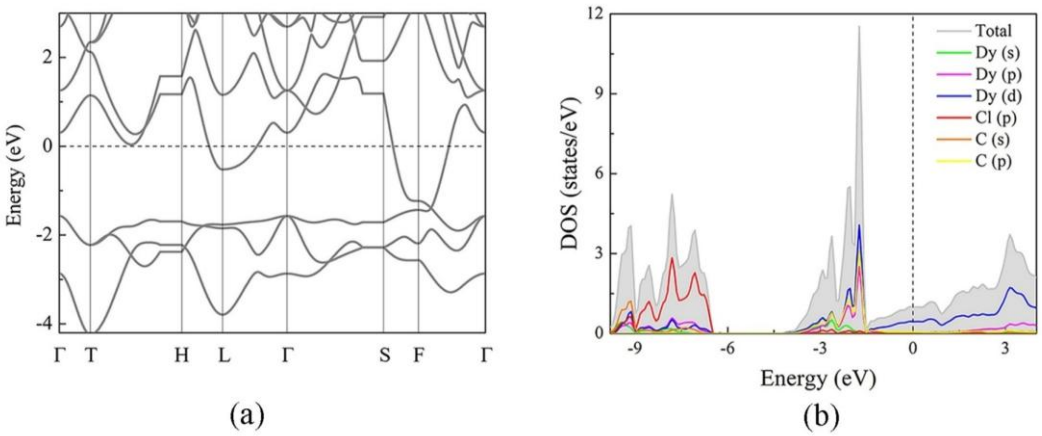

Supplementary Figure 12. (a) Calculated band structure of Dy_2ClC at 40 GPa; (b) TDOS and PDOS curves of Dy_2ClC at 40 GPa. The Fermi energy level was set to 0 eV.

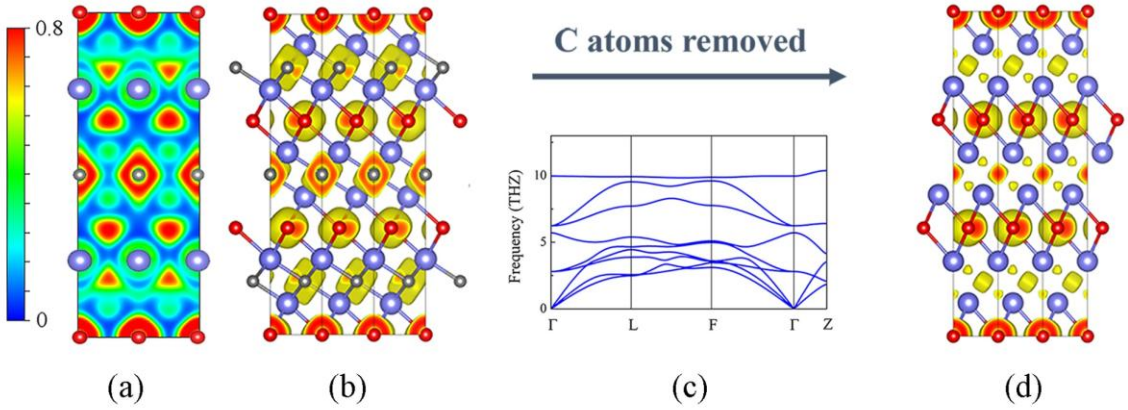

Supplementary Figure 13. (a) The 2D ELF map of Dy_2ClC (1 0 0) plane; (b) ELF of Dy_2ClC with the isosurfaces value of 0.6; (c) Phonon dispersion curves along high-symmetry directions in the Brillouin zone for $R\bar{3}m$ Dy_2Cl calculated at 40 GPa; (d) ELF of $R\bar{3}m$ Dy_2Cl with the isosurfaces value of 0.6.

Supplementary Discussion

Electronic properties of Y_2ClC and Dy_2ClC.

With the C atoms removed in this novel $R\bar{3}m$ Y_2ClC compound, DFT calculations succeeded in optimizing this novel $R\bar{3}m$ Y_2Cl structure. The anionic electrons (Supplementary Figure 11c) perfectly localized in the place of the C atoms in Y_2ClC (Supplementary Figure 11a). The equation of states (EoS) of Y_2ClC and Y_2Cl together with the enthalpies of reactants and product of the reaction ($Y_2Cl + C \rightarrow Y_2ClC$) were shown in Supplementary Figure 11b, which further explained that in the experiments we synthesized the Y_2ClC compound. Notably,

the electride $R\bar{3}m$ Y_2Cl is also a dynamically stable structure at 40 GPa (Supplementary Figure 11d). Like the $R\bar{3}m$ YCl studied by Wan et al.[2], $R\bar{3}m$ Y_2Cl also has two ELF attractors in the centers of the Y_4 tetrahedra and Y_6 octahedra (Supplementary Figure 11c). It is obvious that even though the introduction of the C layers in $R\bar{3}m$ Y_2ClC elongates the Y-Y bond length, the electron localization in the Y_4 tetrahedra caused by the *d*-orbital overlapping still exist (Supplementary Figure 11 e-f). An intuitive display of the charge transfer after the introduction of C atoms can be obtained from Supplementary Figure 11g, which is consistent with the above analysis. Introduction of the C atoms causes charge loss in the blue region (Y_4 tetrahedra) and charge gain in the yellow region (Y_6 octahedra), leaving a weak electron bridge in Figure 4b.

The band structure and the DOS curves of Dy_2ClC (Supplementary Figure 12) show a very close distribution pattern with Y_2ClC. The hybridization of the Dy-*d* orbitals disperses electrons at the Fermi level (E_F), leading to the metallic phase. Similar features of the electron bridges in ELF induced by the Dy *d*-orbital are shown in Supplementary Figure 13. Likewise, if the C atoms are removed, the dynamically stable structure $R\bar{3}m$ Dy_2Cl (Supplementary Figure 13c) will be obtained after the structure optimization at 40 GPa.

The introduction of C atoms clearly affects the bond length in the layered structure (see Supplementary Table 9). Due to the larger volume of C atoms, the distances between the first (Y1/Dy1-Y1/Dy1) and second (Y1/Dy1-Y2/Dy2) neighboring Y/Dy atoms become longer with the addition of C atoms, thus providing a larger Y_6/Dy_6 octahedra volume for C atoms. But the metal-Cl bond lengths (Y1/Dy1-Cl1) and the distances between the two metal layers (Y1/Dy1-Y3/Dy3) connecting the chlorine atoms become smaller. This also leads to the compression of the unit cell parameters on the *c*-axis after the introduction of C atoms, which means that there is a stronger binding force between the layers, making Y_2ClC/Dy_2ClC a more favoured phase.

Supplementary References

1. Ohmer, D., Qiang, G., Opahle, I., Singh, H. K. & Zhang, H. High-throughput design of 211-M2AX compounds. *Phys. Rev. Mater.* **3**, 053803 (2019).
2. Wan, B. *et al.* Identifying quasi-2D and 1D electrides in yttrium and scandium chlorides via geometrical identification. *npj Comput. Mater.* **4**, 77 (2018).

List of all author publications

[1] Y. Yin, **F. I. Akbar**, E. Bykova, A. Aslandukova, D. Laniel, A. Aslandukov, M. Bykov, M. Hanfland, G. Garbarino, Z. Jia, L. Dubrovinsky, N. Dubrovinskaia, Synthesis of Rare-Earth Metal Compounds through Enhanced Reactivity of Alkali Halides at High Pressures, *Communications Chemistry*, 5, 8–13 (2022), DOI: 10.1038/s42004-022-00736-x.

[2] A. Aslandukova, A. Aslandukov, D. Laniel, S. Khandarkhaeva, G. Steinle-Neumann, T. Fedotenko, S. V. Ovsyannikov, Y. Yin, **F. I. Akbar**, K. Glazyrin, M. Hanfland, L. Dubrovinsky, N. Dubrovinskaia, High-pressure *hP*3 yttrium allotrope with $CaHg_2$-type structure as a prototype of the *hP*3 rare-earth hydride series, *Physical Review B*, 107, 014103 (2023), DOI: 10.1103/PhysRevB.107.014103.

[3] Y. Yin, A. Aslandukova, N. Jena, F. Trybel, I. A. Abrikosov, B. Winkler, S. Khandarkhaeva, T. Fedotenko, E. Bykova, D. Laniel, M. Bykov, A. Aslandukov, **F. I. Akbar**, K. Glazyrin, G. Garbarino, C. Giacobbe, E. L. Bright, Z. Jia, L. Dubrovinsky, N. Dubrovinskaia, Unraveling the Bonding Complexity of Polyhalogen Anions: High-Pressure Synthesis of Unpredicted Sodium Chlorides Na_2Cl_3 and Na_4Cl_5 and Bromide Na_4Br_5, *JACS Au*, 3, 1634-1641 (2023), DOI: 10.1021/jacsau.3c00090.

[4] **F. I. Akbar**, A. Aslandukova, A. Aslandukov, Y. Yin, F. Trybel, S. Khandarkhaeva, T. Fedotenko, D. Laniel, M. Bykov, E. Bykova, N. Dubrovinskaia, L. Dubrovinsky, High-Pressure Synthesis of Dysprosium Carbides, *Frontiers in Chemistry*, 11, 1–9 (2023), DOI: 10.3389/fchem.2023.1210081.

[5] A. Aslandukov, P. L. Jurzick, M. Bykov, A. Aslandukova, A. Chanyshev, D. Laniel, Y. Yin, **F. I. Akbar**, S. Khandarkhaeva, T. Fedotenko, K. Glazyrin, S. Chariton, V. Prakapenka, F. Wilhelm, A. Rogalev, D. Comboni, M. Hanfland, N. Dubrovinskaia, L. Dubrovinsky, Stabilization Of The CN_3^{5-} Anion In Recoverable High-pressure $Ln_3O_2(CN_3)$ (Ln=La, Eu, Gd, Tb, Ho, Yb) Oxoguanidinates, *Angewandte Chemie International Edition*, 62, 1-7 (2023), DOI: 10.1002/anie.202311516.

[6] Y. Yin, A. Aslandukov, M. Bykov, D. Laniel, A. Aslandukova, A. Pakhomova, T. Fedotenko, W. Zhou, **F. I. Akbar**, M. Hanfland, K. Glazyrin, C. Giacobbe, E. L. Bright, G. Garbarino, Z. Jia, N. Dubrovinskaia, L. Dubrovinsky, Polytypism of Incommensurately Modulated Structures of Crystalline Bromine upon Molecular Dissociation under High Pressure, preprint, DOI: 10.48550/arXiv.2311.12966.

[7] D. Laniel, F. Trybel, A. Aslandukov, S. Khandarkhaeva, T. Fedotenko, Y. Yin, N. Miyajima, F. Tasnádi, A. V. Ponomareva, N. Jena, **F. I. Akbar**, B. Winkler, A. Néri, S.

Chariton, V. Prakapenka, V. Milman, W. Schnick, A. N. Rudenko, M. I. Katsnelson, I. A. Abrikosov, Leonid Dubrovinsky, Natalia Dubrovinskaia, Synthesis of Ultra-Incompressible and Recoverable Carbon Nitrides Featuring CN_4 Tetrahedra, *Advanced Materials*, 36, 2308030 (2024), DOI: 10.1002/adma.202308030.

[8] A. Aslandukov, A. Aslandukova, D. Laniel, S. Khandarkhaeva, Y. Yin, **F. I. Akbar**, S. Chariton, V. Prakapenka, E. L. Bright, C. Giacobbe, J. Wright, D. Comboni, M. Hanfland, Natalia Dubrovinskaia, L. Dubrovinsky, Stabilization of N_6 and N_8 anionic units and 2D polynitrogen layers in high-pressure scandium polynitrides, *Nature Communications*, 15, 2244 (2024), DOI: 10.1038/s41467-024-46313-9.

[9] A. Aslandukova, A. Aslandukov, D. Laniel, Y. Yin, **F. I. Akbar**, M. Bykov, T. Fedotenko, K. Glazyrin, A. Pakhomova, G. Garbarino, E. L. Bright, J. Wright, M. Hanfland, S. Chariton, V. Prakapenka, N. Dubrovinskaia, L. Dubrovinsky, Diverse high-pressure chemistry in Y- NH_3BH_3 and Y–paraffin oil systems, *Science Advances*, 10, eadl5416 (2024), DOI: 10.1126/sciadv.adl5416.

[10] S. Khandarkhaeva, T. Fedotenko, A. Aslandukova, **F. I. Akbar**, M. Bykov, D. Laniel, A. Aslandukov, U. Ruschewitz, C. Tobeck, B. Winkler, S. Chariton, V. Prakapenka, K. Glazyrin, C. Giacobbe, E. L. Bright, M. Belov, N. Dubrovinskaia, L. Dubrovinsky, Extending carbon chemistry at high-pressure by synthesis of CaC_2 and Ca_3C_7 with deprotonated polyacene- and para-poly(indenoindene)-like nanoribbons, *Nature Communications*, 15, 2855 (2024), DOI: 10.1038/s41467-024-47138-2.

[11] X. Li, E. Bykova, D. Vasiukov, G. Aprilis, S. Chariton, V. Cerantola, M. Bykov, S. Müller, A. Pakhomova, **F. I. Akbar**, Elena Mukhina, I. Kantor, K. Glazyrin, D. Comboni, A. I. Chumakov, C. McCammon, L. Dubrovinsky, C. Sanchez-Valle, I. Kupenko, Monoclinic distortion and magnetic transitions in FeO under pressure and temperature, preprint, (under review at *Nature Portfolio*), DOI: 10.21203/rs.3.rs-4102447/v1.

[12] **F. I. Akbar**, A. Aslandukova, Y. Yin, A. Aslandukov, D. Laniel, E. Bykova, M. Bykov, E. L. Bright, J. Wright, D. Comboni, M. Hanfland, N. Dubrovinskaia, L. Dubrovinsky, High-Pressure Dysprosium Carbides Containing Carbon Dimers, Trimers, Chains, and Ribbons. Submitted to *Carbon*.

[13] **F. I. Akbar**, A. Aslandukova, A. Aslandukov, Y. Yin, E. Bykova, M. Bykov, D. Laniel, P. Milkin, W. Zhou, T. Fedotenko, K. Glazyrin, H.-P. Liermann, E. L. Bright, J. Wright, A. Pakhomova, G. Garbarino, M. Mezouar, S. Chariton, V. Prakapenka, D. Comboni, M. Hanfland, N. Dubrovinskaia, L. Dubrovinsky, High-Pressure Synthesis of Rare-Earth Metals Carbides Featuring Carbon Polyanions. To be submitted to *JACS*.

(Eidesstattliche) Versicherungen und Erklärungen

(§ 9 Satz 2 Nr. 3 PromO BayNAT)

Hiermit versichere ich eidesstattlich, dass ich die Arbeit selbstständig verfasst und keine anderen als die von mir angegebenen Quellen und Hilfsmittel benutzt habe (vgl. Art. 97 Abs. 1 Satz 8 BayHIG).

(§ 9 Satz 2 Nr. 3 PromO BayNAT)

Hiermit erkläre ich, dass ich die Dissertation nicht bereits zur Erlangung eines akademischen Grades eingereicht habe und dass ich nicht bereits diese oder eine gleichartige Doktorprüfung endgültig nicht bestanden habe.

(§ 9 Satz 2 Nr. 4 PromO BayNAT)

Hiermit erkläre ich, dass ich Hilfe von gewerblichen Promotionsberatern bzw. -vermittlern oder ähnlichen Dienstleistern weder bisher in Anspruch genommen habe noch künftig in Anspruch nehmen werde.

(§ 9 Satz 2 Nr. 7 PromO BayNAT)

Hiermit erkläre ich mein Einverständnis, dass die elektronische Fassung meiner Dissertation unter Wahrung meiner Urheberrechte und des Datenschutzes einer gesonderten Überprüfung unterzogen werden kann.

(§ 9 Satz 2 Nr. 8 PromO BayNAT)

Hiermit erkläre ich mein Einverständnis, dass bei Verdacht wissenschaftlichen Fehlverhaltens Ermittlungen durch universitätsinterne Organe der wissenschaftlichen Selbstkontrolle stattfinden können.

…….
Ort, Datum, Unterschrift